CENTRO DE INVESTIGACIONES
EN OPTICA, A.C.

“PROFILOMETRY OF SOLIDS UTILIZING STEREO PROJECTION AND CO-PHASE OF STRUCTURED LIGHT”

Tesis que para obtener el grado de Doctor en Ciencias (Óptica)

Presenta: Sotero Ordoñes Nogales

Director de Tesis: Dr. Manuel Servín Guirado

León · Guanajuato · México
Julio de 2021

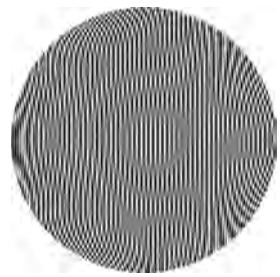

A mi Mamá y a mi Papá...
gracias por enseñarme que
a veces conviene soñar...

Acknowledgments

...Bueno es dar cuando nos piden; pero mejor es dar sin que nos pidan, como buenos entendedores...

Gibrán Khalil Gibrán

He llegado al final de una pequeña travesía en el viaje de la vida; durante este trayecto he adquirido experiencia que han dejado estelas imborrables. Este marinero no es nadie sin la ayuda de aquellos que lo han acompañado en el barco. Quiero agradecer a esas personas con las que no sólo compartí este viaje, sino colaboraron en la toma del rumbo, me refiero a la tripulación:

A mi familia. Por estar allí siempre apoyándome, toda la paciencia y esfuerzo que han realizado para ver cumplido este sueño. **Mi pitufina** por siempre estar allí apoyándome con una sonrisa como solo ella sabe; espero todo esto te haga sonreir.

Al Dr. Manuel Servin. Gracias por todas las lecciones y su dedicación para esclarecer los temas de interferometría digital y proyección de franjas. Por hacer de esta estancia en el CIO toda una experiencia académica y personal.

Al grupo de investigación que pertenezco: los doctores Moisés Padilla, Guillermo Garnica, Iván Choque, José Antonio Muñoz y Jorge Luis Flores. Gracias por su apoyo y su tiempo invertido en la discusión de tantos temas de metrología óptica como de técnicas experimentales.

A mis sinodales: los doctores Abundio Dávila, Apolinar Muñoz, Francisco Cuevas y Amalia Martínez. Gracias por su apoyo como parte del comite de seguimiento doctoral de un servidor. También agradezco todos sus comentarios y cuestionamientos que me permitieron mejorar este proyecto.

To John Kang, Ph.D. Thanks for the opportunity to do a academic stay in San Diego State University.

Para llevar a puerto esta pequeña embarcación, colaboraron personas como los doctores Abimael Jiménez y Omar Aguilar a quienes agradezco no solo por sus valiosas revisiones a la presente y a los artículos publicados sino también por su amistad. En el mismo sentido, a mis compañeros de laboratorio Monse, Chente, Chava, así como a los doctores David Monzón, David Moreno y Geminiano Ponce entre muchas otras personas que por

ahora me es imposible nombrar; gracias por todos esos momentos que hicieron divertida la travesía. También quiero agradecer al Centro de Investigaciones en Óptica (CIO) por las facilidades y recursos asignados. A Mario Ruiz por sus valiosas correcciones a mis artículos; a Carlos Pérez por su apoyo con el manejo del equipo Wyko. En especial quiero agradecer al Consejo Nacional de Ciencia y Tecnología (CONACyT) por poner el combustible del barco a través de mi beca doctoral.

...Debe haber algo extrañamente sagrado en la sal: está en nuestras lágrimas y en el mar...

Gibrán Khalil Gibrán

Abstract

Measurement of three-dimensional objects has become a current industrial issue to improve manufacturing verification processes and reverse engineering. Measurements should not modify or influence the manufacturing lines; therefore, they should be high-quality, high-speed, and online. Hence, fringe projection profilometers (FPPs) have become a feasible solution because of their low-cost hardware, speed, and proficiency to measure static and dynamic objects. FPPs can be straightforwardly implemented with a multimedia projector and a digital camera.

Initially, most proposals acquire one image to be processed digitally later using spatial filtering. Although they can achieve the speed goal, the estimation quality can be deficient for complex shapes. In order to improve the reconstruction quality, several techniques have proposed color encoding to project and acquire three images. They are later processed by phase-shifting algorithms (PSAs). It is noticeable that these FPPs fulfill the high-speed requirement. Nonetheless, they must also have a very well-calibrated system and satisfy the following conditions: (1) non-linear intensity distortion, (2) shapes with a good diffuse reflection function, (3) avoidance or calibration of cross-talking problems, and (4) a geometry configuration eliminating/reducing self-occluding shadows. Industrial items or applications usually do not accomplish these requirements.

This thesis introduces an FPP (a proof-of-the-concept) gathering the above four requirements and performing online measurements. This FPP can also estimate or inspect a shape in a rectilinear uniform motion. The inspection is carried out by comparing a testing shape to a calibrated one with a proposed technique.

When reconstructing industrial items, this FPP needs a temporal sequence of phase-shifted fringe patterns (PS-FPs). The PS-FPs are obtained by translating the item's movements to a phase shift through image registration. The latter is done by computing a rough estimation of the shape for each pattern. Later, a pixel matching method translates the acquired images into PS-FPs. Hence, one can employ the PSAs' framework for phase/shape retrieval in the classical sense, considering that shapes are static. We proposed several PSAs with their spectral description and analysis to correctly retrieve the phase and phase differences from the observed patterns. By acquiring many PS-FPs, the first and second conditions are overcome. By encoding in the red and blue channels, the third requirement is met. The last one is addressed by using a co-phased technique having two projectors and a camera. This technique is a contribution to this thesis.

List of publications

Articles

- A. Muñoz, J. L. Flores, G. Parra-Escamilla, L. A. Morales, **S. Ordones**, and M. Servin, "Least-squares gamma estimation in fringe projection profilometry," Appl. Opt., vol. 60, no. 5, 1137–1142, 2021.
- **S. Ordones**, M. Servin, M. Padilla, I. Choque, A. Muñoz, and J. L. Flores, "Tukey's robust m-estimator for phase demodulation of interferograms with nonuniform shifts," Appl. Opt., vol. 59, no. 20, pp. 6224–6230, 2020.
- **S. Ordones**, M. Servin, M. Padilla, I. Choque, J. L. Flores, and A. Muñoz,"Shape defect measurement by fringe projection profilometry and phase-shifting algorithms," Optical Engineering, vol. 59, no. 1, pp. 1–10, 2020.
- I. Choque, M. Padilla, M. Servin, M. Asmad, and **S. Ordones**, "Suppressing ripple distortions and spurious pistons in phase-shifting interferometry," J. Opt. Soc. Am. A, vol. 37, no. 4, 614–620, 2020.
- **S. Ordones**, M. Servin, M. Padilla, A. Muñoz, J. L. Flores, and I. Choque, "Spectral analysis for the generalized least squares phase-shifting algorithms with harmonic robustness," Opt. Lett., vol. 44, no. 9, pp. 2358–2361, 2019.
- I. Choque, M. Servin, M. Padilla, M. Asmad, and **S. Ordones**, "Phase measurement of nonuniform phase-shifted interferograms using the frequency transfer function," Appl. Opt., vol. 58, no. 15, 4157–4162, 2019.
- M. Servin, M. Padilla, I. Choque, and **S. Ordones**, "Phase-stepping algorithms for synchronous demodulation of nonlinear phase-shifted fringes," Opt. Express, vol. 27, no. 4, 5824–5834, 2019.
- A. Muñoz, **S. Ordoñes**, J. L. Flores, O. Aguilar, and A. Jimenez, "Esquemas de corrimiento de fase: estudio comparativo,", Acta Universitaria, vol. 29, e2627, 2019.
- J. L. Flores, M. Stronik, A. Muñoz, G. Garcia-Torales, **S. Ordoñes**, and A. Cruz, "Dynamic 3d shape measurement by iterative phase shifting algorithms and colored fringe patterns," Opt. Express, vol. 26, no. 10, pp. 12403–12414, 2018.

Presentations

- **S. Ordones**, M. Servin, M. Padilla, I. Choque, J. L. Flores, and A. Muñoz, "Windowed generalized phase-shifting algorithms," in Interferometry XX (M. B. N. Morris, K. Creath, and R. Porras-Aguilar, eds.), vol. 11490, pp. 1149004–1–9, International Society for Optics and Photonics, SPIE, 2020.

- I. Choque, M. Padilla, M. Servin, **S. Ordones**, and M. Asmad, "Suppressing ripple distortions and spurious pistons in phase-shifting interferometry," in Interferometry XX (M. B. N. Morris, K. Creath, and R. Porras-Aguilar, eds.), vol. 11490, pp. 1149006–1–10, International Society for Optics and Photonics, SPIE, 2020.

Contents

List of figures

Chapter 1

Introduction

Throughout history, human beings have needed to measure some physical features of the world around them. For this purpose, human has manufactured different instruments that have allowed us to understand nature better. They also have allowed us to create or improve new products. Thus, the need arises for the devices used in the measurements to be more and more exact.

Metrology is the science whose object of study is measurable physical properties, systems of units, measurement methods. Hence, this guarantees measurement normalization through traceability. Nowadays, dimensional metrology has acquired an increasing interest due to the industrial and medical needs, principally, to measure object surfaces and generate their three-dimensional models. Based on their interaction with the testing object, techniques used to build these models are classified into two main categories: invasive and non-invasive.

Invasive techniques have physical contact with the physical feature to be measured. Their main advantage is that mathematical models are not required, but instrument mechanic restricts the measurement resolution. For example, in 3D measurements, a stylus must have contact with the whole surface. Therefore, it makes the required time in each mensuration to be high; so, measuring is a slow task. On the other hand, in non-invasive techniques, the instruments do not have physical interaction with the object, being its main advantage. Novel hardware developments have made possible the creation of measurement devices using acoustic, optical, or magnetic waves to perform measurements. In these instruments, mathematical models allow not only retrieving measurement information possible but also improving their accuracy.

In the area of optics, there are various non-invasive techniques to measure physical properties. For example, photogrammetry works in the three-dimensional reconstruction of objects. This technique requires capturing a sequence of images of a testing object using cameras arranged in suitable positions. The main advantage of the method is that it does not require a specific light source. Its principal disadvantage lies in the fact that it needs to find the localization of common points through acquired pictures. Thus, this task can be challenging [1]. A second non-invasive technique is the projection of laser strips, whose basic principle is active triangulation. This technique obtains the data by

projecting and acquiring laser strips on the testing object so that the camera captures the object's reflection map [2]. This technique can perform high-precision measurements. One can vary the precision because the technique's accuracy is subject to both the field of view of the optical array and the sensitivity angle. The latter can be as large as the object's topography does not introduce self-occluding shadows.

Another technique is called shadow moiré that consists of projecting a pattern onto the object under testing. By illuminating a modulating grating, this pattern is generated. To distinguish the object and grating information, one requires to utilize a reference pattern; it has only the grid's data. Thus, the superposition of both projected patterns will generate the called moiré pattern. So it has only the information corresponding to the object under testing [3]. To recover the surface information, one employs the active triangulation principle to relate the pattern displacements to heights.

Fringe projection is an analogous technique to shadow moiré. In the fringe projection technique, one uses a multimedia projector to generate the projection pattern instead of the grating. Typically, this technique consists of projecting and acquiring a sequence of sinusoidal patterns containing the surface heights encrypted in their modulating phase [4]. One then needs to retrieve it to obtain the height information. As in the previous technique, fringe projection is also based on the active triangulation principle. Its main advantage is the simplicity of the optical setup requiring a multimedia projector and a camera. Whereas its disadvantage lies mainly in that the surface height and the recovered information (phase) have a non-linear correspondence, needing to pay special attention to.

In the same sense, optical interferometry is a non-invasive technique that uses light to measure physical properties with wavelength as the measurement unit [5, 6]. The measurements are determined indirectly since the observed values are interference patterns (intensity values with a certain distribution) generated by the interaction with the testing object. Light will see optical path lengths or optical path differences (OPDs) when the testing object is present and is not; OPDs will translate into phase differences. Therefore, these OPDs have the result of the interaction between light and the testing object. For example, a mirror may introduce OPDs due to their topography; therefore, one can measure it through the OPDs. In other words, physical feature measurements are determined by solving an inverse problem that seeks to determine the cause, phase difference, generating the observed phenomenon, which is an interference pattern.

There are several techniques based on optical interference such as interferometric moiré, holography, speckle interferometry, photoelasticity, and others [6]; even though this fact, they should be thought to be complete technique themselves. Furthermore, the technique of fringe projection is employed, where a multimedia projector projects the digitally-generated fringe pattern. Although this process does not require the optical interference of light, we believe that reviewing optical interference concepts is needed to give a better understanding of the image processing needed. Refer to [5, 6] for a detailed description. Furthermore, there are several fringe projection techniques in which one utilizes fringe patterns coming from optical interference phenomena. For example, when using an interferometer to obtain fringe patterns [7–9] or using a microscopic fringe projection profilometer [10].

1.1 Three-dimensional scanning using structured light

I would like to indicate that the term *structured light* will have the meaning of *structured illumination* referring to the projection of light with a known shading pattern. This definition is used thorough this thesis instead of *structured beams*; even though both terms are much closed, the latter should be thought to be more specific. Hence, *structured light* here refers to the light (being noncoherent and non-monochromatic) that one can digitally shape and project using a multimedia projector and a computer. Some examples of this kind of projection are grid lines, single lines, a cloud of pseudo-random dots, and sinusoidal patterns.

One can use fringe projection to measure and observe changes in transparent or diffuse objects. For example, considering the deflection of the projected fringes, one can visualize flows [11], measure the optical aberration of lenses [12], measure temperature gradients [13], and other applications. Although its effectiveness for measuring phase objects, the fringe projection has been more extensively used to measure the surface of diffuse solids [14].

By employing fringe projection, one can analyze static and dynamic objects. When working with static surfaces, one needs to face the following drawbacks:

1. Gamma distortion is observed as a non-linear modification of the intensity values that one introduces to the multimedia projector.

2. Temporal variations of the intensity modulation in the camera-projector system.

3. Self-occluding shadows generated by the topography of the object under study.

Because the object is static, one can acquire a large number of fringe patterns so that one can cope with the gamma distortion. A common working frequency for both the camera and projector will eliminate the second drawback. One can face the last one by performing the measurement from several directions. These issues are now only mentioned; Chapter 3 goes through them in detail. On the other hand, when the under-study object is moving through the field of view, one needs not only accomplishing the aforementioned drawbacks but also the following ones:

4. Tracking the movement of the object.

5. When using sinusoidal patterns, the projected fringes' spatial frequency needs to be constant through the whole image. If the spatial frequency is not constant, the measurement will have different sensitivities.

6. The camera's exposition time *versus* the velocity of the object. When the object's velocity is so high compared with the exposition time, the observed fringe pattern will be blurred.

To face the fourth issue, one can employ not only image registration methods but also utilizing a projector whose transducer be parallel to the camera's one and the reference plane. In other words, one should homogenize the spatial frequency digitally or in the setup; for extra explanations, refer to [15]. The last drawback can be faced by using a fast camera or illuminating the object strongly.

1.1.1 Three dimensional scanning of a moving object

This Section reviews the state of the art in scanning of moving object by means of fringe projection profilometry. We believe that these works are the most representative one in this topic.

Pawlowski and Kujawińska utilized the fringe projection method to reconstruct a dynamic object whose shape is thought to evolve with time [16]. They developed their technique for creating 3D animations. The authors describe the observed fringe pattern mathematically as

$$I(x,y;t) = a(x,y;t) + b(x,y;t)\cos\left[u_0 x + \omega_0 t + \varphi(x,y;t)\right] \tag{1.1}$$

where $a(x,y;t)$ is background intensity, $b(x,y;t)$ is the fringe modulation; u_0 is the spatial carrier frequency and ω_0 is the temporal one; $\varphi(x,y;t)$ is the phase for a given time t. Notice that the a, b and φ are considered to have time evolution. Paulowski propose to phase demodulate Eq. (1.1) using both the Fourier-Takeda method and carrier phase-shifting algorithms; these methods have the ability of retrieve the phase $\varphi(x,y;t)$ for a single image at certain time t [16]. The proposed technique shows that it might follow and measure the dynamic object; however, it cannot measure the dynamic object with high accuracy due to the phase demodulation methods used. In the same sense, Tan *et al.* uses a similar technique to measure the shape of a swimming fish [17]; in which, the authors projects laser strips and also uses a laser tracker to observe the position of the fish. Other techniques have been proposed to measure an evolving object using the fringe projection technique [18–20].

On the other hand, this technique has been also employed to measure a rigid object while moving through the projected fringe pattern. In this kind of application, one usually assumes that the object's movement will translate into a fringe pattern movement; under this condition, one can think the captured fringe patterns are being phase shifted. The next paragraphs review the state of the art of techniques using both fringe projection and phase-shifting algorithms.

Yoneyama and associates propose a technique to estimate a rigid shape which is in line motion [21, 22]. Their technique requires to project an interferometric, sinusoidal fringe pattern, and three linear sensors placed a certain disposition such that each one observes a phase-shifted fringe pattern. Then, a phase-shifting algorithm is employed to retrieve the phase map. The acquired sequence can be given mathematically by

$$I(x,y;t) = a(x,y;t) + b(x,y;t)\cos\left[u_0 x + \varphi(x,y) + \omega_0 t\right]. \tag{1.2}$$

Here one can observe that both background illumination and fringe modulation functions have time variations because of the beam profile. However, when these time variations are slight, the phase-shifting algorithm can cope with this kind of data; otherwise, the algorithm must be robust again those changes.

Hu and Haifeng proposed to measure an object with line motion by means of the Fourier-Takeda method using two scanning resolutions [23]. They project a composite pattern, in grayscale, with two spatial frequencies: a low one in the left (first scanning line and a high one in the right (second scanning line). Thus, the authors acquired two fringe

patterns in two different moments. Thence, one can mathematically describe the fringe patterns as

$$\begin{aligned} I_1(x,y) &= a(x,y) + b(x,y)\cos\left[u_1 x + \varphi_1(x,y)\right] \\ I_2(x+\Delta x,y) &= a(x+\Delta x,y) + b(x+\Delta x,y)\cos\left[u_2 x + \varphi_2(x,y)\right]; \end{aligned} \tag{1.3}$$

where Δx is a displacement in the moving direction. From Eq. (1.3), one can realize that the fringe patterns have different fringe modulation and background functions. These facts are not an issue because phase demodulation is done by the Fourier-Takeda method. However, this demodulation method is expected to filter out the small shape details, and so high accurate measurements are restricted.

Zuo and colleagues implemented a technique based on projecting a binary pattern with dual-frequency for measuring a surface in a pseudo-dynamic scene [24]. The latter is thought to be static while a sequence of five binary patterns is projected; then, the object will start moving again. The authors utilized very high-speed hardware that allows them to have the pseudo-dynamic scene; the time spent in projecting/acquiring was very short such that they said the technique could achieve a speed of 1250 frames per second [24]. One can realize that this proposal does consider a static object. Therefore, the acquired patterns should be modeled by means of the classic model for fringe patterns with high-order harmonic contributions:

$$\begin{aligned} I(x,y,t) = &\sum_{k=0}^{\infty} b_k(x,y)\cos k\left[u_1 x + \varphi_1(x,y) + \omega_1 t\right] \\ &+ \sum_{k=0}^{\infty} c_k(x,y)\cos k\left[u_2 x + \varphi_2(x,y) + \omega_2 t\right]; \quad t = 0,1,\ldots,4. \end{aligned} \tag{1.4}$$

Here, b_k and c_k are the amplitudes of the k-th harmonic of the low and high frequencies, respectively. The observed fringe patterns are described in terms of the Fourier series since the projected binary patterns are defocused. It is noticeable that the way the authors generated the binary patterns make the amplitudes of the first harmonics having very low power (almost zero). Thence, the phase is well estimated because it does not have those distortions due to harmonic.

Xi *et al.* have proposed a technique in which they considered an object moving not only in (x,y) directions but also rotating [25]. The authors employed sinusoidal fringe patterns and phase shifting algorithms, so the acquired patterns are mathematically given by

$$I(x,y;t) = a(r,\theta;t) + b(r,\theta;t)\cos\left[u_0 x + \varphi(r,\theta;t) + \omega_0 t\right]; \quad t = 0,1,\ldots,N-1. \tag{1.5}$$

In this case, the author propose to use the sequence of N-patterns to determine the phase $\varphi(x,y)$. It is noticeable that the temporal changes in φ corresponds only a rotation and a translation because of measuring a rigid shape. Let $\mathbf{R}$ and $\mathbf{t}$ be the rotation matrix and translation vector, then one can match the pixels of two patterns by means of

$$\tilde{\mathbf{I}}_{\in(\xi,\eta)} = \mathbf{R}\mathbf{I}_{\in(r,\theta)} + \mathbf{t}; \tag{1.6}$$

hence, one can have the patterns centered in the plane (ξ, η); this task is done for each fringe pattern. Thence, one needs to perform a image registration in order to obtain the sequence of fringe patterns given by

$$\tilde{I}(\xi, \eta, t) = a(\xi, \eta, t) + b(\xi, \eta, t) \cos\left[u_0 x + \varphi(\xi, \eta) + \omega_0 t\right]; \quad t = 0, 1, \ldots, N-1. \tag{1.7}$$

Here the temporal variations of the background and fringe modulation functions are due to reflection conditions and background intensity. One can realize that phase φ can be straightforwardly retrieved by a phase shifting algorithm in piece-wise manner. To this end, the authors employed the N-step algorithm which performs well provided that the acquired fringe patterns were acquired while moving in a small neighborhood; this mean that the temporal variations of a and b are neglected. In these conditions, one should also expect that the sensitivity of the corrected pattern is slightly different because the fringe pattern is obliquely projected.

In the same sense, Lu *et al.* introduced a technique to 3D scan objects being translation and rotation motion [26]. The main differences between proposal [25] and this one is the fact Lu *et al.* [26] codify the projected fringe patterns in the red channel; meanwhile, they use the captured image in the blue channel as the input to the pixel matching algorithm.

With the same aim, Yuan *et al.* proposed their technique in which the multimedia projector is orthogonal to the reference plane, and its camera is in oblique view [27]. Their proposal considers the object is moving in the rectilinear direction along the x-axis; so the acquired fringe patterns are given by Eq. (1.5) but without the rotations. The authors propose to first re-project the acquired patterns such that the re-projected ones are in an aerial view. Therefore, re-projected patterns would have uniform spatial sensitivity. After applying a pixel matching algorithm, the object will appear stationary. Finally, the $N-$step phase-shifting algorithm will retrieve the phase. However, as in Reference [25], movements should be small to neglect the influence of the temporal variations of a and b.

Wan and co-workers proposed a technique needing to project and acquire 15 fringe patterns [28]. To reduce the projection/acquisition time, the authors codified three patterns into a red-green-blue (RGB) image, and in this manner, the technique now requires to project and acquire only five RGB patterns. The authors also employ patterns with three different spatial carriers, one in each color channel; hence, they can improve not only the signal-to-noise ratio of the estimated phase but also simplify the estimation. The author also consider the under-study object is in linear motion; so the acquired patterns, in red channel, are given by

$$\begin{aligned} I_{\mathrm{r}}(x, y; t) = {} & a_{\mathrm{r}}(x, y; t) + b_{\mathrm{r}}(x, y; t) \cos\left[u_1 x + \varphi_1(x, y; t) + \omega_0 t\right] \\ & + \alpha_{\mathrm{r}\leftarrow\mathrm{g}} b_{\mathrm{g}}(x, y; t) \cos\left[u_2 x + \varphi_2(x, y; t) + \omega_0 t\right] \\ & + \alpha_{\mathrm{r}\leftarrow\mathrm{b}} b_{\mathrm{b}}(x, y; t) \cos\left[u_3 x + \varphi_3(x, y; t) + \omega_0 t\right]; \quad t = 0, 1, \ldots, 4. \end{aligned} \tag{1.8}$$

Here subscripts r,g,b indicates the color channels; $\alpha_{\mathrm{r}\leftarrow\mathrm{g}}$ and $\alpha_{\mathrm{r}\leftarrow\mathrm{b}}$ are the cross-talking coefficients. In an analogous way, one can describe the patterns coming from the other two channels. With the aim of phase demodulating the fringe patterns, the authors performed a cross-taking correction and a pixel matching algorithm such that the corrected patterns

are described as

$$\begin{aligned} I_{\mathrm{r}}(x,y,t) &= a_{\mathrm{r}}(x,y) + b_{\mathrm{r}}(x,y)\cos\left[u_1 x + \varphi_1(x,y) + \omega_0 t\right], \\ I_{\mathrm{g}}(x,y,t) &= a_{\mathrm{g}}(x,y) + b_{\mathrm{g}}(x,y)\cos\left[u_2 x + \varphi_2(x,y) + \omega_0 t\right], \\ I_{\mathrm{b}}(x,y,t) &= a_{\mathrm{b}}(x,y) + b_{\mathrm{b}}(x,y)\cos\left[u_3 x + \varphi_3(x,y) + \omega_0 t\right]; \quad t = 0,1,\ldots,4. \end{aligned} \tag{1.9}$$

These three sets of fringe patterns are straightforward to be phase demodulated, and so, the global phase is determined by means of the three phases. One can realize that this technique will perform well when the fringe patterns are acquired herein a small neighborhood.

Li *et al.* developed a very complete profilometer to measure moving objects in linear and rotational motion scale-invariant feature transform [29]. The authors used phase-shifted fringe patterns with a linear carrier for measuring rectilinear-moving objects; whereas, a quadratic carrier (closed fringes) for measuring objects in a rotation motion. The technique also utilizes a re-projection method to correct the oblique view of the camera. The author spent special attention on the pixel matching task so that their proposal seems to perform well even with patterns that have low fringe contrast. By using a phase-shifting algorithm for randomly-distributed shifts, the phase estimation is highly accurate. They obtain phase errors around 0.01 rad. It is noticeable that this technique can cope with large movements because the authors correct the spatial frequency deviations and correct the fringe modulation in a normalization sense.

Guo and associates' technique can scan a moving object based on multiple captures, and Fourier-Takeda method [30]. In this technique, the authors phase demodulate each acquired pattern separately; hence, each phase map is temporal. By working with the temporal phase maps, a pixel matching algorithm applies the translations and rotations until all phase maps are aligned. Once the previous task ended, the authors employ a weighted average method to combine the temporal phases, and hence, the global phase map is determined. Because of data redundancy, this phase will have a good signal-to-noise ratio; nonetheless, it will not have a high exactitude due to the global spatial filtering. Whence, one should expect that the final phase will be over-smooth.

Flores *et al.* developed a profilometer to reconstruct objects moving in a linear direction based on color (RB) codification and a phase-shifting algorithm for non-uniformly spaced shifts [31]. Their technique projects and acquires the sinusoidal patterns in the red channel, and the blue channel has only a picture of the object. The authors employ the latter to do the pixel matching algorithm. The acquired patterns are given by

$$I_{\mathrm{r}}(x,y;t) = a(x,y;t) + b(x,y;t)\cos\left[u_0 x + \varphi(x,y;t)\right]. \tag{1.10}$$

Here the authors employ only one fringe patterns. After capturing, performing the pixel matching correction, and the fringe normalization the fringe patterns, the authors obtain corrected the phase-shifted patterns described by

$$\tilde{I}_{\mathrm{r}}(x,y,t) = 1 + \cos\left[u_0 x + \varphi(x,y) + \Theta(t)\right]; \tag{1.11}$$

where $\Theta(t)$ is the phase-shift function. In this technique, objects are considered to move in a small neighborhood, despite the authors corrected temporal variations of the fringe

modulation function. This fact is because they also did not address the spatial, sensitivity changes due to spatial non-monochromatic.

Lu *et al.* proposed a technique that can measure objects with discontinuous shape being also in motion [32]. To cope with shape discontinuities, the authors project two kinds of fringe patterns: the first one has a low spatial frequency and the other has a high spatial frequency. The authors proposed to employ scale-invariant feature transform (SIFT) to track the object. The phase retrieval is done using a phase-shifting algorithm. The authors also perform a phase correction to improve its accuracy. Nonetheless, the main advantage of this technique is that the phase is computed using only two fringe patterns: one low- and one high-frequency pattern. However, its main disadvantage is that the patterns are projected alternatively, so it makes the technique lose velocity.

1.2 Aim and objectives

Reconstruct the three-dimensional shape of solids in linear motion using fringe projection and co-phased techniques.

1.2.1 Objectives

1. Study and develop phase demodulation methods using the formalism based on the Fourier transform; it is called the frequency transfer function (FTF) formalism.
2. Study and develop co-phase techniques for profilometry.
3. Solve the spatial frequency variations due to surface depth.
4. Implement the proposed fringe projection profilometer.

1.3 Thesis structure

The rest of this thesis is organized in four Chapters. Chapter 2 goes through digital interferometry; it describes the procedure to obtain the phase from fringe patterns. This Chapter pays special attention in phase demodulation of phase-shifted fringe patterns by means of linear quadrature filters. Chapter 3 introduces fringe projection profilometry; it describes the procedure to obtain heights by projecting sinusoidal patterns. The gamma distortion is also explained and overcome in this Chapter. Moreover, this Chapter describes how one can overcome the self-occluding shadows commonly seen in this technique. The Chapter's last Section describes the procedure to perform the three-dimensional reconstruction of an object in rectilinear motion. Chapter 4 shows some results depicting the feasibility of the proposal. Finally, Chapter 5 mentions our main conclusions.

Chapter 2

Fringe analysis

El principio consiste en que la suma de los cuadrados de las diferencias entre lo observando y las cantidades calculadas debe ser mínimo.

Carl Friedrich Gauss

This Chapter discusses the topic of fringe analysis that mainly consists of retrieving the information with the measurement. It is well-known that such information is code in the intensity pattern. To this end, one has to analyze the fringes of one o more intensity patterns; this topic is called fringe analysis. Usually, one is interested in recovering the modulating phase, which determines the intensity distribution, having the optical path difference related to the physical feature to be measured. Fringe analysis needs to perform three steps: (1) phase demodulation, (2) phase unwrapping, and (3) mapping the phase to real units. Phase demodulation consists of retrieving the wrapped phase with 2π discontinuities. The phase unwrapping procedure removes these discontinuities, and hence, the continuous phase is obtained. Finally, the third step entails the interpretation of the continuous phase in terms of real unities. By reason, the experimental setup determines the mapping step, the present Chapter does not examine this topic.

The Chapter is organized into three Sections: the first two talk about the phase demodulation process with one and multiple fringe patterns, respectively. The last Section goes through the phase unwrapping procedure.

2.1 Phase demodulation of a single fringe pattern

This Section briefly introduces the techniques developed for phase retrieval from a single intensity pattern. Let one consider the acquired intensity pattern mathematically given by

$$\begin{aligned} I(x,y) &= a(x,y) + b(x,y)\cos\left[\varphi(x,y)\right] \\ &= a(x,y) + \frac{b(x,y)}{2}e^{i\varphi(x,y)} + \frac{b(x,y)}{2}e^{-i\varphi(x,y)} \end{aligned} \tag{2.1}$$

where $a(x, y)$ is the background illumination, $b(x, y)$ is the fringe modulation and $\varphi(x, y)$ is the phase map. From this equation, one can observe that $a(x, y)$, $b(x, y)$, and $\varphi(x, y)$ are unknown variables to be calculated while having a single observation $I(x, y)$; there are three unknowns variables and one equation. Thus, the phase retrieval problem is ill-posed in the Hadamard's sense [33].

There exist two categories to classify the fringe patterns depending on introducing a known carrier or not. The former is named a carrier fringe pattern having open fringes, whereas the latter has close ones. Servin and associates have called the algorithms to retrieve the phase from such fringe patterns as *methods with carrier* and *without carrier*, respectively [34].

First, *methods with carrier* take advantage of the introduced carrier as prior information. The latter allows separating the three terms of interferometric signal in Eq. (2.1); hence, its spectrum is composed of three lobes. Consequently, the searched signal can be retrieved by using frequency-domain low-pass filters [15, 35–38] or spatial-domain quadrature filters [39–42]. Several carrier functions have been proposed like 1D and 2D tilt [43, 44] and parabolic [45] in optical shop testing, pixelated carrier for dynamic measurements [44, 46, 47], and so on. Perhaps the tilted carrier is the most widely employed because it is straightforwardly introduced by titling the wavefront. But also, one can easily estimate the tilted carrier in the frequency domain. In the fringe projection profilometry area, one usually projects a sequence of tilted carrier fringe patterns where this carrier is *the sensor* of the system.

On the other hand, when using *methods without carrier*, the lobes appearing in the spectrum of the intensity pattern in Eq. (2.1) will overlap one another. In particular, the two lobes having the phase map; thence, the separation of them by frequency-domain filtering is impossible in a global sense. While in a local sense, several methods bear in mind that the fringe pattern is monochromatic in a neighborhood. Hence, by a robust quadrature filter tuned at the local frequency, the phase map is locally approximated. The next neighborhood is then phase demodulated following a path through the fringe pattern; refer works [48, 49]. In these methods, the phase is assumed to be smooth and has a good range. It also has been proposed nonlinear optimization methods to demodulate a neighborhood of closed-fringe patterns. These methods recover the whole phase solving the nonlinear cost function following a tracker algorithm [50–53] and others; however, they also assume that the phase is smooth. Proposals [48–53] are not only strongly depended of the phase demodulation path, but also they are very high computationally expensive. Alternatively, the method based on the 2D Hilbert transform and the spiral operator [54–56] is a low computational cost, as well as it can retrieve the phase map very well when the fringe patterns are locally quasi-monochromatic. A more detailed description of *methods without carrier* is beyond the thesis scope because they are not seen commonly in fringe projection profilometry.

The rest of this Section draws the case of interferometry signal having a spatial carrier. One mostly observes this kind of data in dynamic measurements where a single interferogram is usually acquired. In this context, one usually introduces a spatial carrier into a fringe pattern as prior information that one then uses to phase demodulate the data. It is noticeable that a well-selected spatial carrier will make the phase demodulation procedure to be significantly straightforward than without it.

It is common to call spatial carrier fringe patterns those having a spatial carrier. They can be mathematically described by

$$I(x,y) = a(x,y) + b(x,y)\cos\left[\varphi(x,y) + c(x,y)\right], \tag{2.2}$$

where $I(x,y)$ is the intensity acquired, $a(x,y)$ indicates the background illumination, $b(x,y)$ is the fringe contrast, $\varphi(x,y)$ is the phase searched, and $c(x,y)$ is the spatial carrier introduced. By taking the bi-dimensional Fourier transform of the fringe pattern, one obtains its spectrum given by

$$\begin{aligned} I(u,v) &= \mathcal{F}_{(x,y)}\left\{I(x,y)\right\} \\ &= \mathcal{F}_{(x,y)}\left\{a(x,y) + \frac{b(x,y)}{2}e^{i[\varphi(x,y)+c(x,y)]} + \frac{b(x,y)}{2}e^{-i[\varphi(x,y)+c(x,y)]}\right\} \\ &= \mathcal{F}_{(x,y)}\left\{a(x,y)\right\} + \mathcal{F}_{(x,y)}\left\{\frac{b(x,y)}{2}e^{i[\varphi(x,y)+c(x,y)]}\right\} + \\ &\quad + \mathcal{F}_{(x,y)}\left\{\frac{b(x,y)}{2}e^{-i[\varphi(x,y)+c(x,y)]}\right\} \\ &= A(u,v) + W(u,v) + W^*(-u,-v). \end{aligned} \tag{2.3}$$

Here $i = \sqrt{-1}$, $\mathcal{F}_{(x,y)}\left\{\bullet\right\}$ is the operator of the bi-dimensional, spatial Fourier transform and (u,v) are the coordinates of the bi-dimensional Fourier domain, commonly called the bi-dimensional frequency domain. The spatial carrier must be as higher frequency such that the three spectral components, in Eq. (2.3), are separable from each other.

Once the spectral components are well separated, the analytic signal or wavefront can be straightforwardly obtained as

$$S(x,y) = \frac{b(x,y)}{2}e^{i\varphi(x,y)} \propto \left[I(x,y)e^{-ic(x,y)}\right] \circledast\circledast h(x,y), \tag{2.4}$$

where $\circledast\circledast$ means bi-dimensional convolution, and $h(x,y)$ is the impulsive response of a filter. By substituting Eq. (2.2) in Eq. (2.4) and the Euler's formula, one we can obtain that

$$\begin{aligned} S(x,y) &\propto \left[a(x,y)e^{-ic(x,y)} + \frac{b(x,y)}{2}e^{i\varphi(x,y)} + \frac{b(x,y)}{2}e^{-i\varphi(x,y)}e^{-i2c(x,y)}\right] \circledast\circledast h(x,y), \\ &\propto a(x,y)e^{-ic(x,y)} \circledast\circledast h(x,y) + \frac{b(x,y)}{2}e^{i\varphi(x,y)} \circledast\circledast h(x,y) \\ &\quad + \frac{b(x,y)}{2}e^{-i\varphi(x,y)}e^{-i2c(x,y)} \circledast\circledast h(x,y). \end{aligned} \tag{2.5}$$

By taking the Fourier transform, Eq. (2.5) can be rewritten as following:

$$\begin{aligned} S(u,v) = \mathcal{F}_{(x,y)}\left\{S(x,y)\right\} \propto \left[A(u,v) \circledast\circledast C(u,v)\right]H(u,v) + S(u,v)H(u,v) \\ + \left[\frac{1}{2}S^*(-u,-v) \circledast\circledast C^*\left(\frac{-u,-v}{2}\right)\right]H(u,v). \end{aligned} \tag{2.6}$$

Here $C(u,v) = \mathcal{F}_{(x,y)}\left\{\exp\left[ic(x,y)\right]\right\}$, and $H(u,v)$ is the spectral response of the filter $h(x,y)$.

Based on Eq. (2.6), it can be stated that the analytic signal estimation needs to fulfill the following conditions:

1. Eliminate the background illumination:

$$[A(u,v) \circledast \circledast C(u,v)]\, H(u,v) = 0. \tag{2.7}$$

2. Remove the complex-conjugated signal:

$$\left[\frac{1}{2}S^*(-u,-v) \circledast \circledast C^*\left(\frac{-u,-v}{2}\right)\right] H(u,v) = 0. \tag{2.8}$$

3. Keep the searched signal:

$$S(u,v)H(u,v) \neq 0. \tag{2.9}$$

These conditions in Eq. (2.7) – (2.9) are called the spatial quadrature conditions.

On the other hand, the spatial carrier must fulfill the conditions

$$\left|\frac{\partial\varphi}{\partial x}\right|_{\max} < \left|\frac{\partial c}{\partial x}\right|_{\max}, \qquad \left|\frac{\partial\varphi}{\partial y}\right|_{\max} < \left|\frac{\partial c}{\partial y}\right|_{\max} \tag{2.10}$$

Meanwhile, the sampling Nyquist criterion requires that

$$\left|\frac{\partial\varphi}{\partial x}\right|_{\max} + \left|\frac{\partial c}{\partial x}\right|_{\max} < \pi, \qquad \left|\frac{\partial\varphi}{\partial y}\right|_{\max} + \left|\frac{\partial c}{\partial y}\right|_{\max} < \pi. \tag{2.11}$$

Moreover, one must know the carrier sign to obtain the correct one of the phase maps.

2.1.1 The Fourier-transform method

This method is based on frequency-domain filtering out lobes $A(u,v)$ and $S^*(-u,-v)$ while keeping $S(u,v)$. It was introduced by Takeda *et al.* [15,35] where the authors initially use one-dimensional analysis with a linear carrier. Then, the method was extended to the bi-dimensional analysis [36].

This method is mathematically equivalent to Eq. (2.4) – (2.6), from these equations, the phase can be straightforwardly estimated as

$$\hat{\varphi}_{\mathcal{W}}(x,y) = \arctan\left[\frac{\operatorname{Im}\{S(x,y)\}}{\operatorname{Re}\{S(x,y)\}}\right] \tag{2.12}$$

where arctan has range $(-\pi,\pi]$, it is commonly called `artan2` in numerical libraries. $\operatorname{Re}\{\bullet\}$ computes the real part of a complex number, and $\operatorname{Im}\{\bullet\}$ the imaginary part. Algorithm 1 describes the so-called Takeda's method, where `fft2` and `ifft2` indicate the usual computational implementation of the discrete Fourier transform and the inverse discrete Fourier transform, respectively; details about `fft2` and `ifft2` can be found in books [57–59].

Input: Fringe pattern $I(x,y)$, frequency domain filter $H(u,v)$, and carrier $c(x,y)$.
Make the product $I_s(x,y) \longleftarrow I(x,y)e^{-ic(x,y)}, \quad \forall(x,y)$.
Compute the Fourier transform $I(u,v) \leftarrow \texttt{fft2}\,[I_s]$.
Perform the spatial filtering $S_{\in\mathcal{F}}(u,v) \longleftarrow I(u,v)H(u,v), \quad \forall(u,v)$.
Compute the inverse Fourier transform $S_{\in(x,y)} \longleftarrow \texttt{ifft2}\,(S_{\in\mathcal{F}})$.
Obtain the phase $\hat{\varphi}(x,y) \longleftarrow \arctan\left[\frac{\operatorname{Im}\{S(x,y)\}}{\operatorname{Re}\{S(x,y)\}}\right]$.
return the estimated phase $\hat{\varphi}(x,y)$.

Algorithm 1: Takeda's method for phase demodulation.

Perhaps the most employed filters, when using the Takeda's method, are the rectangular binary, the circular binary, and the Gaussian windows; they are mathematically described as

$$H_{\text{Rect}}(u,v) = \begin{cases} 1 & \text{if } |u| < u_{\max} \text{ and } |v| < v_{\max} \\ 0 & \text{otherwise.} \end{cases} \tag{2.13}$$

$$H_{\text{Circle}}(u,v) = \begin{cases} 1 & \text{if } \sqrt{(u_0-u)^2+(v_0-v)^2} \leq r \\ 0 & \text{otherwise.} \end{cases} \tag{2.14}$$

$$H_{\text{Gaussian}}(u,v) = \exp\left[-\frac{(u_0-u)^2}{2\sigma_u^2} - \frac{(v_0-v)^2}{2\sigma_v^2}\right]. \tag{2.15}$$

In Eq. (2.13), $u_{\max}$ and $v_{\max}$ define the bandwidth of the filter along u and v directions, respectively; in Eq. (2.14), r is the radius of the circle and it determines the pass-band; in Eq. (2.15), σ_u^2 is the variance along u direction and σ_v^2 in the v direction, they both determine the bandwidth of the pass band. It is noticeable the Gaussian filter does not fulfill the spatial quadrature conditions in Eq. (2.7) – (2.9), and so these have to be relaxed trivially.

2.1.2 The linear carrier fringe pattern

The linear carrier is given by $c(x,y) = u_0 x + v_0 y$. Then, the fringe pattern with a linear carrier is described mathematically by

$$I(x,y) = a(x,y) + b(x,y)\cos\left[\varphi(x,y) + u_0 x + v_0 y\right] \tag{2.16}$$

where u_0, v_0 are the frequencies along the x and y direction, respectively; these frequencies must fulfill the conditions in Eq. (2.10) to obtain open fringes and Eq. (2.11) to accomplish the Nyquist criterion. Moreover, one must know the sign of the carrier to obtain the correct sign of the searched phase.

To understand how the interferogram is phase demodulated, let one take the Fourier transform of $I(x,y)$ in Eq. (2.16);

$$I(u,v) = \mathcal{F}_{(x,y)}\{I(x,y)\} = A(u,v) + W(u,v) + W^*(-u,-v);$$

where,

$$\begin{aligned} A(u,v) &= \mathcal{F}_{(x,y)}\{a(x,y)\} \\ S(u-u_0, v-v_0) &= \mathcal{F}_{(x,y)}\left\{W(x,y)\right\} = \mathcal{F}_{(x,y)}\left\{\frac{1}{2}b(x,y)e^{i[\varphi(x,y)+u_0x+v_0y]}\right\} \\ &= \mathcal{F}_{(x,y)}\left\{\frac{1}{2}b(x,y)e^{i[\varphi(x,y)}\right\} \circledast\circledast \mathcal{F}_{(x,y)}\left\{e^{i(u_0x+v_0y)}\right\} \\ &= S(u,v) \circledast\circledast \left[\delta(u-u_0)\delta(v-v_0)\right] \\ S^*(-u-u_0, -v-v_0) &= \mathcal{F}_{(x,y)}\left\{W^*(x,y)\right\} = \mathcal{F}_{(x,y)}\left\{\frac{1}{2}b(x,y)e^{-i[\varphi(x,y)+u_0c+v_0y]}\right\}. \end{aligned}$$

$$= \mathcal{F}_{(x,y)}\left\{\frac{1}{2}b(x,y)e^{-i\varphi(x,y)}\right\} \circledast\circledast \mathcal{F}_{(x,y)}\left\{e^{-i(u_0x+v_0y)}\right\}$$
$$= S^*(-u,-v) \circledast\circledast \left[\delta(-u-u_0)\delta(-v-v_0)\right].$$

Thence, the spectrum of the linear carrier is given by

$$I(u,v) = A(u,v) + S(u-u_0, v-v_0) + S^*(-u-u_0, -v-v_0); \tag{2.17}$$

and so, the searched spectral component is located at (u_0, v_0) where the positive sign of $\varphi(x,y)$ is herein. Continuing with Algorithm 1, the frequency shifted spectrum is given by

$$\begin{aligned} I_s(u,v) &= \mathcal{F}_{(x,y)}\left\{I_s e^{-i(u_0x+v_0y)}\right\} \\ &= I(u,v) \circledast\circledast \left[\delta(u-u_0)\delta(v-v_0)\right] \\ &= I(u+u_0, v+v_0) \\ &= A(u+u_0, v+v_0) + S(u,v) + S^*(u+2u_0, v+2v_0); \end{aligned} \tag{2.18}$$

where one can see that the searched lobe is located at the origin $(u=0, v=0)$. Figure 2.1 depicts the procedure to estimate the phase. $I_s(u,v)$ is shown in Fig. 2.1(a), (b) has the superposition of the spectra $I_s(u,v)$ and the filter's $H_{\text{Rect}}(u,v)$, as well as the spectrum of the estimated analytic signal is herein Fig. 2.1(c). Finally, the estimated phase map is seen in Fig. 2.1(d).

Figure 2.1 depicts Takeda's method for phase demodulation of a linear carrier fringe pattern. One can realize that the method is simple and powerful; however, estimating well a phase requires that the signal lobes be well separated, i.e., the spectral lobes do not overlap each other. When the searched phase has small details or edges (locally no smooth), the spectral lobes $S(u,v)$ will spread out; and therefore, $S(u,v)$ can overlaps with $A(u+u_0, v+v_0)$, or even so, $S^*(u+2u_0, v+2v_0)$. Thence, the filter cannot isolate the spectrum of the analytic signal well, and the phase will not have the small details. In this case, one should employ filter $H_{\text{Gaussian}}(u,v)$ instead of $H_{\text{Rect}}(u,v)$ or $H_{\text{Circle}}(u,v)$ to smooth the amplitude of the spectral components; this fact will translate from waving phases where the derivative of the true phase is large into a smoothed version of the true phase.

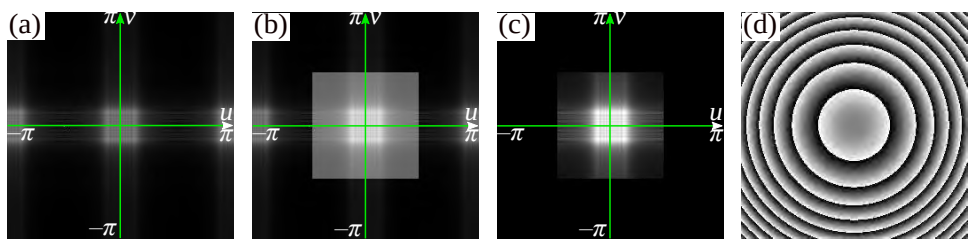

Figure 2.1: Frequency domain filtering of the linear carrier fringe pattern: (a) magnitude of frequency shifted spectrum $|I_s(u,v)|$, (b) $|I_s(u,v)|+|H_{\text{Rect}}(u,v)|$, (c) spectrum of estimated analytic signal $\left|\hat{S}(u,v)\right| = |I_s(u,v)H_{\text{Rect}}(u,v)|$, and (d) the retrieved wrapped phase.

In order to avoid over smoothing the phase, it has been proposed to phase demodulate the fringe pattern in a neighborhood manner by means of the windowed Fourier transform (also called the short-time Fourier transform) [60] as well as its generalization the Wavelet transform [61]. The main idea consists of computing the analytic signal in a neighborhood where spectral lobes do not overlap. Therefore, one needs to repeat the algorithm 1 [adding the Gaussian window while computing $I(u, v)$] at each neighborhood. To automatize such a task, one has to optimize both the Gaussian width and the neighborhood size [62]. Furthermore, the searched spectral lobe's local frequency is needed to be computed [60, 62]. Usually, one fixes the neighborhood size while optimizes both the local frequency and the Gaussian window at each vicinity. These two procedures make the global estimation computationally expensive, although one takes advantage of FFT algorithms and their well-documented computational performance.

2.2 Multiple fringe patterns: phase-shifting algorithms

Phase-shifting interferometry (PSI) is a well-known technique for phase measurement in optical metrology. PSI consists of capturing a time sequence of fringe patterns (intensities) being temporal phase shifted. By moving a mirror, gratings, tilted glass plates, or polarization components, phase shifts are introduced. After, one can compute the searched phase map through methods called phase-shifting algorithms. These methods solve the phase as a linear combination of the captured fringe patterns. It is noticeable that phase shifts may be inexact due to intrinsic and extrinsic problems of the *phase shifter*.

Figure 2.2 draws the idea behind phase retrieval using a temporal phase-shifting algorithm. This figure plots the continuous-time fringe localized at pixel (x, y). One can realize that the aim is to estimate the phase that generates the temporal sinusoidal signal's initial displacement.

In the beginning, PSI consisted of solving a system of equations with the objective of estimating the phase map. However, Servin *et al.* [63] have proposed a modern formulation based on the frequency transfer function (FTF) of the phase-shifting algorithm (PSA). This formulation is called the FTF formalism.

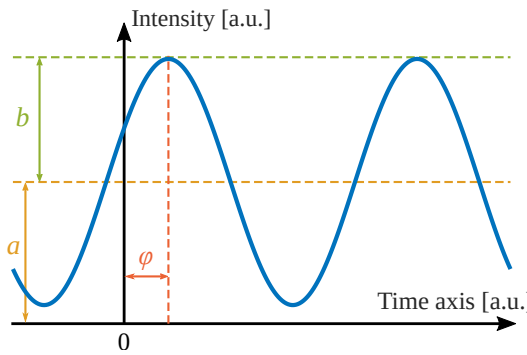

Figure 2.2: Schematically description of phase estimation utilizing temporal phase-shifting algorithms at arbitrary pixel (x, y). Notice that the initial displacement of the temporal, continuous sinusoidal signal corresponds to the phase to be measured.

2.2.1 FTF formalism for phase-shifting algorithms

Considering a continuous-time fringe given by

$$I(x,y,t) = a(x,y) + b(x,y)\cos\left[\varphi(x,y) + \omega_0 t\right], \tag{2.19}$$

where (x,y) are spatial dependencies, $\varphi(x,y)$ is the searched phase coming from a static object, $a(x,y)$ is the background illumination or bias without temporal variation, $b(x,y)$ is the fringe modulation without temporal variation, and ω_0 is the temporal carrier in radians per second [rad/s]; refer to Fig. 2.2. Then, the temporal sequence, having the recorded fringe patterns, is a set of samples of Eq. (2.19), so it is

$$I(x,y,n) = \int_{-\infty}^{\infty} I(x,y,t)\delta(t-t_n)dt = a(x,y) + b(x,y)\cos\left[\varphi(x,y) + \omega_0 t_n\right]. \tag{2.20}$$

Here, $\delta(t)$ is the Dirac delta, $n = 0, 1, \ldots$ is the discrete-time variable, and t_n is the time when the nth sample was taken.

As aforementioned, in PSI, the phase estimation is done one pixel as a function of the time; for simplicity, spatial dependence is dropped. By taking the temporal Fourier transform of $I(x,y,t)$, the temporal spectrum of the continuous-time fringe is determined as

$$\begin{aligned} I(\omega) &= \mathcal{F}_t\left\{I(t)\right\} = \mathcal{F}_t\left\{a\right\} + \mathcal{F}_t\left\{b\cos\left[\varphi + \omega_0 t\right]\right\} \\ &= a\delta(\omega) + \mathcal{F}_t\left\{\frac{b}{2}e^{i\varphi}e^{i\omega_0 t}\right\} + \mathcal{F}_t\left\{\frac{b}{2}e^{-i\varphi}e^{-i\omega_0 t}\right\} \\ &= a\delta(\omega) + \frac{b}{2}e^{i\varphi}\mathcal{F}_t\left\{e^{i\omega_0 t}\right\} + \frac{b}{2}e^{-i\varphi}\mathcal{F}_t\left\{e^{-i\omega_0 t}\right\} \\ &= a\delta(\omega) + \frac{b}{2}e^{i\varphi}\delta(\omega-\omega_0) + \frac{b}{2}e^{-i\varphi}\delta(\omega+\omega_0), \end{aligned} \tag{2.21}$$

where $\mathcal{F}_t\left\{\bullet\right\}$ is the operator of the temporal Fourier transform. Figure 2.3 depicts the temporal Fourier spectrum where one can see that the spectrum is a sum of three Dirac deltas located at $\omega \in \{-\omega_0, 0, \omega_0\}$. Keeping the spectral component at $\omega = \omega_0$ and filtering out at $\omega \in \{0, \omega_0\}$, the wrapped phase can be retrieved by

$$\hat{\varphi}_{\mathcal{W}} = \text{angle}\left(\frac{b}{2}e^{i\varphi}\right) \tag{2.22}$$

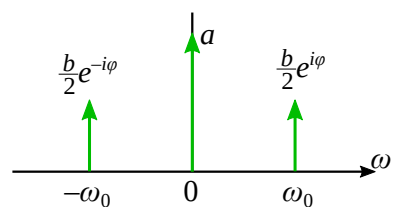

Figure 2.3: The temporal spectrum of the continuous-time fringe. Notice that the spectrum is the sum of three Dirac's deltas.

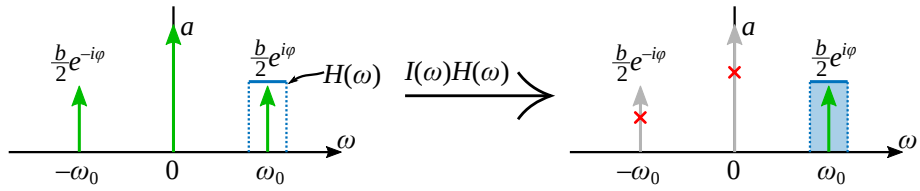

Figure 2.4: Schematic description of the estimation of the analytic signal through a filter $H(\omega)$. Right-hand side shows the estimated component as the product of the fringe's spectrum $I(\omega)$ and the filter's frequency response $H(\omega)$.

where angle$(\bullet)$ is the argument of the complex number, and subscript $\mathcal{W}$ means wrapped phase. The term $(b/2)\exp(i\varphi)$ is called the *analytic signal* and is needed to be insulated in order to retrieve the phase.

With the objective of computing the analytic signal, a filter is required to be designed such that its frequency response $H(\omega)$ is able to estimate the analytic signal. Figure 2.4 schematically depicts the procedure to compute the analytic signal as the product of $H(\omega)$ and the fringe's spectra $I(\omega)$. Thence, the analytic signal –in the Fourier domain– is described as

$$\frac{b}{2}e^{i\varphi}H(\omega_0)\delta(\omega-\omega_0) = I(\omega)H(\omega); \tag{2.23}$$

thus, the frequency transfer function $H(\omega)$ must fulfill the quadrature conditions being given by

$$H(\omega=0)=0, \qquad H(\omega=-\omega_0)=0, \qquad H(\omega=\omega_0)\neq 0. \tag{2.24}$$

Because phase-shifting algorithms fulfill the quadrature conditions, they are named *quadrature linear filters*.

On the other hand, due to the fact that the number of recorded fringe patterns is finite (usually from 3 through 10), the FTF $H(\omega)$ can be given by

$$H(\omega) = \sum_{n=0}^{N-1} c_n e^{-i\omega t_n} \tag{2.25}$$

where N is the number of recorded fringe patterns. In Eq. (2.25), one can see that $H(\omega)$ is a continuous function, furthermore, $H(\omega)$ is the Discrete-Time Fourier transform of the coefficients $\{c_n\}$. Thence, the filter's *impulsive response* is computed as the inverse Fourier transform of its FTF, this is

$$h(t) = \sum_{n=0}^{N-1} c_n \delta(t-t_n). \tag{2.26}$$

Finally, by means of the convolution theorem [64, 65], equation (2.23) is rewritten in the time domain as

$$\frac{b}{2}H(\omega_0)e^{i\varphi} = I(t) \circledast h(t)|_{t=t_N} \tag{2.27}$$

$$= \sum_{n=0}^{N-1} c_{N-n-1} I(t=t_n); \tag{2.28}$$

where $\circledast$ means convolution operation and $H(\omega_0)$ is the value of the FTF at $\omega = \omega_0$. In equations (2.27) – (2.28), the convolution operation is done at $t = t_N$. By means of the Correlation property of the Fourier transform, the equation (2.28) can be rewritten as

$$\frac{b}{2}H(\omega_0)e^{i\varphi} = \sum_{n=0}^{N-1} c_n^* I(t = t_n). \tag{2.29}$$

Here, c_n^* is the complex conjugate of c_n. The last equation is extensively used in the literature even when omitting the complex conjugation; in that case, one must correct the phase sign.

Building-blocks technique to design phase-shifting algorithms

This technique was introduced by Surrel [66] as well as Gonzalez *et al.* [67]; it is commonly employed when the phase steps are uniformly spaced. We believe that this technique is simple and powerful since it requires only adding blocks of zeros at those frequencies to be filtered out. The fundamental block is given by

$$\left[1 - e^{-i(\omega \pm 2\pi\nu)}\right] \tag{2.30}$$

where $2\pi\nu$ is the radial frequency to be rejected; when using this technique, it is usual that $2\pi\nu = M\omega_0$ being M an integer. Then, the quadrature conditions in Eq. (2.24) are fulfilled straightforwardly by adding two blocks tuned at $\omega = 0$ and $\omega = -\omega_0$; and so, one obtains the FTF given by

$$H(\omega) = \overbrace{\left[1 - e^{-i(\omega+0)}\right]}^{H(\omega=0)=0} \overbrace{\left[1 - e^{-i(\omega+\omega_0)}\right]}^{H(\omega=-\omega_0)=0}. \tag{2.31}$$

The impulsive response is obtained by taking the inverse Fourier transform of the FTF; this is

$$\begin{aligned} h(t) &= \mathcal{F}_t^{-1}\left\{H(\omega)\right\} \\ &= \mathcal{F}_t^{-1}\left\{1 - \left(1 + e^{-i\omega_0}\right)e^{-i\omega} + e^{-i\omega_0}e^{-i2\omega}\right\} \\ &= \delta(t) - \left(1 + e^{-i\omega_0}\right)\delta(t-1) + e^{-i\omega_0}\delta(t-2) \\ &= c_0\delta(t) + c_1\delta(t-1) + c_2\delta(t-2); \end{aligned}$$

and hence, the PSA requires three fringe patterns. In general, one can add extra zeroes to eliminate other frequencies; the resulting algorithm will have $(N = num_{\text{blocks}} + 1)$ phase steps.

Finally, it is worth mentioning that the FTF formalism is useful because it provides some formulas that allow one to analyze and describe PSAs analytically. In particular, these formulas mean how an algorithm behaves against: noise, harmonics, and detuning [34]. The Section's rest is describing these formulas.

2.2.2 Noise robustness

It is well-known that there are typically two noise sources corrupting a fringe pattern: electronic noise being additive, whereas the speckle being multiplicative [34]. The former is intrinsic to all measurements, and the latter is due to the reflection of coherence light on optically-rough surfaces [68]. Fringe patterns, having these two kinds of noise, can be written as

$$I_{\text{noised}}(x,y,n) = a(x,y) + b(x,y)\cos\left[\varphi(x,y) + \omega_0 t + \eta_s(x,y)\right] + \eta_a(x,y,t) \tag{2.32}$$

where $\eta_s(x,y)$ is the speckle no having changes in the time axes because it only depends on the surface's roughness. Additive noise is denoted by $\eta_a(x,y,t)$ and changes spatially and temporally.

The speckle can be filtered out though spatially low pass filtering of every fringe pattern, then additive noise will corrupt the fringe patterns. Under this consideration and omitting the spatial dependence, the equation (2.32) can be rewritten as

$$I_{\text{noised}}(t) = I(t) + \eta(t); \tag{2.33}$$

$\eta(t)$ is considered to be ergodic and zero mean. Then, the convolution of the data $I_{\text{noised}}(t)$ and the filter $h(t)$ can be written as

$$s(t) = I_{\text{noised}}(t) \circledast h(t), \tag{2.34}$$

or in the frequency domain as

$$S(\omega) = \mathcal{F}_t\left\{s(t)\right\} = I_{\text{noised}}(\omega)H(\omega) = I(\omega)H(\omega) + N(\omega)H(\omega). \tag{2.35}$$

In the last equation, $N(\omega) = \mathcal{F}_t\left\{\eta(t)\right\}$ for very-large time realizations. One can say that the ensemble average of $s(t)$ is given by

$$E\left[S(\omega)\right] = \frac{b}{2}e^{i\varphi}\delta(\omega - \omega_0) \tag{2.36}$$

and the variance is given by [69]

$$E\left[S^2(\omega)\right] = \sigma_S^2 = \frac{1}{2\pi}\int_{-\pi}^{\pi} |N(\omega)|^2 \, |H(\omega)|^2 \, d\omega. \tag{2.37}$$

By means of equations (2.35) – (2.37), equation (2.34) has solution given by

$$s(t) = I_{\text{noised}}(t) \circledast h(t) = \frac{b}{2}e^{i(\varphi+\omega_0 t)} + \eta_H(t) \tag{2.38}$$

where $\eta_H(t)$ is non-white, complex-valued noise with variance σ_S^2. One is searching the angle of the analytic signal, this is given by

$$\hat{\varphi}_{\text{noised}} = \text{angle}\left\{E\left[S\right]\right\}, \tag{2.39}$$

whose standard deviation is given by [69]

$$\sqrt{E\left[\varphi^2_{\text{noised}}\right]} = \sigma_\varphi = \tan^{-1}\left[\frac{\sigma_S/2}{(b/2)H(\omega_0)}\right] \approx \frac{\sigma_S/2}{(b/2)H(\omega_0)}, \tag{2.40}$$

where one assumes a low noise power. From Eq. (2.39) and (2.40), the variance of the estimated phase can be described as [69]

$$\begin{aligned}\sigma^2_\varphi &= \frac{(\eta/2)^2 \frac{1}{2\pi}\int_{-\pi}^{\pi} |N(\omega)|^2 \, |H(\omega)|^2 \, d\omega}{\left|(b/2)H(\omega_0)\right|^2} = \frac{(\eta/2)^2}{\left|(b/2)\right|^2}\frac{\frac{1}{2\pi}\int_{-\pi}^{\pi} |N(\omega)|^2 \, |H(\omega)|^2 \, d\omega}{\left|H(\omega_0)\right|^2} \\ &= \frac{(\eta/2)^2}{\left|(b/2)\right|^2}\frac{\frac{1}{2\pi}\int_{-\pi}^{\pi} |H(\omega)|^2 \, d\omega}{\left|H(\omega_0)\right|^2} = \frac{\sigma^2_\eta}{\left|(b/2)\right|^2}\frac{\frac{1}{2\pi}\int_{-\pi}^{\pi} |H(\omega)|^2 \, d\omega}{\left|H(\omega_0)\right|^2}.\end{aligned} \tag{2.41}$$

Here it was employed Parseval's theorem; σ^2_η is the variance of original noise $\eta(t)$. From Eq. (2.41), one can realize that the phase's variance is inversely proportional to the fringe modulation function. Moreover, one can see that the phase's variance can be reduced by making lower the right-side fraction having the PSA's characteristics.

From Eq. (2.41), the SNR of the estimated analytic signal is given by

$$\text{SNR} = \frac{(b/2)^2}{\eta/2}\left[\frac{\left|H(\omega_0)\right|^2}{\frac{1}{2\pi}\int_{-\pi}^{\pi} H(\omega)H^*(\omega)d\omega}\right] \tag{2.42}$$

whence, one can define the SNR gain of the PSA as [69]

$$G_{\text{SNR}} \overset{\text{def}}{=} \frac{\text{Quadrature Signal Power}}{\text{Filtered Noise Power}} = \frac{\left|H(\omega_0)\right|^2}{\frac{1}{2\pi}\int_{-\pi}^{\pi} H(\omega)H^*(\omega)d\omega} = \frac{\left|\sum_{n=0}^{N-1} c_n e^{-i\theta_n}\right|^2}{\sum_{n=0}^{N-1}\left|c_n\right|^2} \tag{2.43}$$

Designing of PSAs with noise robustness

I would like to mention that one can improve the noise robustness of algorithms derived from the Building-blocks technique by maximizing the function of noise robustness

$$U(\omega_0) = \frac{\left|H(\omega_0)\right|^2}{\frac{1}{2\pi}\int_{-\pi}^{\pi} H\left(\omega;\omega_0\right) H^*\left(\omega;\omega_0\right) d\omega}, \quad \forall\omega_0 \in (0,\pi]. \tag{2.44}$$

This function is the SNR gain of the algorithm as function of the phase shift ω_0; thus, the highest SNR gain is obtained as

$$\omega_0^+ = \underset{\omega_0}{\text{argmax}}\ U(\omega_0), \quad \forall\omega_0 \in (0,\pi]. \tag{2.45}$$

Considering the tunable 3-step PSA whose FTF is in Eq. (2.31), Figure 2.5 depicts the function $U(\omega_0)$ for such FTF, where the optimal phase shift is $\omega_0^+ = 2\pi/3$.

On the other hand, it is well-known that the least-squares estimator is the best one when additive white Gaussian noise perturbs the observed intensity; this means it maximizes the PSA's SNR gain. Henceforth, the schemes based on the least-squares estimator

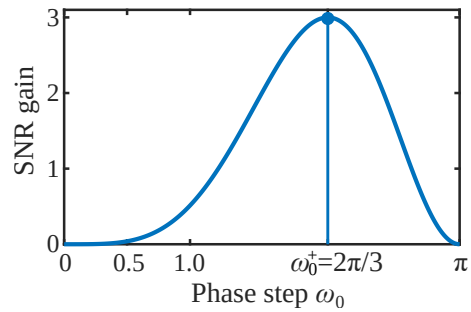

Figure 2.5: SNR gain of the tunable 3 step PSA with respect to the phase shift ω_0. One can observe that the optimal phase shift $\omega_0^+ = 2\pi/3$ in which the algorithm reaches the highest SNR gain.

will be called least-squares (LS-) PSAs. First, one obtains the temporal sequence of fringe patterns by sampling the continuous temporal fringe in Eq. (2.33),

$$\begin{aligned} I_{\text{noise}}(x,y,\theta_n) &= \int_{-\infty}^{\infty} I_{\text{noise}}(x,y,t)\delta(t-t_n)dt \\ &= a(x,y) + b(x,y)\cos\left[\varphi(x,y)+\theta_n\right] + \eta(t_n) \end{aligned} \tag{2.46}$$

where

$$\theta_n = \omega_0 t_n. \tag{2.47}$$

For simplicity, the radial frequency is considered to be normalized or $\omega_0 = 1$ rad/s. Equation (2.46) can be expressed in terms of the first-order trigonometry polynomial as,

$$I_n = I_{\text{noise}}(\theta_n) = a + \alpha\cos\theta_n + \beta\sin\theta_n + \eta(\theta_n), \quad \text{at } (x,y). \tag{2.48}$$

where the spatial dependence of I_{noise}, a, b, and φ, α was dropped, and so, $\alpha = b\cos\varphi$ and $\beta = -b\sin\varphi$.

Rewriting Eq. (2.48) in matrix notation, one has the least-squares optimization problem given by

$$\mathbf{x}^+ = \underset{\mathbf{x}}{\operatorname{argmin}} \|\mathbf{A}\mathbf{x} - \mathbf{b}\|_2^2 \tag{2.49}$$

where $\mathbf{x}^+$ is the optimal solution in the least squares sense, $\|\bullet\|_2$ is the Euclidean norm, as well as

$$\mathbf{x} = \begin{bmatrix} a & \alpha & \beta \end{bmatrix}^{\mathrm{T}} \tag{2.50}$$

$$\mathbf{b} = \begin{bmatrix} I_0 & I_1 & \cdots & I_{N-1} \end{bmatrix}^{\mathrm{T}} \tag{2.51}$$

$$\mathbf{A} = \begin{bmatrix} 1 & \cos\theta_0 & \sin\theta_0 \\ 1 & \cos\theta_1 & \sin\theta_2 \\ \vdots & \vdots & \vdots \\ 1 & \cos\theta_{N-1} & \sin\theta_{N-1} \end{bmatrix}. \tag{2.52}$$

Here, superscript T means transpose operation, and $\mathbf{x} \in \mathbb{R}^3$, $\mathbf{b} \in \mathbb{R}^N$ and $\mathbf{A} \in \mathbb{R}^{N\times 3}$.

The optimal solution $\mathbf{x}^+$ is obtained by solving the *system of normal equations*, this is

$$\begin{aligned} \mathbf{A}^{\mathrm{T}}\mathbf{A}\mathbf{x}^+ &= \mathbf{A}^{\mathrm{T}}\mathbf{b} \\ \therefore \mathbf{x}^+ &= \left(\mathbf{A}^{\mathrm{T}}\mathbf{A}\right)^{-1}\mathbf{A}^{\mathrm{T}}\mathbf{b} = \mathbf{A}^{\dagger}\mathbf{b}; \end{aligned} \tag{2.53}$$

where $\mathbf{A}^{\dagger}$ is called the Moore-Penrose pseudoinverse [70]; refer to Appendix C for a complete deduction of the optimization problem in Eq. (2.49). It is noticeable that matrix inverse $\left(\mathbf{A}^{\mathrm{T}}\mathbf{A}\right)^{-1}$ exists if and only if the number of fringe patterns fulfills $N \geq 3$.

Based in equations (2.28), (2.29), and (2.50), The coefficients of the PSA are computed as

$$c_n = \frac{1}{2}\left(a^{\dagger}_{2,n+1} + i a^{\dagger}_{3,n+1}\right), \tag{2.54}$$

where $a^{\dagger}_{l,n}$ is the element of $\mathbf{A}^{\dagger}$ at the l-th row and n-th column. These coefficients are given explicitly as following [71]

$$\begin{aligned} \mathrm{Re}\left\{c_n\right\} &= \sum_{l=0,m=0}^{N-1} (\sin\theta_m - \sin\theta_l)(\sin\theta_l\cos\theta_m + \sin\theta_m\cos\theta_n + \cos\theta_m\sin\theta_n) \\ \mathrm{Im}\left\{c_n\right\} &= \sum_{l=0,m=0}^{N-1} (\cos\theta_m - \cos\theta_l)(\sin\theta_l\cos\theta_m + \sin\theta_m\cos\theta_n + \cos\theta_m\sin\theta_n). \end{aligned} \tag{2.55}$$

Here, $\mathrm{Re}\left\{c_n\right\}$ means the real part of the n-th coefficient, while, its imaginary part is indicated by $\mathrm{Im}\left\{c_n\right\}$. Finally, the authors of the works [71–73] reported PSAs becoming in the coefficients in Eq. (2.55).

The so-called N-step LS-PSAs, coming from the formula by Bruning and associates [74], is a special case of the optimization problem in Eq. (2.49); the N-step LS-PSA considers that the phase shifts are given by

$$\theta_n = \frac{2\pi}{N}t = \frac{2\pi}{N}n. \tag{2.56}$$

Then, it is straightforwardly showing that auto correlation matrix $\mathbf{A}^{\mathrm{T}}\mathbf{A}$ is diagonal because the trigonometry polynomials in Eq. (2.48) make an orthogonal basis; then one has

$$\begin{aligned} \mathbf{A}^{\mathrm{T}}\mathbf{A} &= \begin{bmatrix} N & \sum_{n=0}^{N-1}\cos\left(\frac{2\pi n}{N}\right) & \sum_{n=0}^{N-1}\sin\left(\frac{2\pi n}{N}\right) \\ \sum_{n=0}^{N-1}\cos\left(\frac{2\pi n}{N}\right) & \sum_{n=0}^{N-1}\cos^2\left(\frac{2\pi n}{N}\right) & \sum_{n=0}^{N-1}\cos\left(\frac{2\pi n}{N}\right)\sin\left(\frac{2\pi n}{N}\right) \\ \sum_{n=0}^{N-1}\sin\left(\frac{2\pi n}{N}\right) & \sum_{n=0}^{N-1}\cos\left(\frac{2\pi n}{N}\right)\sin\left(\frac{2\pi n}{N}\right) & \sum_{n=0}^{N-1}\sin^2\left(\frac{2\pi n}{N}\right) \end{bmatrix} \\ &= \begin{bmatrix} N & 0 & 0 \\ 0 & N/2 & 0 \\ 0 & 0 & N/2 \end{bmatrix}. \end{aligned}$$

Whence, the inverse of the autocorrelation matrix is trivial, and thus, the Moore-Penrose pseudo inverse would be given by

$$\mathbf{A}^{\dagger} = \frac{1}{N}\begin{bmatrix} 1 & 1 & \cdots & 1 \\ 2\cos\left(\frac{2\pi}{N}0\right) & 2\cos\left(\frac{2\pi}{N}1\right) & \cdots & 2\cos\left[\frac{2\pi}{N}(N-1)\right] \\ 2\sin\left(\frac{2\pi}{N}0\right) & 2\sin\left(\frac{2\pi}{N}1\right) & \cdots & 2\sin\left[\frac{2\pi}{N}(N-1)\right] \end{bmatrix}.$$

From this last equation and (2.54), the coefficients for the N-step LS-PSA is given by

$$c_n = \frac{1}{N}\left[\cos\left(\frac{2\pi}{N}n\right) + i\sin\left(\frac{2\pi}{N}n\right)\right] = \frac{1}{N}e^{i2\pi n/N} \tag{2.57}$$

where it is used that Euler's formula states $e^{i\psi} = \cos\psi + i\sin\psi$. Finally, by taking the Fourier transform of the impulsive response of the N-step coefficients, the frequency transfer function of these algorithms is given by

$$\begin{aligned} H(\omega) &= \mathcal{F}_t\left\{\frac{1}{N}\sum_{n=0}^{N-1} e^{i2\pi n/N}\delta(t-n)\right\} \\ &= \frac{1}{N}\sum_{n=0}^{N-1} e^{-in(\omega+2\pi/N)} = \frac{1}{N}\prod_{n=0}^{N-2}\left[1 - e^{-i(\omega-2\pi n/N)}\right]. \end{aligned} \tag{2.58}$$

where Moivre's roots were substituted. Now, by substituting the coefficients (2.57) into Eq. (2.43), one has the SNR gain of the N-step LS-PSAs given by

$$\begin{aligned} G_{\text{SNR}}^{\text{Bruning}} &= \frac{\left|\sum_{n=0}^{N-1}\left[\left(e^{i2\pi n/N}\right)e^{-i2\pi n/N}\right]\right|^2}{\sum_{n=0}^{N-1}\left|e^{i2\pi n/N}\right|^2} = \frac{N^2}{N} \\ G_{\text{SNR}}^{\text{Bruning}} &= N. \end{aligned} \tag{2.59}$$

This last result means that the SNR gain is maximum, and thence, one should employ the N-step LS-PSA whenever possible.

As an example, Figure 2.6 illustrates the noise robustness of N-step least-squares phase-shifting algorithms as function of the number of fringe patterns N. In Fig. 2.6(a), the true, wrapped phase is shown, while, Fig. 2.6(b) depicts a noised fringe pattern. The simulated noise was additive white Gaussian noise so that the SNR of the fringe pattern was 10. Horizontal cuts of the estimated wrapped phases can be seen in Fig. 2.6(c); where $\varphi_{\mathcal{W}}^{\text{True}}$ is the true phase being wrapped, $\hat{\varphi}_{\mathcal{W}}^{N\text{-step}}$ indicates the estimated wrapped phase with 3-, 8-, and 100-step LS-PSA, respectively. One can observe that the phase $\hat{\varphi}_{\mathcal{W}}^{3\text{-step}}$ is too noised, the phase noise has $\hat{\sigma}_{3\text{-step}} = 0.66$ rads and $\hat{\mu}_{3\text{-step}} = 3.5\times10^{-5}$ rads; the unwrapping process would be very hard. Whereas, the phase $\hat{\varphi}_{\mathcal{W}}^{100\text{-step}}$ is so clean of noise whose dispersion $\hat{\sigma}_{100\text{-step}} = 0.03$ rads and $\hat{\mu}_{100\text{-step}} = -9.5\times10^{-5}$ rads; but measurements requiring 100 fringe patterns are impractical. Phase $\hat{\varphi}_{\mathcal{W}}^{8\text{-step}}$ is high noised for which the phase noise has dispersion $\hat{\sigma}_{8\text{-step}} = 0.36$ rads and $\hat{\mu}_{8\text{-step}} = -2.4\times10^{-3}$ rads. Nevertheless, this last level of noise can be handled in the phase unwrapping process, the number of fringe patterns is also practical. On the other hand, Figure 2.7 depicts the relation between the noise variance and the number of fringe patterns. It also draws the expected variance according to Eq. (2.41). One can observe that the noise variance decreases asymptotically. For non-uniformly spaced phase shifts, a similar result was obtained [75].

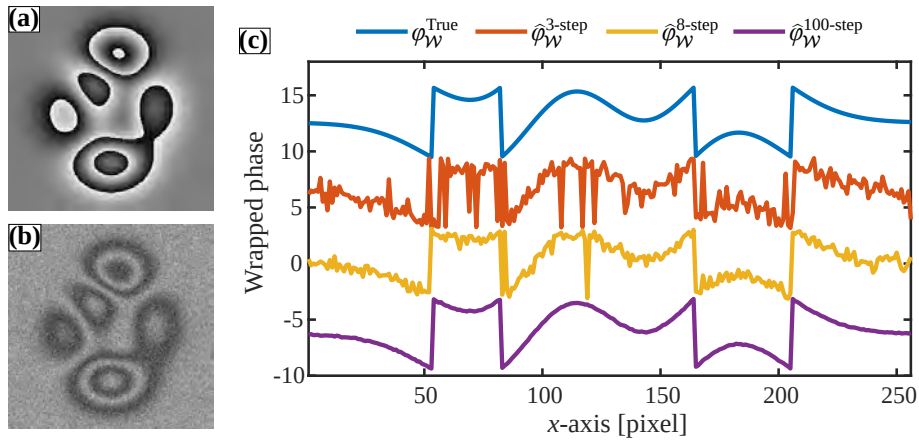

Figure 2.6: Noise robustness versus the number of fringe patterns for the N-step LS-PSA with nominal phase step of $2\pi/N$, particularly, it is depicted the results for 3, 8, and 100 fringe patterns. One can see the test phase in (a), a noised fringe pattern in (b), and in (c) the horizontal cuts of the estimated phase when utilizing those methods.

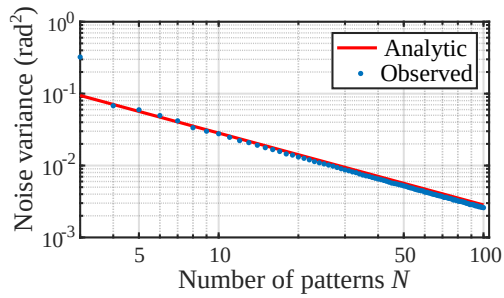

Figure 2.7: Noise variance *versus* the number of fringe patterns. Notice that the expected analytic value, in Eq. (2.41) is plotted.

2.2.3 Harmonic robustness

In general, acquired fringe patterns cannot have a perfect sinusoidal profile due to photodetectors' nonlinear response, intensity saturation, interference of multiple reflected beams, etcetera. Consequently, fringe patterns will have harmonics with higher order than the fundamental one. In order to retrieve the phase map correctly, high-order harmonics are desired to be rejected. A temporal sequence fringe pattern having harmonic contribution can be mathematically described by

$$I_{\text{harmonic}}(x,y,t) = \sum_{k=0}^{K} b_k(x,y)\cos k\left[\varphi(x,y)+\omega_0 t\right] \tag{2.60}$$

where $b_0(x,y) = a(x,y)$, and K is the highest order harmonic so that its level energy is about the energy level of the noise. In Eq. (2.60), we considered that the distortion can be mathematically expressed by a Fourier series.

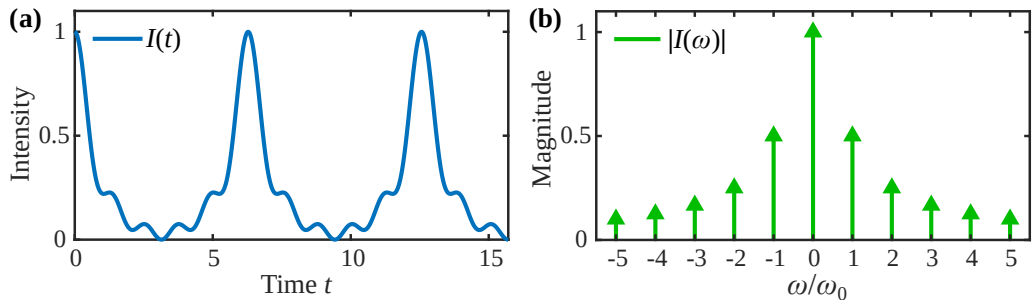

Figure 2.8: Temporal-continuous fringe having harmonic contributions: (a) temporal profile and (b) its spectrum.

Figure 2.8 depicts an example when the intensity is distorted by harmonics. By taking the Fourier transform of Eq. (2.60), one can obtain the spectrum given by

$$I(x,y,\omega) = b_0\delta(\omega) + \sum_{k=1}^{K} \frac{b_k(x,y)}{2}\left[e^{i\varphi(x,y)}\delta(\omega - k\omega_0) + e^{-i\varphi(x,y)}\delta(\omega + k\omega_0)\right]; \qquad (2.61)$$

where the searched signal is $b_1(x,y)\exp[i\varphi(x,y)]/2$. After the sampling procedure, the spectrum in Eq. (2.61) may be difficult to fulfill the Nyquist criterion; it means that this signal is not band-limit and implies that $K\omega_0 < \pi$, being difficult to be hold. Because the fringe pattern is not considered to be band-limited anymore, one must suppose some overlapping in the spectrum due to the finite support of the discrete-time Fourier transform. Therefore, those harmonics with $|k\omega_0| > \pi$ will be redistributed to its alias into the domain $[-\pi,\pi)$ of the discrete-time Fourier transform. By reason of searched signal may not be isolated at ω_0, so the computed analytic signal may have distorting harmonics due to the aliasing.

As an example, considering $\omega_0 = \pi/2$ and $K = 5$, the fringe pattern is given by

$$\begin{aligned} I(x,y,t) = {} & b_0(x,y) \\ & + b_1(x,y)\cos\left[\varphi(x,y) + \frac{\pi}{2}t\right] \\ & + b_2(x,y)\cos\left[2\varphi(x,y) + 2\frac{\pi}{2}t\right] \\ & + b_3(x,y)\cos\left[3\varphi(x,y) + 3\frac{\pi}{2}t\right] \\ & + b_4(x,y)\cos\left[4\varphi(x,y) + 4\frac{\pi}{2}t\right] \\ & + b_5(x,y)\cos\left[5\varphi(x,y) + 5\frac{\pi}{2}t\right]. \end{aligned}$$

Taking its Fourier transform, we have the next mathematical expression

$$\begin{aligned} I(x,y,\omega) &= \mathcal{F}_t\{I(x,y,t)\} \\ &= b_0(x,y)\delta(\omega) \\ &\quad + \frac{b_1(x,y)}{2}e^{i\varphi(x,y)}\delta\left(\omega - \frac{\pi}{2}\right) + \frac{b_1(x,y)}{2}e^{-i\varphi(x,y)}\delta\left(\omega + \frac{\pi}{2}\right) \end{aligned}$$

$$
\begin{aligned}
&+\frac{b_2(x,y)}{2}e^{i2\varphi(x,y)}\delta\left(\omega-2\frac{\pi}{2}\right)+\frac{b_2(x,y)}{2}e^{-2i\varphi(x,y)}\delta\left(\omega+2\frac{\pi}{2}\right)\\
&+\frac{b_3(x,y)}{2}e^{i3\varphi(x,y)}\delta\left(\omega-3\frac{\pi}{2}\right)+\frac{b_3(x,y)}{2}e^{-3i\varphi(x,y)}\delta\left(\omega+3\frac{\pi}{2}\right)\\
&+\frac{b_4(x,y)}{2}e^{i4\varphi(x,y)}\delta\left(\omega-4\frac{\pi}{2}\right)+\frac{b_4(x,y)}{2}e^{-4i\varphi(x,y)}\delta\left(\omega+4\frac{\pi}{2}\right)\\
&+\frac{b_5(x,y)}{2}e^{i5\varphi(x,y)}\delta\left(\omega-5\frac{\pi}{2}\right)+\frac{b_5(x,y)}{2}e^{-5i\varphi(x,y)}\delta\left(\omega+5\frac{\pi}{2}\right).
\end{aligned}
$$

Now, we project the ω-axis such that $\omega\in(-\pi,\pi]$ or the Discrete-Time Fourier transform

$$
\begin{aligned}
I'(x,y,\omega) &= b_0(x,y)\delta(\omega)\\
&+\frac{b_1(x,y)}{2}e^{i\varphi(x,y)}\delta\left(\omega-\frac{\pi}{2}\right)+\frac{b_1(x,y)}{2}e^{-i\varphi(x,y)}\delta\left(\omega+\frac{\pi}{2}\right)\\
&+=\frac{b_2(x,y)}{2}e^{i2\varphi(x,y)}\delta\left(\omega+\pi\right)+\frac{b_2(x,y)}{2}e^{-2i\varphi(x,y)}\delta\left(\omega+\pi\right)\\
&+\frac{b_3(x,y)}{2}e^{i3\varphi(x,y)}\delta\left(\omega+\frac{\pi}{2}\right)+\frac{b_3(x,y)}{2}e^{-3i\varphi(x,y)}\delta\left(\omega-\frac{\pi}{2}\right)\\
&+\frac{b_4(x,y)}{2}e^{i4\varphi(x,y)}\delta\left(\omega\right)+\frac{b_4(x,y)}{2}e^{-4i\varphi(x,y)}\delta\left(\omega\right)\\
&+\frac{b_5(x,y)}{2}e^{i5\varphi(x,y)}\delta\left(\omega-\frac{\pi}{2}\right)+\frac{b_5(x,y)}{2}e^{-5i\varphi(x,y)}\delta\left(\omega+\frac{\pi}{2}\right). \qquad (2.62)
\end{aligned}
$$

From (2.62), one can realize that the pairs $k=0,4$ are indistinguishable, and for $k=1,5$ are the same case. Moreover, other harmonics are overlapping one another. It is important to point out that if we design a PSA removing the background illumination at $\omega=0$, then this PSA will also eliminate the fourth harmonic *for this example*. On the other hand, if the PSA estimates the first harmonic at $\omega=\pi/2$, this PSA could not remove the positive fifth-harmonic because it is also located at $\omega=\pi/2$.

In the previous example, we depict a classical problem when phase demodulation fringe pattern with high harmonic distortion. We can employ a simple technique to identify those harmonics that a PSA will filter out. This technique consists of the PSA's FTF evaluation in a wider domain of ω, e.g., $\omega\in[-K\omega_0,K\omega_0]$. Figure 2.9 illustrates this example where we use the 4-step PSA proposed by Bruning *et al.* [74]; whose coefficients are given by

$$
c_n=\frac{1}{4}\exp\left[-i\frac{\pi}{2}n\right]; \qquad n=0,1,2,3.
$$

The PSA's FTF was evaluated for all $\omega\in(-5\pi/2,5\pi/2)$, this result is depicted by Fig. 2.9(a); it can be seen that the removed harmonic are $\{-5,\,-4,\,-2,\,-1,\,0,\,2,\,3,\,4\}$, while, the PSA keeps the harmonics $\{-3,\,1,\,5\}$. From Eq. (2.62), the unrejected harmonics are alias of the positive fundamental one at $\omega=\pi/2$, and the rejected are alias of the background illumination at $\omega=0$, or the negative fundamental harmonic at $\omega=-\pi/2$. Figure 2.9(b) depicts the spatial spectrum of the simulated data. This frame shows all harmonics since the spatial fringe patterns are band-limited, i.e., there are not alias as it happens in the temporal spectrum. Finally, the spectrum of the estimated analytic signal is drawn in Fig. 2.9(c) where one can realize that $\{-3,\,5\}$ distorting harmonics jeopardizes the estimation.

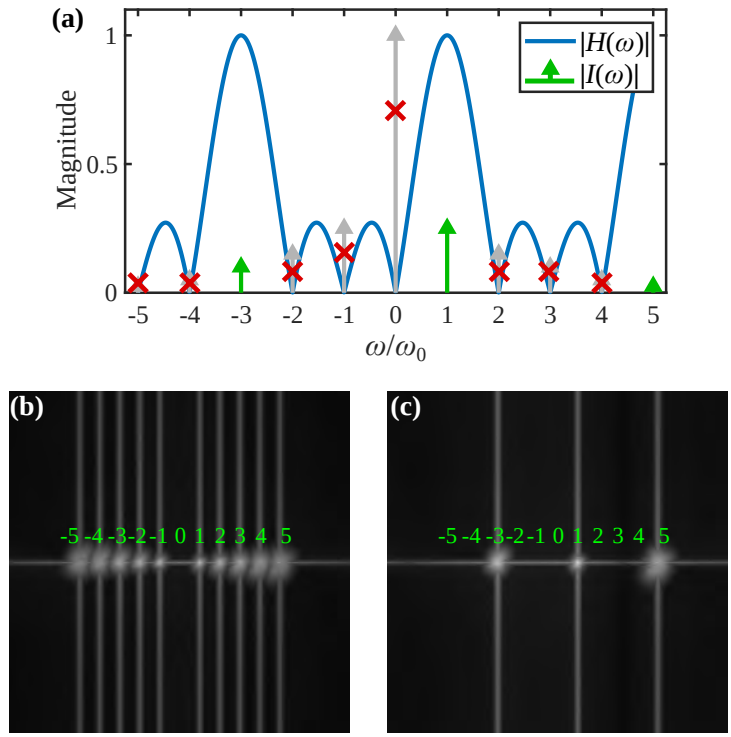

Figure 2.9: Harmonic rejection using the four-step PSA of Bruning *et al.* where $\omega_0 = \pi/2$. This PSA's frequency transfer function and the temporal spectrum of the data are in (a). Where one can observe the PSA would keep green Dirac deltas and reject the gray ones. The spatial spectrum of the simulated data is in (b), and the estimated analytic signal's one is in (c).

As a consequence of the previous example, it is required that the analytic signal's formula takes into account the amplitude contributions due to those distorting harmonics. Therefore, one has that

$$\frac{\hat{b}}{2}e^{i\hat{\varphi}} = \overbrace{\frac{b_1}{2}e^{i\varphi}H(\omega_0)}^{\text{Searched}} + \overbrace{\sum_{k=2}^{K}\frac{b_k}{2}\left[H(k\omega_0)e^{ik\varphi} + H(-k\omega_0)e^{-ik\varphi}\right]}^{\text{Harmonic distortion}}. \tag{2.63}$$

Besides, one can define a figure of merit to quantify the PSA's harmonic robustness as [76]

$$R_{\mathrm{H}} \overset{\text{def}}{=} \frac{\text{Quadrature Signal Power}}{\text{Total Harmonic Power}} = \frac{|H(\omega_0)|^2}{\sum_{k=2}^{K}\left(\frac{1}{k^2}\left[|H(k\omega_0)|^2 + |H(-k\omega_0)|^2\right]\right)}; \tag{2.64}$$

where it is assumed that the harmonics' amplitude decreases as $1/k$. By means of R_{H}, a PSA with a large value of R_{H} is preferable to other with smaller R_{H}. In advance, the author will call R_{H} as the harmonic robustness index.

Designing of PSAs with harmonic rejection capabilities

It now describes a method to obtain a PSA with harmonic rejecting capabilities by design its FTF in the frequency domain. With the aim of filtering out the first K harmonics and accomplishing the quadrature conditions, the PSA's FTF must fulfill the conditions:

$$H(k\omega_0) = 0, \quad \forall k \in \{0, -1, \pm 2, \pm 3, \ldots, \pm K\}; \tag{2.65}$$

where the quadrature conditions are for $k = 0, -1$; in addition, the FTF also has to accomplish that $H(\omega_0) \neq 0$.

Using the Building-Block technique and considering that the phase steps are uniformly-spaced, it is straightforwardly to design a PSA accomplishing the conditions in Eq. (2.65), so its frequency transfer function would be given by

$$H(\omega) = \overbrace{\left[1 - e^{-i\omega}\right]\left[1 - e^{-i(\omega+\omega_0)}\right]}^{\text{Quadrature conditions}} \prod_{k=2}^{K} \left(\overbrace{\left[1 - e^{-i(\omega+k\omega_0)}\right]}^{\text{Negative harmonics}} \overbrace{\left[1 - e^{-i(\omega-k\omega_0)}\right]}^{\text{Positive harmonics}} \right) \tag{2.66}$$

Here, the highest-order harmonic needs to be band-limited, this is $|K\omega_0| < \pi$. Because the FTF in Eq. (2.66) has $2K$ roots, the resulting PSA would have $2K + 1$ coefficients. Then the impulsive response can be computed as

$$h(t) = \mathcal{F}_t^{-1}\left\{H(\omega)\right\} = \sum_{n=0}^{2K} c_n \delta(t - n); \tag{2.67}$$

where $\mathcal{F}_t^{-1}\left\{\bullet\right\}$ is the operator of the temporal inverse Fourier transform.

When considering both uniform and non-uniform phase shifts, one can obtain a generalized PSA rejecting the first K distorting harmonics by a least-squares fit to the trigonometric polynomial of degree K [77]. Technique and analysis in [77] are a contribution derived from this thesis. Taking a sequence of fringe patterns by sampling the model in Eq. (2.60), this sequence can be described as

$$\begin{aligned} I_{\text{harmonic}}(x, y, \theta_n) &= \int_{-\infty}^{\infty} I_{\text{harmonic}}(x, y, t)\delta(t - t_n)dt \\ &= \sum_{k=0}^{K} b_k(x, y) \cos k\left[\varphi(x, y) + \theta_n\right]; \end{aligned} \tag{2.68}$$

whence

$$\theta_n = \omega_0 t_n. \tag{2.69}$$

For simplicity the temporal radial frequency is considered to be normalized $\omega_0 = 1(\text{rad/s})$ [77, 78], implying that $\theta_n = t_n$. Moreover, one can rewrite I_{harmonic} by means of the trigonometric identity $\cos(a + b) = \cos(a)\cos(b) - \sin(a)\sin(b)$, and so one has that

$$I_{\text{harmonic}}(x, y, \theta_n) = \sum_{k=0}^{K} \left[b_k(x, y) \cos\left[k\varphi(x, y)\right] \cos(k\theta_n)\right.$$

$$-b_k(x,y)\sin\left[k\varphi(x,y)\right]\sin(k\theta_n)\big]\,. \tag{2.70}$$

Due to the fact that the phase steps θ_n have no variation through the spatial axis (x,y), then the intensity can be described as a trigonometric polynomial as

$$I_n = I_{\text{harmonic}}(\theta_n) = a + \sum_{k=1}^{K}\left[\alpha_k\cos(k\theta_n) + \beta_k\sin(k\theta_n)\right], \quad \text{at } (x,y); \tag{2.71}$$

where the coefficients of the polynomial for (x,y) are given by $\alpha_k = b_k\cos(k\varphi)$ and $\beta_k = -b_k\sin(k\varphi)$.

In the model of Eq. (2.71), one needs to find the $2K+1$ unknown variables corresponding to the coefficients of the polynomial. To achieve them, one can solve the least-squares optimization problem given by

$$\mathbf{x}^{+} = \underset{\mathbf{x}}{\operatorname{argmin}}\,\|\mathbf{A}\mathbf{x}-\mathbf{b}\|_2^2\,; \tag{2.72}$$

whence $\|\bullet\|_2$ is the Euclidean norm, and

$$\mathbf{A} = \begin{bmatrix} 1 & \cos\theta_0 & \sin\theta_0 & \cdots & \cos K\theta_0 & \sin K\theta_0 \\ 1 & \cos\theta_1 & \sin\theta_1 & \cdots & \cos K\theta_1 & \sin K\theta_1 \\ \vdots & \vdots & \vdots & \ddots & \vdots & \vdots \\ 1 & \cos\theta_{N-1} & \sin\theta_{N-1} & \cdots & \cos K\theta_{N-1} & \sin K\theta_{N-1} \end{bmatrix}, \tag{2.73}$$

$$\mathbf{x} = \begin{bmatrix} a & \alpha_1 & \beta_1 & \cdots & \alpha_K & \beta_K \end{bmatrix}^{\mathrm{T}}, \tag{2.74}$$

$$\mathbf{b} = \begin{bmatrix} I_0 & I_1 & \cdots & I_{N-1} \end{bmatrix}^{\mathrm{T}}. \tag{2.75}$$

Here T means transpose operation as well as $\mathbf{A}\in\mathbb{R}^{N\times 2K+1}$, $\mathbf{x}\in\mathbb{R}^{2K+1}$, and $\mathbf{b}\in\mathbb{R}^{N}$.

The optimal solution in the least squares sense of Eq. (2.72) is given by solving the system of normal equations; this is

$$\mathbf{A}^{\mathrm{T}}\mathbf{A}\mathbf{x}^{+} = \mathbf{A}^{\mathrm{T}}\mathbf{b}, \tag{2.76}$$

and therefore,

$$\mathbf{x}^{+} = \left(\mathbf{A}^{\mathrm{T}}\mathbf{A}\right)^{-1}\mathbf{A}^{\mathrm{T}}\mathbf{b} = \mathbf{A}^{\dagger}\mathbf{b} \tag{2.77}$$

where $\mathbf{A}^{\dagger}$ is the Moore-Penrose pseudoinverse [70]. According to Eq. (2.77), autocorrelation matrix $\mathbf{A}^{\mathrm{T}}\mathbf{A}$ has matrix inverse if the number of fringe patterns fulfills $N \geq 2K+1$. Refer to Appendix C for the mathematical development of the optimization problem.

From Eq. (2.77), the coefficients of the PSA are computed as [77]

$$c_n = \frac{1}{2}\left(a^{\dagger}_{2,n+1} + i a^{\dagger}_{3,n+1}\right), \tag{2.78}$$

where $a^{\dagger}_{l,m}$ is the element of $\mathbf{A}^{\dagger}$ at the l-th row and the m-th column. Moreover, one can retrieve the phase from whenever harmonic employing the coefficients as

$$c_n^{\kappa\text{-th}} = \frac{1}{2}\left(a^{\dagger}_{2\kappa,n+1} + i a^{\dagger}_{2\kappa+1,n+1}\right), \quad \kappa\in\{1,2,\ldots,K\}, \tag{2.79}$$

where κ indicates the order of the harmonic; and its frequency transfer function fulfills

$$H(k\omega_0) = 0, \quad \forall k \in \{0, \pm 1, \ldots, \pm K\} - \{\kappa\}. \tag{2.80}$$

Therefore, the analytic signal for the κ-th harmonic is given by

$$\frac{\hat{b}^{\kappa\text{-th}}}{2} e^{i\kappa\hat{\varphi}} = \sum_{n=0}^{N-1} c_{N-n-1}^{\kappa\text{-th}} I_n; \tag{2.81}$$

whose phase is κ times more sensitive.

We now describe an example of harmonic rejection when the phase shifts are non-uniformly spaced. To this end, the intensity profile in Fig. 2.8 describes the fringe patterns; in other words, the fringe patterns have harmonic distortion until the fifth one.Nine nonuniformly-spaced phase steps are selected to be

$$\theta = \frac{2\pi}{9} \{0, 0.8, 1.6, 2.9, 3.3, 4.5, 5.7, 6.5, 7.2\}.$$

Then, one is able to reject until the fourth harmonic due to $[2(4)+1] = N = 9$; this means that these PSAs would not be able to reject the harmonic distortion completely. Based on equations (2.71) – (2.78), one can obtain four different FTFs (or PSAs) by setting the value of K; these are

$$\begin{aligned}
(K=1) \qquad & H_1(\omega) = \sum_{n=0}^{8} c1_n e^{i\theta_n \omega/\omega_0} \implies S_1(\omega) = H_1(\omega) I(\omega) \\
(K=2) \qquad & H_2(\omega) = \sum_{n=0}^{8} c2_n e^{i\theta_n \omega/\omega_0} \implies S_2(\omega) = H_2(\omega) I(\omega) \\
(K=3) \qquad & H_3(\omega) = \sum_{n=0}^{8} c3_n e^{i\theta_n \omega/\omega_0} \implies S_3(\omega) = H_3(\omega) I(\omega) \\
(K=4) \qquad & H_4(\omega) = \sum_{n=0}^{8} c4_n e^{i\theta_n \omega/\omega_0} \implies S_4(\omega) = H_4(\omega) I(\omega);
\end{aligned}$$

where $H_{\#}(\omega)$ and $S_{\#}(\omega)$ have normalized-frequency domain. Figure 2.10 illustrates the spectral description of the analytic signal estimation employing the aforementioned phase-shifting algorithms. Figure 2.10(a) corresponds to $K = 1$, where one can see that this PSA fulfills only the quadrature conditions; however, it significantly reduces the power of the distorting harmonics. For $K = 2$, the PSA fulfills the quadrature conditions, and also, it rejects the second harmonic correctly, and at the same time, it attenuates the higher-order harmonics, as seen in Fig. 2.10(b). For $K = 3$, the PSA removes the spectral components until the third harmonic and also attenuates the others as depicted in Fig. 2.10(c), but the negative fifth harmonic seems to be equal to the positive fourth for $K = 2$; refer to Fig. 2.10(b) and 2.10(c). Finally, Figure 2.10(d) shows the estimation for $K = 4$; the PSA rejects correctly until the fourth distorting harmonic; however, it does not attenuate significantly the fifth harmonic. In fact, its power seems to be greater than fourth and

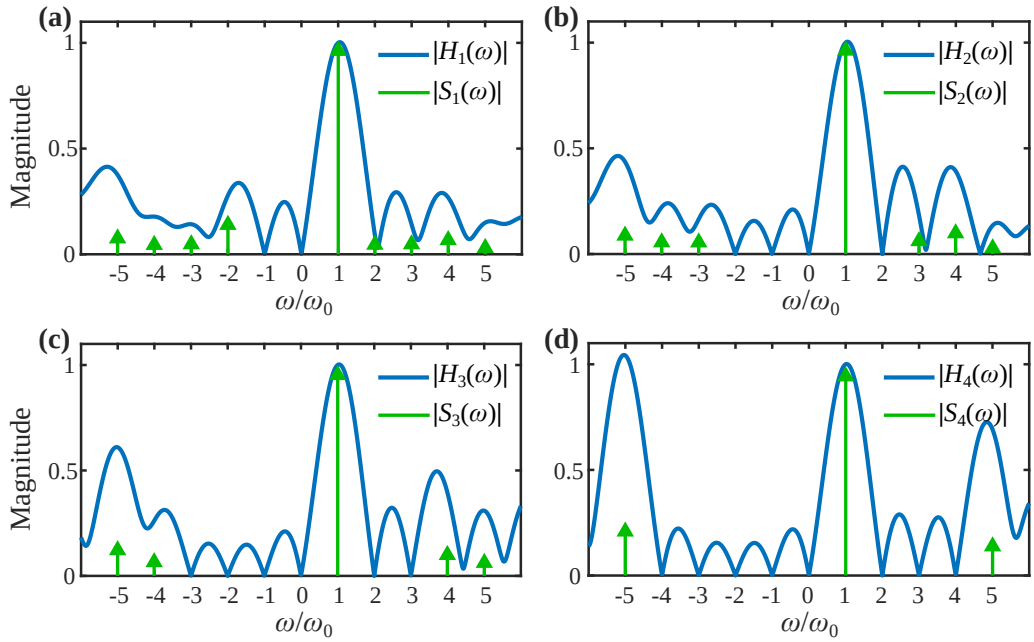

Figure 2.10: Spectral description of estimation of the analytic signal S_K using several 9-step PSAs $H_K(\omega)$ rejecting the first K harmonics: (a) $K = 1$, (b) $K = 2$, (c) $K = 3$, and (d) $K = 4$.

fifth ones corresponding to $K = 4$, refer to Figures 2.10(c) and 2.10(d); thence, $S_4(\omega)$ has distorting ripples whose amplitude is the largest for this numerical experiment. By computing the harmonic robustness index in Eq. (2.64), one obtains the values {25.76, 36.19, 30.63, 15.98 meaning the PSA with $K = 2$ is the most robust against harmonic distortion. Finally, by increasing the number of rejected harmonics, the PSA's SNR gain is jeopardized. For this example, the SNR gains are, respectively, {8.85, 8.80, 7.14, and 4.93} telling one the first PSA is the most robust against noise. In most cases, when $N = 2K + 1$, the resulting PSA will have a low SNR gain. Taking into account the Harmonic robustness index and the SNR gain, one should use that PSA with $K = 2$ when phase demodulating the fringe patterns; Figure 2.11 draws this fact where the phase of S_2 has the lowest amplitude of the harmonic distortion, whereas the highest amplitude corresponds to S_4. The reader realizes that these results are for this numerical experiment, and so, one should study every case using these figures of merit. Through this analysis based on figures of merit, we have determined the best PSA to phase demodulate this fringe patterns. Moreover, we want to point out that it may be thought that these results are not counterintuitive; however, it is expected that rejecting the large number of harmonics will not mostly translate into a better phase estimation when seeing non-uniformly-spaced phase shifts.

A particular kind of PSAs is obtained when the uniformly-spaced phase shifts are given by

$$\theta_n = \frac{2\pi}{N} n, \tag{2.82}$$

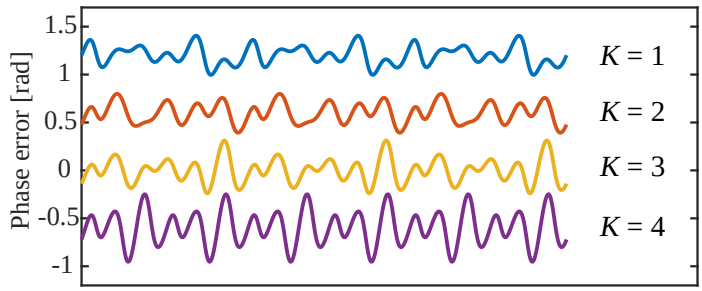

Figure 2.11: Phase error obtained when rejecting K harmonics. The description of the numerical experiment is in the main text.

where $n = t = 0, 1, \ldots, N-1$. Based on Eq. (2.72) – (2.77), one obtains that

$$\mathbf{A}^{\mathrm{T}}\mathbf{A} = \begin{bmatrix} \langle \mathbf{a}_1, \mathbf{a}_1 \rangle & \langle \mathbf{a}_1, \mathbf{a}_2 \rangle & \cdots & \langle \mathbf{a}_1, \mathbf{a}_{2K+1} \rangle \\ \langle \mathbf{a}_2, \mathbf{a}_1 \rangle & \langle \mathbf{a}_2, \mathbf{a}_2 \rangle & \cdots & \langle \mathbf{a}_2, \mathbf{a}_{2K+1} \rangle \\ \vdots & \vdots & \ddots & \vdots \\ \langle \mathbf{a}_{2K+1}, \mathbf{a}_1 \rangle & \langle \mathbf{a}_{2K+1}, \mathbf{a}_2 \rangle & \cdots & \langle \mathbf{a}_{2K+1}, \mathbf{a}_{2K+1} \rangle \end{bmatrix}$$

where $\langle \bullet, \bullet \rangle$ indicates the dot product and $\mathbf{a}_m$ is the $m-$th column of the matrix $\mathbf{A}$, and the elements of auto correlation matrix $\mathbf{A}^{\mathrm{T}}\mathbf{A}$ are given by

$$\begin{aligned}
\langle \mathbf{a}_1, \mathbf{a}_1 \rangle &= \sum_{n=0}^{N-1} 1 = N \\
\langle \mathbf{a}_1, \mathbf{a}_m \rangle &= \sum_{n=0}^{N-1} \cos\left[m \frac{2\pi}{N} n \right] = 0, && \forall m \in \{2, 4, \ldots, 2K\} \\
\langle \mathbf{a}_m, \mathbf{a}_m \rangle &= \sum_{n=0}^{N-1} \cos^2\left[m \frac{2\pi}{N} n \right] = \frac{N}{2}, && \forall m \in \{2, 4, \ldots, 2K\} \\
\langle \mathbf{a}_1, \mathbf{a}_m \rangle &= \sum_{n=0}^{N-1} \sin\left[m \frac{2\pi}{N} n \right] = 0, && \forall m \in \{3, 5, \ldots, 2K+1\} \\
\langle \mathbf{a}_m, \mathbf{a}_m \rangle &= \sum_{n=0}^{N-1} \sin^2\left[m \frac{2\pi}{N} n \right] = \frac{N}{2}, && \forall m \in \{3, 5, \ldots, 2K+1\} \\
\langle \mathbf{a}_l, \mathbf{a}_m \rangle &= \sum_{n=0}^{N-1} \cos\left[l \frac{2\pi}{N} n \right] \sin\left[m \frac{2\pi}{N} n \right] = 0, \; l \neq m \text{ and } \forall l, m \in \{2, 3, \ldots, 2K+1\};
\end{aligned}$$

therefore, the columns of $\mathbf{A}$ are an orthogonal basis. Thence, the Moore-Penrose pseu-

doinverse is given by

$$\mathbf{A}^{\dagger} = \frac{1}{N}\begin{bmatrix} 1 & 1 & \cdots & 1 \\ 2\cos\theta_0 & 2\cos\theta_1 & \cdots & 2\cos\theta_{N-1} \\ 2\sin\theta_0 & 2\sin\theta_1 & \cdots & 2\sin\theta_{N-1} \\ \vdots & \vdots & \vdots & \vdots \\ 2\cos K\theta_0 & 2\cos K\theta_1 & \cdots & 2\cos K\theta_{N-1} \\ 2\sin K\theta_0 & 2\sin K\theta_1 & \cdots & 2\sin K\theta_{N-1} \end{bmatrix}.$$

One can realize that the n-th coefficient of this PSA is given by

$$c_n = \frac{1}{N}\left[\cos\left(\frac{2\pi}{N}n\right) + i\sin\left(\frac{2\pi}{N}n\right)\right] = \frac{1}{N}e^{i2\pi n/N}; \tag{2.83}$$

where $1/N$ is a normalization term. Then, the impulsive response and the frequency transfer function are straightforwardly determined as

$$h(t) = \frac{1}{N}\sum_{n=0}^{N-1} e^{i2\pi n/N}\delta(t-n) \tag{2.84}$$

$$H(\omega) = \frac{1}{N}\sum_{n=0}^{N-1} e^{-in(\omega+2\pi/N)} = \frac{1}{N}\prod_{n=0}^{N-2}\left[1 - e^{-i(\omega-2\pi n/N)}\right]. \tag{2.85}$$

This FTF in Eq. (2.85) is the well-known formula by Bruning and associates [74] called the N-step least-squares PSAs. From Eq. (2.59), the SNR gain for these phase-shifting algorithms is computed as

$$G_{\text{SNR}}^{\text{Bruning}} = N. \tag{2.86}$$

Moreover, according to Eq. (2.57) and (2.83), the designed PSA is independent of the selected K value. Finally, these algorithms have the ability to reject the first $N-2$ harmonics instead of the $(N-1)/2$ as shown in Eq. (2.65); due to the aliasing phenomenon. Figure 2.12 draws the frequency transfer functions of this kind of PSAs where $N = 4, 5, 6$ and their FTFs were evaluated for all $\omega \in [-10\omega_0, 10\omega_0]$. One can observe that the 4-step LS-PSA rejects effectively the harmonics at $\{-10,\ -9,\ -8,\ -6,\ -5,\ -4,\ -3,\ 2,\ 3,\ 4,\ 6,\ 7,\ 8,\ 10\}$ while it is not able to remove the ones at $\{-7,\ -3,\ 5,\ 9\}$; as shown in Fig. 2.12(a). Figure 2.12(b) depicts that the 5-step LS-PSA eliminates the harmonics located at $\{-10,\ -8,\ -7,\ -6,\ -5,\ -3,\ 2,\ 2,\ 3,\ 4,\ 5,\ 7,\ 8,\ 9,\ 10\}$, but it is unsuccessful with the ones $\{-9,\ -4,\ 6\}$. The spectral description of harmonics robustness is illustrated in Fig. 2.12(c); where one can observe that this PSA rejects correctly the harmonics $\{-10,\ -9,\ -8,\ -7,\ -6,\ -4,\ -3,\ -2,\ 2,\ 3,\ 4,\ 5,\ 6,\ 8,\ 9,\ 10\}$, and it fails rejecting the others located at $\{-5,\ 7\}$. From these results, one is able to realize that the negative $(N-1)$-th harmonic is the first one to be not rejected when using the formula by Bruning *et al.* [74]. Finally, the harmonic robustness of the PSAs were $\{5.44,\ 9.74,\ 16.55\}$, respectively, for all $N \in \{4, 5, 6\}$; computed R_{H} in Eq. (2.64). It was thought that the tenth harmonic was the highest-order one. In this numerical experiment, the 6-step PSA is the most robust against harmonic distortion.

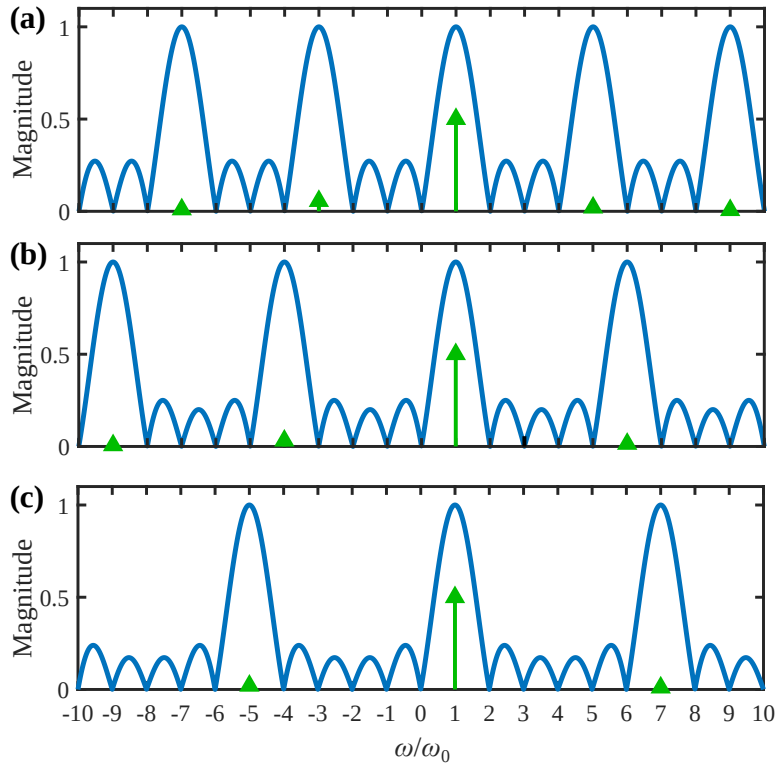

Figure 2.12: Spectral description of the harmonic-rejection capabilities of the N-step LS-PSA with: (a) $N = 4$, (b) $N = 5$, and (c) $N = 6$. Here, the FTFs were evaluated through the first ten harmonics for each FTF.

2.2.4 Detuning robustness

This error is systematic, and its domain is time. It occurs when the temporal tune frequency ω_0 of phase-shifting algorithm mismatches with that in the interferometry data tuned at $\omega_0 + \Delta\omega$; then one has the mathematical model given by

$$I_{\text{detuning}}(x, y, t) = a(x, y) + b(x, y) \cos\left[\varphi(x, y) + (\omega_0 + \Delta\omega)t\right] \tag{2.87}$$

where $\Delta\omega$ is a real scalar. Equation (2.87) defines the so-called linear detuning. Henceforth, the spatial dependence of I, a, b, and φ is dropped for clarity proposes. By taking the temporal Fourier transform of Eq. (2.87), one obtains

$$\begin{aligned} I_{\text{detuning}}(\omega) &= \mathcal{F}_t\left\{I_{\text{detuning}}(t)\right\} \\ &= a\delta(\omega) + \frac{b}{2}e^{i\varphi}\delta\left(\omega - \omega_0 - \Delta\omega\right) + \frac{b}{2}e^{-i\varphi}\delta\left(\omega + \omega_0 + \Delta\omega\right). \end{aligned} \tag{2.88}$$

Here one can see that the spectra components, corresponding to the cosine function, were shifted $\Delta\omega$ with respect to the fringe mathematical model without frequency detuning in Eq. (2.21).

The spectrum of the estimated analytic signal under linear detuning is determined by

$$S_{\text{detuning}}(\omega) = I(\omega)H(\omega)$$

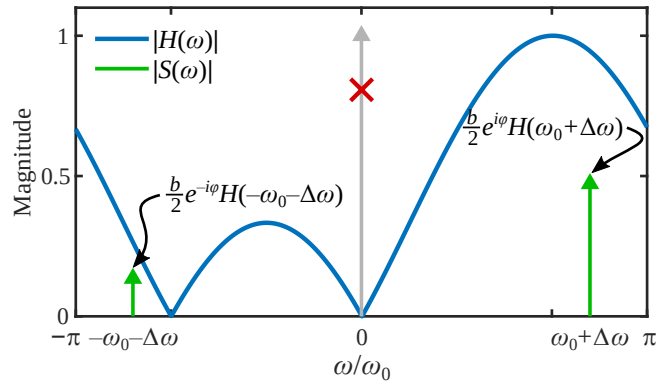

Figure 2.13: Spectral description of the detuning error.

$$= aH(0)\delta(\omega) + \frac{b}{2}e^{i\varphi}H(\omega_0+\Delta\omega)\delta\left(\omega-\omega_0-\Delta\omega\right) + \frac{b}{2}e^{-i\varphi}H(-\omega_0-\Delta\omega)\delta\left(\omega+\omega_0+\Delta\omega\right); \tag{2.89}$$

where $H(\omega)$ is the frequency transfer function of an arbitrary PSA, and $H(0)$, $H(\omega_0+\Delta\omega)$, and $H(-\omega_0-\Delta\omega)$ are complex scalars. From the quadrature conditions in Eq. (2.24), one has that $H(0)=0$. However, one would usually have that $H(\omega_0+\Delta\omega)\neq 0$ and $H(-\omega_0-\Delta\omega)\neq 0$. Therefore, the analytic signal's spectrum is given by

$$S_{\text{detuning}}(\omega) = \frac{b}{2}e^{i\varphi}H(\omega_0+\Delta\omega)\delta\left(\omega-\omega_0-\Delta\omega\right) + \frac{b}{2}e^{-i\varphi}H(-\omega_0-\Delta\omega)\delta\left(\omega+\omega_0+\Delta\omega\right); \tag{2.90}$$

whence

$$H(\omega_0+\Delta\omega) = \left|H(\omega_0+\Delta\omega)\right|e^{i\phi_1} \tag{2.91}$$

$$H(-\omega_0-\Delta\omega) = \left|H(-\omega_0-\Delta\omega)\right|e^{i\phi_2}. \tag{2.92}$$

Equation (2.90) is drawn in Figure 2.13, where one realizes that the negative component at $\omega=-\omega_0-\Delta\omega$ is not completely removed. Then, in the time domain, the analytic signal is mathematically described by

$$\frac{\hat{b}}{2}e^{\hat{\varphi}} = \frac{b}{2}H(\omega_0+\Delta\omega)e^{i\varphi} + \frac{b}{2}H(-\omega_0-\Delta\omega)e^{-i\varphi} \tag{2.93}$$

$$= \frac{b}{2}H(\omega_0+\Delta\omega)e^{i\varphi}\left(1+\frac{H(-\omega_0-\Delta\omega)}{H(\omega_0+\Delta\omega)}e^{-i2\varphi}\right). \tag{2.94}$$

Figure 2.14 schematically depicts the phasor sum in the last two equations. Figure 2.14, it is considered that

$$P_1 = H(\omega_0+\Delta\omega) = \left|H(\omega_0+\Delta\omega)\right|e^{i(\varphi+\phi_1)}$$

$$P_2 = H(-\omega_0-\Delta\omega) = \left|H(-\omega_0-\Delta\omega)\right|e^{-i(\varphi+\phi_2)}.$$

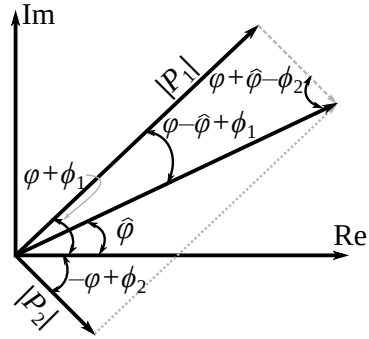

Figure 2.14: Phasor representation of the estimated analytic signal under detuning error.

Based on Fig. 2.14 and the sine law, one can obtain that

$$\sin(\varphi-\hat{\varphi}+\phi_1)=\frac{|H(-\omega_0-\Delta\omega)|}{|H(\omega_0+\Delta\omega)|}\sin(\varphi+\hat{\varphi}-\phi_2). \tag{2.95}$$

Now, considering the $\phi_1 \ll 1$ and the detuning error is small $\Delta\omega \ll 1$, then considering the approximations $\sin(\varphi-\hat{\varphi}+\phi_1)\approx\varphi-\hat{\varphi}+\phi_1$ and $\sin(\varphi+\hat{\varphi}-\phi_2)\approx\sin(2\varphi-\phi_2)$; by substituting them into Eq. (2.95), one has

$$\hat{\varphi}\approx\varphi+\phi_1-\frac{|H(-\omega_0-\Delta\omega)|}{|H(\omega_0+\Delta\omega)|}\sin(2\varphi-\phi_2). \tag{2.96}$$

Equation (2.96) was reported in previous works [34, 79]. In Eq. (2.96), one can observe that the estimated phase will have both distorting ripples at double frequency of the fringes and a phase piston ϕ_1 from the PSA when detuning error shows up. The phase piston is usually neglected, except when measuring optical thickness. The amplitude of the double-frequency distorting ripples defines the so-called detuning amplitude given by

$$\mathcal{D}(\Delta\omega)\overset{\text{def}}{=}\frac{|H(-\omega_0-\Delta\omega)|}{|H(\omega_0+\Delta\omega)|}=\frac{\left|\sum_{n=0}^{N-1}c_n e^{-in(-\omega_0-\Delta\omega)}\right|}{\left|\sum_{n=0}^{N-1}c_n e^{-in(\omega_0+\Delta\omega)}\right|}. \tag{2.97}$$

It is worth mentioning that $\mathcal{D}(\Delta\omega)$ gives the exact amplitude of the detuning error as seen in Eq. (2.94).

Designing of PSAs with detuning robustness

It is important to say that there exist two main efforts to deal with detuning error: PSAs having broad stopbands [80–87] or the self-tuning capability [39, 88–90]. The first ones have constant coefficients, and therefore, one can straightforwardly analyze them in the frequency domain by means of the FTF formalism. The second PSAs can estimate both the temporal fringe's frequency and the phase, and thence, they should be thought to have dynamic coefficients fulfilling the quadrature conditions. Furthermore, self-tuning PSAs are nonlinear phase estimators which usually have both a tunable linear PSA and a phase-step estimator; accordingly, one can analyze the former in the frequency domain,

as done in [34]. The following section goes through self-tuning algorithms; before that, it will be describing how to design PSAs with broad stopbands.

Considering the fringe pattern described by the following equation

$$\begin{aligned} I_{\text{detuning}}(x,y,t) &= a(x,y) + b(x,y)\cos\left[\varphi(x,y) + \Theta(t)\right] \\ &= a(x,y) + \frac{b(x,y)}{2}e^{i[\varphi(x,y)+\Theta(t)]} + \frac{b(x,y)}{2}e^{-i[\varphi(x,y)+\Theta(t)]} \end{aligned} \tag{2.98}$$

where $\Theta(t)$ is a smooth function describing phase shifts; this function is also thought to be band limited, this means that

$$\left|\frac{d\Theta(t)}{dt}\right|_{\max} < \pi; \tag{2.99}$$

during the observation time interval. Without loss of the generality, taking the temporal Fourier transform of Eq. (2.98), one obtains its spectrum given by

$$I_{\text{detuning}}(\omega) = \mathcal{F}_t\left\{I_{\text{detuning}}(t)\right\} = a\delta(\omega) + \frac{b}{2}e^{i\varphi}C(\omega) + \frac{b}{2}e^{-i\varphi}C^*(-\omega). \tag{2.100}$$

where spatial dependence (x,y) was dropped for clarity purposes, as well as

$$\begin{aligned} C(\omega) &= \mathcal{F}_t\left\{\exp\left[i\Theta(t)\right]\right\}, \\ C^*(-\omega) &= \mathcal{F}_t\left\{\exp\left[-i\Theta(t)\right]\right\}. \end{aligned} \tag{2.101}$$

From equations (2.99) – (2.101), one is able to realize that the lobe of the spectrum are not Dirac deltas when $\Theta(t)$ is not a straight line. Figure 2.15 draws a schematic description of the spectra in Eq. (2.100), so this plot depicts the need of using a phase-shifting algorithm having a broad stopband that eliminates the unwanted lobe on the negative side.

Since the phase-shifting function is smooth, it can be described through a polynomial expansion as following

$$\Theta(t) = \varrho_0 + \varrho_1 t + \varrho_2 t^2 + \varrho_3 t^3 + \cdots \tag{2.102}$$

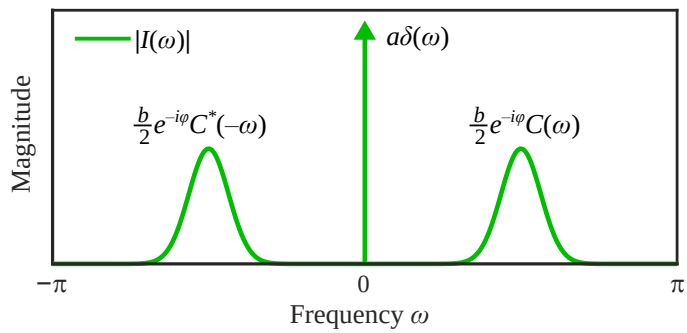

Figure 2.15: Temporal spectrum of phase-shifted fringe patterns when the phase-shifting function is smooth and band-limited. Observe that the spectral lobes are broad bands.

In phase-shifting interferometry, the constant term is usually $\varrho_0 = 0$ when the interferometer is in *optical contact* or measuring with respect to another. Then, one can approximate $\Theta(t)$ by the first two terms as

$$\Theta(t) \approx \tilde{\Theta}(t) = \overbrace{\omega_0 t + \kappa_1 t}^{\varrho_1 t} + \kappa_2 t^2; \tag{2.103}$$

where κ_1 is the linear (first-order) detuning and κ_2 is the quadratic (second-order) detuning. Hence, the approximate n-th phase shift is given by

$$\tilde{\theta}_n = \omega_0 n + \kappa_1 n + \kappa_2 n^2. \tag{2.104}$$

Here, one can observe that time sampling of the phase-shift function is uniform; however, phase shifts $\tilde{\theta}_n$ become nonuniformly-spaced due to the quadratic term. Moreover, when coefficients κ_1, κ_2 are known, one should use the algorithm for non-uniform phase shifts described in Eq. (2.54). Below, these terms will be unknown variables.

Let c_n be the coefficients of an arbitrary PSA with uniform phase shifts whose nominal phase step is ω_0; therefore, the estimated analytic signal is describes as [91, 92]

$$\frac{\hat{b}}{2} e^{i\hat{\varphi}} = \frac{b}{2} e^{i\varphi} \sum_{n=0}^{N-1} c_n e^{-i\tilde{\theta}} \left(1 + \frac{\sum_{n=0}^{N-1} c_n e^{i\tilde{\theta}}}{\sum_{n=0}^{N-1} c_n e^{-i\tilde{\theta}}} e^{-i2\varphi} \right). \tag{2.105}$$

From this last equation, one can see that the analytic signal is well estimated, provided that

$$S_1 = \sum_{n=0}^{N-1} c_n e^{-i\tilde{\theta}} = z \neq 0, \tag{2.106}$$

$$S_2 = \sum_{n=0}^{N-1} c_n e^{i\tilde{\theta}} = 0 \tag{2.107}$$

where $\arg\{z\}$ is a phase piston, so it should be $z = 1$. However, one is not able to computes S_1 nor S_2 because both κ_1 and κ_2 are unknown. Considering the second order Taylor series expansion of the detuning term, so one has that

$$e^{i(\kappa_1 n + \kappa_2 n^2)} \approx 1 + i\kappa_1 n - \frac{\kappa_1}{2} n^2 + i\kappa_2 n^2. \tag{2.108}$$

Substituting this result into Eq. (2.107), one has that

$$S_2 \approx \sum_{n=0}^{N-1} c_n e^{in\omega_0} + i\kappa_1 \sum_{n=0}^{N-1} n c_n e^{in\omega_0} - \frac{\kappa_1}{2} \sum_{n=0}^{N-1} n^2 c_n e^{in\omega_0} + i\kappa_2 \sum_{n=0}^{N-1} n^2 c_n e^{in\omega_0}; \tag{2.109}$$

due to the fact that

$$H'(-\omega_0) = \left. \frac{dH(\omega)}{d\omega} \right|_{\omega=-\omega_0} = -i \sum_{n=0}^{N-1} n c_n e^{i\omega_0}$$

$$H''(-\omega_0) = \left.\frac{d^2H(\omega)}{d\omega^2}\right|_{\omega=-\omega_0} = -\sum_{n=0}^{N-1} n^2 c_n e^{i\omega_0}.$$

Thereby, one is able to rewrite S_2 in terms of the frequency transfer function and its derivatives as

$$S_2 \approx H(-\omega_0) - \kappa_1 H'(-\omega_0) + \left(\frac{\kappa_1}{2} - i\kappa_2\right) H''(-\omega_0); \tag{2.110}$$

and in the same way, one obtains that

$$S_1 \approx H(\omega_0) - i\kappa_1 H'(\omega_0) + \left(\kappa_2 - \frac{\kappa_1}{2}\right) H''(\omega_0). \tag{2.111}$$

Result in Eq. (2.110) is important because it allows one to define the following new conditions

$$H'(-\omega_0) = 0, \quad \text{linear detuning} \tag{2.112}$$
$$H''(-\omega_0) = 0, \quad \text{Second-order detuning.} \tag{2.113}$$

Besides, the FTF must fulfill the quadrature conditions, and hence, these five conditions are sufficient to obtain a well estimated analytic signal from the fringe patterns in Eq. (2.98).

As an example, robustifying the 4-step LS-PSA against linear detuning has to fulfill the conditions

$$\begin{aligned}
H(\pi/2) &= \sum_{n=0}^{N-1} c_n e^{-in\pi/2} = 1,\\
H(0) &= \sum_{n=0}^{N-1} c_n = 0,\\
H(-\pi/2) &= \sum_{n=0}^{N-1} c_n e^{in\pi/2} = 0\\
H(\pi/2) &= \sum_{n=0}^{N-1} c_n e^{-in\pi} = 0\\
H'(-\pi/2) &= -in \sum_{n=0}^{N-1} c_n e^{in\pi/2} = 0,
\end{aligned}$$

Because there are five conditions, so the number of coefficients will be $N = 5$. These conditions are translated into the system of linear equations:

$$\begin{bmatrix} 1 & i & -1 & -i & 1 \\ 1 & 1 & 1 & 1 & 1 \\ 1 & -i & -1 & i & 1 \\ 1 & -1 & 1 & -1 & 1 \\ 0 & 1 & -2i & -3 & 4i \end{bmatrix} \begin{bmatrix} c_0 \\ c_1 \\ c_2 \\ c_3 \\ c_4 \end{bmatrix} = \begin{bmatrix} 1 \\ 0 \\ 0 \\ 0 \\ 0 \end{bmatrix},$$

and so, by solving it, one obtains the coefficients given by

$$c = \frac{1}{8}\{1, 2i, -2, -2i, 1\},$$

or the Schwider-Hariharan (S-H) PSA [80,81], whose roots are located at $\{-1, 1, -i, -i\}$; the algorithm has a root at $-i$ with multiplicity two. Now, adding the condition in Eq. (2.113), one has the coefficients given by

$$c = \frac{1}{16}\{1, 3i, -4, -4i, 3, i\},$$

and its roots are $\{-1, 1, -i, -i, -i\}$; now, the root at $-i$ has multiplicity three. In general, increasing the number of terms in the polynomial expansion of the phase-shift function, Eq. (2.102), will translate into increasing the multiplicity of the root corresponding to $\omega = -\omega_0$ [66]. Therefore, the building-blocks technique allows one to design this kind of phase-shifting algorithms by increasing the stopband root's multiplicity.

Perhaps the S-H algorithm [80, 81] is the most-known scheme being robust against detuning, its tune frequency is $\omega_0 = \pi/2$. Figure 2.16 draws the idea behind the use of broad stop bands to compensate the linear detuning error. In this Figure, one can observe that the FTF of this scheme is almost zero around $\omega = -\omega_0$, and therefore, it significantly attenuates the component at $-\omega_0 - \Delta\omega$. Comparing this example with the one depicted in Fig. 2.13 where the 3-step PSA was employed, the amplitudes of the detuning errors are 0.03 and 0.29 supposing $\Delta\omega = 0.2\omega_0$ for both methods, respectively. For this case, it is observed that the phase estimation using the S-H PSA has almost ten times smaller detuning amplitude than the one using the 3-step PSA.

By means of the Building-block technique is quite simple to design broad stopbands: one can increase the multiplicities of the root/zero at $-\omega_0$ or putting extra roots in the vicinity of $-\omega_0$ adding new Building blocks [87]. It is straightforwardly showed that the FTF of the S-H scheme is given by

$$H(\omega) = \left[1 - e^{-i\omega}\right]\left[1 - e^{-i(\omega+\pi/2)}\right]^2\left[1 - e^{-i(\omega+\pi)}\right]; \tag{2.114}$$

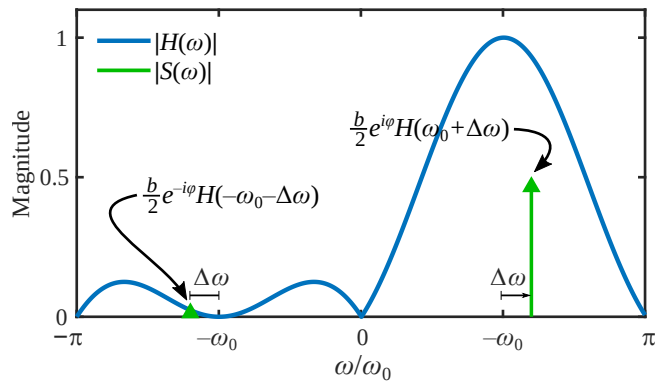

Figure 2.16: Spectral description of the detuning-error compensation using wide stopbands; particularly, it plots the FTF of the Schwider-Hariharan algorithm.

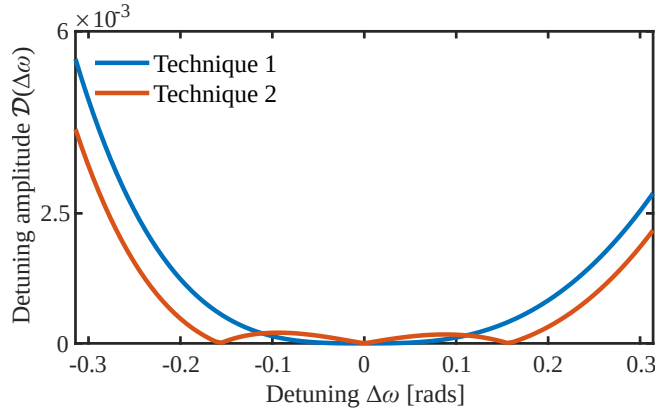

Figure 2.17: Comparison of two technique to design broad stop band to compensate detuning error: the first one consist of increasing the multiplicities of the root/zero at ω_0; in the second technique, one add extra zeros around ω_0.

where it is noticeable that the root/zero at $-\omega_0$ has multiplicity 2, whereas the zero at π has no relation with the detuning error. In general, the frequency transfer function being robust against detuning error can be described as

$$H(\omega) = \left[1 - e^{-i\omega}\right] \left[1 - e^{-i(\omega+\omega_0)}\right]^p, \quad p \geq 2; \tag{2.115}$$

then, the phase-shifting algorithm would has $(p + 2)$ steps and the root/zero at ω_0 will have multiplicity p.

An example of FTF putting extras zeroes around ω_0 is given by

$$H(\omega) = \left[1 - e^{-i\omega}\right] \left[1 - e^{-i(\omega+\omega_0)}\right] \left[1 - e^{-i(\omega+1.1\omega_0)}\right] \left[1 - e^{-i[\omega+0.9\omega_0)}\right], \tag{2.116}$$

where it was put arbitrarily two extra zeroes at $-1.1\omega_0$ and $-0.9\omega_0$; then, this algorithm requires five phase steps. Considering a PSA designed by Eq. (2.115) where $p = 3$, one can obtain another method with five steps and detuning robustness. Figure 2.17 depicts a comparison between these two techniques, where one can realize that the amplitude for the first technique is smaller in the nearby neighborhood $[-0.1, 0.1]$ rads; whereas, the second technique would have better estimations. Because detuning error is expected to be more frequently small ($|\Delta\omega| < .2\omega_0$), one should employ Eq. (2.115) instead of adding extra zeroes in the vicinity of ω_0.

On the other hand, several works have proposed PSAs for which the broad stopband is obtained using weighting functions [82–84]. In a work derived from this thesis, we formulated a weighted least-squares fit to the acquired intensity of the temporal fringe as [93]

$$\mathbf{x}^+ = \underset{\mathbf{x}}{\operatorname{argmin}} \left\| \mathbf{W}^{\frac{1}{2}} (\mathbf{b} - \mathbf{A}\mathbf{x}) \right\|_2^2 \tag{2.117}$$

where $\|\bullet\|_2$ is the Euclidean norm, $\mathbf{W} \in \mathbb{R}^{N\times N}$ is a diagonal matrix having the weights, as well as

$$\mathbf{x} = \begin{bmatrix} a & b\cos\varphi & -b\sin\varphi \end{bmatrix}^{\mathrm{T}}$$

$$\mathbf{b} = \begin{bmatrix} I_0 & I_1 & \cdots & I_{N-1}, \end{bmatrix}^{\mathrm{T}},$$
$$\mathbf{A} = \begin{bmatrix} 1 & \cos 0\omega_0 & \sin 0\omega_0 \\ 1 & \cos 1\omega_0 & \sin 1\omega_0 \\ \vdots & \vdots & \vdots \\ 1 & \cos(N-1)\omega_0 & \sin(N-1)\omega_0 \end{bmatrix}.$$

The optimal value is reached where the gradient with respect to $\mathbf{x}$ is equal to zero, i.e. $\nabla_{\mathbf{x}} \left\| \mathbf{W}^{\frac{1}{2}} (\mathbf{b} - \mathbf{A}\mathbf{x}) \right\|_2 = \mathbf{0}$; hence, we obtained the optimal value solving the weighted system of normal equations as

$$\mathbf{A}^{\mathrm{T}}\mathbf{W}\mathbf{A}\mathbf{x}^{+} = \mathbf{A}^{\mathrm{T}}\mathbf{W}\mathbf{b} \implies \mathbf{x}^{+} = \left(\mathbf{A}^{\mathrm{T}}\mathbf{W}\mathbf{A}\right)^{-1}\mathbf{A}^{\mathrm{T}}\mathbf{W}\mathbf{b} = \mathbf{D}\mathbf{b}; \tag{2.118}$$

and so, the PSA's coefficients are computed by

$$c_n = \frac{1}{2}\left(d_{2,n+1} + i d_{3,n+1}\right), \quad n = 0, 1, \ldots, N-1 \tag{2.119}$$

where $d_{j,n}$ is the element of $\mathbf{D}$ at the j-th row and n-th column. Also, the coefficients can be explicitly given by [93]

$$\begin{aligned} \mathrm{Re}\{c_n\} = & \\ & \sum_{\substack{l=0 \\ m=0}}^{N-1} \overbrace{[w_n w_l w_m]}^{\text{window}} \overbrace{[(\sin\theta_m - \sin\theta_l)(\sin\theta_l\cos\theta_m + \sin\theta_m\cos\theta_n + \cos\theta_m\sin\theta_n)]}^{\text{Least squares solution}} \\ \mathrm{Im}\{c_n\} = & \\ & \sum_{\substack{l=0 \\ m=0}}^{N-1} [w_n w_l w_m]\,[(\cos\theta_m - \cos\theta_l)(\sin\theta_l\cos\theta_m + \sin\theta_m\cos\theta_n + \cos\theta_m\sin\theta_n)] \end{aligned} \tag{2.120}$$

where $\theta_n = n\omega_0$, also these coefficients are non-significantly scaled for clarity in exposition. It is worth mentioning that the expression allows one to compute the weighted coefficients even the phase shifts would be non-uniformly spaced. To deal with the detuning error, it is recommendable that the nominal phase shift of the fringe patterns is close to $\pi/2$, so PSAs would be designed with $\omega_0 = \pi/2$.

Without losing generality, several weighting windows are following presented

$$w_n^{\mathrm{Hann}} = \frac{1}{2}\int_{-\infty}^{\infty} \left[1 - \cos(2\pi t/\tau)\right] \delta(t - t_n) dt \tag{2.121}$$

$$w_n^{\mathrm{Gaussian}} = \frac{1}{2}\int_{-\infty}^{\infty} \exp\left[-\frac{1}{2}\left(\alpha\frac{t-\bar{t}}{\tau/2}\right)^2\right] \delta(t - t_n) dt \tag{2.122}$$

$$w_n^{\mathrm{Riemann}} = \int_{-\infty}^{\infty} \frac{\sin\left[2\pi\left(t-\bar{t}\right)/\tau\right]}{2\pi(t-\bar{t})/\tau} \delta(t - t_n) dt; \tag{2.123}$$

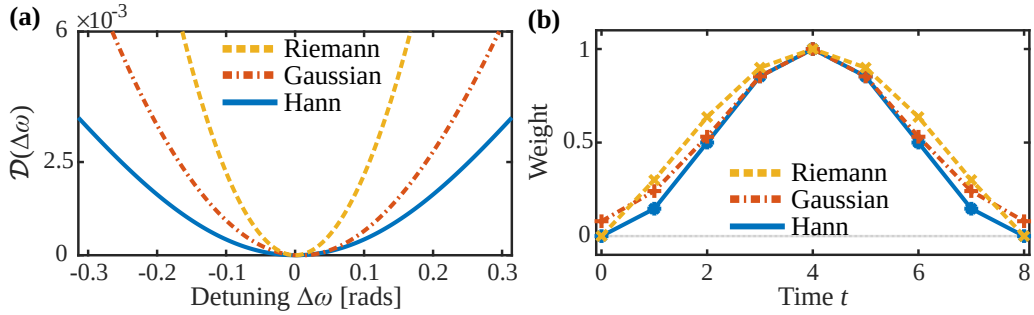

Figure 2.18: Comparison of detuning amplitude performed by windowed PSAs with Hann, Gaussian and Riemann windows in (a). The weighting windows are shown in (b).

Here $t_n = n$, and τ and $\bar{t}$ are the maximum and center of $\{t_n\}_{n=0}^{N-1}$, respectively. Moreover, it is noticeable that the Gaussian window has a parameter α being the reciprocal of the standard deviation. Other windows can be found in [94]. Figure 2.18 illustrates a comparison of the detuning robustness of the obtained algorithms using 9-steps and the windows in equations (2.121) – (2.123); it was selected that $\alpha = 2.25$ for the Gaussian window. One can observe that the Hann-PSA was the most detuning robust, and the weakest was the Riemann-PSA. It is worth mentioning that the Hann-PSA has coefficients $c_0 = c_{N-1} = 0$; therefore, it would be neglecting the first and the last records; this can be avoided by computing the window with length $N + 2$.

Even though the windowed PSAs have been employed to deal with the detuning error, I believe that they should be utilized when the fringe modulation function has time variations as done in the next Chapter. One can straightforwardly realize this fact from Eq. (2.117).

2.2.5 Nonlinear phase-shifting algorithms

It is called non-linear phase-shifting algorithms to those having the ability to estimate both the phase shifts and the phase map. In general, these schemes can be divided into two *sub methods*: one for phase retrieval, and the other to estimate the phase shifts; here, they are named phase-shift estimators. Therefore, one can formulate the nonlinear problem as

$$\varphi^{+} = \underset{\varphi}{\operatorname{argmin}}\ U\left(\varphi; \theta_n\right) \tag{2.124}$$

$$\left\{\theta_n^{+}\right\} = \underset{\{\theta_n\}}{\operatorname{argmin}}\ U\left(\{\theta_n\}; \varphi\right) \tag{2.125}$$

where $U(\bullet)$ is a cost function relating the observed data I and the estimated one $\hat{I}$ by means of a metric. Equations (2.124) and (2.125) can be iterated to improve the quality of the estimation.

Phase-shift estimators can be organized into two categories; the first ones estimates a local frequency ω_0 supposing that $\theta_n = n\omega_0$, then the PSA is tuning to ω_0, for example the scheme in references [39, 88–90, 95, 96]; the second ones extracts every phase step θ_n, and then, a generalized PSA is employed for phase retrieval, some of this kind of methods are

in the references [97–112], and with frequency description in [113, 114], as well as methods for two fringe patterns, however, these are not useful in fringe projection profilometry due to gamma distortion and their weakness against to noise.

Because acquired fringe patterns are expected to be non-uniformly phase-shifted, tunable PSAs are not described. Instead, in the rest of this subsection, it is revised those algorithms for such kind of fringe patterns. First, it is analyzed a phase-shifting estimator based on the sinusoidal fitting of the fringe pattern. Then, this Section goes through the algorithms based on principal component analysis and Gramm-Schmidt ortho-normalization methods.

Before presenting nonlinear phase-shifting algorithms, it is suitable determining what it happen if the phase shifts are not exactly given. Let $\{\tilde{\theta}_n\}$ and $\{\theta_n\}$ be the poorly-estimated and exact phase shifts, also $\{\tilde{\theta}_n\}$ fulfills the following condition

$$\tilde{\theta}_n \neq \theta_n + \Delta\theta, \quad \Delta\theta \in \mathbb{R} \quad \text{and} \quad \forall n; \tag{2.126}$$

where $\Delta\theta$ is a piston. Then, poorly-estimated coefficients $\tilde{c}$ are computed using $\tilde{\theta}_n$. From Eq. (2.29), the analytic signal is given by

$$\frac{\tilde{b}}{2}e^{i\tilde{\varphi}} = \frac{b}{2}H(\omega_0)e^{i\varphi}\left[1 + \frac{H(0)}{H(\omega_0)}\frac{2a}{b}e^{-i\varphi} + \frac{H(-\omega_0)}{H(\omega_0)}e^{-i2\varphi}\right], \quad \forall(x,y) \tag{2.127}$$

where

$$H(0) = \sum_{n=0}^{N-1}\tilde{c}_n, \quad H(-\omega_0) = \sum_{n=0}^{N-1}\tilde{c}_n e^{i\theta_n/\omega_0}, \quad H(\omega_0) = \sum_{n=0}^{N-1}\tilde{c}_n e^{-i\theta_n/\omega_0} \tag{2.128}$$

with $\theta_n = \omega_0 t_n$, one can observe in Eq. (2.128) that exact phase steps $\{\theta_n\}$ is used to compute the frequency transfer function of the PSA; it is remarkable that if one uses the poorly-estimated phase step to compute the PSA's FTF, then one will obtain an FTF not working with Eq. (2.127) due to the fact that that FTF will depicts that the poorly-estimated coefficients accomplish the quadrature conditions. Figure 2.19 displays this fact: first the real PSA's FTF is in Fig. 2.19(a) where one can clearly see that the lobe at $-\omega_0$ was not eliminated completely; second, the wrong FTF in Fig. 2.19(b) exposes that the analytic signal would have been estimated correctly. Based on Eq. (2.127), the poorly-estimated $\tilde{\varphi}(x,y)$ will have distorting waves at the single-frequency of the fringe pattern when $H(0) \neq 0$ and at the double-frequency when $H(-\omega_0) \neq 0$; in most cases, it is expected that the FTF accomplishes $H(0) = 0$, and hence, one should assume that phase step mismatching will introduce a detuning-like error of $|H(-\omega_0)| \,/\, |H(\omega_0)|$. Moreover, we want to point out that these distorting ripples' amplitudes cannot be estimated, in practice, because it needs to know the phase steps exactly.

Phase-shift estimator based on sinusoidal fitting

In optical interferometric measurements, it is typical that some area of interferograms has no measuring information about a testing object because the latter is not commonly rectangular nor square as camera sensors are. Considering that Ω is the set of those pixels

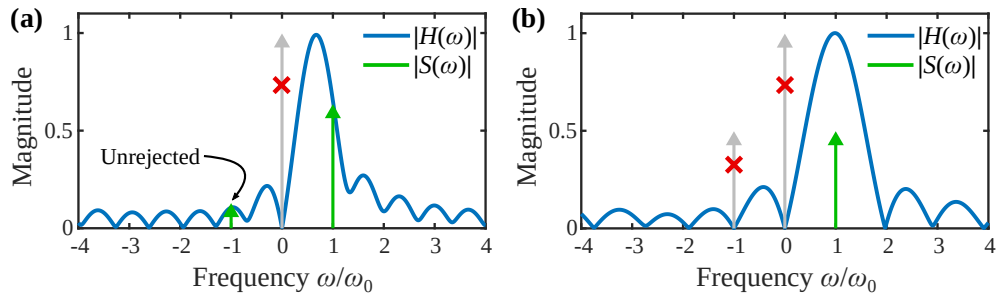

Figure 2.19: Frequency transfer function of a PSA for which the phase steps were poorly-estimated: (a) shows the true FTF with the exact phase shifts, and (b) illustrates the FTF using the poorly-estimated phase steps. One can observe that the distorting ripples' amplitude can be estimated, provided that the exact phase shifts are known.

having the measuring information about a test object, then the spatial position for a valid pixel is $p \in \Omega$, and M is the number of pixels in Ω.

Let both background intensity and fringe modulation be spatially constant, and they change only between interferograms; this is, they are time-variant; hence one has the cost function given by

$$U\left(\theta_n, a_n, b_n; \varphi, n\right) = \sum_{p=1}^{M} \rho\Big(a_n + b_n \cos\left(\varphi_p + \theta_n\right) - I_{p,n}\Big), \tag{2.129}$$

where φ is the phase previously-estimated using the PSA in Eq. (2.54). $\rho : \mathbb{R} \longrightarrow \mathbb{R}$ is a weighted function which will be described above. As one can see in Eq. (2.129), one requires optimizing U for each fringe pattern.

Rewriting Eq. (2.129) in is matrix formulation, one obtains

$$U\left(\mathbf{y}; \varphi\right) = \sum_{p=1}^{M} \rho\left(\mathbf{B}_p \cdot \mathbf{y} - z_p\right) = \sum_{p=1}^{M} \rho\left(r_p\right), \tag{2.130}$$

where

$$\mathbf{y} = \begin{bmatrix} a & b\cos\theta & -b\sin\theta \end{bmatrix}^{\mathrm{T}}, \tag{2.131}$$

$$\mathbf{z} = \begin{bmatrix} I_1 & I_2 & \cdots & I_M \end{bmatrix}^{\mathrm{T}}, \tag{2.132}$$

$$\mathbf{B} = \begin{bmatrix} 1 & \cos\varphi_1 & \sin\varphi_1 \\ 1 & \cos\varphi_2 & \sin\varphi_2 \\ \vdots & \vdots & \vdots \\ 1 & \cos\varphi_M & \sin\varphi_M \end{bmatrix}. \tag{2.133}$$

Here one has the linear model $\mathbf{B}\mathbf{y} = \mathbf{z}$, and $r_p = I_{\text{estimated}} - I_{\text{measured}}$ are the residuals for each pixel p; $\mathbf{B}_p \cdot \mathbf{y}$ is the dot product of the pth row of $\mathbf{B}$ and the vector of unknowns $\mathbf{y}$.

With the aim of optimizing Eq. (2.130), one needs to satisfy the condition:

$$\nabla_{\mathbf{y}} U\left(\mathbf{y}; \varphi\right) = \mathbf{0}. \tag{2.134}$$

Whence, one obtains the equations

$$\frac{\partial U}{\partial y_j} = \sum_{p=1}^{M} \psi\left(\mathbf{B}_p \cdot \mathbf{y} - z_p\right) B_{p,j} = 0, \quad j = 1, 2, 3. \tag{2.135}$$

Here, $\psi : \mathbb{R} \longrightarrow \mathbb{R}$ is the first derivative of ρ and is called the *influence curve* indicating how strong large residuals will pull the estimation [115].

One can observe that equations (2.135) are a system of nonlinear equations which must be optimized in order to obtain the optimal value $\mathbf{y}^{+}$. With the aim of solving (2.135), one can rewritten them as

$$\frac{\partial U}{\partial y_j} = \sum_{p=1}^{M} B_{p,j}\left(\mathbf{B}_p \cdot \mathbf{y} - z_p\right) w_p = 0, \quad j = 1, 2, 3. \tag{2.136}$$

where $B_{p,j}$ is the element of $\mathbf{B}$ at p-th row and j-th column, as well as the weight given by

$$w_p = \frac{\psi\left(\mathbf{B}_p \cdot \mathbf{y} - z_p\right)}{\left(\mathbf{B}_p \cdot \mathbf{y} - z_p\right)}. \tag{2.137}$$

Thence, this nonlinear optimization problem can be solved through the iteratively reweighted least-squares method (IRLS) [116, 117]; in the k-th iteration, this method consists of estimating $\mathbf{y}^{(k+1)}$ holding certain weights $w_p^{(k)}$, and then, updating the weights $w_p^{(k+1)}$ holding the just previously-estimated $\mathbf{y}^{(k+1)}$. These two steps are:

1. **Estimating $\mathbf{y}^{(k+1)}$.** One can obtain the system of weighted normal equations as

$$\begin{aligned} \mathbf{B}^{\mathrm{T}}\mathbf{W}^{(k)}\mathbf{B}\mathbf{y}^{(k+1)} &= \mathbf{B}^{\mathrm{T}}\mathbf{W}^{(k)}\mathbf{z} \\ \therefore \mathbf{y}^{(k+1)} &= \left[\mathbf{B}^{\mathrm{T}}\mathbf{W}^{(k)}\mathbf{B}\right]^{-1}\mathbf{B}^{\mathrm{T}}\mathbf{W}^{(k)}\mathbf{z} \end{aligned} \tag{2.138}$$

   where $\mathbf{W} = \mathrm{diag}\left(\mathbf{w}\right)$ being $\mathbf{w}$ the vector of weights. Eq. (2.138) represents a 3×3 system of linear equations, in which the matrix and vector of observations are given by

$$\mathbf{B}^{\mathrm{T}}\mathbf{W}^{(k)}\mathbf{B} = \begin{bmatrix} \sum_{p=1}^{M} w_p^{(k)} & \sum_{p=1}^{M} w_p^{(k)} \cos\hat{\varphi}_p & \sum_{p=1}^{M} w_p^{(k)} \sin\hat{\varphi}_p \\ \sum_{p=1}^{M} w_p^{(k)} \cos\hat{\varphi}_p & \sum_{p=1}^{M} w_p^{(k)} \cos^2\hat{\varphi}_p & \sum_{p=1}^{M} w_p^{(k)} \cos\hat{\varphi}_p \sin\hat{\varphi}_p \\ \sum_{p=1}^{M} w_p^{(k)} \sin\hat{\varphi}_p & \sum_{p=1}^{M} w_p^{(k)} \cos\hat{\varphi}_p \sin\hat{\varphi}_p & \sum_{p=1}^{M} w_p^{(k)} \sin^2\hat{\varphi}_p \end{bmatrix}$$

$$\mathbf{B}^{\mathrm{T}}\mathbf{W}^{(k)}\mathbf{z} = \begin{bmatrix} \sum_{p=1}^{M} w_p^{(k)} I_p \\ \sum_{p=1}^{M} w_p^{(k)} \cos\hat{\varphi}_p I_p \\ \sum_{p=1}^{M} w_p^{(k)} \sin\hat{\varphi}_p I_p \end{bmatrix}.$$

where $\hat{\varphi}$ is a phase map estimation. One can observe that system of equations (2.138) has unique solution due to the number of non-zero elements of $\mathbf{w}$ will be much larger than three.

2. **Updating $\mathbf{W}^{(k+1)}$.** Considering the Stundentized residuals computed as

$$s_p = \frac{r_p}{\hat{\sigma}\sqrt{1-h_p}} \tag{2.139}$$

where estimated standard deviation $\hat{\sigma}$ is obtained as

$$\hat{\sigma} = \text{mad}\,(r_p) = \frac{|r_p - \text{median}\,(\{r_p\})|}{0.6745}. \tag{2.140}$$

Here $\text{mad}\,(\bullet)$ is called *the median of the absolute deviations*, h_p is p-th diagonal element of the hat matrix described by $\mathbf{H} = \mathbf{B}\left(\mathbf{B}^{\mathrm{T}}\mathbf{B}\right)^{-1}\mathbf{B}^{\mathrm{T}}$. In particular, we want to note that

$$h_p = \mathbf{B}_p^{\mathrm{T}}\left(\mathbf{B}^{\mathrm{T}}\mathbf{B}\right)^{-1}\mathbf{B}_p, \tag{2.141}$$

where it is noticeable that h_p measures the location of the p-th point with respect to the centroid of the y space. As a consequence, we are able to mention that the points violating the assumptions of the mathematical model will be translated into remote points from the centroid; and hence, these remote points are easy to be detected by computing the Studentized residuals. Based on equations (2.137) and (2.139) – (2.141), the new weights can be computed as follows

$$w^{(k+1)} = \frac{\psi\left(s_p^{(k)}\right)}{s_p^{(k)}}. \tag{2.142}$$

These two steps are iterated until a convergence condition is met; for example

$$\left\|\mathbf{y}^{(k+1)} - \mathbf{y}^{(k)}\right\|_2 < \text{threshold}. \tag{2.143}$$

Once this iterative procedure had converged, one obtains the optimal solution $\mathbf{y}^{+}$, and the phase steps are given by

$$\theta_n^{+} = \tan^{-1}\left(-\frac{y_3^{+}}{y_2^{+}}\right). \tag{2.144}$$

It is noticeable that this iterative procedure is performed for each fringe pattern.

Using Greivenkamp's phase-shifting algorithm for phase retrieval, then the pseudocode

for nonlinear phase demodulation would be describe as:

Input: $I(x, y, t_n)$, $\theta^{(0)}$, and Ω.
while $\left\|\theta^{(k_1+1)} - \theta^{(k_1)}\right\| <$ threshold **do**
  $c_n^{(k_1+1)} \leftarrow \left(a_{2,n}^{\dagger} + i a_{3,n}^{\dagger}\right)/2$; $\theta^{(k_1)}$. See Eq. (2.55).
  $\varphi^{(k_1+1)} \leftarrow \text{angle}\left[\sum_{n=0}^{N-1} c_{N-n-1}^{(k_1+1)} I_n\right]$, $\forall p$.
  $h_p \leftarrow \mathbf{B}_p^{\mathrm{T}} \left(\mathbf{B}^{\mathrm{T}}\mathbf{B}\right)^{-1} \mathbf{B}_p$, $\forall p$; $\varphi_p^{(k_1+1)}$.
  foreach $n \in \{0, 1, \ldots, N-1\}$ **do**
    $\mathbf{z} \leftarrow I_n$.
    $w_p^{(0)} \leftarrow 1$, $\forall p$.
    while $\left\|\mathbf{y}^{(k_2+1)} - \mathbf{y}^{(k_2)}\right\| <$ threshold **do**
      $\mathbf{y}^{(k_2+1)} \leftarrow \left[\mathbf{B}^{\mathrm{T}}\mathbf{W}^{(k_2)}\mathbf{B}\right]^{-1} \mathbf{B}^{\mathrm{T}}\mathbf{W}^{(k_2)}\mathbf{z}$.
      $s_p^{(k_2+1)} \leftarrow \texttt{Studentized}\left(\mathbf{B}_p \cdot \mathbf{y}^{(k_2+1)} - \mathbf{z}\right)$, $\forall p$.
      $w_p^{(k_2+1)} \leftarrow \psi\left(s_p^{(k_2+1)}\right)/s_p^{(k_2+1)}$, $\forall p$.
    end
    $\theta_n^{(k+1)} \leftarrow \tan^{-1}\left(-y_3^+/y_2^+\right)$.
  end
end
$\varphi_p^+ \leftarrow \varphi_p^{(\text{last})}$, $\forall p$.
$\theta_n^+ \leftarrow \theta_n^{(\text{last})}$, $\forall n$.

Algorithm 2: Nonlinear phase demodulation with the generalized least-squares PSA and phase-shift estimators based on sinusoidal fitting.

On the other hand, several robust estimators are listed below:

- ρ function for the least-squares estimator (or norm L^2):

$$\rho_{\text{ls}}(s) = \frac{s^2}{2}; \quad \psi_{\text{ls}}(s) = s; \quad w_{\text{ls}}(s) = 1. \tag{2.145}$$

- Least absolute estimator (or norm L^1):

$$\rho_{\text{la}}(s) = |s|; \quad \psi_{\text{la}}(s) = \frac{s}{|s|}; \quad w_{\text{la}}(s) = \frac{1}{|s|}. \tag{2.146}$$

- Huber's minimax estimator:

$$\begin{aligned} \rho_{\text{Hu}}(s;\tau) &= \begin{cases} \frac{s^2}{2\tau} + \frac{\tau}{2} & |s| \geq \tau \\ |s| & |s| > \tau \end{cases} \\ \psi_{\text{Hu}}(s;\tau) &= \min[\tau, \max(s, -\tau)] \\ w_{\text{Hu}}(s;\tau) &= \frac{\tau}{\max(1, |s|)}. \end{aligned} \tag{2.147}$$

  A 95% asymptotic efficient is obtained when $\tau = 1.345\sigma$.

- Tukey's biweigthed estimator:

$$\rho_{\text{bi}}(s;\tau) = \begin{cases} \frac{\tau^2}{6}\left[1-\left(1-\frac{s^2}{\tau^2}\right)^3\right] & \text{if } |s| \leq \tau \\ \frac{\tau^2}{6} & \text{otherwise} \end{cases}$$

$$\psi_{\text{bi}}(s;\tau) = \begin{cases} s\left[1-\left(\frac{s}{\tau}\right)^2\right]^2 & \text{if } |s| \leq \tau \\ 0 & \text{otherwise} \end{cases}$$

$$w_{\text{bi}}(s;\tau) = \begin{cases} \left(1-\frac{s^2}{\tau^2}\right)^2 & \text{if } |s| \leq \tau \\ 0 & \text{otherwise.} \end{cases} \tag{2.148}$$

  A 95% asymptotic efficient is obtained when $\tau = 4.685\sigma$.

- Leclerc's estimator:

$$\rho_{\text{le}}(s;\tau) = 1 - \frac{1}{\tau}e^{-\tau s^2}; \quad \psi_{\text{le}}(s;\tau) = 2se^{-\tau s^2}; \quad w_{\text{le}}(s;\tau) = 2e^{-\tau s^2}. \tag{2.149}$$

Other robust estimators can be found in the work by Black and Rangarajan [118].

Figure 2.20 draws the influence curves of these estimators. One can see that a residual has as much contribution as large it is; therefore, it means that outliers or pixels violating the mathematical model will have *too much* contribution. In other words, these pixels will pull the estimated intensity much stronger than those pixels following the model well, and whence the estimation would be depending mainly on pixels violating the mathematical model in Eq. (2.129). L^1-norm estimator considers all residuals have the same weight even if they are small. This fact makes that solving the optimization problem be hard; the author enlists it only for comparison purposes. For Huber's minimax estimator: small residuals are weighted as least squares, whereas large residuals will have the same weight one another as L^1-norm. So, it makes some protection against heavy noise and outliers.

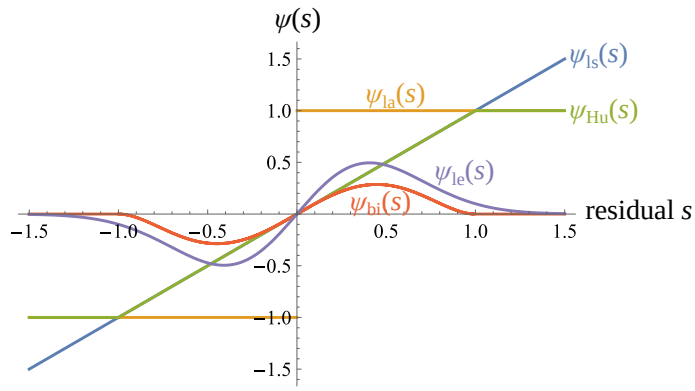

Figure 2.20: Comparison of several influence curves from the M estimators: least-squares $\psi_{\text{ls}}(s)$, least absolute $\psi_{\text{la}}(s)$, Huber's minimax $\psi_{\text{Hu}}(s)$ with $\tau = 1.0$, Tukey's biweighted $\psi_{\text{bi}}(s)$ with $\tau = 1.0$, and Leclerc's $\psi_{\text{le}}(s)$ with $\tau = 3.0$.

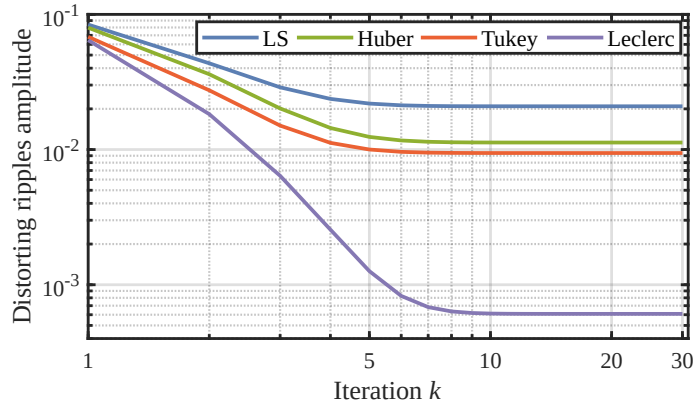

Figure 2.21: Convergence comparison using the estimators described in the main text. One can see that Leclerc's estimator performed the best results, and the least-squares method obtained the worst results. It is also noticeable that the iterative procedure will converge by the 10th iteration for all cases studied.

Tukey's biweighted also considers small residuals as the least-squares method does, but also large residuals are neglected; thence, one has good protection against outliers. A similar case is obtained with Leclerc's function, but large residuals are not neglected completely; instead, the estimator only reduces their contribution significantly. To sum up, the M-estimators can hand those pixels passing over the mathematical model; it means that the ψ-function does not pull estimation $\mathbf{y}$ towards pixels being outliers or having large influence. Therefore, these pixels are discarded from the whole optimization process since they are considered to be *too dominant* to take them into account.

In order to show the iterative process, numerical experiments were carried out using five fringe patterns whose signal-to-noise ratio was 15. To estimate the phase map was employed that PSA in Eq. (2.55) as authors did in [119]. The amplitude of the ripple distortions in Eq. (2.127) is employed as a metric to depict the iterative procedure's convergence. Figure 2.21 illustrates the results obtained for the aforementioned estimators. First, Leclerc's estimator reaches the best result (amplitude around 0.6×10^{-3}), and the worst one was obtained by the least-squares method (amplitude around 20×10^{-3}). Moreover, it is noticeable that the iterative procedure will converge by the 10th iteration; or even five iterations can be enough when using a robust estimator. Hence, the method would spend less computational time.

Continuing with the iterative procedure evaluation using the robust M estimator, some temporal sequences of fringe patterns were acquired. A Wyko 6000 Fizeau interferometer with a laser operating at $\lambda = 632.8$ nanometers (nm) and a CCD camera with 1600×1200 pixels of resolution and 12-bit pixel depth. This interferometer is in CIO's optical-testing laboratory was employed to record the fringe patterns. Every temporal sequence has nine fringe patterns, and it was introduced a phase step $\omega_0 = \pi/2$ plus those errors coming from the experimental conditions and piezo-electric device. The testing object was the first surface of the fused silica plane, with 140 mm in diameter and a $\lambda/20$ flatness peak-to-valley (P–V), into 80% of its aperture as reported in [119]. Spatial carriers were introduced

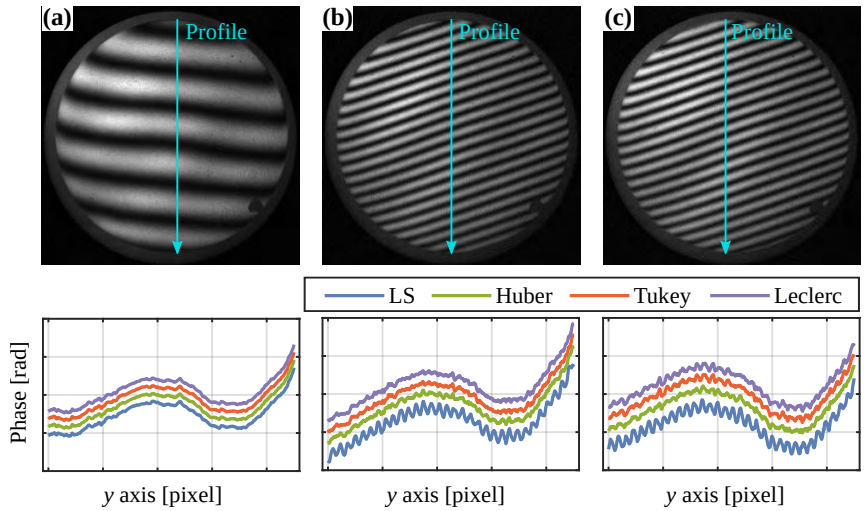

Figure 2.22: Phase demodulation of three sequences of fringe patterns. A Wyko 6000 Fizeau interferometer acquired the patterns. Every sequence has 9 phase shifts and a different spatial carrier. Below plots depict the estimated phases' horizontal profiles after removing the spatial carrier (also estimated). The y range of the plots is $[-1, 1]$ radians. For exposition purposes, a phase piston was introduced.

in order to compare the estimations qualitatively from each scheme. Figure 2.22 shows three obtained results; images depict a fringe pattern from each sequence; plots have the estimated phases' profiles along the x-axis. We point out that the spatial carrier was estimated by fitting the least-squares plane; then, he subtracted it to the estimated phase map. Since the testing object's phase has a low dynamic range, it is unwrapped after removing the spatial carrier, and hence, a phase unwrapping method was not required. For the better exposition, the estimations were denoised by employing a second-order, bi-dimensional, smoothing Savitzky–Golay filter with a 9×9 window [120]. Fig. 2.22(a) shows four estimations are almost the same, so the schemes performed well. In the second result in Fig. 2.22(b), the estimation with least-squares has distorting ripples due to a poor step extraction; the M estimators did better than the LS method. In this case, Leclerc's estimator seemed to do the best; although such, this estimation was worse than the one obtained in the previous experiment. In the third result in Fig. 2.22(c), one can observe that all estimations have distorting waves at the fringe patterns' double-frequency. The LS estimation got the largest distortion; instead, the smallest one was obtained by Huber's minimax estimator. The estimations with Tukey's and Leclerc's estimator have distorting ripples having almost the same amplitude. Based on these results, we would like to mention that the tuning constant of an M estimator requires to be selected depending on data; for these estimations, the tuning constant remained the same for each M estimator.

Phase demodulation based on subspace projection

Phase estimation based on the Gram-Schmidt orthogonalization method. This procedure is a simple way to make a orthogonal or orthonormal basis for any subspace in

$\mathbb{R}^n$ with $n > 0$. Let $V = \{\mathbf{v}_1, \mathbf{v}_2, \ldots, \mathbf{v}_N\}$ be a vector set, then one can generate from V other vector set $U = \{\mathbf{u}_1, \mathbf{u}_2, \ldots, \mathbf{u}_M\}$ whose elements $\mathbf{u}_l$ are orthogonal each other; it means that the inner product $\langle \mathbf{u}_l, \mathbf{u}_m \rangle = \mathbf{u}_l^{\mathrm{T}} \mathbf{u}_m = 0$ for $l \neq m$. The way one computes orthonormal U is [121]:

1. Normalize $\mathbf{v}_1$ to be $\mathbf{u}_1$:
$$\mathbf{u}_1 = \frac{\mathbf{v}_1}{\|\mathbf{v}_1\|_2}.$$

2. Compute the orthogonal vector $\mathbf{p}_1$ form $\mathbf{v}_2$ with respect to $\mathbf{u}_1$, and then normalize it:
$$\begin{aligned} \mathbf{p}_1 &= \mathbf{v}_2 - \left(\mathbf{v}_2^{\mathrm{T}} \mathbf{u}_1\right) \mathbf{u}_1, \\ \mathbf{u}_2 &= \frac{\mathbf{p}_1}{\|\mathbf{p}_1\|_2}. \end{aligned}$$

3. Compute the orthogonal vector $\mathbf{p}_2$ form $\mathbf{v}_3$ with respect to $\mathbf{u}_1$ and $\mathbf{u}_1$, then normalize it:
$$\begin{aligned} \mathbf{p}_2 &= \mathbf{v}_3 - \left(\mathbf{v}_3^{\mathrm{T}} \mathbf{u}_1\right) \mathbf{u}_1 - \left(\mathbf{v}_3^{\mathrm{T}} \mathbf{u}_2\right) \mathbf{u}_2, \\ \mathbf{u}_3 &= \frac{\mathbf{p}_2}{\|\mathbf{p}_2\|_2}. \end{aligned}$$

4. Compute the orthogonal vector $\mathbf{p}_{l-1}$ form $\mathbf{v}_l$ with respect to $\mathbf{u}_1, \mathbf{u}_2, \ldots, \mathbf{u}_{l-1}$:
$$\begin{aligned} \mathbf{p}_{l-1} &= \mathbf{v}_l - \left(\mathbf{v}_l^{\mathrm{T}} \mathbf{u}_1\right) \mathbf{u}_1 - \left(\mathbf{v}_l^{\mathrm{T}} \mathbf{u}_2\right) \mathbf{u}_2 - \cdots - \left(\mathbf{v}_l^{\mathrm{T}} \mathbf{u}_{l-1}\right) \mathbf{u}_{l-1}, \\ \mathbf{u}_l &= \frac{\mathbf{p}_{l-1}}{\|\mathbf{p}_{l-1}\|_2}. \end{aligned}$$

5. Repeat 4th step until the M orthonormal vectors are computed.

For fringe analysis, Vargas and coworkers have proposed to employ the Gram-Schmidt (G-S) method for demodulating a sequence of two fringe patterns [122]. In their work, the authors consider removed-DC fringe patterns being mathematically described by

$$I(x, y, t_n) = b(x, y) \cos\left[\varphi(x, y) + \omega_0 t_n\right]; \; n = 0, 1. \tag{2.150}$$

Also, they define the inner product as

$$\langle \mathbf{I}_1, \mathbf{I}_2 \rangle = \sum_{\forall (x,y)} I_1(x, y) I_2(x, y), \tag{2.151}$$

where $\mathbf{I}_l \leftarrow I_1(x, y)$ and $\mathbf{I}_2 \leftarrow I_2(x, y)$.

Tracking the G-S procedure, one requires to normalize the fringe patterns as

$$\bar{\mathbf{I}}_1 = \frac{\mathbf{I}_1}{\sqrt{\langle \mathbf{I}_1, \mathbf{I}_1 \rangle}} \tag{2.152}$$

where

$$\sqrt{\langle \mathbf{I}_1, \mathbf{I}_1 \rangle} = \left[\sum_{\forall(x,y)} I_1(x,y) I_1(x,y) \right]^{\frac{1}{2}} = \left[\sum_{\forall(x,y)} \left[b(x,y) \cos \varphi(x,y) \right]^2 \right]^{\frac{1}{2}}; \tag{2.153}$$

and hence,

$$\bar{\mathbf{I}}_1 \leftarrow \frac{b(x,y) \cos \varphi(x,y)}{\left[\sum_{\forall(x,y)} \left[b(x,y) \cos \varphi(x,y) \right]^2 \right]^{\frac{1}{2}}}. \tag{2.154}$$

Continuing with the G-S method, one then compute the orthonormalized pattern from the second fringe pattern with respect to $\bar{\mathbf{I}}_1$; this is

$$\mathbf{p}_1 = \mathbf{I}_2 - \left\langle \mathbf{I}_2, \bar{\mathbf{I}}_1 \right\rangle \bar{\mathbf{I}}_1 = \mathbf{I}_2 - \frac{\langle \mathbf{I}_2, \mathbf{I}_1 \rangle}{\langle \mathbf{I}_1, \mathbf{I}_1 \rangle} \mathbf{I}_1 \tag{2.155}$$

whence

$$\begin{aligned} \langle \mathbf{I}_2, \mathbf{I}_1 \rangle &= \sum_{\forall(x,y)} b^2(x,y) \cos \left[\varphi(x,y) + \theta \right] \cos \varphi(x,y) \\ &= \sum_{\forall(x,y)} b^2(x,y) \left[\cos^2 \varphi(x,y) \cos \theta - \cos \varphi(x,y) \sin \varphi(x,y) \sin \theta \right] \\ &\approx \sum_{\forall(x,y)} b^2(x,y) \cos^2 \varphi(x,y) \cos \theta; \end{aligned}$$

here it is considered that $\sum_{\forall(x,y)} \cos \varphi(x,y) \sin \varphi(x,y) \approx 0$ when the fringe pattern has more than one fringe. Therefore, one has that

$$\mathbf{p}_1 \approx \tilde{\mathbf{p}}_1 \leftarrow -\sin \theta b(x,y) \sin \varphi(x,y); \tag{2.156}$$

Here $\mathbf{p}_1 \approx \tilde{\mathbf{p}}_1$ implies that $[\mathbf{p}_1]_l \approx [\tilde{\mathbf{p}}_1]_l$ for all l, with $[\mathbf{v}]_l$ is the l-th element of vector $\mathbf{v}$. Then, one can compute the orthonormalized $\bar{\mathbf{I}}_2$ as

$$\bar{\mathbf{I}}_2 = \frac{\mathbf{p}_1}{\sqrt{\langle \mathbf{p}_1, \mathbf{p}_1 \rangle}} \approx \tilde{\mathbf{I}}_2 \leftarrow \frac{-b(x,y) \sin \varphi(x,y)}{\left[\sum_{\forall(x,y)} \left[b(x,y) \sin(\varphi) \right]^2 \right]^{\frac{1}{2}}}. \tag{2.157}$$

For fringe patterns having more than one fringe, one obtains that

$$\left[\sum_{\forall(x,y)} \left[b(x,y) \cos \varphi(x,y) \right]^2 \right]^{\frac{1}{2}} \approx \left[\sum_{\forall(x,y)} \left[b(x,y) \sin(\varphi) \right]^2 \right]^{\frac{1}{2}}. \tag{2.158}$$

Thence, one is able to say that $\bar{\mathbf{I}}_1$ and $\bar{\mathbf{I}}_2$ are in quadrature, and so the estimated analytic signal would be estimated as

$$\hat{b}(x,y) e^{i\hat{\varphi}(x,y)} \leftarrow \left[\bar{\mathbf{I}}_1 \right]_l - i \left[\bar{\mathbf{I}}_2 \right]_l. \tag{2.159}$$

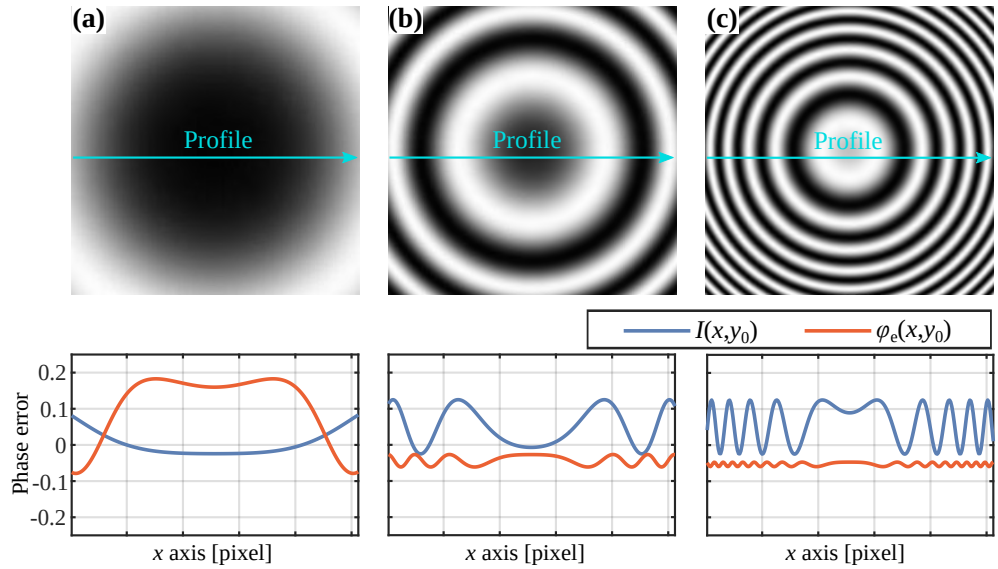

Figure 2.23: Phase demodulation of three sequences of two fringe patterns, every sequence has a different spatial carrier. Below graphs depict the horizontal profiles of the fringe patterns and the phase error; three plots are on the same scale. For exposition purposes, a piston was introduced.

The G-S method is weak against noise from which the estimated "orthonormal" vector set will not be orthogonal at all; consequently, the vectors will not be in quadrature. Thence, the estimated analytic signal, in Eq. (2.159), will have distorting ripples at the double frequency of the initial fringe pattern because of the relation in Eq. (2.158). To overcome this issue, Servin and associates proposed to compensate it by finding the proportional constant with the aim of achieving the equality of the analytic signal's real and imaginary parts [76]. On the other hand, the main disadvantage perhaps has roots in the necessity of eliminating the background intensity due to underestimating.

As an example, Figure 2.23 draws three examples of phase demodulation using the G-S method. First, the fringe patterns have one-half fringe for which the extracted phase has double-frequency distorting ripples with 0.15 radians as seen in Fig. 2.23(a). Second, the fringe patterns have three fringes; the amplitude of the distorting ripples is around 0.05 radians, see Fig. 2.23(b). In Fig. 2.23(c), the last numerical experiment shows a fringe pattern with 7.5 fringes, and the ripples' amplitude is less than 0.01 radians. Thence, one can realize that the estimation will improve its quality by increasing the spatial frequency or introducing a spatial carrier.

Phase estimation based on *principal component analysis*. The scheme of *principal component analysis* (PCA) is briefly introduced. Let $\mathbf{x}$ be a vector of N random variables, in PCA is of interest the variables of the N variances as well as the structure of the correlation between the N random variables. The following description of the PCA method is inspired in Jolliffe's book [123]. In the first step, one looks for a linear

combination of the elements of $\mathbf{x}$ such that the variance would be maximum

$$\mathbf{v}^{\mathrm{T}}\mathbf{x} = \sum_{n=1}^{N} v_n x_n \tag{2.160}$$

where superscript T means transpose operation. In the second step consists of finding another linear combination $\mathbf{v}_2^{\mathrm{T}}\mathbf{x}$ being uncorrelated with $\mathbf{v}_1^{\mathrm{T}}\mathbf{x}$; it means that they both are orthogonal. This second linear combination has maximum variance, and so forth. Every linear combination must be uncorrelated with the others; therefore the k-th linear combination $\mathbf{v}_k^{\mathrm{T}}\mathbf{x}$ is the k-th *principal component* (PC). Let $\boldsymbol{\Sigma}$ be the covariance matrix of $\mathbf{x}$, one needs to maximize the variance $\mathrm{Var}\left(\mathbf{v}_k^{\mathrm{T}}\mathbf{x}\right) = \mathbf{v}_k^{\mathrm{T}}\boldsymbol{\Sigma}\mathbf{v}_k$. Due to the fact that the maximum will not be achieved for finite a $\mathbf{v}_k$, so normalization constraint $\mathbf{v}_k^{\mathrm{T}}\mathbf{v}_k = \|\mathbf{v}\|_2^2 = 1$ must be imposed; this restriction means that the sum of the squares of the elements of $\mathbf{v}_k$ is equal to 1. Hence, the optimization problem for $k = 1$ is given by,

$$\max_{\mathbf{v}_1} \mathbf{v}_1^{\mathrm{T}}\boldsymbol{\Sigma}\mathbf{v}_1, \qquad \text{subject to} \qquad \mathbf{v}_1^{T}\mathbf{v}_1 = 1. \tag{2.161}$$

Optimizing through the Lagrange multipliers method, the Lagrangian is given by

$$\mathcal{L}\left(\mathbf{v}_1\right) = \mathbf{v}_1^{\mathrm{T}}\boldsymbol{\Sigma}\mathbf{v}_1 - \Lambda\left(\mathbf{v}_k^{\mathrm{T}}\mathbf{v}_k - 1\right) = \mathbf{0}; \tag{2.162}$$

where Λ is the Lagrange multiplier. Then, the optimal is obtaining by deriving Eq. (2.162) with respect to $\mathbf{v}_1$, so one obtains that

$$\frac{d\mathcal{L}(\mathbf{v_1})}{d\mathbf{v}_1} = \boldsymbol{\Sigma}\mathbf{v}_1 - \Lambda\mathbf{v}_1 = \left(\boldsymbol{\Sigma} - \Lambda\mathbf{I}_N\right)\mathbf{v}_1 = \mathbf{0}, \tag{2.163}$$

where I_N is the N identity matrix. As one is able to see in Eq. (2.163) that $\mathbf{v}_1$ is a eigenvector of $\boldsymbol{\Sigma}$ and Λ is its corresponding eigenvalue; particularly, Λ is the largest eigenvalue of $\boldsymbol{\Sigma}$ due to maximization problem in Eq. (2.161).

The second PC must maximize $\mathbf{v}_2^{\mathrm{T}}\boldsymbol{\Sigma}\mathbf{v}_2$ subject to being uncorrelated with $\mathbf{v}_1\mathbf{x}$, so it implies that

$$\mathrm{Cov}\left(\mathbf{v}_1\mathbf{x}, \mathbf{v}_2\mathbf{x}\right) = \mathbf{v}_1^{\mathrm{T}}\boldsymbol{\Sigma}\mathbf{v}_2 = \mathbf{v}_2^{\mathrm{T}}\boldsymbol{\Sigma}\mathbf{v}_1 = \mathbf{v}_2^{\mathrm{T}}\Lambda_1\mathbf{v}_1^{\mathrm{T}} = \Lambda_1\mathbf{v}_2^{\mathrm{T}}\mathbf{v}_1 = \Lambda_1\mathbf{v}_1^{\mathrm{T}}\mathbf{v}_2 = 0; \tag{2.164}$$

where $\mathrm{Cov}(\bullet)$ means covariance, Λ_1 is the largest eigenvalue corresponding to the first PC, the Lagrange multiplier in Eq. (2.163). From the condition of uncorrelation of both PCs $\mathbf{v}_1^{\mathrm{T}}\mathbf{v}_2 = 0$, hence one can obtain a second optimization problem given by

$$\max_{\mathbf{v}_2} \mathbf{v}_2^{\mathrm{T}}\boldsymbol{\Sigma}\mathbf{v}_2, \qquad \text{subject to} \qquad \begin{cases} \mathbf{v}_2^{\mathrm{T}}\mathbf{v}_2 = 1 \\ \mathbf{v}_1^{\mathrm{T}}\mathbf{v}_2 = 0. \end{cases} \tag{2.165}$$

Again, using the method of Lagrange multipliers, one obtains that

$$\begin{aligned} \mathcal{L}\left(\mathbf{v}_2\right) &= \mathbf{v}_1^{\mathrm{T}}\boldsymbol{\Sigma}\mathbf{v}_1 - \Lambda_2\left(\mathbf{v}_k^{\mathrm{T}}\mathbf{v}_k - 1\right) - \tau\mathbf{v}_1^{\mathrm{T}}\mathbf{v}_2 = \mathbf{0} \\ \frac{d\mathcal{L}(\mathbf{v}_2)}{d\mathbf{v}_2} &= \boldsymbol{\Sigma}\mathbf{v}_2 - \Lambda_2\mathbf{v}_2 - \tau\mathbf{v}_1 = \mathbf{0}. \end{aligned} \tag{2.166}$$

Here, Λ_2 and τ are the Lagrange multipliers. Now, performing the dot product

$$\mathbf{v}_2^{\mathrm{T}}\left[\frac{d\mathcal{L}(\mathbf{v}_2)}{d\mathbf{v}_2}\right] = \mathbf{v}_2^{\mathrm{T}}\boldsymbol{\Sigma}\mathbf{v}_1 - \Lambda_2\mathbf{v}_2^{\mathrm{T}}\mathbf{v}_1 - \tau\mathbf{v}_2^{\mathrm{T}}\mathbf{v}_1 = 0; \tag{2.167}$$

in which one can observe that $\Lambda_2\mathbf{v}_2^{\mathrm{T}}\mathbf{v}_1 = 0$ and $\mathbf{v}_2^{\mathrm{T}}\boldsymbol{\Sigma}\mathbf{v}_1 = 0$; it implies that $\tau = 0$. Thus, as computing the first PC, one has the following relation

$$(\boldsymbol{\Sigma} - \Lambda_2\mathbf{I}_N)\,\mathbf{v}_2 = \mathbf{0}. \tag{2.168}$$

Equation (2.168) denotes that Λ_2 is the largest eigenvalue of $\boldsymbol{\Sigma}$ and $\mathbf{v}_2$ its corresponding eigenvector, but it implies that $\mathbf{v}_2\mathbf{x} = \mathbf{v}_1\mathbf{x}$; thus, Λ_2 is the second largest eigenvalue of $\boldsymbol{\Sigma}$ and $\mathbf{v}_2$ its corresponding eigenvector, so both conditions in Eq. (2.165) are fulfilled. In general, the k-th PC is computing by

$$t_k = \mathbf{v}_k\mathbf{x} \qquad \text{subject to} \qquad \begin{cases} (\boldsymbol{\Sigma} - \Lambda_k\mathbf{I}_N)\,\mathbf{v}_k = \mathbf{0} \\ \Lambda_{k-1} \geq \Lambda_k \geq \Lambda_{k+1}; \end{cases} \tag{2.169}$$

where Λ_k is the k-th eigenvalue and $\mathbf{v}_k$ is its corresponding eigenvector. From Eq. (2.169), the covariance matrix's eigenvectors determine those directions where data have the greater variances.

Let $\mathbf{I}_n$ be the n-th *vectored* fringe pattern, then one can estimate of the background intensity as the temporal average; this is

$$[\hat{\mathbf{a}}]_l = \sum_{n=0}^{N-1}[\mathbf{I}_n]_l\,, \quad l = 1, 2, \ldots, L_xL_y \tag{2.170}$$

where each interferogram has $L_x \times L_y$ pixels; other methods can be employed to estimate the center of the temporal intensity values. Using this notation, one can represent the acquired fringe patterns with the DC term removed as the matrix of observations

$$\mathbf{A} = \begin{bmatrix} \mathbf{I}_0^{\mathrm{T}} - \hat{\mathbf{a}}^{\mathrm{T}} \\ \mathbf{I}_1^{\mathrm{T}} - \hat{\mathbf{a}}^{\mathrm{T}} \\ \vdots \\ \mathbf{I}_{N-1}^{\mathrm{T}} - \hat{\mathbf{a}}^{\mathrm{T}} \end{bmatrix} = \begin{bmatrix} \bar{\mathbf{I}}_0^{\mathrm{T}} \\ \bar{\mathbf{I}}_1^{\mathrm{T}} \\ \vdots \\ \bar{\mathbf{I}}_{N-1}^{\mathrm{T}} \end{bmatrix} \tag{2.171}$$

where $\mathbf{A} \in \mathbb{R}^{N\times(L_xL_y)}$ and each interferogram has $L_x \times L_y$ pixels. Also Then, the estimated covariance matrix is given by

$$\hat{\mathbf{S}} = \frac{1}{L_xL_y - 1}\mathbf{A}\mathbf{A}^{\mathrm{T}} = \frac{1}{L_xL_y - 1}\begin{bmatrix} \langle\bar{\mathbf{I}}_0, \bar{\mathbf{I}}_0\rangle & \langle\bar{\mathbf{I}}_0, \bar{\mathbf{I}}_1\rangle & \cdots & \langle\bar{\mathbf{I}}_0, \bar{\mathbf{I}}_{N-1}\rangle \\ \langle\bar{\mathbf{I}}_1, \bar{\mathbf{I}}_0\rangle & \langle\bar{\mathbf{I}}_1, \bar{\mathbf{I}}_1\rangle & \cdots & \langle\bar{\mathbf{I}}_1, \bar{\mathbf{I}}_{N-1}\rangle \\ \vdots & \vdots & \ddots & \vdots \\ \langle\bar{\mathbf{I}}_{N-1}, \bar{\mathbf{I}}_0\rangle & \langle\bar{\mathbf{I}}_{N-1}, \bar{\mathbf{I}}_1\rangle & \cdots & \langle\bar{\mathbf{I}}_{N-1}, \bar{\mathbf{I}}_{N-1}\rangle \end{bmatrix} \tag{2.172}$$

where $\hat{\mathbf{S}} \in \mathbb{R}^{N\times N}$ is a symmetric and semi-defined positive matrix, and $\langle\bullet, \bullet\rangle$ is the dot product and also it is defined in Eq. (2.151).

With the aim of obtaining the *principal components*, one requires computing the eigenvectors and eigenvalues of $\hat{\mathbf{S}}$. From the mathematical model in equations (2.48) – (2.52) and the fact of removing the background intensity, one can realize that there will be two *principal components*: the first related with $\cos\varphi(x,y)$ and the other with $\sin\varphi(x,y)$; this is because these signals represents the redundant information through the matrix of observations. The quadrature filter's coefficients, given by the PCA method, are simply computed as [76]

$$c_n = \frac{1}{2}\left([\mathbf{v}_1]_{n+1} + i\,[\mathbf{v}_2]_{n+1}\right); \quad n = 0, 1, \ldots, N-1 \tag{2.173}$$

where $\mathbf{v}_1$ is the eigenvector associated with the largest eigenvalue λ_1 and $\mathbf{v}_2$ is associated with the second largest eigenvalue of the covariance matrix. From Eq. (2.173), the analytic signal is computed. Moreover, the phase steps are given by [76]

$$\hat{\theta}_n = \text{angle}\,(c_n^*)\,. \tag{2.174}$$

Now, the demodulation through this method based on PCA is analyzed. Let

$$\mathbf{c} = \begin{bmatrix} \cos\theta_0 & \cos\theta_1 & \cdots & \cos\theta_{N-1} \end{bmatrix}^{\mathrm{T}}, \text{ and} \tag{2.175}$$

$$\mathbf{s} = \begin{bmatrix} \sin\theta_0 & \sin\theta_1 & \cdots & \sin\theta_{N-1} \end{bmatrix}^{\mathrm{T}} \tag{2.176}$$

be the vector of the column space of a modified (without the DC term) matrix in Eq. (2.48), it means that the interferometry data is represented in terms of $\mathbf{c}$ and $\mathbf{s}$. Thence, one can identify three scenarios coming from the phase steps:

1. The phase steps are uniformly spaced $\theta_n = \omega_0 n$, but also they complete cycles (one or more), this is $\exp(i\theta_0) = \exp(i\theta_N)$; whence, one has that $\mathbf{c}^{\mathrm{T}}\mathbf{s} = 0$, and so, one usually obtains that

$$c_n = \frac{1}{2}\left([\mathbf{v}_1]_{n+1} + i\,[\mathbf{v}_2]_{n+1}\right) = |c_n|\, e^{in\omega_0 - i\psi} \tag{2.177}$$

   where $\psi = \cos^{-1}\left(\mathbf{c}^{\mathrm{T}}\mathbf{v}_1 / \|\mathbf{c}_2\|\right) = \cos^{-1}\left(\mathbf{s}^{\mathrm{T}}\mathbf{v}_2 / \|\mathbf{s}_2\|\right)$, then the estimated phase will is exact and it has a global piston ψ. Furthermore, the basis $\mathbf{v}_1$ and $\mathbf{v}_2$ is just a rotation of the basis $\mathbf{c}$ and $\mathbf{s}$. Figure 2.24(a) illustrates this case, where one can see that intensity values plots a Lissajous circle.

2. The phase steps are uniformly-spaced $\theta_n = \omega_0 n$ but they do not complete cycles; it means that the phase steps are not uniformly-distributed on $[0, 2\pi\kappa]$ for integer κ. For this case, one has that vectors $\mathbf{c}$ and $\mathbf{s}$ are no orthogonal, this is $\mathbf{c}^{\mathrm{T}}\mathbf{s} \neq 0$; this means that the first PC catches some information from both cosine and sine terms, and it happens the same for the second PC. From construction, the first PC will catch more information than the second PC; thereby, it is expected that the intensity values projected onto the *principal components* space will plot a Lissajous ellipse, as depicted in Fig. 2.24(b). The phase can be corrected *a posteriori* by transforming the Lissajous ellipse to a circle one.

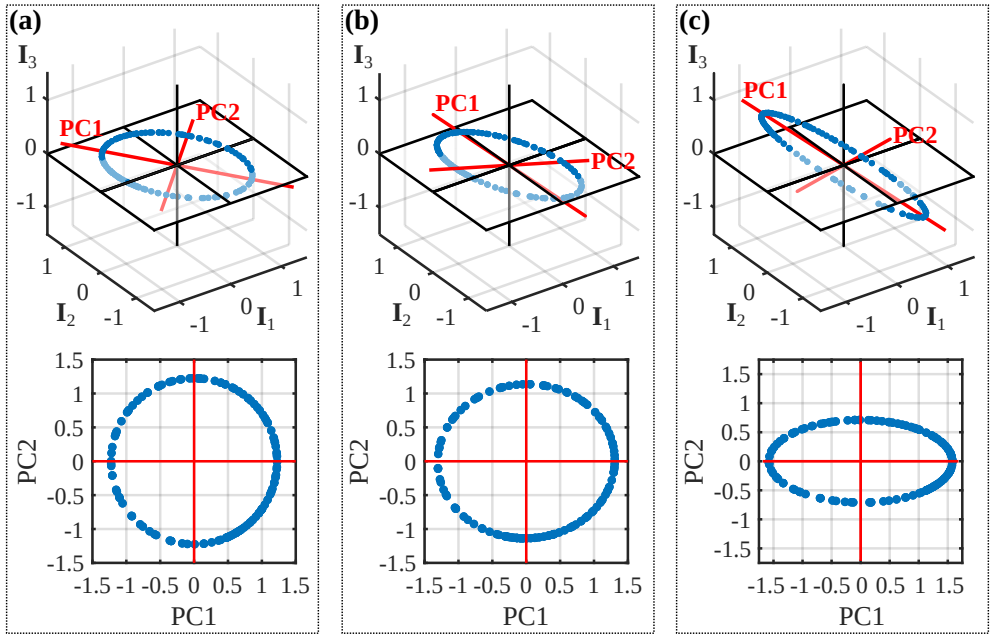

Figure 2.24: Estimation of the first two *principal components* in phase demodulation. Figure draws three typical cases: (a) the phase shifts are given by $\theta_n = \omega_0 n$, but also, they complete cycles (one, two, or more); (b) the phase shifts are also given by $\theta_n = \omega_0 n$ but they do not complete periods; and (c) the phase shifts are non-uniformly spaced.

3. The phase steps are non-uniformly spaced $\theta_n = \omega t_n$. Vectors $\mathbf{c}$ and $\mathbf{s}$ are not orthogonal, and whence the PCs will catch information from both cosine and sine terms. As aforementioned, the intensity values plots a Lissajous ellipse in the PCs space as seen in Fig. 2.24(c). Hence, the estimated analytic signal can be corrected by transforming the ellipse into a circle.

I do point out that these scenarios take into account that a well the background illumination estimation. However, when it did not, one should suppose that the ellipse will not be centered at (0,0). The latter makes that the analytic signal correction will be tricky; for example, the proposal in [124].

Figure 2.25 shows the estimated phase from the interferogram in Fig. 2.22 where PCA is employed to phase demodulate. The scale of these plots is the same as in Fig. 2.22, so these results are comparable. One can see that the estimated phases have distorting waving as expected. In all cases, the previously discussed nonlinear PSAs retrieved a better estimation. Indeed, one should expect that PCA will obtain a poorer phase estimation than the others.

2.3 Phase unwrapping

This task consists of reconstructing the estimated wavefront or unwrapped phase from the wrapped phase or phase modulus 2π; i.e., one obtains the phase having no 2π discontinu-

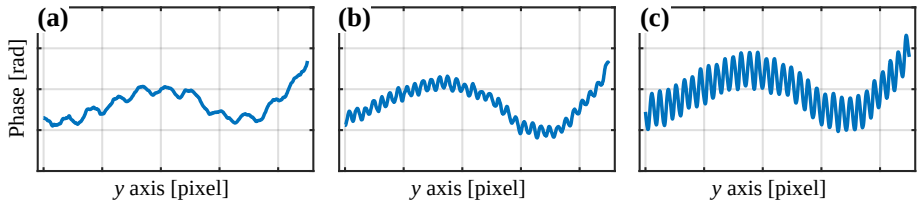

Figure 2.25: Phase estimation using the algorithm based on the *principal component analysis*. Plots are the same as those in in Fig. 2.22, and also the demodulated interferograms are depicted in that Figure. The y range of the plots is $[-1, 1]$ radians.

ities. The wrapped phase can be computed as

$$\varphi_{\mathcal{W}} \stackrel{\text{def}}{=} \mathcal{W}\{\varphi\} \stackrel{\text{def}}{=} \varphi - 2\pi \left\lfloor \frac{\varphi}{2\pi} \right\rfloor \tag{2.178}$$

$$\stackrel{\text{def}}{=} \tan^{-1}\left(\frac{\sin\varphi}{\cos\varphi}\right) \tag{2.179}$$

where $\lfloor x \rfloor$ rounds x to the nearest lower integer, $\varphi \in \mathbb{R}$, $\tan^{-1}$ is the arc tangent of four quadrants, and $\mathcal{W}\{\bullet\}$ is the wrapping operator; which $\mathcal{W} : \mathbb{R} \longrightarrow (-\pi, \pi]$. Then, the unwrapping procedure can be given by

$$\varphi = \mathcal{W}^{-1}\{\varphi_{\mathcal{W}}\} = \varphi_{\mathcal{W}} + 2\pi \left\lfloor \frac{\varphi}{2\pi} \right\rfloor \tag{2.180}$$

where $\mathcal{W}^{-1}\{\bullet\}$ is the unwrapping operator so that $\varphi = \mathcal{W}^{-1}\{\mathcal{W}\{\varphi\}\}$ for all $\varphi \in \mathbb{R}$. Here, one can observe that the Wrapper operator is a surjective function, but it is not injective; i.e. the range of $\mathcal{W}\{\varphi\}$ is the image of the element $2\pi n\varphi \in \mathbb{R}$ for any integer n. Thence, the integer $\lfloor \varphi/2\pi \rfloor$ is needed to be known to compute the unwrapped phase φ. However, when one retrieves the wrapped phase by phase demodulating the fringe patterns. One cannot compute the map of integers $\lfloor \varphi(x, y)/2\pi \rfloor$, and whence, the unwrapping problem will require prior information.

Itoh proposed to unwrap the phase progressively in a one-dimensional way [125]. Considering that

$$k(x) = \lfloor \varphi(x)/2\pi \rfloor, \tag{2.181}$$

and substituting $k(x)$ in Eq. (2.180), one has that

$$\varphi(x) = \varphi_{\mathcal{W}}(x) + 2\pi k(x). \tag{2.182}$$

Then, taking the discrete derivative of Eq. (2.182), this is

$$\begin{aligned} D\{\varphi(x)\} &= D\{\varphi_{\mathcal{W}}(x)\} + 2\pi D\{k(x)\} \\ \varphi(x) - \varphi(x-1) &= \varphi_{\mathcal{W}}(x) - \varphi_{\mathcal{W}}(x-1) + 2\pi\left[k(x) - k(x-1)\right], \end{aligned} \tag{2.183}$$

where $[k(x) - k(x-1)] \in \mathbb{Z}$. Appying the wrapping operator, one has that

$$\mathcal{W}\{D\{\varphi(x)\}\} = \mathcal{W}\{D\{\varphi_{\mathcal{W}}(x)\} + 2\pi D\{k(x)\}\}$$

$$= \mathcal{W}\left\{D\left\{\varphi_{\mathcal{W}}(x)\right\}\right\}. \tag{2.184}$$

This last result indicates that the derivative of the unwrapped phase is equal to the derivative of the wrapped phase. Whence, one can retrieve the phase using the Euler's method for linear integration given by

$$\hat{\varphi}(x) = \varphi(x-1) + 1 \cdot \frac{d\varphi(x)}{dx} \tag{2.185}$$

$$= \varphi(x-1) + \mathcal{W}\left\{\varphi_{\mathcal{W}}(x) - \varphi_{\mathcal{W}}(x-1)\right\}. \tag{2.186}$$

Here, one can state that $\hat{\varphi}(0) = cte$ when this value is unknown. Notice that the derivative is approximated by first order finite difference scheme. Equations (2.185) and (2.186) summarize the so-called Itoh's method [125] which comes from the Euler's method for linear integration.

The previously described algorithm can be straightforwardly used to unwrap an image by selecting an integration path. The simplest path is when unwrapping in a zigzagging way, while a better path can be computed based on the flood-fill scheme [126] where the flood path follows those pixels having better signal-to-noise ratio, they all together are called the quality map. Next, the pseudocode for this last algorithm is described as follows:

Input: $\varphi_{\mathcal{W}}$, P_0, Ω and $\mathcal{Q}$.
if $P_n \in \Omega$ and $M(P_n) \neq 1$ **then**
  $\varphi(P_n) \leftarrow \varphi(P_p) + \mathcal{W}\left\{\varphi_{\mathcal{W}}(P_n) - \varphi_{\mathcal{W}}(P_a)\right\}$.
  $M(P_n) \leftarrow 1$.
  $R \leftarrow \texttt{sort}\left(\{r : r \in \mathcal{L}\}\right)$; $\mathcal{L} \subset \mathcal{Q}$.
  while R **is not** empty **do**
    $P_{n+1} \leftarrow \texttt{pop}\left(R\right)$.
    $\texttt{FloodFillUnwrapper}\left(P_{n+1}, P_n\right)$.
  end
end

Algorithm 3: Phase unwrapping employing a line integration method with that path given by flood-filling a quality map. It is thought that the computer function is called `FloodFillUnwrapper`. The description is in the main text.

In this pseudocode, P_n is the n-th pixel, R is the integration path, M is the unwrapping mask, Ω is the image lattice, $\mathcal{Q}$ is the quality map, $\mathcal{L}$ is a neighboring around P_n such that $\text{cad}(R) = 8$, $\texttt{sort}(\bullet)$ arranges the list in numerical order, and $\texttt{pop}(\bullet)$ is a computer function returning the top item in the list; and at the same time, it removes this item from the list. The pseudocode, in Algorithm 3, assumes that the corresponding computer function is called $\texttt{FloodFillUnwrapper}(\bullet)$. The reader can realize that this function is executed recursively until every pixel had been unwrapped.

Figure 2.26 shows an example of how the algorithm unwraps the given phase map. One can see that the 13th unwrapped point was unwrapping using the 12th instead of the 6th, which has better fringe contrast; other cases are 16th, 17th, 18th, 19th, and 20th. Based on it, one can say that a point would not always be unwrapping using its best neighbor. Thus, both unwrapping and quality maps could jeopardize the retrieved unwrapped-phase map.

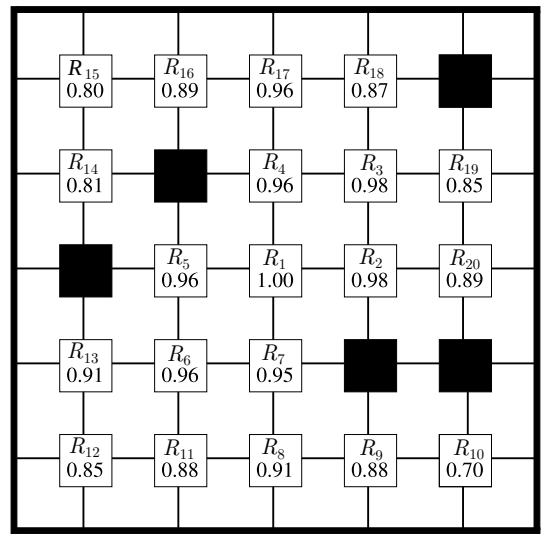

Figure 2.26: Phase unwrapping procedure using the quality-guided, flood-fill algorithm. Notice that subscripts mean the order of unwrapping: R_1 is the first point that will be unwrapping, R_2 is the second, and so on.

2.3.1 Unwrapping noised phases

The wrapped phases usually have noise because the demodulation process could not filter out it. So, one can either employ an algorithm with robustness against noise, or else one can low-pass filter the wrapped phase before phase unwrapping. One also can combine the uses of a noise-robust phase scheme to unwrap a smoothed wrapped phase. This subsection will describe two algorithms with noise robustness for phase unwrapping, and it will also present three algorithms for denoising a wrapped phase.

A variation of the aforementioned method consists in making a recursive method. This method is described as [127]

$$\hat{\varphi}\left(P_n\right) = \hat{\varphi}\left(P_a\right) + \alpha \mathcal{W}\left\{\varphi\left(P_a\right) - \hat{\varphi}_{\mathcal{W}}\left(P_n\right)\right\} \tag{2.187}$$

where $P \in R$ and the latter is the integration path, hence, P_n means the actual pixel and P_a is the previous one. The parameter $\alpha \in (0, 1]$ and it controls the amount of noise is filtered out; the noise level decreases as α does [127]. Therefore, this method has a low-pass response. In this work, it is used Eq. (2.187) and the quality-guided flood-fill algorithm when phase unwrapping with *line-integration method*.

Ghilia and Romero proposed the second method [128], this method consists in optimization a bi-dimensional cost function given by

$$\begin{aligned} U = &\sum_{(x,y)} \left[\varphi(x,y) - \varphi(x-1,y) - \Delta_x \varphi_{\mathcal{W}}(x,y)\right]^2 \\ &+ \sum_{(x,y)} \left[\varphi(x,y) - \varphi(x,y-1) - \Delta_y \varphi_{\mathcal{W}}(x,y)\right]^2; \end{aligned} \tag{2.188}$$

where

$$\Delta_x \varphi_{\mathcal{W}}(x,y) = \begin{cases} \mathcal{W}\left\{\varphi_{\mathcal{W}}(x,y) - \varphi(x-1,y)\right\} & \text{in} \quad \Omega \\ 0 & \text{over } \partial\Omega. \end{cases} \tag{2.189}$$

$$\Delta_y \varphi_{\mathcal{W}}(x,y) = \begin{cases} \mathcal{W}\left\{\varphi_{\mathcal{W}}(x,y) - \varphi(x,y-1)\right\} & \text{in} \quad \Omega \\ 0 & \text{over } \partial\Omega. \end{cases} \tag{2.190}$$

One can see that equation (2.188) is a least-squares problem where one wants to fit the derivative of the unwrapped phase to the one computed from the wrapped phase. Taking the partial derivatives of U with respect to φ and equal them to zero, and hence, one can obtain Poisson's equation

$$\frac{\partial^2}{\partial x^2}\varphi(x,y) + \frac{\partial^2}{\partial y^2}\varphi(x,y) = \varrho(x,y) \tag{2.191}$$

where the second order partial derivative can be approximated by a second order finite difference scheme as

$$\frac{\partial^2}{\partial x^2}\varphi(x,y) \approx \varphi(x-1,y) - 2\varphi(x,y) + \varphi(x+1,y) \tag{2.192}$$

$$\frac{\partial^2}{\partial y^2}\varphi(x,y) \approx \varphi(x,y-1) - 2\varphi(x,y) + \varphi(x,y+1) \tag{2.193}$$

$$\varrho(x,y) = \Delta_x \varphi_{\mathcal{W}}(x,y) - \Delta_x \varphi_{\mathcal{W}}(x-1,y) + \Delta_y \varphi_{\mathcal{W}}(x,y) - \Delta_y \varphi_{\mathcal{W}}(x,y-1). \tag{2.194}$$

Equations (2.189) and (2.190) impose Neumann boundary conditions on Poisson's equation (2.191) [128].

From equations (2.191) – (2.194), one can estimate the unwrapped phase by using the Gauss-Seidel iterative algorithm as

$$\hat{\varphi}^{(k+1)}(x,y) = \frac{1}{4}\Big[\hat{\varphi}^{(k+1)}(x-1,y) + \hat{\varphi}^{(k)}(x+1,y) + \hat{\varphi}^{(k+1)}(x,y-1) + \hat{\varphi}^{(k)}(x,y+1) - \varrho(x,y)\Big]; \tag{2.195}$$

where $(k+1)$ indicates the actual iteration and (k) the previous. Equation (2.195) is valid for all pixels that do not touch the boundary. From Eq. (2.189) and (2.190), the derivatives of pixels reaching the boundary are computed as

$$\left.\frac{\partial^2}{\partial x^2}\varphi\right|_{(x_a,y)} \approx -2\varphi(x_a,y) + 2\varphi(x_a+1,y) \quad \text{(left)} \tag{2.196}$$

$$\left.\frac{\partial^2}{\partial x^2}\varphi\right|_{(x_b,y)} \approx -2\varphi(x_b,y) + 2\varphi(x_b-1,y) \quad \text{(right)} \tag{2.197}$$

$$\left.\frac{\partial^2}{\partial y^2}\varphi\right|_{(x,y_a)} \approx -2\varphi(x,y_a) + 2\varphi(x,y_a+1) \quad \text{(up)} \tag{2.198}$$

$$\left.\frac{\partial^2}{\partial y^2}\varphi\right|_{(x,y_b)} \approx -2\varphi(x,y_b) + 2\varphi(x,y_b-1) \quad \text{(down)}. \tag{2.199}$$

Here, subscripts a and b indicate the boundaries. Also the values of $\varrho(x, y)$ for these pixels are computed in the same way. The Gauss-Seidel iteration can be straightforwardly obtained for these pixels. Finally, this iterative method can be stopped by meeting the condition

$$\left\| \hat{\varphi}^{(k+1)} - \hat{\varphi}^{(k)} \right\|_2 < \text{threshold}. \tag{2.200}$$

As an example, considering the parabolic wrapped phase shown in Fig. 2.27(a), this phase is corrupted by speckle noise. Figure 2.27 draws the curve of levels of the free-noise ground-true phase. The estimated phase maps using the line-integration method and the global least-squares one are illustrated in Fig. 2.27(c) and (d), respectively. One can see that the line-integration scheme did not unwrap the phase correctly, i.e., this estimation still having 2π discontinuities. Alternatively, the LS method solved all discontinuities, and its solution is also a little noiseless than the other. Besides, the estimation, coming from the line-integration unwrapping, has a comparable dynamic range to the one from the current phase. Instead, the global LS method reduced the phase's dynamic range, i.e., the algorithm modified the parabola's curvature. Because one does not want to change the unwrapped phase's dynamic range, the line-integration method will be employed henceforward.

Based on the obtained results in the last example, one should apply a denoising procedure in order to deal with heavy noised phases. To this end, one can use the properties of the complex exponential functions [129], then one has

$$g(x, y) = e^{i\varphi_{\mathcal{W}}(x,y)}. \tag{2.201}$$

Function $g(x, y)$ can be filtered in the usual way, i.e., using convolution filters.

One can smooth $g(x, y)$ by means of a singular value decomposition (SVD) of a neighborhood $\mathcal{L} \in \Omega$. Let $\mathbf{G}$ be the matrix whose elements are the values of $g(x, y)$ in neighborhood $\mathcal{L}_1$, then this matrix can be decomposed as

$$\mathbf{G} = \mathbf{U}\boldsymbol{\Sigma}\mathbf{V}^{\mathrm{T}}, \tag{2.202}$$

where $\mathbf{U}$ has the left-side eigenvectors, $\mathbf{V}$ has the right-side eigenvectors, and $\boldsymbol{\Sigma}$ is diagonal whose elements are singular values Σ_i in a descending order, i.e. $\Sigma_1 > \Sigma_2 > \cdots \Sigma_N$. The

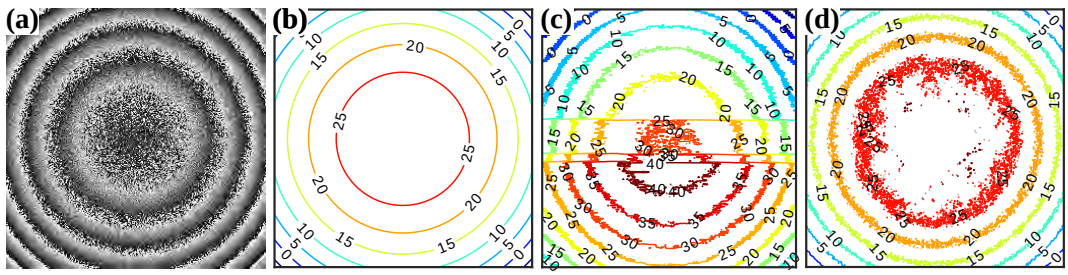

Figure 2.27: Phase unwrapping of a noised, wrapped phase with speckle noise: (a) the wrapped phase. Curve levels of the unwrapped phases of (b) the free-noise, test phase, using the line-integration method (c), and the global LS method (d).

singular values are inflated due to noise, so one should truncate the SVD decomposition to the first r larger singular values to filter out noise. Then, one has the smooth phase as

$$g_{\text{smooth}}(x,y) = \sum_{n=1}^{r} \mathbf{USV}^{\mathrm{T}}, \quad \forall (x,y) \in \mathcal{L}_1 \tag{2.203}$$

where

$$\mathbf{S} = \operatorname{diag}\left(\begin{bmatrix} \Sigma_1 & \Sigma_2 & \cdots & \Sigma_r & 0 & 0 & \cdots & 0 \end{bmatrix}^{\mathrm{T}} \right); \tag{2.204}$$

hence, it is also a diagonal matrix. One is able to realize that the smooth phase corresponds to the truncated SVD of the noised phase. When the value of r decreases, the amount of filtered noise increases; in my experience, values $r \in \{1,2,3\}$ should be used. Finally, this process is repeated thorough the phase map.

The truncation of the singular values in Eq. (2.203) can generate that the smoothed phase may have distorting waves because the truncation also removes part of the phase information. To reduce such distorting waves, one can employ a Tikhonov filter [130]

$$T\left(\Sigma_i\right) = \frac{\Sigma_i^2}{\Sigma_i^2 + \alpha}, \tag{2.205}$$

where α is the regularization parameter; one can increase the amount of filtered out noise by increasing this parameter.

The windowed Fourier filtering method proposes to use a bank of Gabor filters for denoising both an intensity pattern or a wrapped phase [38], this is given by

$$\begin{aligned} \sum_{\pm n} \tilde{g}_n(x,y) &= \sum_{\pm n} g(x,y) \circledast \circledast h_n(x,y) \\ &= \sum_{\pm n} g(x,y) \circledast \circledast \left[\frac{4\Delta x \Delta y}{\pi^2} e^{-\frac{x^2+y^2}{4\sigma_x^2 \sigma_y^2}} e^{-i(u_n x + v_n y)} \right] \end{aligned} \tag{2.206}$$

where $h_n(x,y)$ is the n-th Gabor filter, σ_x^2 and σ_y^2 controls the band-pass width, $u_n = n\Delta x$ and $v_n = \Delta y$ and the tuning frequencies of the Gabor filter, as well as Δx, Δy are the window size in the x and y axis, respectively. The filtering process is performed as [38]

$$\mathcal{F}_{(x,y)}\left\{g_{\text{smooth}}(x,y)\right\} = \sum_{\pm n} \begin{cases} \mathcal{F}_{(x,y)}\left\{\tilde{g}_n(x,y)\right\} & \text{if } \left|\mathcal{F}_{(x,y)}\left\{\tilde{g}_n(x,y)\right\}\right| > \varepsilon \\ 0 & \text{otherwise;} \end{cases} \tag{2.207}$$

where ε is a threshold, usually this value is into the interval from 4 to 10; the correct selection of this threshold requires to know the noise power. Also, as indicated in Section 2.1, the window size as well as the band-pass with parameter σ_x^2, σ_y^2 are very important because they determine whether the spectrum is separable or not; so dynamic selection is recommended [62, 131, 132].

Figure 2.28 draws an example of denoising a wrapped phase corresponding to a parabolic function; to that end, it was added speckle noise to the phase as seen in Fig. 2.28(a). The denoised phase, using the truncated SVD, is depicted by Fig. 2.28(b). One can observe that this technique reduced the noise level significantly, but this phase map also shows

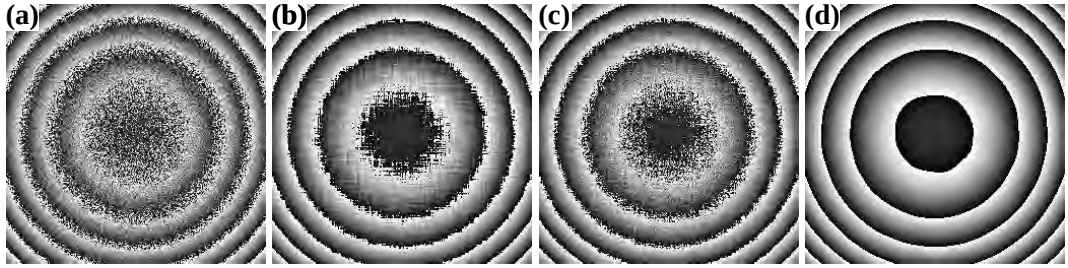

Figure 2.28: Denoising of a wrapped phase using several algorithms: (a) the noised phase map, (b) the truncated SVD method, (c) the Tikhonov filter, and (d) the windowed Fourier filtering.

a tiling-like distortion. Figure 2.28(c) illustrates the obtained result using the Tikhonov filter, this result has a greater noise level than the truncated SVD, but this result has no tiling-like distortion. Figure 2.28(d) shows the wrapped phase denoised through the windowed Fourier filtering; this result is very smooth such that it has the highest signal-to-noise ratio. However, one can observe that it has distortions such that the parabolic phase is clipped.

Continuing with this example, because the line-integration method has the lowest robustness against noise, it is employed to unwrap the phase. Figure 2.29 (a) shows the true phase without noise. Figure 2.29(b) depicts the phase using the truncated singular-value decomposition as a denoising method. Here one can see that the unwrapped phase lost part of its curvature. In other words, it seems that its local frequencies significantly deviate from those on the ground-true phase; this is due to the rejection of several eigenvectors having some phase information. Figure 2.29(c) shows the phase corresponding to the Tikhonov filter, and the noise level of this phase is the highest. However, we can see that the denoising process did not jeopardize the phase's curvature; this is because the Tikhonov filter may keep extra eigenvectors having phase information, as small changes of the local frequencies. In Figure 2.29(d), this unwrapped phase has not only the lowest noise level, but it also has lost some part of its curvature since the filter bank removed it.

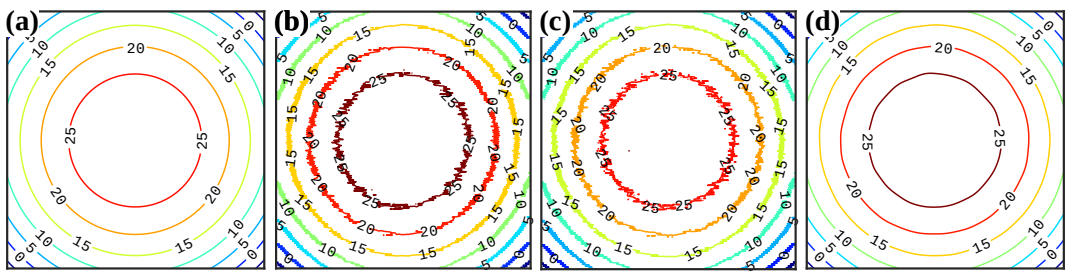

Figure 2.29: Phase unwrapping of a denoised, wrapped phase employing several algorithms: (a) the free-noise, true phase, (b) the truncated SVD method, (c) the Tikhonov filter, and (d) the windowed Fourier filtering. The line-integration method carried out the phase unwrapping procedure.

This issue occurs when the instantaneous frequency is close to zero around the peak for this case, making the spectrum, into that window, may not be separated well.

2.4 Contributions

I enlist and summarize my published papers related to this Chapter:

- A. Muñoz, **S. Ordoñes**, J. L. Flores, O. Aguilar, and A. Jimenez, "*Phase shifting schemes: comparative analysis*,", Acta Universitaria, vol. 29, e2627, 2019; corresponding to Reference [75]. This paper depicts a comparative study between linear and non-linear least-squares phase-shifting algorithms for non-uniform steps. The main result indicates that their behavior against noise is similar to the observed one using least-squares PSA for uniform phase shifts. I would like to mention that this work was mostly done while I was at the University of Guadalajara.

- **S. Ordones**, M. Servin, M. Padilla, A. Muñoz, J. L. Flores, and I. Choque, "*Spectral analysis for the generalized least squares phase-shifting algorithms with harmonic robustness*," Opt. Lett., vol. 44, no. 9, pp. 2358–2361, 2019; corresponding to reference [77]. This paper introduced the frequency transfer function (FTF) formalism for LS-PSA with non-uniform phase shifts. It also allows one to design and analyze this kind of PSA when rejecting high-order harmonics. Particularly, this paper provided the generalized LS-PSA's impulsive and frequency responses whose coefficients is given by (2.78). These equations are here reproduced:

$$
\begin{aligned}
c_n &= \frac{1}{2}\left(a^{\dagger}_{2,n+1} + i a^{\dagger}_{3,n+1}\right), \\
h(t) &= \sum_{n=0}^{N-1} c_n \delta(t - t_n), \\
H(\omega) &= \sum_{n=0}^{N-1} c_n e^{-i(\theta_n/\omega_0)\omega}.;
\end{aligned}
$$

  where $a^{\dagger}_{l,m}$ is the element of Moore-Penrose pseudoinverse, in Eq. (2.77), at the l-th row and the m-th column; $\theta_n = \omega_0 t_n$ is the n-th phase shift. A complete description is in second part of Subsection 2.2.3, page 28.

- I. Choque, M. Padilla, M. Servin, M. Asmad, and **S. Ordones**, "*Suppressing ripple distortions and spurious pistons in phase-shifting interferometry*," J. Opt. Soc. Am. A, vol. 37, no. 4, 614–620, 2020; corresponding to reference [91] and its derived presentation [92]. These works give the relationship between the root multiplicities of a PSA's FTF and the detuning error. Moreover, they introduce the new conditions to design PSA for optical thickness measurements. The new conditions make a PSA having a plane phase response around the tuning frequency. Particularly, these papers establish that the n-th order detuning error can be corrected as long as the PSA's FTF fulfills the following conditions:

$$
H(-\omega_0) = H'(-\omega_0) = \cdots = H^{(n)}(-\omega_0) = 0.
$$

Also, these papers say that the PSA can avoid a spurious phase piston, provided that its FTF accomplishes the conditions:

$$H(\omega_0) = H'(\omega_0) = \cdots = H^{(n)}(\omega_0) = 0;$$

under a n-th order detuning. Therefore, the PSA must need $(3 + 2n)$ phase shifts. In page 37, these papers are described in detail.

- **S. Ordones**, M. Servin, M. Padilla, I. Choque, J. L. Flores, and A. Muñoz, "*Windowed generalized phase-shifting algorithms*," in Interferometry XX (M. B. N. Morris, K. Creath, and R. Porras-Aguilar, eds.), vol. 11490, pp. 1149004–1–9, International Society for Optics and Photonics, SPIE, 2020; corresponding to reference [93]. This work presents the spectral description for PSAs whose coefficients are weighted by an arbitrary window. The paper scope is to compensate for the detuning error since the window function will translate into broad stopbands. However, we also introduce the concept of dynamic window computed according to the data. The paper proposed the PSA's coefficients given by Eq. (2.120)

$$\operatorname{Re}\{c_n\} = \sum_{\substack{l=0\\m=0}}^{N-1} \overbrace{[w_n w_l w_m]}^{\text{window}} \overbrace{[(\sin\theta_m - \sin\theta_l)(\sin\theta_l\cos\theta_m + \sin\theta_m\cos\theta_n + \cos\theta_m\sin\theta_n)]}^{\text{Least squares solution}}$$

$$\operatorname{Im}\{c_n\} = \sum_{\substack{l=0\\m=0}}^{N-1} [w_n w_l w_m]\,[(\cos\theta_m - \cos\theta_l)(\sin\theta_l\cos\theta_m + \sin\theta_m\cos\theta_n + \cos\theta_m\sin\theta_n)]\,.$$

The window can be given by a static function, or a dynamic one as

$$w_n^{(k+1)} = \frac{1}{\left\| I_n - \hat{I}_n^{(k)} \right\|_F};$$

where $n = 0, 1, \ldots, N-1$; $\|\bullet\|_F$ is the Frobenius norm; $\hat{I}_n$ means the least-squares fitted intensity; the $(k+1)$ and (k) indicate the actual and previous iteration, respectively. This article was described in the end of Subsection 2.2.4, page 41.

- M. Servin, M. Padilla, I. Choque, and **S. Ordones**, "*Phase-stepping algorithms for synchronous demodulation of nonlinear phase-shifted fringes*," Opt. Express, vol. 27, no. 4, 5824–5834, 2019; corresponding to reference [113]. This paper presents a phase retrieval technique using the concept of the matched filter with a Gaussian window. In particular, the resulting linear quadrature filter can keep the searched spectral component, but it does not fulfill the so-called quadrature conditions; i.e., one has that $H(0)I(\omega) \neq 0$, and $H(\omega)I(\omega) \neq 0$ in the vicinity around $\omega = -\omega_0$. Thence, one should expect estimated phase maps having ripple distortions. This

PSA's impulsive response can be given by

$$h(t) = \sum_{n=0}^{N-1} w_n e^{in\omega_0 + i\Delta_n} \delta(t-n);$$

where the phase steps are given as $\theta_n = n\omega_0 + \Delta_n$, begin Δ_n a real number. One can realize that the frequency response corresponds to the window's spectrum centered at the local temporal frequency.

- I. Choque, M. Servin, M. Padilla, M. Asmad, and **S. Ordones**, "*Phase measurement of nonuniform phase-shifted interferograms using the frequency transfer function*," Appl. Opt., vol. 58, no. 15, 4157–4162, 2019; corresponding to reference [114]. This work proposes a technique to phase demodulate a set of fringe patterns with non-uniform phase shifts by means of a PSA designed for linear steps. As depicted in Fig. 2.15, non-uniform phase shifts imply that the searched spectral component spreads out. In particular, this work states that one can modify the temporal fringe's spectrum so that the searched spectral component becomes a Dirac's delta; this is mathematically given by

$$\begin{aligned} I(\omega) &= \mathcal{F}_t\left\{\left(a + b\cos[\varphi + \omega_0 t + \Delta(t)]\right) e^{-i\omega_0 t + \Delta(t)}\right\} = \mathcal{F}_t\left\{I(t) e^{-i[\omega_0 t + \Delta(t)]}\right\} \\ &= aD(\omega) + \frac{b}{2} e^{i\varphi}\delta(\omega - \omega_0) + \frac{b}{4} e^{-i\varphi} D^*\left(\frac{-\omega - \omega_0}{2}\right); \end{aligned}$$

where $D(\omega) = \mathcal{F}_t\{\exp[i\Delta(t)]\}$. Then, one employs a filter with broad stopbands at $\omega = 0$ and $\omega = -\omega_0$. The paper's aim is to eliminate the phase piston coming from a detuning error.

- **S. Ordones**, M. Servin, M. Padilla, I. Choque, A. Muñoz, and J. L. Flores, "*Tukey's robust m-estimator for phase demodulation of interferograms with nonuniform shifts*," Appl. Opt., vol. 59, no. 20, pp. 6224–6230, 2020; corresponding to reference [119]. This paper reports a non-linear algorithm and its spectral analysis for phase retrieval from fringe patterns with non-uniform phase shifts. This paper proposes a new phase-shift estimator based on robust estimation in terms of robust statistics. The cost function is in Eq. (2.129):

$$U\left(\theta_n, a_n, b_n; \varphi, n\right) = \sum_{p=1}^{M} \rho\Big(a_n + b_n \cos\left(\varphi_p + \theta_n\right) - I_{p,n}\Big),$$

where $\rho(\bullet)$ is the well-known Tukey's weighting function. The solution of this function is illustrated in the Algorithm 2. This function allows one to neglect those pixels violating the interference equation. This algorithm was described in Subsection 2.2.5, page 45.

Chapter 3

Fringe projection profilometry

Fringe projection profilometry (FPP) is a technique employing structured light; commonly used for measuring solid, diffuse surfaces. Due to development in computer vision systems in recent years, FPP has advantages such as its high-speed, high-resolution, non-contacting, and wide field of view properties [14, 133, 134]. In FPP, fringe patterns are projected onto a solid to be measured, and then, a digital camera records the phase-modulated fringe patterns [14, 133, 134]. To address the 3-D shape, one needs to retrieve the phase from the recorded fringe patterns, and hence, the 3-D surface is retrieved by translating phase units into real-world ones, usually in millimeters.

According to the phase demodulation way, there are two categories of FPP. The first is phase-shifting profilometry (PSP), and the second is Fourier profilometry (FP) [135, 136]. In PSP, the phase is computed by temporally filtering a sequence of fringe patterns; since it is also estimated locally at each pixel, thus preserving small-surface details. Whereas in FP, the phase is computed from a single fringe pattern in a global sense as frequency domain filtering, and therefore, small-surface details are often filtered out. After phase demodulation, a phase-unwrapping scheme is required to retrieve the continuous phase map. Refer to Chapter 2 for details about fringe demodulation.

Figure 3.1 shows a sketch of a typical configuration for a profilometer using the fringe projection technique. The system requirements are quite simple: a video projector, a

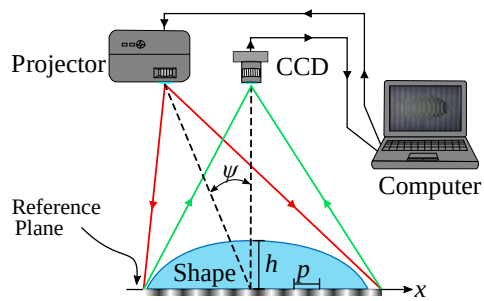

Figure 3.1: Sketch of a typical fringe projection profilometer. Notice that the projector's imaging device and the camera's sensor are parallel to the reference plane

camera, a computer, and a board as the reference plane. The projector's light first hits the testing object, and then the camera records the fringe pattern's modulation introduced by testing objects. In the end, the computer analysis the acquired images to solve the object surface.

Section 3.1 looks through several issues about phase retrieval in fringe projection profilometry. On the other hand, in the state-of-the-art, technologies project several kinds of patterns with different capabilities [137]. Section 3.2 reviews several techniques to generate fringe patterns and their main properties. On the other hand, there are several issues when analyzing the acquired images, such as camera-projector non-linearity, phase-to-height calibration, and shading areas. The camera-projector non-linearity, also called gamma-distortion, is due to a nonlinear mapping between the scale values and the intensity ones. Section 3.3 goes through gamma-distortion. Section 3.4 describes three methods to perform well the translation from phase values (radians) into height values (millimeters). Shading areas turn into areas without measurement information; Section 3.5 describes a technique to cope with them. Finally, it is worth mentioning that one should overcome these troubles with the aim of ensuring accurate measurements.

3.1 Measuring with a fringe projection profilometer

The Section introduces the overall information to measure an object. Figure 3.2 draws completely the process to measure an solid surface through a fringe projection technique. Independently the scheme used for phase retrieval, one must acquire one or more fringe patterns before and after placing the solid to be measured. From the first acquisition, one obtains the carrier through a first phase demodulation process. From the second acquisition, one gets the object's phase plus the spatial carrier. As the third step, one subtracts the spatial carrier from the one retrieved using the second acquisition. The subtraction is done as

$$\begin{aligned}\mathcal{W}\{\hat{\varphi}_{\text{obj}}(x,y)\} &= \text{angle}\left\{\hat{z}_{\text{obj}}(x,y)[\hat{z}_{\text{carrier}}(x,y)]^*\right\} \\ &= \mathcal{W}\left\{\hat{\varphi}_{\text{obj}}(x,y) - \hat{\varphi}_{\text{carrier}}(x,y)\right\}. \end{aligned} \tag{3.1}$$

Here $\hat{z}_{\text{obj}}(x,y)$ and $\hat{z}_{\text{carrier}}(x,y)$ are the estimated analytic signals; in the same way, $\hat{\varphi}_{\text{obj}}(x,y)$ and $\hat{\varphi}_{\text{carrier}}(x,y)$ are the phases. Notice that z^* is the complex conjugated of z. Remember that $\mathcal{W}\{\hat{\varphi}_{\text{obj}}(x,y)\}$ is the wrapped phase corresponding only to the object to be measured, as depicted in Fig. 3.2. Thereafter, one must unwrap it as

$$\hat{\varphi}_{\text{obj}}(x,y) = \mathcal{W}^{-1}\left\{\mathcal{W}\{\hat{\varphi}_{\text{obj}}(x,y)\}\right\}; \tag{3.2}$$

where $\mathcal{W}^{-1}\{\bullet\}$ indicates a phase unwrapping algorithm. Finally, one applies the system parameters to map the unwrapped phase into the real world coordinates; this process can be posed by

$$h(x,y) = G\left[\hat{\varphi}_{\text{obj}}(x,y)\right]. \tag{3.3}$$

Here, $G(\bullet)$ is the function mapping phase values to height ones; Subsection 3.4 describes it.

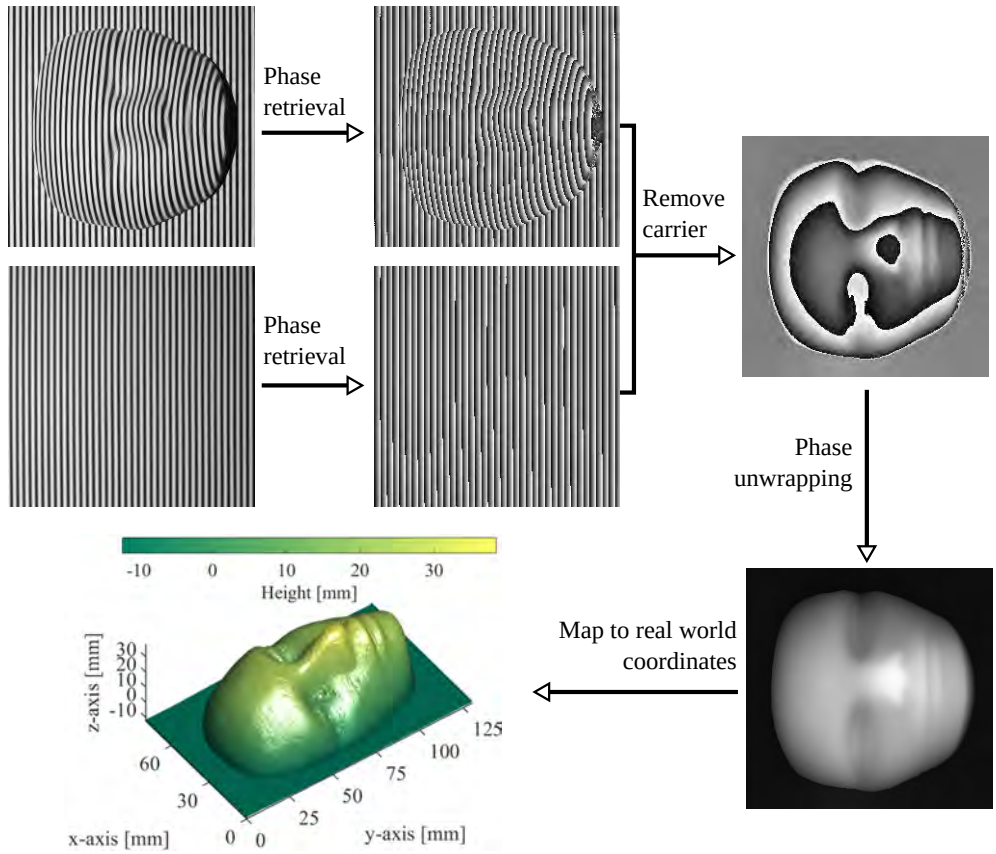

Figure 3.2: Schematic description of the measurement of a solid surface using the fringe projection technique. The description is in the main text.

On the other hand, most fringe projection techniques are applied to measure a solid surface directly. Nonetheless, an interesting application is to measure the shape differences between the testing object and a template in an inspection way. To this end, it has proposed the technique called adaptive-object method or inverse fringe projection [138–140]. This technique consists of projecting a digitally adapted fringe pattern in such a way that the observed fringe pattern has straight vertical fringes [139]. It is not hard to realize that one can map the template surface into phase values, which are then used to create the named adapted fringe pattern [140]. After projecting this pattern onto the testing surface, the camera records a fringe pattern having almost straight fringes whose small phase modulation is due to the surface differences. Thence, this technique should be thought to be a null test. The inverse fringe projection technique's main disadvantage is maybe the inverse fringe pattern is created using the projector's pixel resolution instead of the camera's one. Hence, the estimation will have low pixel resolution. Finally, it is worth mentioning that this technique should be thought t be analogous to the double-exposure holographic technique since the acquired fringe pattern has the phase difference between the testing and the reference surface.

In the same sense, it has recently proposed to modify PSA's phase response so that it

allows one to get the phase differences [141]. The following technique is a collaboration derived from this thesis. Let one write the mathematical description of the $n-$th fringe pattern as

$$I(x,y,n) = a(x,y) + b(x,y)\cos\left[\phi(x,y) + \theta_n\right], \quad n = 0,1,\ldots,N-1. \tag{3.4}$$

Notice that $\phi(x,y) = \varphi(x,y) + q(x,y)$, being $q(x,y)$ the carrier. Now, considering the modified impulsive response given by

$$h(t) = \sum_{n=0}^{N-1} w_n e^{-i[\phi_{\text{ref}}+\theta_n]}\delta(t-t_n), \quad \text{at } (x,y); \tag{3.5}$$

where w_n are the real weights of a PSA and ϕ_{ref} is the phase corresponding to the template surface plus the spatial carrier. Then, its frequency transfer function is obtained by taking the temporal Fourier transform of Eq. (3.5); and hence, one obtains

$$\begin{aligned} H(\omega) &= \mathcal{F}_t\left\{h(t)\right\} = e^{-i\phi_{\text{ref}}}\mathcal{F}_t\left\{w_n e^{-i\theta_n}\delta(t-t_n)\right\} \\ &= e^{-i\phi_{\text{ref}}}\sum_{n=0}^{N-1} c_n e^{-i\omega t_n}, \qquad \text{at } (x,y); \end{aligned} \tag{3.6}$$

where $c_n = w_n\exp(-i\theta_n)$. From Eq. (3.6), one can realized that the modified PSA now has an extra phase piston; refer to Eq. (2.25) in page 17. Performing the temporal convolution in the frequency domain, one has that

$$\begin{aligned} \frac{b}{2}\left|H(\omega_0)\right| e^{i\Delta\varphi} &= I(t) \circledast h(t)\big|_{t=t_N} \\ &= ae^{-i\phi_{\text{ref}}}\left|H(0)\right| + \frac{b}{2}\left|H(\omega_0)\right| e^{i(\phi-\phi_{\text{ref}})} \\ &\quad + \frac{b}{2}\left|H(-\omega_0)\right| e^{-i(\phi+\phi_{\text{ref}})}, \qquad \text{at } (x,y). \end{aligned} \tag{3.7}$$

Here, one can observe that the PSA must accomplish the quadrature conditions; see Eq. (2.24). Considering that both phases are in the same system setup, then one has that

$$\Delta\varphi = \phi - \phi_{\text{ref}} = \varphi + q - \varphi_{\text{ref}} - q = \varphi - \varphi_{\text{ref}}, \quad \text{at } (x,y). \tag{3.8}$$

Finally, assuming that $G(\bullet)$ is a lineal function, so one has the following relation

$$h_{\text{diff}} = h_{\text{obj}} - h_{\text{ref}} = G\left(\Delta\varphi\right), \quad \text{at } (x,y); \tag{3.9}$$

where h_{obj} and h_{ref} are, respectively, the testing and template surfaces, and so, h_{diff} corresponds to the difference between both surfaces.

Figure 3.3 illustrates an example using the technique previously mentioned. Figure 3.3(a) shows the acquired fringe patterns where the video projector's remote control is the surface under study. In order to simulate a small surface defect, a small clay ball was put on the remote control; it is highlighted in the green box. Whence, one should obtain only the surface corresponding to the clay ball. Figure 3.3(b) shows the inspection results where

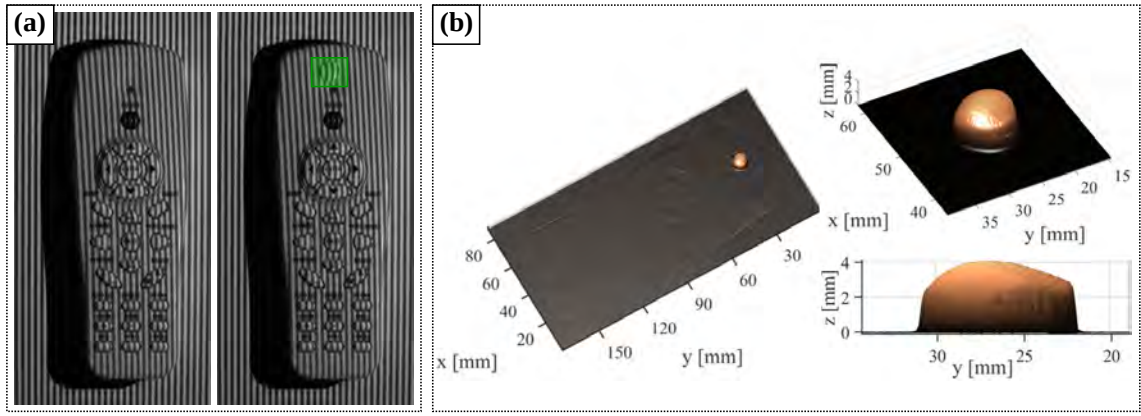

Figure 3.3: Estimating the surface differences using fringe projection profilometry: (a) surfaces under study where one can see that the surface differences are highlighted in the green box; (b) the estimated surface differences corresponding to that simulated one. The description is in the main text.

one can observe that it was carried out correctly; the only surface retrieved came from the clay ball. One can see that the technique also allows estimating that surface corresponding to the fingerprint made on the clay when putting it on. Finally, it is noticeable that one cannot retrieve the clay ball's surface utilizing only the fringe patterns acquired because of 2π ambiguities between the reference plane and the remote control's surface. Thence, one has to employ a temporal unwrapping technique for which one would have to acquires at least two sets of fringe patterns with low spatial frequency.

3.2 Digital pattern generation

This Section goes through the making of fringe patterns for fringe projection profilometry. It is well-known that sinusoidal fringe patterns are the most utilized patterns in fringe projection profilometry. This pattern is generated as

$$I(x, y) = 0.5 + 0.5\cos(v_0 y); \tag{3.10}$$

where $v_0 = 2\pi\nu$ is the radial (angular) frequency of the fringe patterns being ν the number of fringes, which will be vertical oriented. Figure 3.4 depicts the acquired fringe pattern over the reference plane (a) and the testing solid (b). One can observe that the testing surface makes that the fringes suffer displacements along (x, y) axes; these displacements translate into phase modulation; whence, the phase differences, between the pattern's phase with and without modulation, is related to the testing surface; refer to Fig. 3.2.

This Section does not pretend to be an exhaustive review of the generation of the fringe patterns; the following references review in detail this topic [14, 137, 142–145]. Salvi and associated classified the patterns in three main categories: (1) time multiplexing, (b) spatial neighborhood, and (c) depth-color coding [142]. It should be thought that a

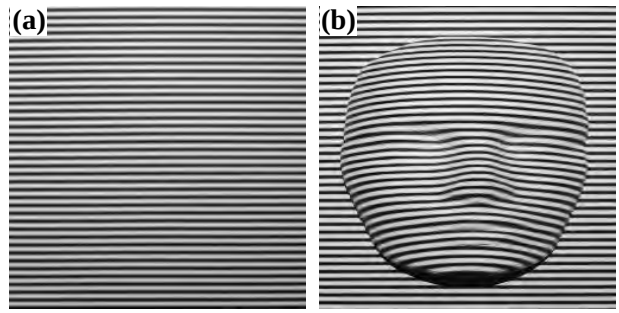

Figure 3.4: A projected sinusoidal fringe pattern: (a) over the reference plane and the testing object (b).

coded pattern belongs from not only one of these categories; these are complementary to one another. Therefore, one can have fringe patterns coded not only spatially but also temporally and in color. The rest of this Section briefly looks at each category.

3.2.1 Temporal coded patterns

To retrieve the testing surface using this kind of pattern, one could require projecting a sequence of fringe patterns. Here, it only looks at binary codes and sinusoidal patterns.

In 1982, Posdamer and Altschuler proposed employing a sequence of binary-coded fringe patterns to measure the surface [146]. Their fringe patterns have white (on-bit) and black (off-bit) stripes; the stripes number increases as the pattern number does. The first pattern has a black stripe and another white; the second one has two black and two white stripes; the third one has four black and four white stripes, and so on. See Figure 3.5(a). When each pattern is projected over the object's surface, the pattern will suffer displacement along $(x-)$ or $y-$direction, and so this fact will be related to the surface. The latter is estimated through a triangulation method needing the center of each stripe. Before that, it is necessary to detect and localize the transition between two consecutive stripes (0-to-1 or 1-to-0); to that end, one can maximize Hamming distance as proposed in [147]. Perhaps this technique's main disadvantage comes from the fact that high-resolution needs many patterns; it makes the technique is very low.

On the other hand, the phase-shifted fringe patterns are perhaps the most known and utilized in fringe projection profilometry. One can digitally generate them by

$$I(x,y,t) = 0.5 + b_1 \cos(u_0 x + v_0 y + \omega_0 t) + b_2 \cos(u_1 x + v_1 y + \omega_1 t) + \cdots \tag{3.11}$$

Here one selects $b_{\#}$ such that $I(x,y,t) \in (0,1)$ for all (x,y) in a normalized sense; $u_{\#}$ and $v_{\#}$ are the spatial-radial frequencies and $w_{\#}$ are the temporal frequencies. It is noticeable that (x,y,t) axes are orthogonal to one another, so one can independently retrieve the phase from a pixel in a time sense as explained in Section 2.2. Moreover, one can see that one is able to temporally multiplex several signals in a manner that they will be separable in the time direction. Figures 3.5(b) and (c) depict the classical sinusoidal patterns with only one harmonic (b) and a multiplexed (c), with two harmonics; the second harmonic has a spatial frequency four times larger than the first one. For this case, one needs to employ

two PSAs; the first one would obtain the phase corresponding to the first frequency, and so it needs to fulfill the following conditions:

$$H_1(0) = 0,\ H_1(-\omega_0) = 0,\ H_1(\omega_0) \neq 0, \text{ and } H_1(-\omega_1) = 0,\ H_1(\omega_1) = 0. \tag{3.12}$$

The other has to accomplish the analogous conditions given by

$$H_2(0) = 0,\ H_2(-\omega_1) = 0,\ H_2(\omega_1) \neq 0, \text{ and } H_2(-\omega_0) = 0,\ H_2(\omega_0) = 0. \tag{3.13}$$

In this way, the estimated analytic signals will have the phase from a single frequency.

3.2.2 Spatially coded patterns

This Subsection describes two kinds of patterns being spatially coded. One usually obtains a binary pattern as the result of employing these methods. A complete review can be found in [14, 142, 143].

The first method gives a well-known De Bruijn sequence. This sequence is composed of words; which each one appears exactly once as one travels around the cycle either clockwise or counterclockwise [148]. This unique feature makes it to be uncorrelated to any other word in the same De Bruijn sequence. Therefore, the auto-correlation function has a unique peak at moment 0; thence, one can decode the patterns straightforwardly [149, 150]. Figure 3.6(a) illustrates a sequences with alphabet $\{0, 1\}$ and word length equal to 6.

However, one should utilize these patterns to measure objects with shapes locally smoothed; when one violates this assumption, one should expect large errors in the shape retrieved.

On the other hand, with the aim of generating a spatially uncorrelated pattern, one can generate a pseudo-random binary pattern. Instead of it, one also can use a multivalued pseudo-random array. To do this, several mini-patterns, called the word, can be indexed randomly to make a new pattern [151]. Thus, the generated pattern will have unique sub-windows, and also, they are uncorrelated to one another. Figure 3.6(b) shows a pattern generated by a three-words (sub-windows) with a random grid-indexing. This pattern has a back square to ease the pattern segmentation in the camera. However, when there is a lot of data loss, the segmentation process will be complex.

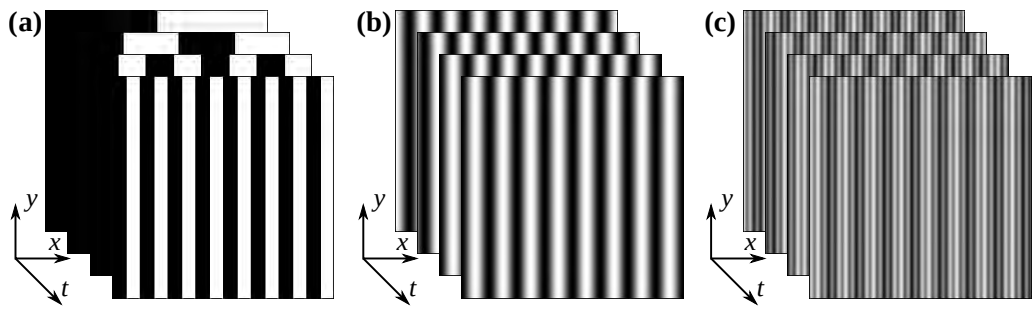

Figure 3.5: Examples of patterns with time coding: (a) binary code with 4-bits, (b) phase-shifted sinusoidal patterns, and (c) multiplexed phase-shifted sinusoidal patterns.

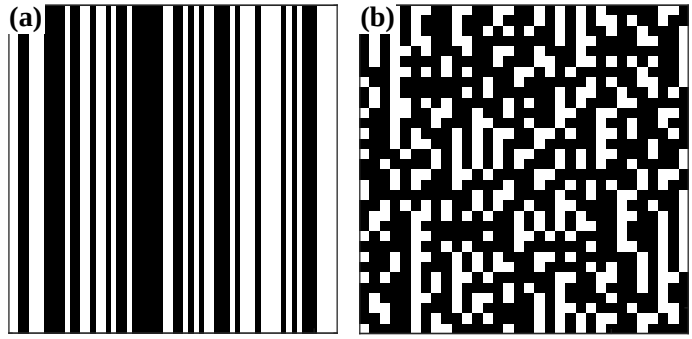

Figure 3.6: Examples of patterns with spatial coding: (a) a De Bruijn sequence with $k = 2$ and $n = 6$ and (b) a pattern using a 2×2 code word and a pseudo-random arrangement.

3.2.3 Color coded patterns

There are some techniques to build color-encoded patterns. They take advantage of the reed-green-blue (RGB) technology to introduce some information *a prior*. This kind of pattern has been employed to reduce the acquisition time because a single projection/acquisition is enough to retrieve the object's phase. Here, it goes through only RGB sinusoidal patterns and the rainbow pattern. Tornero and colleagues review in detail this topic [145].

The rainbow pattern is a single pattern that spatially varies the color due to a diffraction grating [152]. Therefore, it arranges the color from the shortest wavelength to the largest one; see Fig. 3.7(a). This pattern also can be generated digitally by a large set of vertical-narrow slits, which each one has a different color. One can see this process as a sampling of the color from blue to red. Although one can use this pattern to perform online measurements, surface estimation is difficult because of color identification. To overcome this issue, Sato proposed introducing shifts to simplify the color removal, and then, it allows finding correspondences between the projected pattern and the acquired one [153].

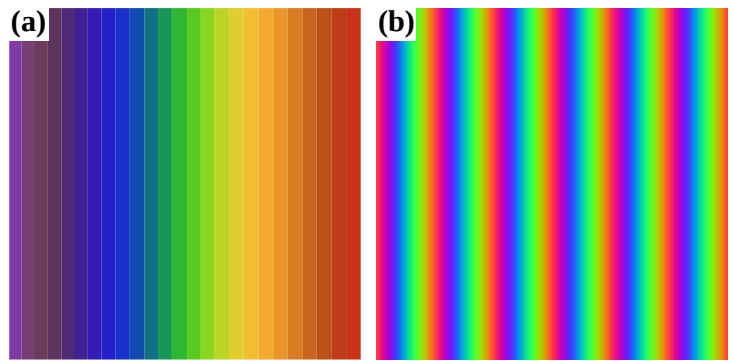

Figure 3.7: Examples of patterns with color coding: (a) the rainbow pattern and (b) a colored, phase-shifted, sinusoidal fringe pattern with phase shift of $2\pi/3$.

From the Sato's paper [153], it is easy to think the shape estimation by means of phase-shifting algorithms. Considering three phase-shifted fringe patterns, one can encode them in each color to obtain the one in Fig. 3.7(b). The main advantage of this RGB pattern is that a phase-shifting algorithm can be employed to perform the phase demodulation process in a pixel-wise way. To build the sinusoidal pattern of each channel, Equation (3.11) can be used. Perhaps, the main issue, using these patterns is due to the fact that the acquired one can suffer of cross-talking between channels, in this sense, it can be mathematically expressed as

$$\begin{bmatrix} I_{\mathrm{R}}^{\mathrm{cam}} \\ I_{\mathrm{G}}^{\mathrm{cam}} \\ I_{\mathrm{B}}^{\mathrm{cam}} \end{bmatrix} = \begin{bmatrix} a_{\mathrm{rr}} & a_{\mathrm{gr}} & a_{\mathrm{br}} \\ a_{\mathrm{gr}} & a_{\mathrm{gg}} & a_{\mathrm{bg}} \\ a_{\mathrm{rb}} & a_{\mathrm{bg}} & a_{\mathrm{bb}} \end{bmatrix} \begin{bmatrix} I_{\mathrm{R}} \\ I_{\mathrm{G}} \\ I_{\mathrm{B}} \end{bmatrix}, \quad \forall (x, y). \tag{3.14}$$

Here, $I_{\mathrm{R,G,B}}^{\mathrm{cam}}$ are the intensities observed by the camera, $I_{\mathrm{R,G,B}}$ are the projected intensities, and $a_{m,n}$ with $m, n \in \{\mathrm{r}, \mathrm{g}, \mathrm{b}\}$ are the coupling factor between color channels.

Based on Eq. (3.14), every observed channel will have not only different background-intensity and fringe modulation functions, but also the phase shifts will be non-uniformly spaced even so projection uniform ones. Although it is preferable to estimate the de-coupling matrix, it is challenging to meet the optimal point; and so small deviations (from the optimal point) will translate into an erroneous decoupling process. Thus, appropriate algorithms should be employed to retrieve the phase correctly, for example, References [154–156]. We would like to point out that one can combine this kind of pattern with temporal multiplexing to reduce the acquisition time while, at the same time, increasing the data redundancy.

3.3 Gamma correction

As previously mentioned, the setup for fringe-projection profilometry consists of a video projector and a digital camera. Despite the simplicity of the setup, the projector-camera system introduces a non-linear intensity distortion translating into acquired patterns being non-sinusoidal owing to undesired high-order harmonics. This intensity distortion is mainly generated by the video projector [157], and it consists of non-linear mapping of the grayscale to intensity values. Because the intensity pattern has undesired high-order harmonics, one is able to reject them straightforwardly through a phase-shifting algorithm, as described in Subsection 2.2.3. However, this way will require acquiring at least seven fringe patterns (in the best case).

When one has a small number of fringe pattern or want to do high-speed measurements, overcoming the gamma distortion is a crucial subject to get a high accuracy measurement. The techniques for gamma calibration and compensation can be classified into two categories: those modifying the intensity distribution before projection [158–160], or those compensating the phase error from gamma-distorted fringe patterns [161–166] and others through a post-processing task. One usually does not want to employ the last ones when doing high-speed solutions.

Huang *et al.* [158] proposed fitting a high-order polynomial to a ramp function of the observed intensity; nonetheless, this approach does not take into account the ambient

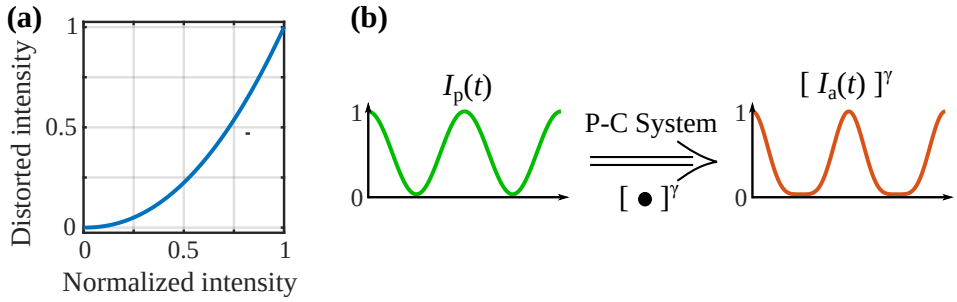

Figure 3.8: Gamma distortion: (a) nonlinear function $[\bullet]^\gamma$ with $\gamma = 2.16$, and (b) distorting the temporal fringe due to γ-factor of the projector-camera (P-C) system.

light nor the intensity profile of the projector. In Reference [160], the ambient light was born in mind. Whereas, Zhang *et al.* [159] proposed to obtain the gamma value as its correspondence with the amplitude of the coefficients of the Fourier series of the temporal fringe. This proposal will perform well, provided that the data had a good signal-to-noise ratio.

Currently, it is defined as this intensity distortion; one can mathematically describe a fringe pattern by Eq. (2.20), which is written here for aid; this equation asserts that

$$I(x,y,n) = a(x,y) + b(x,y)\cos\left[\varphi(x,y) + \theta_n\right], \tag{3.15}$$

where $\theta_n = \omega_0 t_n$ is the phase shift, $a(x,y)$ is the background illumination, $b(x,y)$ is the amplitude modulation, and $\varphi(x,y)$ is the modulating phase. However, when a fringe pattern comes from a fringe-projection system, it will have the so-called gamma distortion, and then, this fringe pattern can be now mathematically expressed as [159]

$$I_a(x,y,n) = [I_p(x,y,n)]^\gamma \tag{3.16}$$

where $I_p(x,y,n)$ is the fringe pattern projected agreeing Eq. (3.15), and $I_a(x,y,n)$ corresponds to the recorded frame; this model is valid when intensity values are into the range $[0,1]$.

Figure 3.8 draws the gamma distortion for $\gamma = 2.16$, one can see that function $[\bullet]^\gamma$ is nonlinear as seen in Fig. 3.8(a), and whence, it introduces a nonlinear intensity distortion as depicted in Fig. 3.8(b). However, the gamma-distorted intensity can be represented by a harmonic sum of the fundamental signal as

$$I_a(x,y,n) = a(x,y) + \sum_{k=1}^{\infty} b_k(x,y)\cos k\left[\varphi(x,y) + \theta_n\right]; \tag{3.17}$$

here b_k is the amplitude of the k-order harmonic [159].

Equation (3.17) is a very important result because it asserts that the gamma distortion will translate into a harmonic distortion. Thus, one can straightforwardly overcome the gamma distortion by employing a PSA that can reject those harmonics with high power levels; usually, the first five ones [167]. This kind of PSAs was described in Subsection 2.2.3 in page 24. Nonetheless, if one wants to improve the speed between measurements by acquiring little fringe patterns, one should correct the gamma distortion.

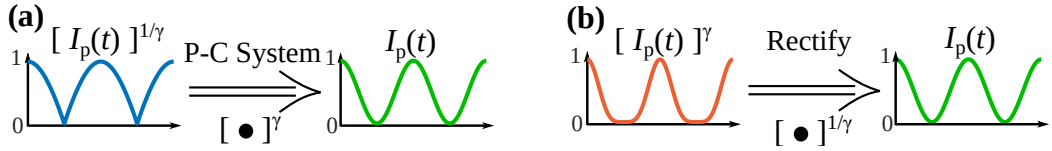

Figure 3.9: Addressing the gamma distortion: (a) generating and projecting a set of anti-gamma-distortion fringe patterns and (b) rectifying digitally the gamma-distorted patterns.

3.3.1 Estimation of the non-linear Gamma-factor

First, considering that one had estimated non-linear factor $\hat{\gamma} \approx \gamma$, one can overcome the gamma distortion by [168]:

1. Projecting a new set of digitally-generated, anti-gamma-distortion fringe patterns so that the new acquired one will have no gamma distortion, this case can be mathematically described as
$$\left[[I_p(x,y)]^{1/\hat{\gamma}}\right]^{\gamma} \approx I_p(x,y). \tag{3.18}$$
Figure 3.9(b) depicts this procedure. Theoretically speaking, the gamma correction allows us to capture the fringe pattern without gamma distortion.

2. One can rectify legacy data being gamma-distorted as seen in Fig 3.9(b), this process would correspond to
$$[[I_p(x,y)]^{\gamma}]^{1/\hat{\gamma}} \approx I_p(x,y). \tag{3.19}$$
Rectifying data also allows us to process the fringe patterns *a posteriori*.

With the aim of estimating the gamma factor, it is propose to the optimization problem given by [168]
$$\hat{\gamma} = \underset{\gamma}{\operatorname{argmin}}\, U(\gamma) = \underset{\gamma}{\operatorname{argmin}} \left\| \varphi_{1/\gamma}(x,y) - P(x,y) \right\|_2 . \tag{3.20}$$
Here $\varphi_{1/\gamma}(x,y)$ is the unwrapped phase corresponding to the reference plane after rectifying the fringe patterns utilizing the estimated gamma value. $P(x,y)$ is the best-fitted plane over a region in the unwrapped phase map. It is worth mentioning that the unwrapped map contains waving phase errors superposing the actual phase; these errors are due to the projector's non-linearity. Based on Eq. (3.20), one can realize that attaining the gamma factor $\hat{\gamma} \to \gamma$, then the ripples distortion, seen in the reference plane's phase, will be reduced. This optimization problem can be solved by employing the Nelder-Mead simplex method [169].

One can see that cost function (3.20) needs the estimation of $\varphi(x,y)$ and $P(x,y)$. Let $I_n^{1/\gamma}$ be the n-th fringe pattern being gamma rectified, so the phase of the reference plane can be extracted by
$$\varphi_{1/\gamma}(x,y) = \mathcal{W}^{-1}\left\{ \text{angle}\left[\sum_{n=0}^{N-1} c_n^* I_n^{1/\gamma} \right] \right\}; \tag{3.21}$$

where c_n is the coefficients of a PSA, particularly, the 3-step LS-PSA has been employed. $\mathcal{W}^{-1}\{\bullet\}$ is the unwrapping operator. Once the phase was estimated, one compute the least-squares plane to a region Ω of this phase; hence, one has the least-squares problem given by

$$\mathbf{b} = \underset{\mathbf{b}}{\operatorname{argmin}} \sum_{m=1}^{M} \left[b_1 + b_2 x_m + b_3 y_m - \varphi_{1/\gamma}(x_m, y_m) \right]^2, \tag{3.22}$$

where M is the number of pixels in Ω, $\mathbf{b}$ is the vector with the coefficients of the least-squares plane, and they are computed by solving the following systems of linear equations

$$\begin{bmatrix} N & \sum_{m=1}^{M} x_i & \sum_{m=1}^{M} y_m \\ \sum_{m=1}^{M} x_m & \sum_{m=1}^{M} x_m^2 & \sum_{m=1}^{M} x_m y_m \\ \sum_{m=1}^{M} y_m & \sum_{m=1}^{M} x_m y_m & \sum_{m=1}^{M} y_m^2 \end{bmatrix} \begin{bmatrix} b_1 \\ b_2 \\ b_3 \end{bmatrix} = \begin{bmatrix} \sum_{m=1}^{M} \varphi_{1/\gamma}(x_m, y_m) \\ \sum_{m=1}^{M} \varphi_{1/\gamma}(x_m, y_m) x_m \\ \sum_{m=1}^{M} \varphi_{1/\gamma}(x_m, y_m) y_m \end{bmatrix}. \tag{3.23}$$

In order to illustrate the feasibility of this method, a numerical experiment was carried out. Let $\gamma = 2.16$ be the actual gamma factor. Figure 3.10 shows the synthetic fringe pattern with gamma distortion, (a) the profile of the normalized intensity and (b) its spatial spectrum of magnitude; where one is able to see that the first three harmonics have significant power. With the aim of comparing the cost function in (3.20) with respect to the scheme employed for phase demodulation, three PSAs are used to retrieve the phase in Eq. (3.21). The first PSA has the coefficients $c^{1\text{st}} = \{2, -1 + i\sqrt{3}, -1 - i\sqrt{3}\}$, $\theta^{1\text{st}} = \{0, 2\pi/3, 4\pi/3\}$, and its SNR gain is 3.0. The second PSA has the coefficients $c^{2\text{nd}} = \{1, -1 - i, i\}$, $\theta^{2\text{nd}} = \{0, \pi/2, \pi\}$, and its SNR gain is 2.0. The last PSA has the coefficients $c^{3\text{rd}} = \{2, -1+i, -1-i\}$, $\theta^{3\text{rd}} = \{0, \pi/2, 3\pi/2\}$, and its SNR gain is 2.0. Figure 3.11 depicts the cost function for each PSA in log-scale. The minimum of the cost function are, respectively, located at $\hat{\gamma}^{1\text{st}} = 2.1770$, $\hat{\gamma}^{2\text{nd}} = 2.1586$, and $\hat{\gamma}^{3\text{rd}} = 2.1646$. Thence, the second PSA has the best cost function because its minimum is the closest to the optimal value $\gamma = 2.16$. Whereas, the worst case is obtained by the 3-step LS-PSA algorithm. For this case, the best choice is employing the second PSA, however, this PSA has a lower SNR gain than the first PSA; however, in some cases, the 3-step PSA will work the best.

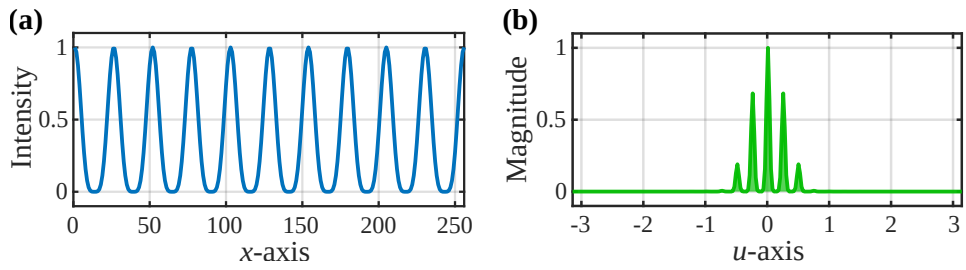

Figure 3.10: A gamma-distorted fringe pattern with 10 fringes: (a) the profile of the intensity along x-axis and (b) the profile of the magnitude of its spatial spectrum along u-axis; where one can see that the first three harmonics have significant power.

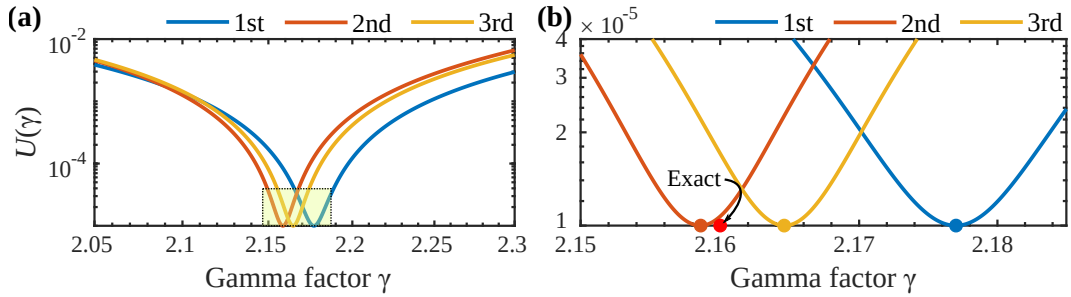

Figure 3.11: Comparison of the cost function in Eq. (3.21) in function of the PSA used for phase demodulation. Figure (b) is a zoom-in of Figure (a); both plots are in log-scale. Pistons are introduced for exposition purpose. Description is in the main text.

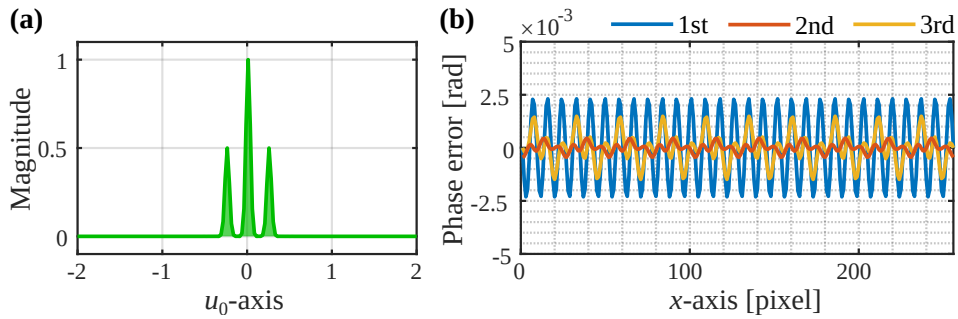

Figure 3.12: Gamma rectification of fringe patterns: (a) magnitude of the spectrum of the rectified fringe pattern using $\hat{\gamma}^{2\text{nd}} = 2.1586$; the others seem almost the same; and (b) phase error obtained when rectifying the gamma-distorted fringe patterns. The exact gamma factor was $\gamma = 2.16$, and the estimated are $\hat{\gamma}^{1\text{st}} = 2.1770$, $\hat{\gamma}^{2\text{nd}} = 2.1586$, and $\hat{\gamma}^{3\text{rd}} = 2.1646$.

Finally, Figure 3.12 draws the effect of rectifying the fringe pattern as Eq. (3.19). Figure 3.12(a) depicts the rectified fringe pattern's spectrum where one can see that it has only the fundamental harmonics, i.e., the fringe patterns seem to be sinusoidal. Figure 3.12(b) shows the estimation's phase error once the fringe patterns had been gamma rectified. One can observe that the second PSA obtained the best result being slightly better than the worst one obtained with the 3-step LS-PSA. To this end, I want to emphasize that the distorting waves' amplitudes may be considered irrelevant for real applications due to noise dispersion.

3.4 Phase to height mapping

This Section goes through the theoretical description of three classical techniques to calibrate a fringe projection profilometer. Several work has been proposed, they are based on the geometry model [170–172] and polynomial fitting [173–176]. The first one requires that geometry parameters must be accurately determined, but these parameters are usually challenging to be determined. Otherwise, the methods based on polynomial fitting

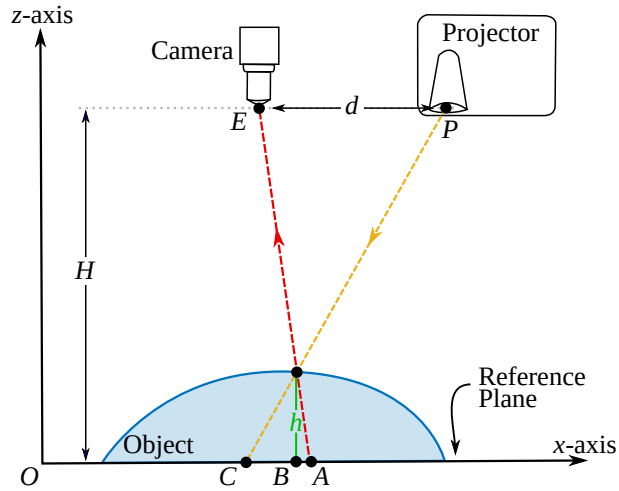

Figure 3.13: Typical setup for fringe projection profilometry. Notice that the Projector's imaging device is parallel to the CCD camera's sensor and the reference plane.

do not only allow one to estimate the geometry parameters accurately but also allows one to arrange the system arbitrarily. For these reasons, calibration methods based on polynomial fitting are here considered.

Figure 3.13 shows a sketch of a typical experimental setup. The light for the projector hits the testing object, and then the camera records the modulation that the testing objects introduce to the projected fringe pattern. In Fig. 3.13, E and P are, respectively, the entrance pupil's center of the camera and the exit pupil's center of the projector; also E and P are assumed to be in the sample plane, whose distance is d along the x-axis. The distance between these pupils and the reference plane is termed by H. Moreover, C is the point where the principal ray of the projector hits the reference plane; analogously, A is for the camera. The searched height of the object is given by h, as seen Fig. 3.13. By similar triangles, the object height can be determined as [170]

$$h = \frac{H}{1 + \frac{2\pi}{p}\frac{d}{\Delta\varphi}}; \tag{3.24}$$

where p is the fringe pitch and $\Delta\varphi = \varphi_A - \varphi_C$ being φ_A and φ_C the phases at point A and C, respectively.

3.4.1 Linear model

As mentioned by Jia and associates [173], when H is much larger than h, then one can considered the linear relation

$$h \approx \frac{pH}{2\pi d}\Delta\varphi. \tag{3.25}$$

by taking into account the spatial dependence of H, Eq. (3.25) can be completely written as

$$h(x,y) \approx \frac{pH(x,y)}{2\pi d}\Delta\varphi(x,y) = K(x,y)\Delta\varphi(x,y), \tag{3.26}$$

where $K(x,y) \in \mathbb{R}$ are the linear calibration coefficients to be found.

To determine the coefficients $K(x,y)$, one can move the plane of reference to several well known calibration position along z-axis; this is

$$h_l(x,y) = K(x,y)\Delta\varphi_l(x,y), \quad l = 1,2,\ldots,L \tag{3.27}$$

where L is the number of introduced translations along the z-axis, and $\Delta\varphi_l(x,y) = \varphi_l(x,y) - \varphi_R(x,y)$ with is the phase corresponding to the reference plane at position $l = 0$. The phases $\varphi_l(x,y)$ and $\varphi_R(x,y)$ can be straightforwardly estimated through a PSA.

Using the phase difference maps as the observed data, one can propose the least-square problem given by

$$U_1(K) = \sum_{l=1}^{L} \left(h_l - K\Delta\varphi_l\right)^2, \quad \text{at } (x,y). \tag{3.28}$$

Here, one can notice that $U_1(K)$ is the least-squares fitting to a straight line, where K is its slope. Solving $U_1(K)$, one obtains that

$$K(x,y) = \frac{\sum_{l=1}^{L} \Delta\varphi_l(x,y)h_l}{\sum_{l=1}^{L} \Delta\varphi_l^2(x,y)}. \tag{3.29}$$

On the other hand, one also can use a second-order polynomial instead of the straight line to describe better the phase differences (along z-axis) as

$$U_2(K_0,K_1,K_2) = \sum_{l=1}^{L} \left(K_0 + K_1\Delta\varphi_l + K_2\Delta\varphi_l^2 - h_l\right)^2, \quad \text{at } (x,y). \tag{3.30}$$

From here, one can estimate $\{K_0,K_1,K_2\}$ by solving the system of linear equations

$$\begin{bmatrix} L & \sum_{l=1}^{L}\Delta\varphi_l & \sum_{l=1}^{L}\Delta\varphi_l^2 \\ \sum_{l=1}^{L}\Delta\varphi_l & \sum_{l=1}^{L}\Delta\varphi_l^2 & \sum_{l=1}^{L}\Delta\varphi_l^3 \\ \sum_{l=1}^{L}\Delta\varphi_l^2 & \sum_{l=1}^{L}\Delta\varphi_l^3 & \sum_{l=1}^{L}\Delta\varphi_l^4 \end{bmatrix} \begin{bmatrix} K_0 \\ K_1 \\ K_2 \end{bmatrix} = \begin{bmatrix} \sum_{l=1}^{L} h_l \\ \sum_{l=1}^{L}\Delta\varphi_l h_l \\ \sum_{l=1}^{L}\Delta\varphi_l^2 h_l \end{bmatrix}; \tag{3.31}$$

which is solved at each pixel. Once the maps of coefficients are computed, the height of a testing object is given by

$$h(x,y) = K_0(x,y) + K_1(x,y)\Delta\varphi(x,y) + K_2(x,y)\Delta\varphi^2(x,y). \tag{3.32}$$

3.4.2 Non-linear model

Continuing as the work [173], one obtains from Eq. (3.24) that

$$\Delta\varphi = \frac{2\pi d h}{pH(1 - \frac{1}{H}h)} = \frac{\frac{2\pi d}{pH}h}{1 - \frac{1}{H}h}, \quad \text{at } (x,y); \tag{3.33}$$

and then, considering the spatial dependence of H, one can obtain the following expression

$$\Delta\varphi(x,y) = \frac{m(x,y)h(x,y)}{1 - n(x,y)h(x,y)}, \tag{3.34}$$

and finally, the height of the object is given by

$$h(x,y) = \frac{\Delta\varphi(x,y)}{m(x,y) + n(x,y)\Delta\varphi(x,y)}. \tag{3.35}$$

The calibration procedure implies estimating parameters $n(x,y)$ and $m(x,y)$; to this end, one can rewrite Eq. (3.34) in the nonlinear way, i.e.,

$$\Delta\varphi(x,y) = m(x,y)h(x,y) + n(x,y)h(x,y)\Delta\varphi(x,y). \tag{3.36}$$

Thereby, one can pose the least-square problem given by

$$U_3(n,m) = \sum_{l=1}^{L} \left(\Delta\varphi - mh_l - nh_l\varphi_l\right)^2, \quad \text{at } (x,y); \tag{3.37}$$

whose solution is obtained by solving the following system of normal equations for each pixel

$$\begin{bmatrix} \sum_{l=1}^{L} h_l^2 & \sum_{l=1}^{L} h_l^2\Delta\varphi_l \\ \sum_{l=1}^{L} h_l^2\Delta\varphi_l & \sum_{l=1}^{L} h_l^2\Delta\varphi_l^2 \end{bmatrix} \begin{bmatrix} m \\ n \end{bmatrix} = \begin{bmatrix} \sum_{l=1}^{L} h_l\Delta\varphi_l \\ \sum_{l=1}^{L} h_l\Delta\varphi_l^2, \end{bmatrix}, \quad \text{at } (x,y). \tag{3.38}$$

Here, one can observe that the solution of a 2×2 system of linear equations is required for each pixel position.

3.4.3 Comparative analysis of the calibration methods.

In order to compare the different calibration methods, a series of experiment was carried out. First, 12 calibration planes were acquired to perform this analysis. These planes were translated by 5 mm each other, so one can measured object with a depth until 60 mm. Figure 3.14 shows the reconstruction of the calibration planes; here one would expect 12 straight lines located at 5 mm, 10 mm,..., 60 mm, respectively. In Fig. 3.14(a) depicting the line model Eq. (3.27), one can realize that the expected lines are not straight strictly. Moreover, it was observed that the measurement has a average standard deviation of $\bar{\sigma} = 0.81$ mm (maximum $\sigma_{\max} = 0.94$, minimum $\sigma_{\min} = 0.52$ mm), and a piston error of 0.68 mm. The results from the quadratic scheme in Eq. (3.32) can be seen in Fig. 3.14(b); this plot shows that the calibrated planes were correctly reconstructed employing this scheme. The observed average standard deviation was $\bar{\sigma} = 0.05$ mm (maximum $\sigma_{\max} = 0.09$, minimum $\sigma_{\min} = 0.01$ mm) and a piston error lower than 0.01 mm. Finally, the reconstructed planes using the non-linear technique is shown in Fig. 3.14(c) where one can see that results have almost the same quality as the quadratic scheme. The average standard deviation was of $\bar{\sigma} = 0.09$ mm (maximum $\sigma_{\max} = 0.27$, minimum $\sigma_{\min} = 0.03$ mm) and a piston error of 0.02 mm. From these results, one should employ the quadratic model to make the phase-to-height conversion.

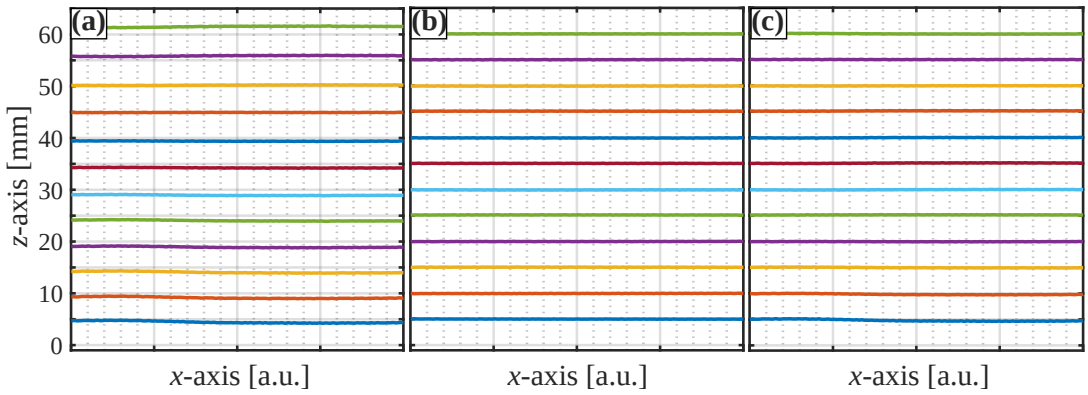

Figure 3.14: Reconstruction of the calibration planes: (a) using the linear model fitting a straight line, (b) with the quadratic model fitted to the linear model, and (c) using the nonlinear model. Notice that (b) and (c) seem to have the same accuracy, whereas, (a) has worse results.

3.5 Co-phased fringe projection

In the typical setup of a fringe projection profilometer, recorded fringe patterns usually have areas without intensity information. This information loss is because object depth generates shadows due to the projection direction. In Figure 3.15, one can observe these shadows appear while illuminating the object shape from the left and right. In order to reduce this loss of information, Servin and colleagues [177] proposed the technique called co-phase that consists of projecting and acquiring the fringe patterns at several locations. It is noticeable that for each projecting direction, a fringe pattern set is needed. By summing all phase maps, coming from each fringe pattern set, one may reconstruct the object completely without information loss. This technique has been developed to 3D scan objects moving rotationally; it requires projecting from two points and recording with only one camera [178]. Other interesting applications of the technique can be found in [179–182].

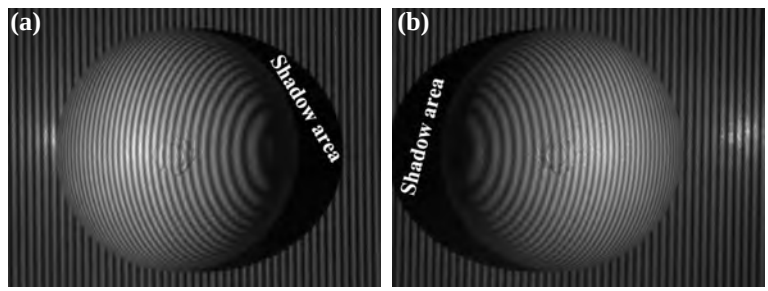

Figure 3.15: Fringe pattern having loss of information due to object shadows: (a) projecting from the left side and (b) from the right side. Notice that both fringe patterns have shading areas, but they are in different areas and do not overlap one to the other. Hence, one would expect to overcome the information loss by putting them together.

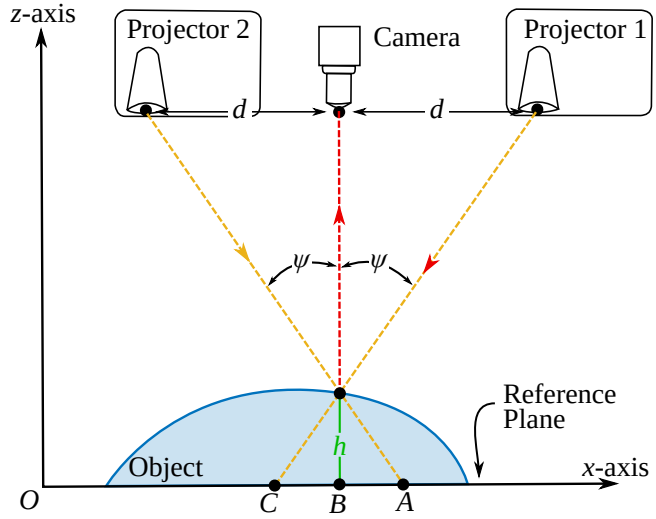

Figure 3.16: Setup of a co-phase, fringe projection profilometer. Notice that pupils of projectors and the camera are in the same plane; moreover, the Projectors' imaging device and camera's sensors are parallel to the reference plane.

Figure 3.16 depicts a sketch of the experimental setup where two projectors and a camera (a normal view) are used. The projector's exit pupils and the entrance pupil of the camera are into the same plane. The distance between the camera and projector 1 is d, and it is the same from camera to projector 2. The angle ψ is the sensitivity angle of the setup. The acquired fringe patterns are given by

$$\begin{aligned} I^{\mathrm{p}_1}(x,y,n) &= a^{\mathrm{p}_1}(x,y) + b^{\mathrm{p}_1}(x,y)\cos\left[\varphi(x,y) + C^{\mathrm{p}_1}(x,y) + \theta_n\right], \\ I^{\mathrm{p}_2}(x,y,n) &= a^{\mathrm{p}_2}(x,y) + b^{\mathrm{p}_2}(x,y)\cos\left[\varphi(x,y) + C^{\mathrm{p}_2}(x,y) + \theta_n\right]; \end{aligned} \tag{3.39}$$

where $n = 0, 1, \ldots, N-1$ and superscript $\mathrm{p}_{\#}$ relates the set of fringe pattern with the projector. By using the correct phase-shifting algorithm, the analytic signals are computed as

$$\begin{aligned} Z^{\mathrm{p}_1}(x,y) &= \frac{b^{\mathrm{p}_1}(x,y)}{2} e^{i[\varphi(x,y)+C^{\mathrm{p}_1}(x,y)]} = \sum_{n=0}^{N-1} c_n I^{\mathrm{p}_1}(x,y,n) \\ Z^{\mathrm{p}_2}(x,y) &= \frac{b^{\mathrm{p}_2}(x,y)}{2} e^{i[\varphi(x,y)+C^{\mathrm{p}_2}(x,y)]} = \sum_{n=0}^{N-1} c_n I^{\mathrm{p}_2}(x,y,n). \end{aligned} \tag{3.40}$$

One can previously measure the carriers $C^{\mathrm{p}_1}(x,y)$ and $C^{\mathrm{p}_2}(x,y)$, e.g., through a phase-shifting algorithm. After, one can obtain the analytic signal as

$$A(x,y)e^{i\varphi(x,y)} = Z^{\mathrm{p}_1}(x,y) + Z^{\mathrm{p}_2}(x,y) \tag{3.41}$$

One expect that $\varphi(x,y)$ does not have any area where the object's surface was not measured.

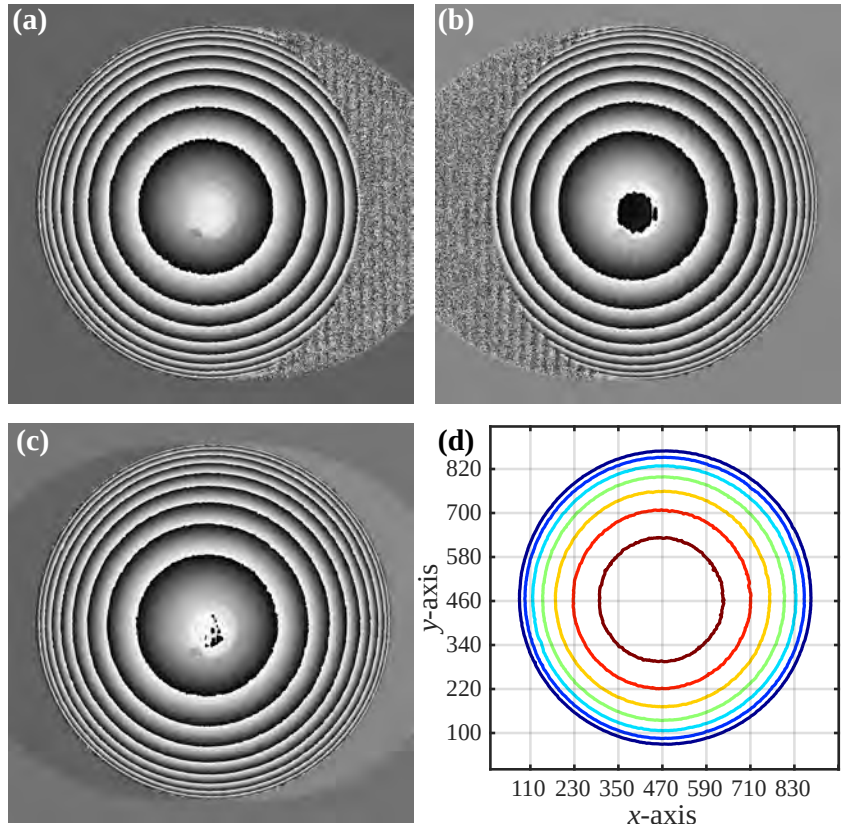

Figure 3.17: 3D reconstruction using a profilometer through the co-phase fringe projection technique with two projectors and a camera: wrapped phase resulting from projector 1 (a) and 2 (b). The co-phase wrapped is in (c) and unwrapped in (d).

As an example, Figure 3.17 shows the phase retrieval of the fringe patterns shown in Fig. 3.15. The testing object is a polystyrene spherical cap. By using the 4-step LS PSA, the wrapped phases were estimated. Figure 3.17(a) depicts the wrapped phase from projector 1, as it can be seen the spatial carrier was removed previously. The wrapped phase from projector 2 is in Fig. 3.17(b). One is able to observe that the shadowed areas have mainly phase noise as expected. By summing these phases according to Eq. (3.41), one obtains the phase in Fig. 3.17(c) where there is the whole phase of the spherical cap; the first two wrapped phases complement one another well in such a way that the resulting phase did not lose any information. Figure 3.17(d) shows the unwrapped phase's contour lines, from where the reader may realize that this technique has correctly reconstructed the object's surface.

3.5.1 Co-phase through projecting simultaneously two patterns

We would like to mention that the present Subsection is a contribution of this thesis, but it has not been reported yet in any publication.

Considering the setup drawn in Fig. 3.16 as the profilometer's configuration. Tech-

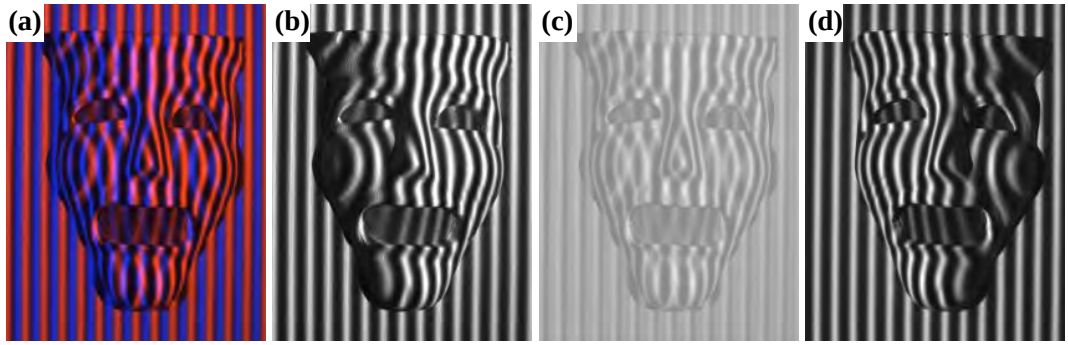

Figure 3.18: Co-phased projection and capturing a RGB pattern: (a) the acquired RGB pattern, grayscale intensities in the red channel (b), in the greed channel, and (d) in the blue channel. Notice that intensity in the green channel is due to cross-talking, a piston was added for exposition purposes.

niques [177–182] utilized gray-scaled fringe patterns and one projects them sequentially: first, projecting and acquiring the N patterns from direction 1, thereafter, from direction 2. However, when one wishes to improve the capturing speed, one should simultaneously project the patterns from these directions. Therefore, one can code both n-th fringe patterns, one from each direction, in an RGB pattern to acquire them simultaneously. This codification can be done as

$$I_{\mathrm{R}}(x,y,n) = I^{\mathrm{P}_1}(x,y,n), \tag{3.42}$$

$$I_{\mathrm{B}}(x,y,n) = I^{\mathrm{P}_2}(x,y,n); \tag{3.43}$$

where $I_{\mathrm{R}}(x,y,n)$ means that the fringe pattern from direction 1 will be coded in the red channel, in the same way, one can define $I_{\mathrm{B}}(x,y,n)$.

Channels red and blue was selected to reduce the cross-talking between channels. By taking the latter into account, the acquired channel will be given by

$$\begin{bmatrix} I_{\mathrm{R}}^{\mathrm{cam}} \\ I_{\mathrm{G}}^{\mathrm{cam}} \\ I_{\mathrm{B}}^{\mathrm{cam}} \end{bmatrix} = \begin{bmatrix} a_{\mathrm{rr}} & a_{\mathrm{gr}} & a_{\mathrm{br}} \\ a_{\mathrm{gr}} & a_{\mathrm{gg}} & a_{\mathrm{bg}} \\ a_{\mathrm{rb}} & a_{\mathrm{bg}} & a_{\mathrm{bb}} \end{bmatrix} \begin{bmatrix} I_{\mathrm{R}} \\ I_{\mathrm{G}} \\ I_{\mathrm{B}} \end{bmatrix}, \quad \forall (x,y). \tag{3.44}$$

Here $I_{\mathrm{R,G,B}}^{\mathrm{cam}}$ are the intensities observed by the camera, $a_{m,n}$ with $m,n \in \{\mathrm{r},\mathrm{g},\mathrm{b}\}$ are the coupling factor between color channels. Figure 3.18 shows an acquired RGB pattern where the object is under co-phased projection. Figure 3.18(a) depicts an acquired fringe pattern in RGB, the gray-scaled intensities of the red channel is in (b), (c) has the ones from the channel green, and gray-scaled intensity corresponding to the blue channel is in (d). I would like to point out that he added a piston in (c) for exposition purposes. The green channel's intensity pattern is due to cross-talking between the green-red and blue-green coupling coefficients in Eq. (3.44). Finally, one can realize that there is a trivial phase piston between the red and blue channels.

Bear in mind that I_{G} is a background intensity $a_{\mathrm{G}}(x,y)$ because any pattern is projected on it. Also, by considering that the diagonal elements are equal to 1, the acquired

intensities are given as

$$\begin{aligned} I_{\mathrm{R}}^{\mathrm{cam}}(x,y,n) &= a^{\mathrm{p}_1}(x,y) + a_{\mathrm{rg}}a_{\mathrm{G}}(x,y) + b^{\mathrm{p}_1}(x,y)\cos\left[\varphi(x,y) + C^{\mathrm{p}_1}(x,y) + \theta_n\right] \\ &\quad + a_{\mathrm{br}}b^{\mathrm{p}_2}(x,y)\cos\left[-\varphi(x,y) + C^{\mathrm{p}_2}(x,y) + \theta_n\right] \\ &= a_{\mathrm{R}}(x,y) + b^{\mathrm{p}_1}(x,y)\cos\left[\varphi(x,y) + C^{\mathrm{p}_1}(x,y) + \theta_n\right] \\ &\quad + a_{\mathrm{br}}b^{\mathrm{p}_2}(x,y)\cos\left[-\varphi(x,y) + C^{\mathrm{p}_2}(x,y) + \theta_n\right]. \end{aligned} \tag{3.45}$$

Taking the temporal Fourier transform of Eq. (3.45), this spectrum is given by

$$\begin{aligned} I_{\mathrm{R}}^{\mathrm{cam}}(\omega) = \mathcal{F}_t\left\{I_{\mathrm{R}}^{\mathrm{cam}}(t)\right\} &= a_{\mathrm{R}}\delta(\omega) + \frac{1}{2}\left[b^{\mathrm{P}_1}e^{i\vartheta_1} + a_{\mathrm{br}}b^{\mathrm{P}_2}e^{i\vartheta_2}\right]\delta(\omega-\omega_0) \\ &\quad + \frac{1}{2}\left[b^{\mathrm{P}_1}e^{-i\vartheta_1} + a_{\mathrm{br}}b^{\mathrm{P}_2}e^{-i\vartheta_2}\right]\delta(\omega+\omega_0). \end{aligned} \tag{3.46}$$

Here, spatial dependence was omitted for simplicity; $\vartheta_1 = \varphi + C^{\mathrm{P}_1}$ and $\vartheta_2 = -\varphi + C^{\mathrm{P}_1}$. In an analogous way, one obtains the expression for the blue channel given by

$$\begin{aligned} I_{\mathrm{B}}^{\mathrm{cam}}(x,y,n) &= a_{\mathrm{B}}(x,y) + b^{\mathrm{p}_2}(x,y)\cos\left[-\varphi(x,y) + C^{\mathrm{p}_2}(x,y) + \theta_n\right] \\ &\quad + a_{\mathrm{br}}b^{\mathrm{p}_1}(x,y)\cos\left[-\varphi(x,y) + C^{\mathrm{p}_1}(x,y) + \theta_n\right]; \end{aligned} \tag{3.47}$$

and then, its Fourier transform is given by

$$\begin{aligned} I_{\mathrm{B}}^{\mathrm{cam}}(\omega) = \mathcal{F}_t\left\{I_{\mathrm{B}}^{\mathrm{cam}}(t)\right\} &= a_{\mathrm{B}}\delta(\omega) + \frac{1}{2}\left[b^{\mathrm{P}_2}e^{i\vartheta_2} + a_{\mathrm{br}}b^{\mathrm{P}_1}e^{i\vartheta_1}\right]\delta(\omega-\omega_0) \\ &\quad + \frac{1}{2}\left[b^{\mathrm{P}_2}e^{-i\vartheta_2} + a_{\mathrm{br}}b^{\mathrm{P}_1}e^{-i\vartheta_1}\right]\delta(\omega+\omega_0). \end{aligned} \tag{3.48}$$

From Eq. (3.45) – (3.48), the analytic signals are, respectively, given by

$$Z_{\mathrm{R}} = \sum_{n=0}^{N-1} c_n^* I_{\mathrm{R}}(n) = \frac{1}{2}\left[b^{\mathrm{P}_1}e^{i\vartheta_1} + a_{\mathrm{br}}b^{\mathrm{P}_2}e^{i\vartheta_2}\right] \tag{3.49}$$

$$Z_{\mathrm{B}} = \sum_{n=0}^{N-1} c_n^* I_{\mathrm{B}}(n) = \frac{1}{2}\left[b^{\mathrm{P}_2}e^{i\vartheta_2} + a_{\mathrm{br}}b^{\mathrm{P}_1}e^{i\vartheta_1}\right]; \tag{3.50}$$

it is noticeable that both analytic signals were computed using the same PSA. Here the reader should also expect the introduced phase shifts will not the same to the observed one due to $a_{\mathrm{br}} \neq 0$. By considering that $C = C^{\mathrm{P}_1} = C^{\mathrm{P}_2}$, and after some algebraic manipulation, one has that

$$Z_{\mathrm{Obj}} = Z_{\mathrm{R}}e^{-iC} + Z_{\mathrm{B}}^* e^{iC} = \frac{b^{\mathrm{P}_1} + b^{\mathrm{P}_2}}{2}e^{i\varphi}\left(1 + a_{\mathrm{rb}}e^{-i2\varphi}\right) \tag{3.51}$$

Here Z_{Obj} is the analytic signal corresponding to the surface to be measured; notice that it is expected to have no shaded areas. Moreover, in Eq. (3.51), one should contemplate that $a_{\mathrm{rb}} \gg 1$, or even, to be zeros, in some cases. Based on this fact, one has the following relationship

$$\mathcal{W}\left\{\varphi(x,y)\right\} \approx \mathcal{W}\left\{\hat{\varphi}(x,y)\right\} = \mathrm{angle}\left[Z_{\mathrm{Obj}}(x,y)\right]. \tag{3.52}$$

Figure 3.19 depicts the fringe demodulation of the patterns in Fig. 3.18; the magnitude of analytic signal Z_{Obj} is in (a) and the wrapped phase is in (b). In this figure, one can observe that the retrieved phase has no information loss due to shaded areas.

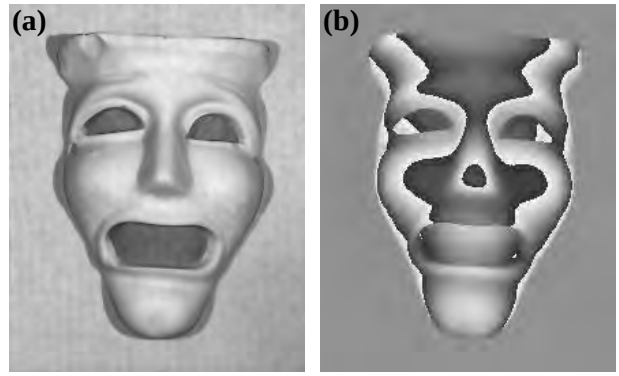

Figure 3.19: Estimation using co-phased fringe projection: (a) the magnitude of the analytic signal and (b) the wrapped phase estimated.

3.5.2 Online reconstruction of a rectilinear-moving object using co-phase with two simultaneously-projected patterns

Considering that the testing object is moving in a rectilinear direction along x-axis, so the n-th acquired fringe pattern can be mathematically described by

$$I(x, y; t_n) = a(x, y) + b(x, y) \cos\left[u_0 x + \varphi(x + \Delta x, y)\right] \tag{3.53}$$

where u_0 is the spatial radial frequency; t_n is the moment when the picture is acquired; and Δx is the among of movement of the testing object, i.e. $\Delta x = \nu / t_n$ being ν the object's velocity. It is noticeable that the fringe pattern is static in Eq. (3.53). If the testing object is thought to be static, one needs to think that the fringe pattern suffers o feels the movement. In this case, one requires to perform a pixel matching procedure to center the testing object in a plane (x', y), this is

$$I(x', y; t_n) = a(x', y; t_n) + b(x', y; t_n) \cos\left[u_0 x + \varphi(x', y) + \theta_n\right]; \tag{3.54}$$

where $\theta_n = \omega_0 t_n$ is the phase shift. By acquiring N fringe pattern, one can then realize that this temporal sequence corresponds of phase-shifted fringe patterns. However, one can also observe that these patterns will have temporal and spatial variations in both the background and fringe modulation functions. These temporal variations will translate into a spreading spectrum. Taking the temporal Fourier transform of Eq. (3.54), one obtains that

$$\begin{aligned} I(\omega) &= \mathcal{F}_t\left\{I(t)\right\} = \mathcal{F}_t\left\{a(t)\right\} + \frac{1}{2} e^{i\varphi} \mathcal{F}_t\left\{b(t) e^{i\omega_0 t_n}\right\} + \frac{1}{2} e^{-i\varphi} \mathcal{F}_t\left\{b(t) e^{-i\omega_0 t_n}\right\} \\ &= A(\omega) + \frac{1}{2} e^{i\varphi} B\left(\omega - \omega_0\right) + \frac{1}{2} e^{-i\varphi} B\left(\omega + \omega_0\right). \end{aligned} \tag{3.55}$$

Here, $A(\omega)$ is the spectrum of the background function, and $B(\omega)$ is from the fringe modulation function. From Eq. (3.55), one can see that the quadrature conditions that the PSA needs to meet are:

$$A(\omega) H(\omega) = 0, \quad B(\omega + \omega_0) H(\omega) = 0, \quad \text{and } B(\omega - \omega_0) H(\omega) \neq 0. \tag{3.56}$$

Here, one can realize that the PSA's frequency response has to have broad-stop bands around $\omega \in \{0, -\omega_0\}$.

In the same way that Chapter 2, let $a_n = a(t_n)$, $b_n = b(t_n)$ and θ_n known parameters, then one can fulfill the conditions (3.56) through the following optimization problem

$$\mathbf{x}^+ = \underset{\mathbf{x}}{\operatorname{argmin}} \|\mathbf{b} - \mathbf{A}\mathbf{x}\|_2^2 \tag{3.57}$$

whence

$$\mathbf{x} = \begin{bmatrix} 1 & \cos\varphi & -\sin\varphi \end{bmatrix}^{\mathrm{T}} \tag{3.58}$$

$$\mathbf{b} = \begin{bmatrix} I_0 & I_1 & \cdots & I_{N-1} \end{bmatrix}^{\mathrm{T}} \tag{3.59}$$

$$\mathbf{A} = \begin{bmatrix} a_0 & b_0\cos\theta_0 & b_1\sin\theta_0 \\ a_1 & b_1\cos\theta_1 & b_2\sin\theta_1 \\ \vdots & \vdots & \vdots \\ a_{N-1} & b_{N-1}\cos\theta_{N-1} & b_{N-1}\sin\theta_{N-1} \end{bmatrix}. \tag{3.60}$$

The optimal value in the least-squares sense is given by $\mathbf{x}^+ = \mathbf{A}^\dagger\mathbf{b}$; thus, the coefficients would be

$$c_n = \frac{1}{2}\left(a^\dagger_{2,n+1} + i a^\dagger_{3,n+1}\right). \tag{3.61}$$

Now, the values of a_n, b_n, as well as θ_n can be computed by solving the optimization problem in Eq. (2.129) in page 45. To this end, one can use the least-squares solution posing $\rho(r_p) = r_p^2/2$. Thence, in an iterative process, the searched phase, shifts, as well as background and fringe modulation functions are computed. One could also employ the algorithms [93, 112] for phase retrieval. We would like to point out that we should pay attention when estimating the Penrose matrix because $\mathbf{A}^{\mathrm{T}}\mathbf{A}$ might be numerically bad conditioned. Particularly, it will happen when the time variations of a and b are noise likely. For that case, the classic coefficients, in Eq. (2.55), should be employed instead of Eq. (3.61). It is noticeable that the PSA's frequency response could not be visualized correctly due to spectrum leakages or the short length of the observation window. Figure 3.20 depicts the estimated background and fringe modulation functions for the setup employed for this thesis. One can observe that the spatial variations around the center are small; therefore, the algorithm in Eq. (3.61) should perform well when the fringe patterns are acquired around the picture's center.

Obtaining the phase-shifted fringe patterns

This part goes through the process of getting those patterns described in Eq. (3.54) from the acquired images. To this end, let one consider a captured fringe pattern in the red channel. Figure 3.21 shows three pictures acquired at different moments; one can observe that the object was moving along the x-axis. Moreover, one can realize fringe patterns have so much redundant information generated by the static projected patterns; whence, an image correlation over these intensity values would fail to isolate the object.

On the other hand, one can obtain the redundant information due to the object by estimating the co-phase of the object by a spatial filtering procedure. One must retrieve

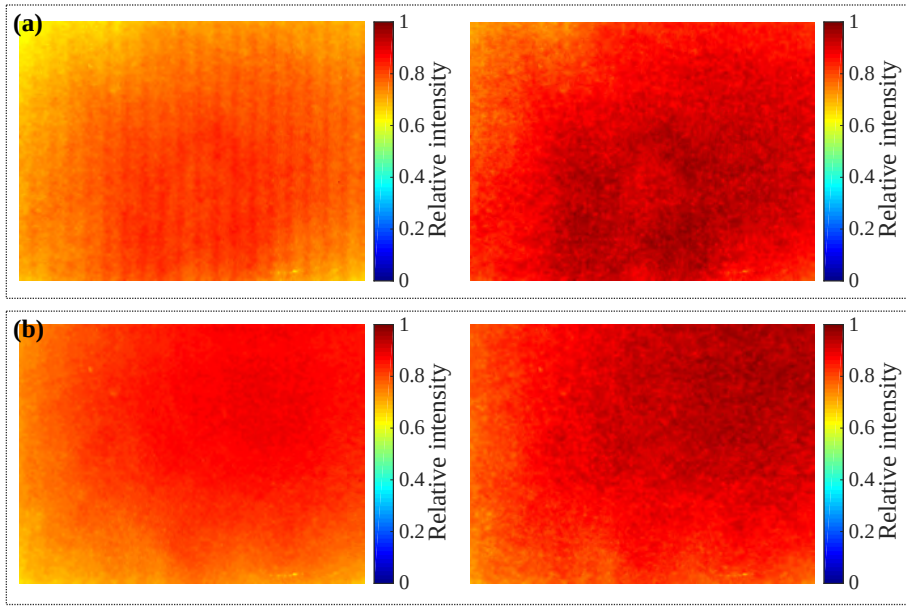

Figure 3.20: Relative intensities for the background and fringe modulation functions for (a) the red channel and (b) the blue one. Notice that they have small spatial variations around the center of the plots.

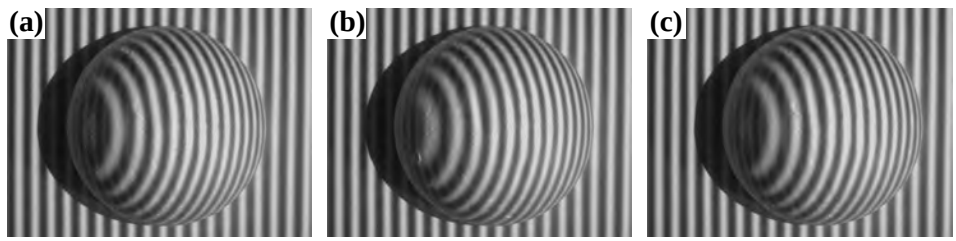

Figure 3.21: Blue channel of three acquired images acquired at three different moments.

the phase of a single fringe pattern in two occasions (for the red and blue channels); then, the co-phase is obtained by the merging them as summation of the analytic signals. Let $u_0 x$ be the spatial carrier which is known. The phase can be retrieved by a low-pass filtering process as

$$\tilde{s}(x,y,n) = \mathrm{LF}\left[I_{\mathrm{r}}(x,y,n)e^{-iu_0x}\right] + \mathrm{LF}\left[I_{\mathrm{b}}(x,y,n)e^{iu_0x}\right]; \quad n = 0,1,\ldots,N-1. \tag{3.62}$$

Here LF[•] means low-pass filtering, $\tilde{s}$ indicates an analytic signal estimated roughly, and so the phase is. From Eq. (3.62), the poorly-estimated phase is given by

$$\tilde{\varphi}(x,y,n) = \mathcal{W}^{-1}\left\{\mathrm{angle}\left[\tilde{s}(x,y,n)\right]\right\}. \tag{3.63}$$

Now, this phase map has redundant information related only to the object.

Considering a reference, centered phase map $\tilde{\phi}(x,y)$; hence, one can compute the translation with respect to it. To obtain the translation vector, one can pose the optimization

problem given by

$$\Delta t_x^+ = \underset{\Delta t_x}{\operatorname{argmin}} \sum_{(x,y)} \left[\tilde{\phi}(x,y) - \tilde{\varphi}(x+\Delta t_x, y)\right]^2. \tag{3.64}$$

This problem is solved for each phase map $\tilde{\varphi}$. Once, one had found optimal value Δt_x^+, then the phase-shifted fringe patterns in Eq. (3.54) are obtained straightforwardly. Finally, these roughly-estimated co-phases can be used as initial point for phase retrieval.

3.6 Contributions

I enlist and summarize my published papers related to this Chapter:

- **S. Ordones**, M. Servin, M. Padilla, I. Choque, J. L. Flores, and A. Muñoz,"*Shape defect measurement by fringe projection profilometry and phase-shifting algorithms*," Optical Engineering, vol. 59, no. 1, pp. 1–10, 2020; corresponding to reference [141]. This article presents a new kind of phase-shifting algorithms with the ability to estimate phase differences. To this end, the PSAs' phase response is stated to a predefined/calibrated value, and thus, the algorithm will compute the phase differences between this value and the retrieved phase (on the fringe patterns). Particularly, the paper's main contribution can be summarized by the following equations:

$$H_{\varphi^+}(\omega) = e^{-i\varphi^+}\,[\text{a PSA's FTF}] = e^{-i\varphi^+}\left[\sum_{n=0}^{N-1} c_n e^{-i(\theta_n/\omega_0)\omega}\right],$$

  where $\theta_n = \omega_0 t_n$ is the n-th phase shift. After, one can estimate the phase differences by

$$\frac{b}{2}e^{i\Delta\varphi} = \sum_{n=0}^{N-1} d_n^* I_n.$$

  Here, d_n are coefficients coming from $H_{\varphi^+}(\omega)$, and $\Delta\varphi = \varphi^+ - \varphi$ is the phase difference between the actual phase φ^+ and the testing one φ. So, it is noticeable that $H_{\varphi^+}(\omega_0) = \left|H_{\varphi^+}(\omega)\right| \exp(-i\varphi^+)$. Section 3.1 describes this technique in detail; refer to page 72.

- A. Muñoz, J. L. Flores, G. Parra-Escamilla, L. A. Morales, **S. Ordones**, and M. Servin, "*Least-squares gamma estimation in fringe projection profilometry*," Appl. Opt., vol. 60, no. 5, 1137–1142, 2021; corresponding to reference [168]. This work presents a technique to estimate and compose the non-linear intensity distortion commonly seen by fringe projection profiles; it is also called gamma distortion. This paper proposed finding the gamma value that minimizes L^2 norm from the least-squares plane and the estimated reference plane. This cost function is described by Eq. (3.20):

$$\hat{\gamma} = \underset{\gamma}{\operatorname{argmin}}\, U(\gamma) = \underset{\gamma}{\operatorname{argmin}} \left\|\varphi_{1/\gamma}(x,y) - P(x,y)\right\|_2.$$

Here, $\varphi_{1/\gamma}(x,y)$ is the reference plane's unwrapped phase coming from the gamma-corrected intensities, and $P(x,y)$ is the least-squares plane adjusted to $\varphi_{1/\gamma}(x,y)$. Hence, the found gamma value is employed to pre- or post-correct the acquired fringe patterns. Section 3.3 goes through this method in detail.

- J. L. Flores, M. Stronik, A. Muñoz, G. Garcia-Torales, **S. Ordoñes**, and A. Cruz, "*Dynamic 3d shape measurement by iterative phase shifting algorithms and colored fringe patterns*," Opt. Express, vol. 26, no. 10, pp. 12403–12414, 2018; corresponding to reference [31]. This paper presents a fringe projection technique to measure rigid objects in continuous movement. The technique translates the rigid movements into phase shifts, and so one obtains phase-shifted fringe patterns. Then, the phase retrieval is done as following: (1) performing a fringe normalization procedure; (2) using a non-linear phase-shifting algorithm; and (3) phase unwrapping the wrapped phase. This technique allows one to obtain good reconstruction, but shadowed areas were not taken into account. I would like to mention that this work was mostly done while I was at the University of Guadalajara.

- **Co-phase fringe projection by simultaneously projecting two patterns**. This topic is described by Subsection 3.5.1; it has not been published yet. Subsection 3.5.1 introduces the use of co-phase fringe projection when simultaneously stereo projecting a sinusoidal pattern. Using this technique, the Subsection also presents a way to scan rigid shapes in a rectilinear motion; for which phase-shifting algorithms are utilized. Using the impulsive response whose coefficients are given by Eq. (3.61), one obtains the analytic signals in Eqs. (3.49) and (3.50). Thereafter, summing them, one obtains the co-phased analytic signal in Eq. (3.51):

$$Z_{\text{Obj}} = Z_{\text{R}} e^{-iC} + Z_{\text{B}}^{*} e^{iC} = \frac{b^{\text{P}_1} + b^{\text{P}_2}}{2} e^{i\varphi} \left(1 + a_{\text{rb}} e^{-i2\varphi}\right).$$

Here, subscripts B and R indicate the color channel, blue or red, the estimation comes from. Superscripts P_1 and P_2 specifies the multimedia projector used. Term a_{rb} means the coupling factor between the blue and red channels; one expects that $a_{\text{rb}} \ll 1$. The last equation points out that the estimated co-phased map will have small distorting ripples due to color cross-talking.

Chapter 4

Experimental results

The present Chapter shows the experimental results obtained by the proposed three-dimensional scanner. This implementation is based in the technique named co-phased fringe-projection. This fringe projection profilometer was then employed to three dimensional scan moving objects as well as perform an inspection of the shape. This Chapter also describes those results from the phase-to-height and the gamma calibration procedures. Section 4.1 provides the characteristics of the profilometer he built. Section 4.2 has the results obtained for calibrating the gamma distortion for both projectors; once at a time. The results of the depth calibration are described by Section 4.3. In Section 4.4, we illustrate some reconstructions of static objects using his profilometer; we later utilizes them as the calibrated shapes for 3D inspection. Section 4.5 depicts several reconstructions while the objects are now moving continuously along the x-axis. Finally, Section 4.6 has the results of 3D inspections while the objects are in a rectilinear, continuous motion along x-axis.

4.1 Experimental setup: co-phased fringe projection profilometer

This section describes the characteristic of our profilometer. Figure 4.1 depicts two pictures of the profilometer, as the reader can see this setup requiring two projectors and a digital camera. The profilometer employs a charge-coupled device (CCD) camera having the sensor UI214xSE-C R3 that has the ability to record red-blue-green (RGB) images. This sensor has a 1280×960-pixel resolution and 32-bit of depth; 8-bit per channel. The profiler works with the whole the camera's pixel resolution. On the other hand, the two multimedia projectors are Dell model S320 with Digital Light Processing (DLP) technology. They have 1024×768-pixel resolution and 8-bits of depth for the channel and are working at 60 Hz. Considering the right-side picture in Fig. 4.1, the projector in the left are projecting in the red channel, and the other in the blue channel. Each projector is short-throw, and thereby, one can focus the projected image in a very short distance given the ability to place the reference plane close to them. The distance between the camera and the reference plane is around 400 mm.

Figure 4.1: Photographs of the fringe-projection profilometer. The description is in the main text.

To build the reference plane, we used a white-bond paper sheet placed on a bathroom mirror; therefore, one must expect that this reference plane has a poor flatness, also it will introduces spurious heights due to the testing objects' weight. These spurious heights were very small.

Finally, It is noticeable that this setup was schematically described in Fig. 3.16 previously. Particularly, sensitivity angle $\psi \approx 30\,\text{deg}$.

4.2 Gamma calibration

This Section describes the system's calibration concerning the non-linear gamma distortion using that technique described in Section 3.3. Figure 4.2 draws the observed data before performing the gamma correction. It is worth mentioning that the spectrum plots correspond to the actual magnitude's square root in order to improve the spectrum presentation. Figure 4.2(a) corresponds to the red channels where one can observe that it has not only mostly second-harmonic distortion, but also it has unwanted lobes around the frequency 1.5 rad/pixels. I believe they are generated due to the projector grating. On the other hand, the other acquired intensity is depicted by Fig. 4.2(b) where one can see intensity distortions are because of the second harmonic contribution. Considering that the PSA only has the ability to accomplish the quadrature conditions. The second harmonic is the main error source in the retrieved phase. Refer to Subsection 2.2.3 for explanations. In this sense, one can quantify roughly the distortion by relation:

$$\frac{2\left|b_2 e^{i2\varphi}\right|}{\left|b_1 e^{i\varphi}\right|} \ll 1.$$

The values of such relations are 0.3673 and 0.3912 for the red and blue channels, respectively. One can realize that these values do not accomplish the aforementioned relation, and whence, the estimated phase would be highly harmonic distorted. Consequently, the gamma distortion should be corrected.

The estimated gamma values were $\gamma_{\text{red}} = 4.78$ and $\gamma_{\text{blue}} = 6.84$. Figure 4.3 shows the results by correcting the gamma distortion. As in the previous Figure, the red and blue

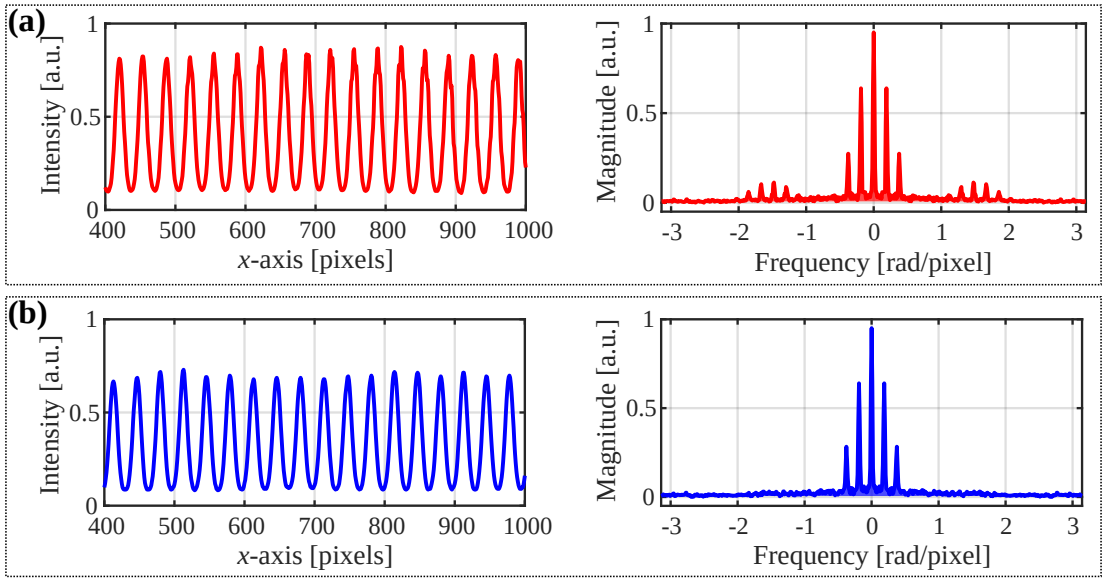

Figure 4.2: Drawing the acquired intensity and its spectrum with gamma distortion: (a) the intensity and spectrum corresponding to the red channel, and (b) the intensity and spectrum of the blue channel. The depicted spectra is the square rooted of the actual ones.

channels correspond to Fig. 4.2(a) and (b), respectively. One can observe that the spectra of the gamma-corrected data seem to have fewer distortions. Based on the spectrum plots, one can realize that the second harmonic's power decreased very significantly; however, the third harmonic's power increased. Although this harmonic now has more power, it is significantly lower than the power of the second harmonic in the first stage; Figure 4.2. Again, considering that the PSA only have the ability to fulfill the quadrature conditions, and due to the fact that the third harmonic should be thought to be the main source of harmonic distortion; therefore, one should consider at least the following relation

$$\frac{2\left|b_3 e^{i3\varphi}\right|}{\left|b_1 e^{i\varphi}\right|} \ll 1$$

is very important because it determines the amount of distortion in the recovered phase. After the gamma correction, such values were 0.034 for the read channel and 0.047 for the blue one. Therefore, this relation was accomplished. By comparing the values before and after the gamma correction, one should expect that the harmonic distortion's amplitude will be reduced by around 10 times. A more meticulous analysis requires taking the power of the fourth harmonic into account due to the fact that it has significant power for the red channel, see Fig. 4.3(a), to determine a more accurate quantification of the amplitude of the harmonic distortion; this fact allows concluding that that phase from the red channel will have a larger harmonic distortion that the one from the blue channel. Finally, one should design a PSA whose FTF rejects the third harmonic to improve the phase estimation's quality. However, it would need to increase in two the number of fringe patterns to be acquired; in other words, one must acquire at least five images.

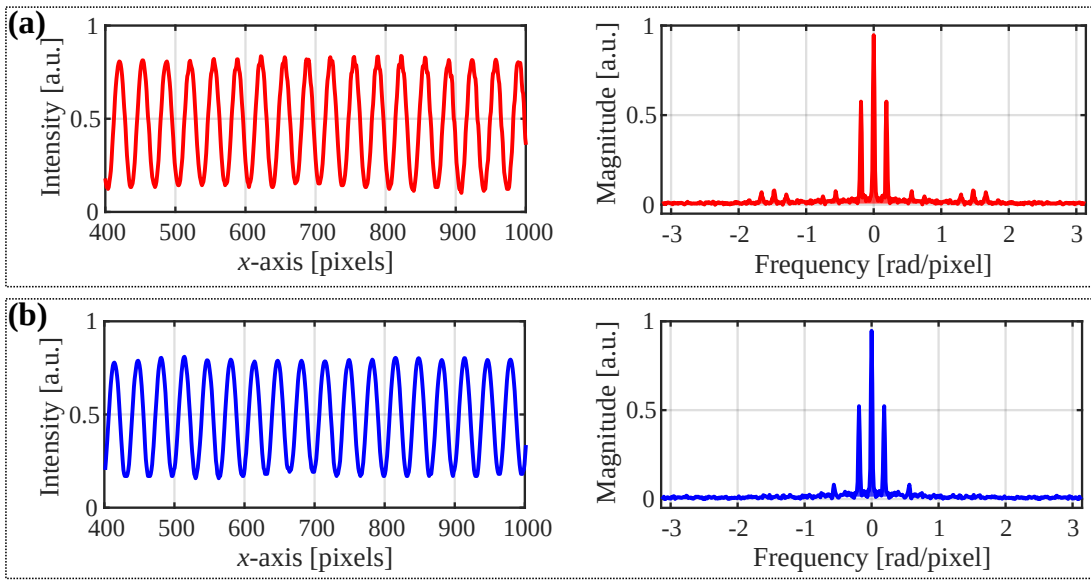

Figure 4.3: Gamma correction of the intensities and the corresponding spectrum: (a) the intensity and spectrum corresponding to the red channel, and (b) the intensity and spectrum of the blue channel. The depicted spectra is the square rooted of the actual ones.

On the other hand, to reduce the computation time, anti-gamma-distortion fringe patterns (one at each channel) are projected instead of correcting the acquired ones as depicted in this Section; refer to Eq. (3.18).

4.3 Phase-to-height calibration

To perform the calibration coefficients, 25 calibrated positions were taken. The distance between position was 4 millimeters, so the system can measure objects that have 96 mm of height. Two vertical positioners were employed to reach the positions, and then, a vernier was employed to calibrate each position. Thence, one should expect that the calibrated positions are not exactly determined because one would surely introduce errors in these conditions. To phase demodulation, 16 fringe patterns were acquired; the large number of fringe patterns was with the aim of reducing the noise. The unwrapped phase was obtained by the line-integration method.

Figure 4.4 draws the changes of phase with respect to the depth. To depict this fact, it was selected five pixels: left-upper corner is P1; right-upper corner is P2; P3 corresponds to the central pixel; left-down corner is P4; and P5 is the right-down one. The plots indicate that these changes can be well explained by a second-order polynomial as described in Section 3.4. In these plots, one also can realize that coefficients $\{K_0, K_1, K_2\}$ are determined for each pixel; refer to Eq. (3.32). In Figure 4.4, one can realize that summing the curves of both channels, P1 with P1, P2 with P2, and so on, the resulting curve tends to be the central one denoted by P3.

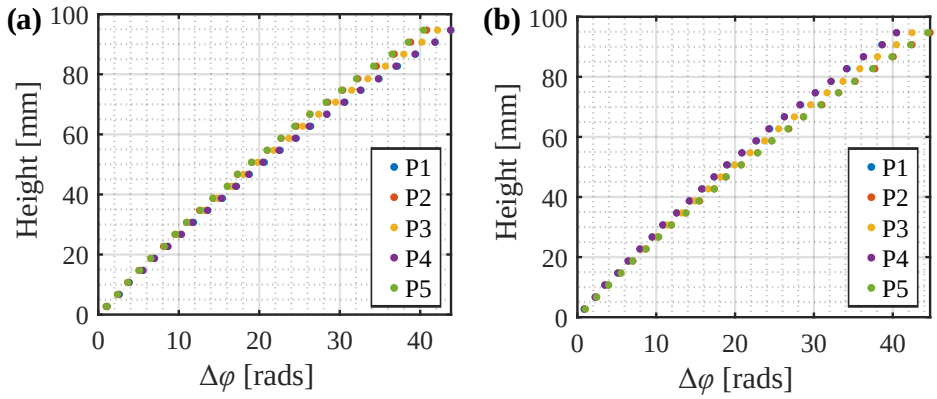

Figure 4.4: Phase differences $\Delta\varphi$ through the height for certain pixels: (a) red channel and (b) blue channel. The description is in the main text.

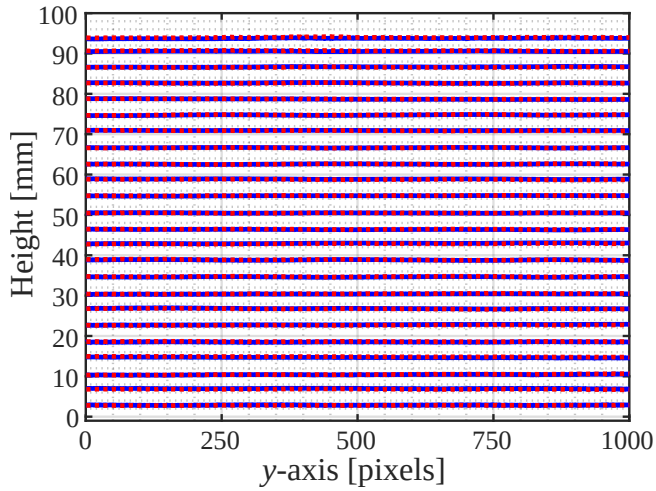

Figure 4.5: Reconstruction of the calibration planes for the blue channel (solid) and red one (dashed). The description is in the main text.

Figure 4.5 shows profiles of the estimation (reconstruction) of each calibration plane. Red-dashed lines correspond to the ones in the red channel, and blue-solid lines to the blue channel. It is noticeable that an insignificant change was introduced for exposition purposes. One can observe that the reconstructed calibration planes were estimated correctly. The residuals' standard deviation (calibrated height minus estimated one) is approximately 0.25 mm, and the residuals' mean is 0.03 mm. Even though the standard deviation is small, one should expect that it increases when employing a small number of fringe patterns.

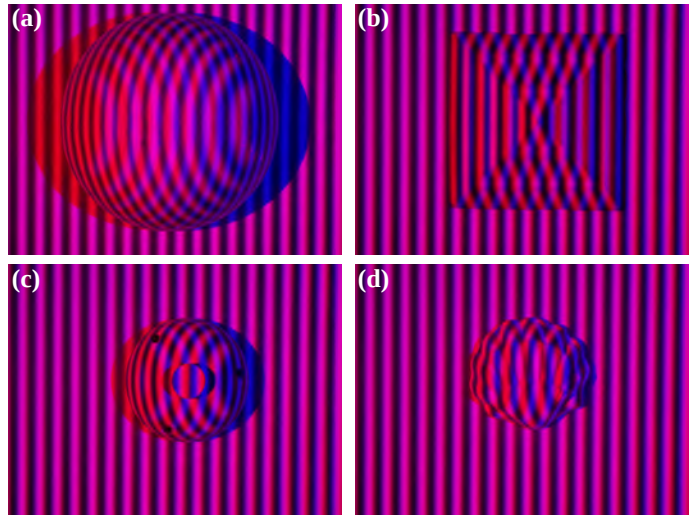

Figure 4.6: Acquired fringe patterns for some testing objects: (a) a polystyrene spherical cap, (b) a step pyramid, a spherical cap plus a cylinder, and (d) a handmade shell.

4.4 Reconstruction of some static objects

Here, some static objects are measured using the co-phase profilometer. To perform these measurements, 16 fringe patterns were projected and acquired for each object. Figure 4.6 shows the first acquired pattern of each object. In this Figure, one can observe that the gamma distortion was compensated successfully.

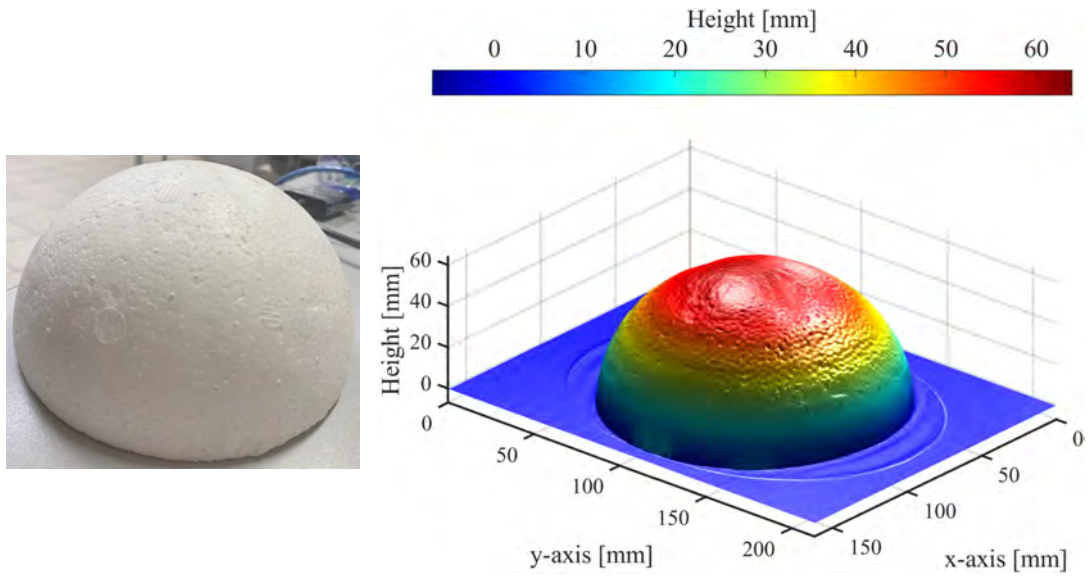

Figure 4.7: Reconstruction of a polystyrene spherical cap. Notice that views are not exactly between the object's pictures and the result of digitalization.

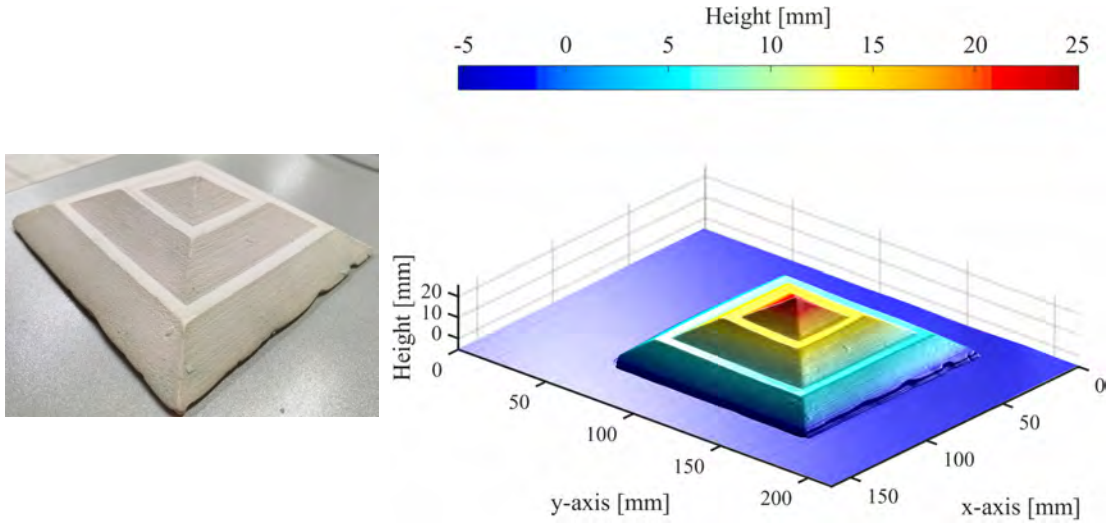

Figure 4.8: Reconstruction of a step pyramid. Notice that views are not exactly between the object's pictures and the result of digitalization.

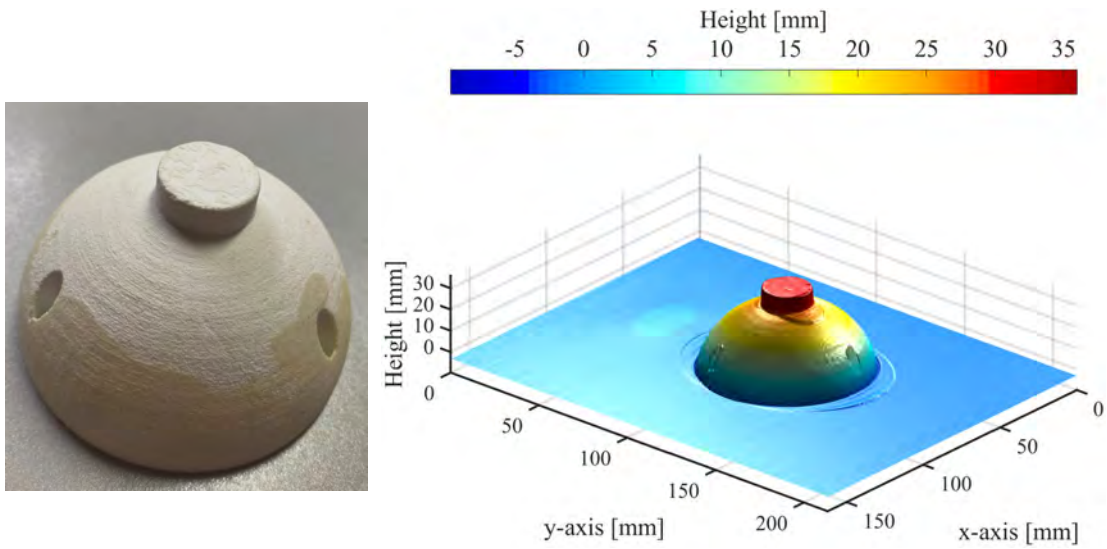

Figure 4.9: Reconstruction of a spherical cap plus a cylinder; one can observe that the reconstruction was wrong. Notice that views are not exactly between the object's pictures and the result of digitalization.

Figures 4.7 – 4.10 depict the reconstruction of the aforementioned solids. One can observe that the first two surfaces, Figs. 4.7 and 4.8, was retrieved correctly, also the last surface was correctly retrieved. However, the third surface, Fig. 4.9, was retrieved incorrectly; this is because the gradient of the surface introduces 2π ambiguities around the edge touching the reference plane. To overcome this issue, one needs to project multiplexed fringe patterns of a least two frequencies: a coarse and a fine measurement; thence, these

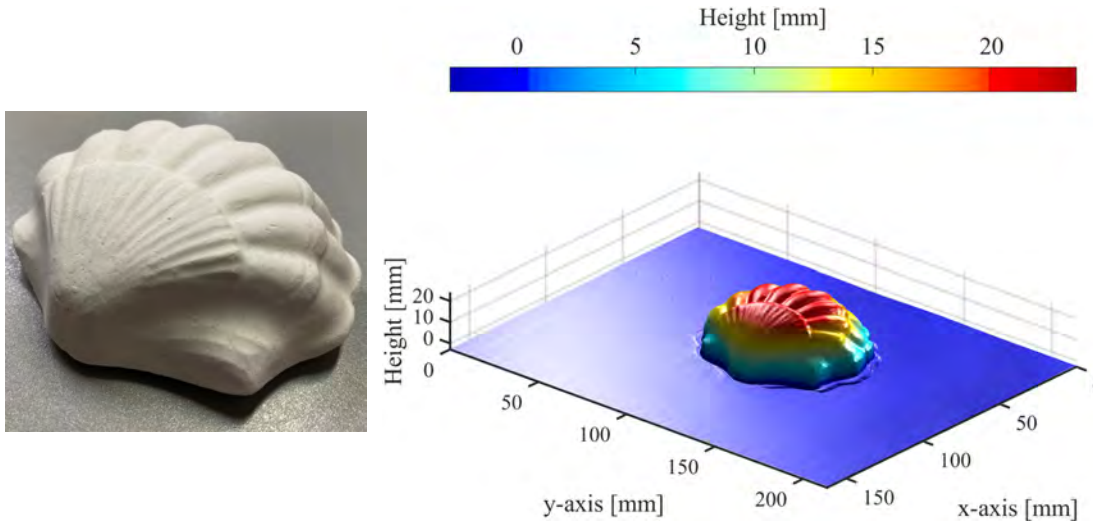

Figure 4.10: Reconstruction of a handmade shell. Notice that views are not exactly between the object's pictures and the result of digitalization.

frequencies together allow one not only to estimate the phase with high accuracy but also neglect the 2π ambiguities. Finally, the last surface was correctly retrieved as shown in Fig. 4.10. We would like to mention that the small ripples observed in Figure 4.7 – 4.10 are due to the projectors' grids, as can be realized in Fig. 4.3. These ripples have a very small amplitude around 0.02 mm, and so they can be neglected.

4.5 Three-dimensional reconstruction of moving objects

This section shows several reconstructions of moving objects using seven fringe patterns as well as nineteen fringe patterns. It is noticeable that one needs at least seven fringe patterns in order to reject the third harmonic using the least-squares phase-shifting algorithm. Therefore, this is the reason why this number was selected. After increasing the number of fringe patterns, I empirically determined that one will always obtain a good phase estimation when phase demodulating 19 fringe patterns. Figures 4.11 – 4.13 depicts such fact. One can observe in Fig. 4.11(a) that the phase estimation will have small rippled distortion because the third harmonic seems to be unrejected completely. Whereas, in Fig. 4.12(a), one can observe a good phase estimation indicating that the third harmonic was rejected completely. This result is comparable with using nineteen fringe patterns 4.12(b). Figure 4.13(a) depicts that the phase was not retrieved correctly; moreover, one should repeat the measurement due to distorting waves' amplitude. Finally, one can realize that the measurements using 19 patterns were all correct.

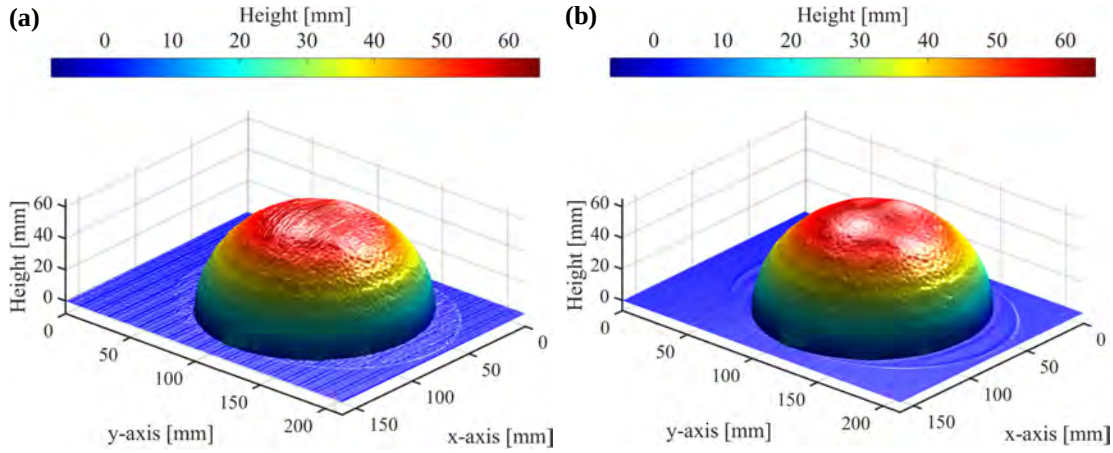

Figure 4.11: Reconstruction the polystyrene spherical cap during moving: acquiring (a) 7 and (b) 19 fringe patterns. One can observe that the first reconstruction has distorting ripples due to third harmonic may not be rejected. Whereas, it was rejected in the second reconstruction.

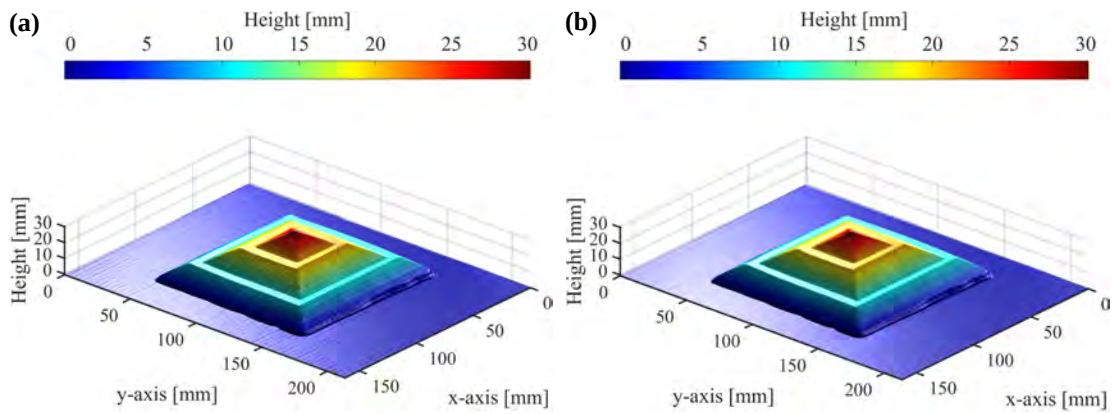

Figure 4.12: Reconstruction the step pyramid during moving: acquiring (a) 7 and (b) 19 fringe patterns. One can see that both reconstructions do not have significantly harmonic distortion; in fact both reconstructions have almost the same quality.

4.6 Three-dimensional inspection of moving objects

This Section depicts several results of the three-dimensional inspection of an object in rectilinear motion. To this end, the concept of phase difference is considered to perform the inspections. Using the result in Eq. (3.7) that can be rewritten as

$$\begin{aligned} H(\omega) &= e^{-i\varphi_{\text{ref}}}[\text{FTF of a non-linear PSA}], \qquad \text{at}(x,y). \\ &= e^{-i\varphi_{\text{ref}}} \sum_{n=0}^{N-1} c_n e^{-i\theta_n \omega/\omega_0}, \qquad \text{at}(x,y). \end{aligned} \tag{4.1}$$

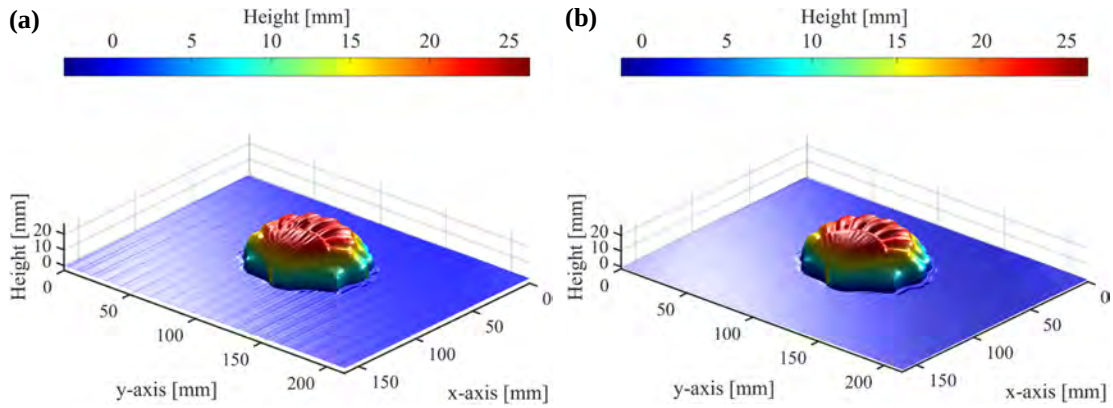

Figure 4.13: Reconstruction of the handmade shell during moving: acquiring (a) 7 and (b) 19 fringe patterns. One can observe that the first reconstruction has ripples distortions due to the same frequency and four times it. These reconstructions do not have the same quality. Whereas the second reconstruction has almost the same quality as the static reconstruction.

Here, The frequency transfer function in Eq. (4.1) is computed using the coefficients in Eqs. (3.57) – (3.61). It is noticeable that this FTF has a phase response equal to zero at $\omega = \omega_0$, so the overall estimation will not have a global phase piston; this fact is important because it would translate into a global shape difference. Moreover, φ_{ref} indicates a reference phase being known previously. Using the phase maps computed in Section 4.4, one has a good estimation of the phase coming from a calibrated object. Although one can map the object's height to phase, utilizing the inverse of Eq. (3.32), one can prefer using a reconstruction in the best conditions.

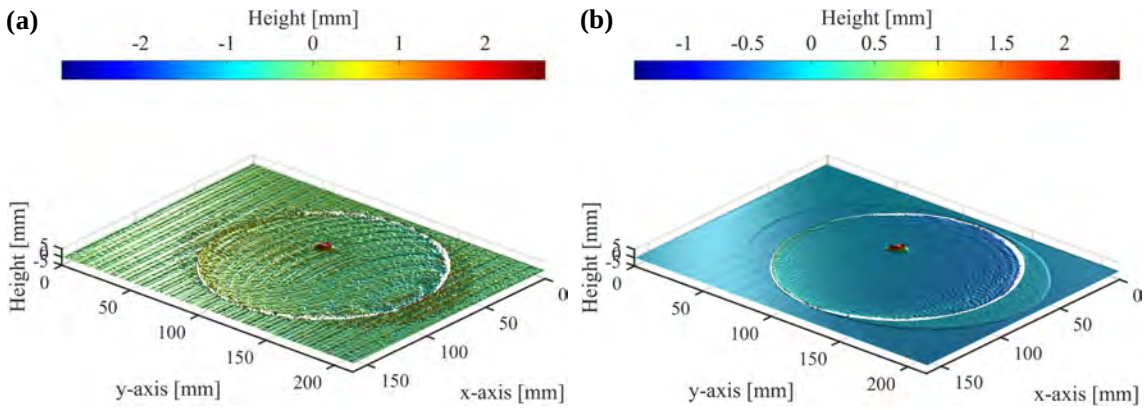

Figure 4.14: Results of the 3D inspection of the polystyrene spherical cap during moving: acquiring (a) 7 and (b) 19 fringe patterns. One can see the first inspection was not correct because the harmonic distortion does not allow seeing the shape deformation clearly. However, the second inspection was correct.

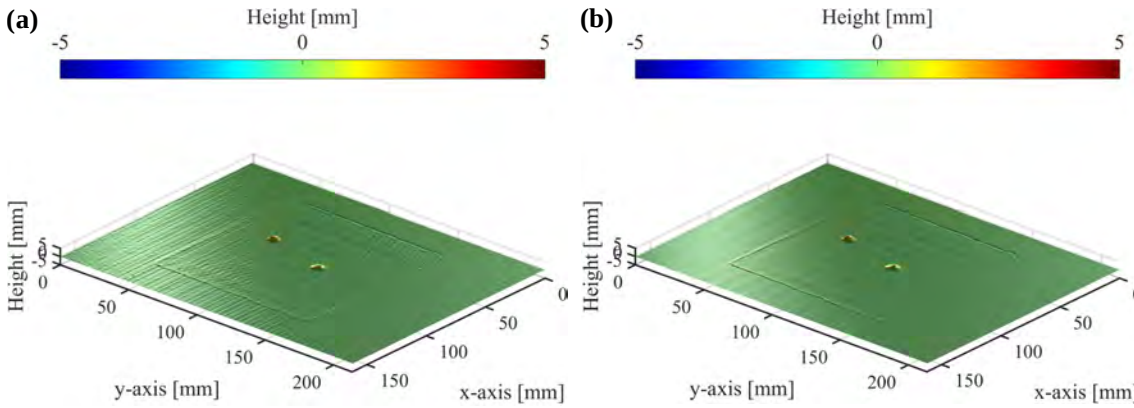

Figure 4.15: Results of the 3D inspection of the step pyramid during moving: acquiring (a) 7 and (b) 19 fringe patterns. One can realize that both inspections were correct, so one can see the clay balls clearly.

As in the previous Section, 3D inspections were performed using 7 and 19 fringe patterns as a consequence of the previous results. With the aim of simulating a small shape defect, several small balls, around 2 mm, were put on the objects; thence, the result of the inspections shall be only the reconstruction of these small clay balls. Figures 4.14 – 4.16 illustrate the obtained results. Figure 4.14(a) depicts the result of inspecting the polystyrene spherical cap with 7 phase shifts.

One can observe that the inspection was wrong because there are several artifacts coming from the phase demodulation procedure. Particularly, the waving distortion does not allow one to identify the shape defect clearly. However, the inspection was correct when acquiring 19 fringe patterns as seen in Fig. 4.14(b); here, one can see clearly the shape defect which amplitude is around 2.3 mm. The inspection of the step pyramid is shown in Fig. 4.15 for 7 (a) and 19 (b) fringe patterns. Here, one can observe that both inspections were correct; the two clay balls had around 2 mm amplitude. We point out that although one may see distorting ripples in Fig. 4.15(a), they have a very small amplitude (< 0.5 mm); therefore, one should neglect them. Finally, Figure 4.16 illustrates the inspection for the handmade shell during a rectilinear motion. One can observe that the inspections do not have the same quality as the first two. The result in Fig. 4.16(a) has distorting waves with amplitude around 1 mm. Whereas, Figure 4.16(b) has error around 0.5 mm. These errors do not come from the phase estimation mainly, but they are generated by small errors in the pixel matching procedure, so one can observe that the errors look like the object's shape. Moreover, shape differences become larger around edges or areas where the gradient does, too. In fact, one should consider that almost all inspections will have this kind of error due to mistakes in the pixel matching procedure.

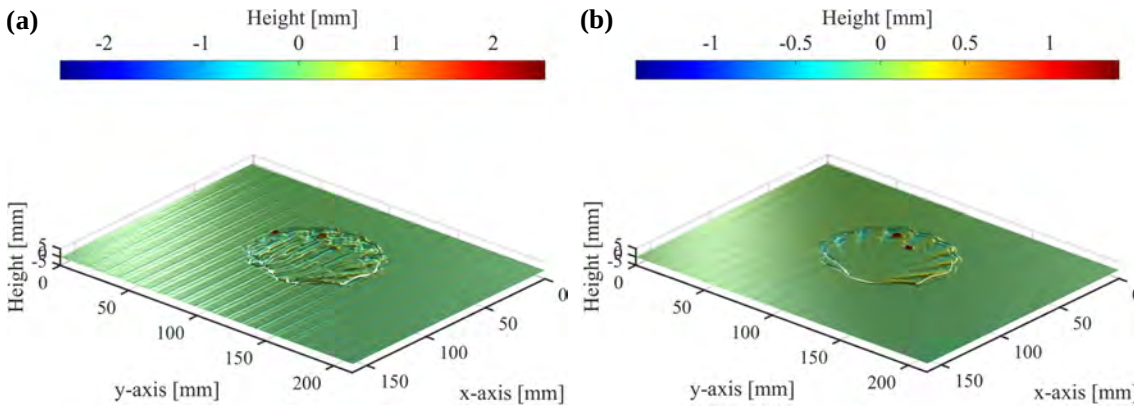

Figure 4.16: Results of the 3D inspection of the handmade shell during moving: acquiring (a) 7 and (b) 19 fringe patterns. One can realize that both inspections were wrong because of height artifacts. These results are incorrect because the pixel matching algorithm failed; one can observe that the shape was not correctly matched translating into shape differences when they were not there.

Chapter 5

Conclusions

In this thesis, we employed the co-phased fringe projection profilometry technique for the three-dimensional (3D) reconstruction of optically diffuse shapes. In particular, we had introduced a new fringe projection technique consisting of simultaneously co-phased projection with color codification. We employed this technique for the 3D reconstruction of static objects and objects in rectilinear motion. In order to retrieve the co-phase map, we have developed and implemented a non-linear phase-shifting algorithm. In this sense, one must translate the object's rectilinear movement into a temporal sequence of phase-shifted fringe patterns utilizing image registration methods.

Furthermore, using the proposed phase-shifting algorithm with especial phase response, the technique is able to estimate the shape differences in an inspection sense. To this end, it was proposed that a reference co-phase map coming from a calibrated shape. The reference co-phased map is utilized to modify the phase response of a phase-shifting algorithm. Whence the computed analytic signal will now have the phase differences, between the testing and the reference co-phase maps. Thereby, this technique should be thought to be a digital null test; thus, the output corresponds to the shape differences. A valuable advantage of this technique lies in avoiding the phase unwrapping procedure when the shape defects are small. This condition is easy to be fulfilled by industrial items in real applications. The phase-unwrapping avoidance can be also observed in shapes with discontinuities; in fact, shape differences would be the only conditions to avoid the phase unwrapping or not. We would like to note that a shape variance around 7 mm will generate a wrap in phase, and so, one must perform a phase unwrapping.

Results suggest that the proposal is suitable for the 3D reconstruction and inspection of objects while being in rectilinear, continuous motion. However, the object's shape shall be smooth because the proposed pixel matching method requires a rough estimation of the phase, using a low-pass filtering process. Albeit the employed components are shaky, the built profilometer can effectively see shape variations around 0.3 mm with a global error piston around 0.5 mm. The latter is because the setup's alignment did not have accuracy in millimeters. For example, vertical distance, the flatness of the reference plane, the accuracy of the calibration position, and others. The built profilometer is able to 3D scan objects having dimensions 210mm along x-axis, 160mm along y-axis, and 96mm

along z-axis.

Derived from this thesis, I published four articles as the first author: *spectral analysis for the generalized least squares phase-shifting algorithms with harmonic robustness* [77]; *windowed generalized phase-shifting algorithms* [93]; *Tukey's robust m-estimator for phase demodulation of interferograms with nonuniform shifts* [119]; and *shape defect measurement by fringe projection profilometry and phase-shifting algorithms* [141]. These works together allow to develop the proposed non-linear phase-shifting algorithm used to phase demodulation. Also, I would like to point out that the proposed technique about *co-phase fringe projection by simultaneously projecting two patterns* has not been published yet. Sections 2.4 and 3.6 briefly describe these papers.

On the other hand, I also have co-authored the seven works: *dynamic 3d shape measurement by iterative phase-shifting algorithms and colored fringe patterns* [31]; *phase shifting schemes: a comparative analysis* [75]; *suppressing ripple distortions and spurious pistons in phase-shifting interferometry* [91, 92]; *phase-stepping algorithms for synchronous demodulation of nonlinear phase-shifted fringes* [113]; *phase measurement of nonuniform phase-shifted interferograms using the frequency transfer function* [114]; and *least-squares gamma estimation in fringe projection profilometry* [168]. These papers support well the idea behind this thesis. Also, Sections 2.4 and 3.6 briefly indicate the contributions to the state-of-the-art derived from these papers.

5.1 Future work

This technique's main weakness resides in obtaining the phase-shifted fringe patterns because of the pixel matching algorithm. So, one can get better results by employing solutions derived from deep learning techniques. Utilizing these techniques, one can reach sub-pixel accuracy when performing the pixel matching. Through deep learning techniques, one could acquire a sequence with more uniformly-space phase shifts. Thus, the phase demodulation will be straighter.

Another improvement would be using temporal multiplexed fringe patterns to scan in different resolutions simultaneously. This technique would allow not only improving the measurement's SNR but also 3D reconstructing shape objects having large discontinuities.

Appendix A

Fourier transform and its properties

The Fourier transform of a function $f(t)$ is given by

$$F(\omega) \stackrel{\text{def}}{=} \int_{-\infty}^{\infty} f(t)e^{-i\omega t}dt \tag{A.1}$$

where $\omega = 2\pi f$ and $i = \sqrt{-1}$. The inverse Fourier transform is defined as

$$f(t) \stackrel{\text{def}}{=} \frac{1}{2\pi} \int_{-\infty}^{\infty} F(\omega)e^{i\omega t}d\omega. \tag{A.2}$$

The associate operators of the Fourier transform and its inverse are $\mathcal{F}\{\bullet\}$ and $\mathcal{F}^{-1}\{\bullet\}$, respectively.

Properties

Some common properties of the Fourier transform are:

1. Linearity: let a, b be scalars, then

$$\mathcal{F}\{af(t) + bg(t)\} = aF(\omega) + bG(\omega). \tag{A.3}$$

2. Time shift:

$$\mathcal{F}\{f(t - t_0)\} = F(\omega)e^{it_0\omega}. \tag{A.4}$$

3. Frequency shift:

$$\mathcal{F}\{F(\omega - \omega_0)\} = f(t)e^{-i\omega_0 t}. \tag{A.5}$$

4. Time reversal:

$$\mathcal{F}\{f(-t)\} = F(-\omega). \tag{A.6}$$

5. Time scaling: let a be a scalar, then

$$\mathcal{F}\{f(at)\} = \frac{1}{|a|} F\left(\frac{\omega}{a}\right). \tag{A.7}$$

6. Complex conjugation:

$$\mathcal{F}\{f^*(t)\} = F^*(-\omega). \tag{A.8}$$

7. Convolution theorem:

$$\mathcal{F}\{f(t) \circledast g(t)\} = F(\omega)G(\omega). \tag{A.9}$$

8. Correlation:

$$\mathcal{F}\{f(t) \star g(t)\} = \mathcal{F}\{f(t) \circledast g(-t)\} = F(\omega)G(-\omega). \tag{A.10}$$

Fourier transform of a sequence of sampled data

Let $h(t)$ be a continuous function, then it can be sampled by

$$f(t) = h(t) \sum_{n=-\infty}^{\infty} \delta(t - n\tau) = \sum_{n=-\infty}^{\infty} h(n\tau)\delta(t - n\tau). \tag{A.11}$$

where τ is the sampling period. Taking its Fourier transform, one has

$$\begin{aligned} F(\omega) &= \int_{-\infty}^{\infty} f(t)e^{-i\omega t}dt = \int_{-\infty}^{\infty} \left[\sum_{n=-\infty}^{\infty} h(n\tau)\delta(t - n\tau)\right] e^{-i\omega t}dt \\ &= \sum_{n=-\infty}^{\infty} h(n\tau) \int_{-\infty}^{\infty} \delta(t - n\tau)e^{-i\omega t}dt \\ &= \sum_{n=-\infty}^{\infty} h(n\tau)e^{-in\tau\omega t} \\ F(\omega) &= \sum_{n=-\infty}^{\infty} h_n e^{-in\omega t} \end{aligned} \tag{A.12}$$

where $h_n = h(n\tau)$. The formula in Eq. (A.12) is called *Discrete-time Fourier transform*. It is noticeable that $F(\omega)$ is continuous and has 2π-periodicity; this is $F(\omega) = F(\omega \pm n2\pi)$ for any integer n.

Appendix B

Dirac delta function and its properties

This function can be define as a metric by

$$\int_{-\infty}^{\infty} f(t)\delta(t)dt = f(0). \tag{B.1}$$

and also it satisfies that

$$\int_{-\infty}^{\infty} \delta(t)dt = 1. \tag{B.2}$$

Properties

1. Sampling: let τ be the sampling period, then

$$f(t)\sum_{n=-\infty}^{\infty}\delta(t-n\tau) = \sum_{n=-\infty}^{\infty} f(n\tau)\delta(t-n\tau). \tag{B.3}$$

2. Time scaling:

$$\delta(at) = \frac{1}{|a|}\delta(t) \tag{B.4}$$

3. Shifting property

$$f(t) \circledast \delta(t-t_0) = f(t-t_0) \tag{B.5}$$

4. Time reversal (even function):

$$\delta(-t) = \delta(t). \tag{B.6}$$

5. Generalization of n-dimensional

$$\delta(t,u,v,\dots) = \delta(t)\delta(u)\delta(v)\cdots. \tag{B.7}$$

6. Fourier transform:

$$\mathcal{F}\{\delta(t-t_0)\} = e^{it_0\omega} \tag{B.8}$$

Appendix C

Linear least squares optimization

The main idea behind optimization using the least squares method consists of solving an over-determined system of linear equations so that the sum of the squared residuals is the minimum. Thereby, this optimization problem is defined as

$$\mathbf{x}^{+} = \underset{\mathbf{x}}{\operatorname{argmin}} \|\mathbf{r}\|_2^2 \,; \tag{C.1}$$

where $\mathbf{x}^{+}$ is the optimal solution in the least squares sense, $\|\bullet\|_2$ is the Euclidean norm, the vector of residual is given by

$$\mathbf{r} = \mathbf{b} - \mathbf{A}\mathbf{x}; \tag{C.2}$$

then, one can reformulated the optimization problem as

$$\mathbf{x}^{+} = \underset{\mathbf{x}}{\operatorname{argmin}} \|\mathbf{b} - \mathbf{A}\mathbf{x}\|_2^2 \,. \tag{C.3}$$

Here $\mathbf{A} \in \mathbb{R}^{m \times n}$ is the matrix of coefficients, $\mathbf{x} \in \mathbb{R}^n$ corresponds to the vector of unknown variables, $\mathbf{b} \in \mathbb{R}^m$ is the vector of observations, and $\mathbf{r} \in \mathbb{R}^m$. When one has that the number of equations is equal or greater than the number of unknown variables, i.e. $m \geq n$; this case is called an overdetermined system.

Based on equations (C.1) – (C.3), we can expand the squared of the residuals as following

$$\begin{aligned} \|\mathbf{r}\|_2^2 &= \mathbf{r}^{\mathrm{T}}\mathbf{r} \\ &= (\mathbf{b} - \mathbf{A}\mathbf{x})^{\mathrm{T}} (\mathbf{b} - \mathbf{A}\mathbf{x}) \\ &= \left(\mathbf{b}^{\mathrm{T}} - \mathbf{A}^{\mathrm{T}}\mathbf{x}^{\mathrm{T}}\right) (\mathbf{b} - \mathbf{A}\mathbf{x}) \\ &= \mathbf{b}^{\mathrm{T}}\mathbf{b} - \mathbf{b}^{\mathrm{T}}\mathbf{A}\mathbf{x} - \mathbf{x}^{\mathrm{T}}\mathbf{A}^{\mathrm{T}}\mathbf{b} + \mathbf{x}^{\mathrm{T}}\mathbf{A}^{\mathrm{T}}\mathbf{A}\mathbf{x}, \end{aligned}$$

where T indicates transpose operation, and the next scalars fulfill that $\mathbf{b}^{\mathrm{T}}\mathbf{A}\mathbf{x} = \mathbf{x}^{\mathrm{T}}\mathbf{A}^{\mathrm{T}}\mathbf{b} = \left(\mathbf{b}^{\mathrm{T}}\mathbf{A}\mathbf{x}\right)^{\mathrm{T}}$; thus, one obtains that

$$\|\mathbf{r}\|_2^2 = \mathbf{b}^{\mathrm{T}}\mathbf{b} - 2\mathbf{x}^{\mathrm{T}}\mathbf{A}^{\mathrm{T}}\mathbf{b} + \mathbf{x}\mathbf{A}^{\mathrm{T}}\mathbf{A}^{\mathrm{T}}\mathbf{x}. \tag{C.4}$$

To find the optimal value $\mathbf{x}^+$ so that minimizes Eq. (C.4), a necessary condition is to equate the gradient of $\|\mathbf{r}\|_2^2$ with respect to $\mathbf{x}$ to zero;

$$\nabla_{\mathbf{x}} \|\mathbf{r}\|_2^2 = 2\mathbf{A}^{\mathrm{T}}\mathbf{A}\mathbf{x} - 2\mathbf{A}^{\mathrm{T}}\mathbf{b} = \mathbf{0}. \tag{C.5}$$

From Eq. (C.5), we obtain the *system of normal equations* given by

$$\mathbf{A}^{\mathrm{T}}\mathbf{A}\mathbf{x}^+ = \mathbf{A}^{\mathrm{T}}\mathbf{b} \tag{C.6}$$

$$\therefore \mathbf{x}^+ = \left(\mathbf{A}^{\mathrm{T}}\mathbf{A}\right)^{-1}\mathbf{A}^{\mathrm{T}}\mathbf{b} = \mathbf{A}^{\dagger}\mathbf{b} \tag{C.7}$$

where $\mathbf{A}^{\dagger}$ is called the Moore-Penrose pseudoinverse. The system of normal equations has the no trivial solution provided that matrix $\mathbf{A}$ has full rank, implying that $\mathbf{A}^{\mathrm{T}}\mathbf{A}$ is a non-singular square matrix and positive defined.

Proof: matrix $\mathbf{A}$ is full rank. If $\mathbf{A}$ is full rank, this implies that $\mathbf{A}^{\mathrm{T}}\mathbf{A}$ is non singular. Supposing that $\mathbf{A}^{\mathrm{T}}\mathbf{A}$ is singular, then it is rank deficient; this implies that for a $\mathbf{x} \neq \mathbf{0}$, it is accomplished that $\mathbf{A}^{\mathrm{T}}\mathbf{A}\mathbf{x} = \mathbf{x}^{\mathrm{T}}\mathbf{A}^{\mathrm{T}}\mathbf{A}\mathbf{x} = \mathbf{0}$, and thence, $\|\mathbf{A}\mathbf{x}\|_2^2 = 0$. Thus, matrix $\mathbf{A}$ must be singular and rank deficient. Furthermore, because $\mathbf{A}^{\mathrm{T}}\mathbf{A}$ is non-singular, it is fulfilled that $\mathbf{x}^{\mathrm{T}}\mathbf{A}^{\mathrm{T}}\mathbf{A}\mathbf{x} = \|\mathbf{A}\mathbf{x}\|_2^2 > 0$; and therefore, $\mathbf{A}^{\mathrm{T}}\mathbf{A}$ shall be positive defined. □

I now provide some analysis about the previous mathematical development. First, defining the column space of matrix $\mathbf{A}$ as following

$$\mathcal{R}(\mathbf{A}) \stackrel{\text{def}}{=} \{\mathbf{z} = \mathbf{A}\mathbf{y} \mid \mathbf{y} \in \mathbb{R}^n\}, \quad \mathcal{R}(\mathbf{A}) \subset \mathbb{R}^m; \tag{C.8}$$

as well as the null space of matrix $\mathbf{A}^{\mathrm{T}}$ is defined as

$$\mathcal{N}\left(\mathbf{A}^{\mathrm{T}}\right) \stackrel{\text{def}}{=} \left\{\mathbf{w} \in \mathbb{R}^m \mid \mathbf{A}^{\mathrm{T}}\mathbf{w} = \mathbf{0}\right\}, \quad \mathcal{N}\left(\mathbf{A}^{\mathrm{T}}\right) \subset \mathbb{R}^m. \tag{C.9}$$

It is worth mentioning that $\mathcal{N}\left(\mathbf{A}^{\mathrm{T}}\right)$ is the orthogonal complement of $\mathcal{R}(\mathbf{A})$ in $\mathbb{R}^m$. Figure C.1 draws a geometric interpretation of the least squares problem when one is estimating two parameters, and so the vector of observations has three dimensions. It is noticeable that $\mathbf{r} \in \mathcal{N}\left(\mathbf{A}^{\mathrm{T}}\right)$ and $\mathbf{b} \notin \mathcal{R}(\mathbf{A})$; and so $\mathbf{A}\mathbf{x}^+ \perp \mathbf{r}$. Then, one is able to say that

$$\mathbf{A}\mathbf{x}^+ = \mathbf{A}\left(\mathbf{A}^{\mathrm{T}}\mathbf{A}\right)^{-1}\mathbf{A}^{\mathrm{T}}\mathbf{b} = \mathbf{A}\mathbf{A}^{\dagger}\mathbf{b}; \tag{C.10}$$

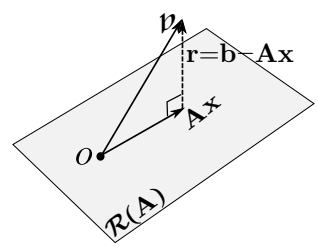

Figure C.1: Schematic representation of the least squares problem when estimating two parameters.

in other words, $\mathbf{A}\mathbf{x}^{+}$ is the orthogonal projection of $\mathbf{b}$ onto $\mathcal{R}(\mathbf{A})$. The orthogonal projector is defined as

$$\mathbf{H} \stackrel{\text{def}}{=} \mathbf{A}\left(\mathbf{A}^{\mathrm{T}}\mathbf{A}\right)^{-1}\mathbf{A}^{\mathrm{T}}, \tag{C.11}$$

which is commonly called the hat matrix. Hence, we can state the residuals of the least squares fitting in terms of the hat matrix as

$$\mathbf{r}_{\mathrm{ls}} \stackrel{\text{def}}{=} \mathbf{b} - \mathbf{H}\mathbf{x}^{+}, \tag{C.12}$$

and the least-squares fit to the vector of observations as

$$\hat{\mathbf{b}}_{\mathrm{ls}} \stackrel{\text{def}}{=} \mathbf{H}\mathbf{x}^{+}. \tag{C.13}$$

This last equation is very important for phase-shifting algorithm based on the least squares method because $\hat{\mathbf{b}}_{\mathrm{ls}}$ corresponds to the intensity value estimated for the algorithm, and so, one can measure the error between the fitted intensity and the acquired one.

Appendix D

Published articles

Research Article | Vol. 26, No. 10 | 14 May 2018 | OPTICS EXPRESS 12403
Optics EXPRESS

Dynamic 3D shape measurement by iterative phase shifting algorithms and colored fringe patterns

JORGE L. FLORES,[1] MARIJA STRONIK,[2,*] ANTONIO MUÑOZ,[3] G. GARCIA-TORALES,[1] SOTERO ORDOÑES,[2] AND ADÁN CRUZ[1]

[1]*Electronic Engineering Department, University of Guadalajara, Av. Revolución 1500, Guadalajara, Jalisco, Mexico*
[2]*Optical Research Center, Loma del Bosque 115, León, C.P. 37150, Guanajuato, Mexico*
[3]*Engineering Department, University of Guadalajara, Av. Independencia Nacional 151, Autlán, Jalisco, Mexico*
[*]*mstrojik@gmail.com*

Abstract: In this work, we propose a novel technique to retrieve 3D shape of dynamic objects by the simultaneous projection of a fringe pattern and a homogeneous white light pattern, both coded in an RGB image. The first one is used to retrieve the phase map by an iterative least-squares method. The second one is used to match object pixels in consecutive images, acquired at various object positions. The proposed method successfully accomplishes the requirement of projecting simultaneously two different patterns. One extracts the object's information while the other retrieves the phase map. Experimental results demonstrate the feasibility of the proposed scheme.

OCIS codes: (120.0120) Instrumentation, measurement, and metrology; (120.2650) Fringe analysis; (100.5070) Phase retrieval.

References and links

1. X. Xu, Y. Cao, C. Chen, and Y. Wan, "On-line phase measuring profilometry based on phase matching," Opt. Quantum Electron. **48**(8), 411 (2016).
2. K. Harding, "3D profilometry: next requests from the industrial viewpoint," Proc. SPIE **7855**, 785513 (2010).
3. S. S. Gorthi and P. Rastogi, "Fringe projection techniques: whither we are?" Opt. Lasers Eng. **48**(2), 133–140 (2010).
4. K. Zhong, Z. Li, X. Zhou, Y. Li, Y. Shi, and C. Wang, "Enhanced phase measurement profilometry for industrial 3D inspection automation," Int. J. Adv. Manuf. Technol. **76**(9–12), 1563–1574 (2015).
5. B. Li, Z. Liu, and S. Zhang, "Motion-induced error reduction by combining Fourier transform profilometry with phase-shifting profilometry," Opt. Express **24**(20), 23289–23303 (2016).
6. L. Lu, J. Xi, Y. Yu, and Q. Guo, "Improving the accuracy performance of phase-shifting profilometry for the measurement of objects in motion," Opt. Lett. **39**(23), 6715–6718 (2014).
7. L. Lu, J. Xi, Y. Yu, and Q. Guo, "New approach to improve the accuracy of 3-D shape measurement of moving object using phase shifting profilometry," Opt. Express **21**(25), 30610–30622 (2013).
8. Z. Chen, X. Wang, and R. Liang, "Snapshot phase shift fringe projection 3D surface measurement," Opt. Express **23**(2), 667–673 (2015).
9. X. Su and W. Chen, "Fourier transform profilometry: a review," Opt. Lasers Eng. **35**(5), 263–284 (2001).
10. S. Zhang, D. Van Der Weide, and J. Oliver, "Superfast phase-shifting method for 3-D shape measurement," Opt. Express **18**(9), 9684–9689 (2010).
11. L. Lu, J. Xi, Y. Yu, and Q. Guo, "New approach to improve the accuracy of 3-D shape measurement of moving object using phase shifting profilometry," Opt. Express **21**(25), 30610–30622 (2013).
12. K. Peng, Y. Cao, Y. Wu, and M. Lu, "A new method using orthogonal two-frequency grating in online 3D measurement," Opt. Laser Technol. **83**, 81–88 (2016).
13. K. Peng, Y. Cao, Y. Wu, C. Chen, and Y. Wan, "A dual-frequency online PMP method with phase-shifting parallel to moving direction of measured object," Opt. Commun. **383**, 491–499 (2017).
14. C. Chen, Y. P. Cao, L. J. Zhong, and K. Peng, "An on-line phase measuring profilometry for objects moving with straight-line motion," Opt. Commun. **336**, 301–305 (2015).
15. K. Peng, Y. Cao, Y. Wu, and Y. Xiao, "A new pixel matching method using the modulation of shadow areas in online 3D measurement," Opt. Lasers Eng. **51**(9), 1078–1084 (2013).
16. H. Guo and Z. Zhang, "Phase shift estimation from variances of fringe pattern differences," Appl. Opt. **52**(26), 6572–6578 (2013).

#317912 https://doi.org/10.1364/OE.26.012403
Journal © 2018 Received 18 Dec 2017; revised 26 Feb 2018; accepted 19 Mar 2018; published 1 May 2018

ACTA UNIVERSITARIA
Multidisciplinary Scientific Journal

| VOLUMEN 29 | 2019 |
ISSN online 2007-9621
http://doi.org/10.15174/au.2019.2627

Esquemas de corrimiento de fase: estudio comparativo

Phase shifting schemes: comparative analysis

Antonio Muñoz[1*], Sotero Ordoñes[2], Jorge L. Flores[3], Omar Aguilar[1], Abimael Jimenez[4]
[1] Departamento de Ingenierías, Universidad de Guadalajara, Av. Independencia Nacional 151, Autlán, Jalisco, México, C.P. 48900.
[2] Centro de Investigaciones en Óptica A.C.
[3] Departamento de Ingeniería en Electrónica, Universidad de Guadalajara.
[4] Departamento de Electrónica y Computación, Universidad Autónoma de Ciudad Juárez.
*Autor de correspondencia: jose.munoz@cucsur.udg.mx

Resumen

La interferometría por corrimiento de fase es una técnica bien establecida para mediciones de fase, la cual requiere de una serie de patrones de franjas corridos en fase. En este trabajo, se analizan dos algoritmos de corrimiento de fase, los cuales se han usado para la recuperación de fase cuando se considera que los corrimientos de fase tienen error de calibración. El primer esquema analizado fue el algoritmo iterativo avanzado (AIA) y el segundo método es un esquema basado en el método de Levenberg-Marquardt (LM). Con el objetivo de mostrar su rendimiento, los evaluamos usando datos sintéticos y tomando en cuenta la exactitud, el orden de convergencia, así como el error por desentonamiento en los pasos. Los resultados muestran que ambos métodos reducen el error linealmente respecto al número de patrones de franjas; sin embargo, el esquema AIA tiene un desempeño significativamente mejor tanto en precisión como en tiempo de procesamiento. Este estudio arroja luz sobre las ventajas y desventajas de uso de las soluciones lineal y no lineal para la demodulación de patrones de franjas.

Palabras clave: Metrología óptica; recuperación de fase; mínimos cuadrados; Levenberg-Marquardt.

Abstract

Phase shifting is a well-established technique for phase measurements in interferometry and 3D profiling, which requires at least three sinusoidal intensity patterns with certain phase-shifts. In this paper, two phase-shifting schemes are analyzed, which have been used to minimize absolute phase errors due to the phase-shift error. The first one is the advance iterative algorithm (AIA) and the second is based on the Levenberg-Marquardt method (LM). In order to show their performance, these schemes are evaluated using synthetic data and taking into account the numerical accuracy, the order of convergence, and the detuning error. The results show that both methods reduce the phase error linearly; however, the AIA scheme significantly improves the accuracy and reduces the processing time. This work sheds light to the advantages and disadvantages of using the linear and non-linear solutions.

Keywords: Optical metrology; phase retrieval; least-squares; Levenberg-Marquardt.

Recibido: 30 de julio de 2019 Aceptado: 30 de octubre de 2019 Publicado: 11 de diciembre de 2019

Como citar: Muñoz, A., Ordoñes, S., Flores, J. L., Aguilar, O., & Jimenez, A. (2019). Esquemas de corrimiento de fase: estudio comparativo Phase shifting schemes: comparative analysis. *Acta Universitaria 29*, e2627. doi. http://doi.org/10.15174.au.2019.2627

Research Article | Vol. 27, No. 4 | 18 Feb 2019 | OPTICS EXPRESS 5824
Optics EXPRESS

Phase-stepping algorithms for synchronous demodulation of nonlinear phase-shifted fringes

MANUEL SERVIN,* MOISES PADILLA, IVAN CHOQUE, AND SOTERO ORDONES

Centro de Investigaciones en Optica A.C., Loma del Bosque 115, Lomas del Campestre, 37000 Leon Guanajuato, Mexico
**mservin@cio.mx*

Abstract: In optical metrology synchronous phase-stepping algorithms (PSAs) estimate the measured phase of temporal linear-carrier fringes with respect to a linear-reference. Linear-carrier fringes are normally obtained using closed-loop, feedback, optical phase-stepped devices. On the other hand, open-loop phase-stepping devices usually give fringe patterns with nonlinear phase steps. The Fourier spectrum of linear-carrier fringes is composed of Dirac deltas only. In contrast, nonlinear phase-shifted fringes are wideband, spread-spectrum signals. It is well known that using linear-phase reference PSA to demodulate nonlinear phase stepped fringes, one obtains a spurious-piston. The problem with this spurious-piston is that it may wrongly be interpreted as a real thickness in any absolute phase measurement. Here we mathematically find the origin of this spurious-piston and design nonlinear phase-stepping PSAs to cope with nonlinear phase-stepping interferometric fringes. We give a general theory to tailor nonlinear phase-stepping PSAs to synchronously demodulate nonlinear phase-stepped wideband fringes.

1. Introduction

Linear reference phase-shifting algorithms (PSAs) have been used in optical metrology to demodulate linear-carrier temporal fringes since the pioneering work by Bruning et al. [1–3]. To generate linear phase-shifting fringes one normally uses well-calibrated optical phase-shifters. However in practice the phase shifters may drift from its nominal phase step producing wideband, spread-spectrum fringes [4,5]. In these cases the PSA must also be wideband to deal with nonuniform/nonlinear phase-shifted fringes [6–13]. Hibino et al. indicated that an spurious piston appears in the estimated phase when a linear-reference PSA is used to demodulate non-uniform phase-shifted fringes [6–13]. This spurious-piston is a numeric artifact of the linear-reference PSA, which may be wrongly interpreted as physical optical thickness [6–13]. Real optical thickness measuring is fundamental when testing optical material slabs in semiconductor and display equipment [6–13]. Many systematic errors in linear-carrier fringes (such as phase-shift miscalibration, fringe harmonics, experiment vibrations) have been attenuated using linear-reference PSAs [2,3]. For precision thickness measurement, and nonlinear phase-shifted fringes, linear-reference PSAs with no spurious-piston have been proposed [6–13]. Recently, Kim and Hibino have pointed-out that this numerical/spurious piston has received little attention because it does not give a waving profiling error (such as detuning or harmonic distortion) when an optical surface is profiled [10–13]. However, when the central interest is to measure absolute optical thickness of transparent slabs by wavelength tuning (for example), this numerical/spurious piston translates into errors in thickness [6–13]. This error is given by the product of the demodulated phase and the synthetic wavelength, which is much greater than the wavelength used [13]. Linear-reference PSAs for demodulating wideband, nonlinear-carrier fringes have

#338205 https://doi.org/10.1364/OE.27.005824
Journal © 2019 Received 9 Jul 2018; revised 20 Sep 2018; accepted 24 Sep 2018; published 15 Feb 2019

Optics Letters

Spectral analysis for the generalized least squares phase-shifting algorithms with harmonic robustness

Sotero Ordones,[1] Manuel Servin,[1,*] Moises Padilla,[1] Antonio Muñoz,[2] Jorge L. Flores,[3] and Ivan Choque[1]

[1]Centro de investigaciones en Optica A.C. Loma del Bosque 115, Lomas del Campestre, C.P. 37150 Leon, Guanajuato, Mexico
[2]Departamento de Ingenierias, Universidad de Guadalajara, Av. Independencia Nacional 151, C.P. 48900, Autlan, Jalisco, Mexico
[3]Departamento de Electronica, Universidad de Guadalajara, Av. Revolucion 1500, C.P. 44840, Guadalajara, Jalisco, Mexico
*Corresponding author: mservin@cio.mx

Received 4 March 2019; revised 1 April 2019; accepted 11 April 2019; posted 11 April 2019 (Doc. ID 361455); published 30 April 2019

We introduce the frequency transfer function (FTF) formalism for generalized least squares phase-shifting algorithms (GLS-PSAs), whose phase shifts are nonuniformly spaced. The GLS-PSA's impulsive response is found by computing the Moore–Penrose pseudoinverse. FTF theory allows analyzing these GLS-PSAs spectrally, as well as easily finding figures of merit such as signal-to-noise ratio (SNR) and harmonic rejection capabilities. We show simulations depicting that the SNR slightly decreases as the harmonic rejection robustness improves.

https://doi.org/10.1364/OL.44.002358

Phase-shifting interferometry (PSI) is a well-known technique for phase retrieval in optical interferometry, which is employed in optical testing and measuring physical features such as shape, stress, strain, etc. [1,2]. PSI consists of capturing a time sequence of fringe patterns, which are phase-demodulated by a phase-shifting algorithm (PSA) [3]. For phase demodulation, several PSAs based on the least squares (LS) method have been proposed due to their simplicity and high signal-to-noise ratio (SNR) [3]. The PSA having the highest SNR has been proposed by Bruning *et al.* [4]. This PSA is based on a linear LS fitting to a temporal sinusoidal signal under the assumption of equispaced phase shifts of $2\pi/N$, with N being the number of steps [5].

However, in practice, phase shifters may lead to systematic errors in the phase shifts due to miscalibration, nonlinearity, and hysteresis [2,6], thus rendering one unable to guarantee that fringe patterns have uniformly spaced phase shifts, except in digital fringe projection; hence, phase shifts should be considered to be nonuniformly spaced. Moreover, when a uniform PSA phase demodulates fringe patterns that have nonuniformly spaced phase shifts, the retrieved phase map will have detuning-like distortion [3]. To reduce this distortion, several PSAs have been proposed with error correction or self-tuning capabilities, as well as several PSAs taking into account nonuniformly spaced phase shifts (generalized PSAs) [3]. In particular, the interest in generalized LS (GLS)-PSAs has increased [7–26] because SNR gain is maximized.

In this sense, Greivenkamp proposed retrieving the phase map through a linear LS fitting to a sinusoidal signal for nonuniformly spaced phase shifts [7]. This PSA has been employed in applications [8,21] and to design nonlinear PSAs [9,19–26]. These nonlinear PSAs are based on the Greivenkamp's algorithm plus a phase-shift estimator: LS fitting to an ellipse [19], LS fitting to the spatial sinusoidal signal [20–26], using the windowed Fourier transform [9], or estimating the signal parameters by rotational invariance techniques [10]. In fact, the last PSA [10] is similar to the one based on principal components analysis [11,12]. Parallelly, Ohyama *et al.* proposed a PSA equivalent to the Greivenkamp's, where the authors used complex exponentials instead of the sinusoidal formulation [13]. On the other hand, Servin *et al.* recently proposed designing generalized PSAs that have an *ad hoc* harmonic rejection response via the frequency transfer function (FTF) formalism [27]. However, Servin's generalized PSA has low SNR gain because the number of rejected harmonics is equal to the number of fringe patterns.

Although the PSAs in [7–26] have been widely cited in the literature, those proposals do not provide any analytic formula to estimate SNR or rejected harmonics, as FTF formalism does [27].

In this Letter, we introduce the FTF formalism for the GLS-PSA with harmonic rejection. We assume that the temporal signal rigorously tracks a continuous-time sinusoidal function, and that the phase steps were accurately estimated. A continuous-time fringe having harmonic contribution can be described as

$$I(x,y,t) = a(x,y) + \sum_{k=1}^{\infty} b_k(x,y)\cos k[\varphi(x,y) - \omega_0 t]; \qquad t \in \mathbb{R}, \tag{1}$$

where $a(x,y)$ is the background intensity, k and K are the index and number of harmonics, respectively, while $b_k(x,y)$ denotes the intensity modulation of the kth harmonic, $\varphi(x,y)$ corresponds to the desired phase, and ω_0 is the angular frequency. The temporal Fourier transform of the continuous-time fringe is

Research Article Vol. 58, No. 15 / 20 May 2019 / Applied Optics 4157

applied optics

Phase measurement of nonuniform phase-shifted interferograms using the frequency transfer function

IVAN CHOQUE,[1] MANUEL SERVIN,[1,*] MOISES PADILLA,[1] MIGUEL ASMAD,[2] AND SOTERO ORDONES[1]

[1]Centro de Investigaciones en Optica A.C., Lomas del Bosque 115, Lomas del Campestre, CP 37150, Leon, Guanajuato, Mexico
[2]Pontificia Universidad Catolica del Peru, Av. Universitaria 1801, San Miguel, Lima 32, Peru
*Corresponding author: mservin@cio.mx

Received 25 February 2019; revised 25 April 2019; accepted 25 April 2019; posted 26 April 2019 (Doc. ID 360789); published 20 May 2019

In this paper, we propose a phase measurement method for interferograms with nonuniform phase shifts. First, we measure the phase shifts between consecutive interferograms. Second, we use these values to modify the spectrum of the interferogram data. Then, by analyzing this spectrum, we design a suitable phase-shifting algorithm (PSA) using the frequency transfer function formalism. Finally, we test our PSA with experimental data to estimate the surface of an aluminum thin film. Our result is better than those obtained using the Fourier transform method, the principal component analysis method, and the least-squares PSA.

https://doi.org/10.1364/AO.58.004157

1. INTRODUCTION

Phase shifting is a powerful technique for phase demodulation in optical metrology. Phase-shifting demodulation requires at least three interferograms with known relative phase steps in order to solve for the searched phase map, proportional to the phenomenon under study [1]. Ideally, the phase steps are linearly and uniformly distributed within a fringe period. In practice, however, they often deviate significantly from their nominal value resulting in nonuniform phase steps or phase-step errors [1–4]. Assuming uniform steps when working with nonuniform steps degrades the accuracy of the estimated phase. Therefore, having experimental provisions, such as a closed-loop operation [5], is highly desirable but not always feasible [1–4,6]. Thus, some amount of uncertainty in the phase steps is unavoidable.

Nonuniform phase shifts have been treated by many authors. Bruning *et al.* proposed in their seminal paper to average many realizations in order to attenuate random errors [7]. Wang and Han proposed the advanced iterative algorithm (AIA), which allows the determination of the modulating phase without any prior knowledge about the phase steps [8]. This method is iterative, and it requires both the background and modulation terms to be spatially and temporally constant. Vargas *et al.* proposed a phase-shifting algorithm (PSA) based on principal component analysis (PCA) [9–11]; this PCA-based PSA is noniterative, and does not require prior knowledge about the phase steps. Hibino *et al.* proposed many-steps PSAs to suppress quadratic nonlinearity and linear miscalibration [12–15].

In this paper, we present a phase demodulation approach based on the Fourier analysis of nonuniform phase-shifted interferograms. Our proposal comprises three stages: first, we determine the experimental phase-step values between successive samples; second, by using these experimental phase steps, we modify the spectrum of the searched analytic signal; finally, we design a custom-made error-correcting PSA based on the frequency transfer function (FTF) formalism. This formalism allows us to evaluate the signal-to-noise ratio (S/N) power gain and the harmonic rejection capability of the proposed algorithm.

We implemented our algorithm to demodulate experimental data obtained from a Michelson interferential microscope, where the phase shifting is produced by displacing the surface under test with a piezoelectric transducer (PZT) in open-loop operation. The PZT has inherent hysteresis and nonlinearity, so the phase shifts have poor repeatability and linearity. Moreover, other error sources such as atmospheric turbulence and mechanical vibration also change the phase shift. Consequently, the resulting phase steps differ significantly from the expected nominal value.

2. NONUNIFORM PHASE-SHIFT ESTIMATION WITH FOURIER METHOD

The first stage of our proposed algorithm is to estimate the nonuniform phase steps. For this, let us consider the following mathematical model of an ideal phase-shifted fringe pattern:

$$I(x,y,t) = a(x,y) + b(x,y)\cos[\phi(x,y) + \omega_0 t], \quad (1)$$

where $a(x,y)$ is the background illumination or bias component; $b(x,y)$ is local contrast function; $\phi(x,y)$ represents the searched modulating phase, which is proportional to the

Shape defect measurement by fringe projection profilometry and phase-shifting algorithms

Sotero Ordones,[a] Manuel Servin,[a,*] Moises Padilla,[a] Ivan Choque,[a] Jorge L. Flores,[b] and Antonio Muñoz[c]

[a]Centro de Investigaciones en Optica A. C., Leon, Mexico
[b]University of Guadalajara, Department of Electronic Engineering, Guadalajara, Mexico
[c]University of Guadalajara, Department of Engineering, Autlan, Mexico

Abstract. We propose a fringe-projection profilometry technique for shape defects measurement, which can be employed for three-dimensional (3-D) quality inspection. The proposal consists of using a template surface to design phase-shifting algorithms with special-purpose phase response via the frequency transfer function. These algorithms can jointly and directly estimate the spatial phase deviations in a 3-D inspection. Phase deviations correspond to shape differences between the template shape and a testing one. The phase-unwrapping procedure is unnecessary when phase differences are small, as is usual in quality inspections. Experimental results show that our technique is so sensitive that the ripples in a fingerprint can be retrieved. © *2020 Society of Photo-Optical Instrumentation Engineers (SPIE)* [DOI: 10.1117/1.OE.59.1.014107]

Keywords: optical metrology; phase measurement; fringe projection; phase differences; defect measurement.

Paper 191221 received Sep. 2, 2019; accepted for publication Dec. 27, 2019; published online Jan. 20, 2020.

1 Introduction

Fringe projection profilometry (FPP) is a well-known technique for retrieving the three-dimensional (3-D) shape of solids. In recent years, it has been extensively deployed for computer-vision systems in automatic inspection because of its high-speed, high-resolution, noncontacting, and wide field of view properties.[1–3] In FPP, fringe patterns are projected onto a solid to be measured, and then, a digital camera records the phase-modulated fringe patterns.[1,3] To address the 3-D shape, one needs to retrieve the phase from the recorded fringe patterns, and hence, the 3-D surface is retrieved by translating phase units into real-world ones, usually in millimeters.

There are two categories of FPP according to how fringe patterns are phase demodulated: the first is phase-shifting profilometry (PSP) and the second is Fourier profilometry (FP).[4,5] In PSP, phase is computed by temporally filtering a sequence of fringe patterns, which are usually three or more, and it is also estimated locally at each pixel, thus preserving small-surface details,[4] whereas in FP, the phase is computed from a single fringe pattern in a global sense as frequency-domain filtering, and therefore, small-surface details are often filtered out.[4] After phase demodulation, a phase-unwrapping scheme is required to retrieve the continuous phase map.[3–7]

In PSP, when a surface is to be inspected by comparing it to a reference/template surface, one should estimate the differences between them. These would be computed by subtracting the template surface from the test object having *a priori* knowledge about the object; hence, the reference surface must be known exactly. For example, in optical shop testing, null tests are usually designed to compare the shape being tested against a designed one, as in the testing of lenses.[8] In double-exposure holographic interferometry, an object is holographically recorded in two different states: the first one is the initial condition or reference, and the second one is the condition of the object after having experienced a change or deformation;[9,10] then, both wavefronts are reconstructed simultaneously to obtain the interferogram that has the phase difference.[9] On the other hand, electronic-hardware advances allowed numerically reconstructing holograms

*Address all correspondence to Manuel Servin, E-mail: mservin@cio.mx

614 Vol. 37, No. 4 / April 2020 / Journal of the Optical Society of America A

Research Article

Journal of the Optical Society of America A

OPTICS, IMAGE SCIENCE, AND VISION

Suppressing ripple distortions and spurious pistons in phase-shifting interferometry

IVAN CHOQUE,[1] MOISES PADILLA,[1] MANUEL SERVIN,[1,*] MIGUEL ASMAD,[2] AND SOTERO ORDONES[1]

[1] Centro de Investigaciones en Optica A.C., Lomas del Bosque 115, Col, Lomas del Campestre, Leon Guanajuato, 37150, Mexico
[2] Pontificia Universidad Catolica del Peru, Av. Universitaria 1801, San Miguel, Lima 32, Peru
*Corresponding author: mservin@cio.mx

Received 13 December 2019; revised 24 February 2020; accepted 25 February 2020; posted 25 February 2020 (Doc. ID 385986); published 17 March 2020

In this paper, we present new phase-shifting algorithms (PSAs) that suppress the ripple distortions and spurious pistons in phase-shifting interferometry. These phase errors arise when non-uniform phase-shifting interferograms are processed with PSAs that assume uniform phase shifts. By modeling the non-uniform phase shifts as a polynomial of the unperturbed phase-shift value ω_0, we show that the conditions for eliminating the ripple distortion and the spurious piston are associated with the mth derivative of the PSA's frequency transfer function (FTF). Thus, we propose an approach to design robust algorithms based on the FTF formalism and we present four ready-to-apply PSAs formulas. Finally, our conclusions are supported by computer simulations.

https://doi.org/10.1364/JOSAA.385986

1. INTRODUCTION

In order to measure the optical phase in phase-shifting interferometry (PSI), numerous phase-shifting algorithms (PSA) have been reported [1–10]. Most PSAs considered that the phase shifts among interferograms are equally spaced (uniform phase shifts). However, in practice, the interferometric data has a different phase shift than the expected value (non-uniform phase shifts) as illustrated in Fig. 1. Most PSI setups use a piezoelectric transducer (PZT) to vary the optical path difference [11], but PZTs have poor repeatability and linearity that translate into non-uniform phase shifts [12]. Moreover, atmospheric turbulence and mechanical vibration also introduce an additional phase-shift uncertainty [13].

Ai and Wyant sum up nonlinearities as linear and quadratic terms [11], whereas Hibino *et al.* proposed that the non-uniform phase shifts can be approximated by a polynomial function of the unperturbed phase-shift value ω_0 and nonlinear coefficients [10,14–16]. It is well known that non-uniform phase shifts cause double-frequency ripple distortions [11,12,17]. In some cases, the ripple distortions can be suppressed by error-correcting PSAs designed for uniform phase shifts [5,6,18]. However, in other cases, it is necessary to rely on more robust approaches such as principal component analysis (PCA) [19–22] or the advanced iterative algorithm (AIA) [23]. Nonetheless, the optical phase computed by the aforementioned PSAs can include a spurious piston [24]. In most cases, this spurious piston is irrelevant. However, it is inadmissible for absolute measurements such as optical thickness [25] and air gap distance [26], in which it can be wrongly interpreted as a real physical magnitude. Hibino and Kim proposed canceling the momentum of a PSA to eliminate the spurious piston [16]. Nevertheless, our analysis shows that the actual conditions to suppress the spurious piston are related to the mth derivative of the PSA's frequency transfer function (FTF) evaluated at ω_0. Similarly, the conditions to suppress the ripple distortions are related to the mth derivative evaluated at $-\omega_0$.

The rest of this paper is organized as follows. In Section 2, we present the theoretical foundations and mathematical analysis to design PSAs that suppress both the ripple distortion and the spurious piston. Some examples of error-correcting PSAs are developed in Section 3. A computer simulation is shown in Section 4. Finally, our conclusions are drawn in Section 5.

2. THEORETICAL FOUNDATION

A sequence of N phase-shifted interferograms can be expressed as [27]

$$I_n(x,y) = a(x,y) + b(x,y)\cos[\varphi(x,y) + \theta_n], \quad n = 0, 1, \ldots, N-1, \tag{1}$$

where $a(x,y)$ and $b(x,y)$ are the background illumination and the local contrast function, respectively; $\varphi(x,y)$ is the searched phase, which is proportional to the phenomenon under study; and θ_n (in radians) is a non-uniform phase shift added to the

6224 Vol. 59, No. 20 / 10 July 2020 / Applied Optics Research Article

applied optics

Tukey's robust M-estimator for phase demodulation of interferograms with nonuniform shifts

SOTERO ORDONES,[1] MANUEL SERVIN,[1,*] MOISES PADILLA,[1] IVAN CHOQUE,[1] ANTONIO MUÑOZ,[2] AND JORGE L. FLORES[3]

[1]Centro de Investigaciones en Optica A.C., Loma del Bosque 115, C.P. 37150, Leon, Guanajuato, Mexico
[2]Departamento de Ingenierias, Universidad de Guadalajara, Av. Independencia Nacional 151, C.P. 48900, Autlan, Jalisco, Mexico
[3]Departamento de Electronica, Universidad de Guadalajara, Av. Revolucion 1500, C.P. 44840, Guadalajara, Jalisco, Mexico
*Corresponding author: mservin@cio.mx

Received 18 March 2020; revised 12 June 2020; accepted 12 June 2020; posted 15 June 2020 (Doc. ID 393153); published 10 July 2020

In this paper, we introduce an iterative scheme for phase demodulation of interferograms with nonuniformly spaced phase shifts. Our proposal consists of two stages: first, the phase map is obtained through a least squares fitting; second, the phase steps are retrieved using a statistical robust estimator. In particular, we use Tukey's biweighted M-estimator because it can cope with both noisy data and outliers in comparison with the ordinary least squares estimator. Furthermore, we provide the frequency description of the algorithm and the phase demodulation allowing us to analyze the procedure and estimation according to the frequency transfer function (FTF) formalism for phase-shifting algorithms. Results show that our method can accurately retrieve the phase map and phase shifts, and it converges by the 10th iteration.

https://doi.org/10.1364/AO.393153

1. INTRODUCTION

Optical interferometry has been employed in optical shop testing and noncontact measurements of physical features such as stress, strain, surface topography, thickness, and so on [1–3]. This technique is free mechanical contact; in the sensing, this technique produces fringe patterns whose modulating phase is proportional to the feature to be measured [1–3]. Particularly, the interferogram's modulating phase has such relation, and, therefore, phase measurement plays a key role.

Phase measurement consists of two steps: demodulation and unwrapping. In the first one, a discontinuous phase is extracted from the data, and in the second one, a continuous phase is reconstructed [4–6]. One should phase demodulate the interferograms correctly to avoid error propagation in the unwrapping process. In the second step, these errors may not be compensated, and so the phase could be impossible to be unwrapped.

There are two main categories in which the demodulation techniques can be agrupped: the Fourier transform and phase-shifting algorithms (PSA) [4–6]. The first one is usually employed in dynamic measurements because it requires a single interferogram [5]. In particular for this case, the retrieved phase is usually over smooth or a rough estimation of the true phase, and so the Fourier transform method should not be used when a high precision is desired [6]. On the other hand, PSAs require of a time sequence, at least three, of phase-shifted interferograms [6]. In this case, the retrieved phase commonly has a high precision due to data redundancy; however, its application is limited to static physical feature with respect of time.

Phase-shifting techniques can reach phase demodulation with a high precision provided that the phase shifts are exactly known. In practice, one cannot guarantee uniformly spaced nor exactly known phase shifts because the phase shifters may lead to systematic errors due to miscalibration, nonlinearity, and hysteresis [7–9]. Thus, the phase steps should be considered to be approximately known and nonuniformly spaced. Thereby, if one employs a uniform PSA to phase demodulate interferograms with nonuniformly spaced phase shifts, the retrieved phase map will have detuning-like distortion. In order to cope with this issue, it has been proposed that PSAs are in two main categories: error correction and nonlinear/self-tuning PSAs. In the first one, phase shifts are considered to be spaced uniformly with small deviations. Whence, phase-shift deviations are approximated by Taylor series, so rippled distortions become smaller as the number of terms increases (refer to Appendix A in Ref. [6]). In our expertise, error-correcting PSAs can significantly reduce detuning-error distortion as long as phase-shift deviations are small and systematic. However, these PSAs will poorly perform the phase extraction against noise and such distortion when phase-shift deviations are large and random.

Windowed generalized phase-shifting algorithms

Sotero Ordones[a], Manuel Servin*[a], Moises Padilla[a], Ivan Choque[a], Jorge L. Flores[b], Antonio Muñoz[c]
[a]Centro de Investigaciones en Optica A. C., Loma del Bosque 115, Leon, Mexico 37150; [b]Electronic Engineering Department, Universidad de Guadalajara, Av. Revolución 1500, Guadalajara, México 44840; [c]Engineering Department, University of Guadalajara, Av. Independencia nacional 151, Autlán, México 48900;

ABSTRACT

In this work, we introduce the windowed generalized phase-shifting algorithms (WG-PSAs) using static and dynamic weighting functions/widows. These algorithms are derived from a weighted least square fitted to the monochromatic temporal fringe, thereby, the selection of the window plays an important role due to the fact that it shall reduce the influence of those intensities jeopardizing the phase estimation. In order to make the best selection, we propose to employ an adaptive/dynamic window which has the ability to detect the fringe patterns that jeopardize the phase retrieval. This window is computed iteratively by analyzing the error between the measured and fitted intensities. Furthermore, we provide the analysis of our scheme using the frequency transfer function (FTF) formalism for phase-shifting algorithms. Finally, we executed numerical experiments with synthetic data in which we compare the performance of the dynamic window versus several static ones from the state-of-the-art; although our scheme is more computationally expensive due to the iterative procedure, it works better than the traditional generalized PSAs with a window included or not.

Keywords: Phase-shifting interferometry, phase retrieval, generalized phase shifting algorithm, window function.

1. INTRODUCTION

Phase-shifting interferometry is a well-known technique employed in non-contact measurements of physical features such as stress, strain, shape, thickness and so on [1,2]. By using this technique, one obtains a temporal sequence of phase-shifted fringe patterns containing the feature to be measured; particularly, spatially phase modulated interferograms has the relation between the optical path and the feature [1,2]. Phase-shifting algorithms (PSAs) are needed to extract the searched phase.

Phase-shifting algorithms are able to estimate the phase with a high precision provided that the phase shifts are known exactly in floating-point precision; however, one cannot usually guarantee exactly-known phase shifts because phase shifters may introduce systematic errors such as miscalibration, its nonlinearity, and hysteresis [3]. Therefore, phase shifts should be considered to have small mismatching, and being non-uniformly spaced; hence, the phase map will have detuning-like distortion [4]. With the aim of coping with this issue, it has been proposed PSAs classified into two main categories: error correcting and non-linear/self-tuning PSAs.

Error correcting (EC-) PSAs consider uniformly-spaced phase shifts with small deviations that are usually approximated by Taylor series expansion [5,6] or employing weighting functions (windows) [7-9]; in terms of the frequency transfer function (FTF) formalism [10], these PSAs have a broad stop band allowing to reduce the detuning error. From this fact, Authors in [11,12] have designed PSAs whose FTFs have broad stop bands to deal with this error. Whereas, self-tuning PSAs consider a global phase shit being estimated [13,14], and also non-uniformly spaced phase shifts being estimated in an iterative way [4,15-18]. In our expertise, self-tuning PSAs can retrieve the phase more accurately than EC-PSAs due to the fact that self-tuning PSAs usually are more robust against noise, as well as they can work well with large phase-shift deviations.

However, phase-shift estimator can poorly estimate the phase shifts of one or more fringe patterns, and hence, the detuning-like distortion will appear in the estimated phase; this is because most algorithms have no retro feedback with the data. In this work, we introduce the windowed generalized PSAs to deal when phase shifts mismatch from the given

Interferometry XX, edited by Michael B. North Morris, Katherine Creath, Rosario Porras-Aguilar, Proc. of SPIE Vol. 11490, 1149004 · © 2020 SPIE · CCC code: 0277-786X/20/$21 · doi: 10.1117/12.2567389

Suppressing ripple distortions and spurious pistons in phase-shifting interferometry

Ivan Choque[a], Moises Padilla[a], Manuel Servin[a], Sotero Ordones[a], and Miguel Asmad[b]

[a]Centro de Investigaciones en Optica A.C., Lomas del Bosque 115, Col, Lomas del Campestre, 37150, Leon, Mexico

[b]Pontificia Universidad Catolica del Peru, Av. Universitaria 1801, San Miguel, Lima 32, Lima, Peru

ABSTRACT

In this work, we deduce explicit conditions to design phase shifting algorithms (PSAs) in order to suppress errors in phase measurement, the double-frequency ripple distortion and the spurious piston. These errors arise when non-uniform phase-shifting interferograms are processed with conventional PSAs which assume uniform phase shifts. By modeling the non-uniform phase shifts as a polynomial of the unperturbed phase shift value ω_0, we show that the conditions for eliminating those errors are associated to the m-th derivative of the PSA's frequency transfer function (FTF). Thus, we propose an approach to design robust algorithms based on the FTF formalism, and we present a ready-to-apply eight-frame PSA. Finally, our conclusions are supported by computer simulations.

Keywords: Phase measurement, non-uniform phase shifts, ripple distortion, spurious piston

1. INTRODUCTION

In order to measure the optical phase in phase-shifting interferometry (PSI), numerous phase-shifting algorithms (PSA) have been reported.[1–10] Most PSAs considered that the phase shifts among interferograms are equally spaced (uniform phase shifts). However, in practice, the interferometric data has a different phase shift than the expected value (non-uniform phase shifts), as illustrated in Fig. 1. Most PSI setups use a piezoelectric transducer (PZT) to vary the optical path difference,[11] but PZTs have poor repeatability and linearity that translate into non-uniform phase shifts.[12] Moreover, atmospheric turbulence and mechanical vibration also introduce an additional phase-shift uncertainty.[13]

Ai and Wyant sum up non-uniform phase shift as linear and quadratic terms,[11] whereas Hibino et al. proposed that the non-uniform phase shifts can be approximated by a polynomial function of the unperturbed phase-shift value ω_0 and nonlinear coefficients.[10,14–16] It is well known that non-uniform phase shifts cause double-frequency ripple distortions.[11,12,17] In some cases, the ripple distortions can be suppressed by error-correcting PSAs designed for uniform phase shifts.[3,4,18]However, in other cases, it is necessary to use more robust approaches such as the principal component analysis (PCA),[19–21] the advanced iterative algorithm (AIA)[22] or VU factorization.[23] Nonetheless, the optical phase computed by the aforementioned PSAs may include a spurious piston.[16,24] In most cases, this spurious piston is not relevant. However, it can be a problem in absolute phase measurements such as optical thickness[25] and air gap distance,[26] in which it can be wrongly interpreted as a real physical magnitude. Hibino and Kim proposed canceling the momentum of a PSA to eliminate the spurious piston.[16] Nevertheless, our analysis shows that the actual conditions to suppress the spurious piston are related to the m-th derivative of the PSA's frequency transfer function (FTF) evaluated at $\omega = \omega_0$. Similarly, the conditions to suppress the ripple distortions are related to the m-th derivative evaluated at $\omega = -\omega_0$.

The rest of this paper is organized as follows. In Section 2, we present the theoretical foundations and mathematical analysis to deduce conditions in order to suppress both the ripple distortion and the spurious piston. Evolution of the well-known four-frame PSA is developed in Section 3. Computer simulation are developed in Section 4. Finally, our conclusions are drawn in Section 5.

Further author information:
Ivan Choque: E-mail: ivanchoque@cio.mx, Telephone: 52 477 106 2173

Interferometry XX, edited by Michael B. North Morris, Katherine Creath, Rosario Porras-Aguilar, Proc. of SPIE Vol. 11490, 1149006· © 2020 SPIE · CCC code: 0277-786X/20/$21 · doi: 10.1117/12.2568138

Research Article Vol. 60, No. 5 / 10 February 2021 / Applied Optics 1137

applied optics

Least-squares gamma estimation in fringe projection profilometry

Antonio Muñoz,[1,*] Jorge L. Flores,[2] Geliztle Parra-Escamilla,[2] Luis A. Morales,[3,5] Sotero Ordones,[4] and Manuel Servin[4]

[1]Engineering Department, University of Guadalajara, Av. Independencia Nacional No. 151, Autlán, Jalisco, Mexico
[2]Electronic Engineering Department, University of Guadalajara, Av. Revolución No. 1500, Guadalajara, Jalisco, Mexico
[3]Faculty of Civil Engineering, Conacyt-Universidad Michoacana de San Nicolás de Hidalgo, Morelia 58030, Michoacán, Mexico
[4]Centro de Investigaciones en Optica A.C., Loma del Bosque No. 115, Leon, Guanajuato, Mexico
[5]e-mail: lamorales@conacyt.mx
*Corresponding author: jose.munoz@cucsur.udg.mx

Received 16 November 2020; revised 12 January 2021; accepted 13 January 2021; posted 13 January 2021 (Doc. ID 415056); published 2 February 2021

This paper introduces a novel, to the best of our knowledge, method to estimate and compensate the nonlinear gamma factor introduced by the optical system in fringe projection profilometry. We propose to determine this factor indirectly by adjusting the least-squares plane to the estimated phase coming from the reference plane. We only require a minimal set of three fringe sinusoidal images to estimate the gamma factor. This value can be used to rectify computational legacy data and also to generate and project the new set of fringe patterns for which we perform the inverse gamma compensation. Experimental results demonstrate the feasibility of the proposed method to estimate and correct the gamma distortion.

https://doi.org/10.1364/AO.415056

1. INTRODUCTION

Fringe projection profilometry (FPP) is a noncontact optical method well established for 3D shape measurement of object surfaces [1–3]. In this technique, one usually employs phase-shifting algorithms (PSAs) for phase retrieval [4]. The system consists of a commercial video projector to display the sinusoidal fringe patterns and a digital camera that records the phase-modulated fringe patterns. Despite its simplicity, the projector-camera system introduces a nonlinear intensity distortion translating into undesired high-order harmonics in the acquired patterns due to the system's nonlinear intensity response mainly determined by the projector [5]. This introduces harmonics in the acquired fringe patterns that generate phase errors.

With the aim of overcoming this issue, for the minimal set of three fringe patterns required in high-speed measurements, we should address the gamma distortion to reduce errors in the recovered phase. In particular, the most fundamental procedure consists of estimating the gamma value and to project a new set of antigamma-distortion patterns for which the inverse of the gamma factor is employed. To the best of our knowledge, the pioneer work for gamma correction in FPP was published in 2004 [6], where the authors proposed implementation of an iterative process to estimate the gamma curve; however, its accuracy is poor since the authors did not take into account the effect of the ambient light; further, it is an expensive computational optimization problem. The authors propose to estimate simultaneously the phase and the gamma factor. Zhang and Yau proposed a more useful technique [7], where a phase-error lookup-table (LUT) was developed to compensate the gamma distortion, but it is well known that the accuracy of methods based on LUTs are limited to the quality of the LUT and the interpolation function. A more elaborated proposal was developed early by Pan *et al.* [8], i.e., the nonlinearity caused by the high-order harmonics is approximated by a zero-order compensator. The authors' main result is an iterative phase-compensation, where the required constant needs to be previously calculated; however, this is an expensive iterative process applied to the whole 2D recovered phase. Despite the aforementioned results, there is room for improvement. In the context of data fitting methods, a couple of solutions have been reported [9,10]. These solutions propose to estimate the curve of intensity response by adjusting a high-degree polynomial and a third-order spline, respectively. Both methods employ only a row of data to perform the estimation. Recently, Babaei *et al.* proposed the codification of the fringe pattern as an exponential function [11]. The authors developed a mathematical model for gamma-independent phase computation for a four-phase step PS algorithm. However, the exponential function produces wide regions of low intensity, i.e., acquired fringe patterns have a low dynamic range. The wide dark areas mean a low signal-to-noise ratio and hence a reduction in accuracy. In order to improve

Bibliography

[1] G. Sansoni, M. Trebeschi, and F. Docchio, "State-of-the-art and applications of 3d imaging sensors in industry, cultural heritage, medicine, and criminal investigation," *Sensors*, vol. 9, no. 1, pp. 568–601, 2009.

[2] F. Blais, M. Rioux, and J.-A. Beraldin, "Practical Considerations For A Design Of A High Precision 3-D Laser Scanner System," in *Optomechanical and Electro-Optical Design of Industrial Systems* (R. J. Bieringer and K. G. Harding, eds.), vol. 0959, pp. 225–246, International Society for Optics and Photonics, SPIE, 1988.

[3] K. Gåsvik, *Optical metrology*. Wiley, 3 ed., 2002.

[4] S. H. Rowe and W. T. Welford, "Surface topography of non-optical surfaces by projected interference fringes," *Nature*, no. 216, pp. 786–787, 1967.

[5] P. Hariharan, *Basics of Interferometry*. Elsevier Science, 2010.

[6] R. Sirohi, *Introduction to Optical Metrology*. Optical Sciences and Applications of Light, CRC Press, 2017.

[7] E. B. Li, X. Peng, J. Xi, J. F. Chicharo, J. Q. Yao, and D. W. Zhang, "Multi-frequency and multiple phase-shift sinusoidal fringe projection for 3d profilometry," *Opt. Express*, vol. 13, no. 5, pp. 1561–1569, 2005.

[8] J. Harizanova and V. Sainov, "Three-dimensional profilometry by symmetrical fringes projection technique," *Optics and Lasers in Engineering*, vol. 44, no. 12, pp. 1270–1282, 2006.

[9] J. I. Harizanova, E. V. Stoykova, and V. C. Sainov, "Phase retrieval techniques in coordinates measurement," in *AIP Conference Proceedings*, vol. 899, pp. 321–322, AIP, 2007.

[10] Y. Hu, Q. Chen, S. Feng, and C. Zuo, "Microscopic fringe projection profilometry: A review," *Optics and Lasers in Engineering*, vol. 135, p. 106192, 2020.

[11] D. Ambrosini, G. Guattari, C. Sapia, and G. S. Spagnolo, "Flow visualization via fringe projection," in *9th international symposium on flow visualization*, vol. 8867, pp. 117–7, 2000.

[12] L. Jiang, X. Zhang, F. Fang, X. Liu, and L. Zhu, "Wavefront aberration metrology based on transmitted fringe deflectometry," *Appl. Opt.*, vol. 56, no. 26, pp. 7396–7403, 2017.

[13] O. E. Castillo, R. Legarda-Sáenz, J. L. Flores, and G. Garcia-Torales, "Measurement of phase objects by the use of color phase-shifting technique," in *Infrared Remote Sensing and Instrumentation XXI* (M. S. Scholl and G. Páez, eds.), vol. 8867, pp. 314–319, International Society for Optics and Photonics, SPIE, 2013.

[14] S. S. Gorthi and P. Rastogi, "Fringe projection techniques: whither we are?," *Opt. Lasers Eng.*, vol. 48, no. 2, pp. 133–140, 2010.

[15] M. Takeda and K. Mutoh, "Fourier transform profilometry for the automatic measurement of 3-d object shapes," *Appl. Opt.*, vol. 22, no. 24, pp. 3977–3982, 1983.

[16] M. E. Pawlowski, M. Kujawinska, and M. G. Wegiel, "Monitoring and measurement of movement of objects by fringe projection method," in *Three-Dimensional Image Capture and Applications III* (B. D. Corner and J. H. Nurre, eds.), vol. 3958, pp. 116–125, International Society for Optics and Photonics, SPIE, 2000.

[17] S. Tan, D. Song, and L. Zeng, "A tracking fringe method for measuring the shape and position of a swimming fish," *Optics Communications*, vol. 173, no. 1, pp. 123–128, 2000.

[18] Z. Zhang, D. P. Towers, and C. E. Towers, "Time resolved high resolution shape and colour measurement using fringe projection," in *Fringe 2009: 6th International Workshop on Advanced Optical Metrology* (W. Osten and M. Kujawinska, eds.), pp. 1–4, Berlin, Heidelberg: Springer Berlin Heidelberg, 2009.

[19] W.-H. Su, C.-Y. Kuo, and F.-J. Kao, "Three-dimensional trace measurements for fast-moving objects using binary-encoded fringe projection techniques," *Appl. Opt.*, vol. 53, no. 24, pp. 5283–5289, 2014.

[20] S. Feng, Q. Chen, and C. Zuo, "Graphics processing unit-assisted real-time three-dimensional measurement using speckle-embedded fringe," *Appl. Opt.*, vol. 54, no. 22, pp. 6865–6873, 2015.

[21] S. Yoneyama, Y. Morimoto, M. Fujigaki, and M. Yabe, "Phase-measuring profilometry of moving object without phase-shifting device," *Optics and Lasers in Engineering*, vol. 40, no. 3, pp. 153–161, 2003.

[22] S. Yoneyama, Y. Morimoto, M. Fujigaki, and Y. Ikeda, "Three-dimensional surface profile measurement of a moving object by a spatial offset phase step method," *Optical Engineering*, vol. 42, no. 1, pp. 137–142, 2003.

[23] E. Hu and F. Haifeng, "Surface profile inspection of a moving object by using dual-frequency fourier transform profilometry," *Optik*, vol. 122, no. 14, pp. 1245–1248, 2011.

[24] C. Zuo, Q. Chen, G. Gu, S. Feng, F. Feng, R. Li, and G. Shen, "High-speed three-dimensional shape measurement for dynamic scenes using bi-frequency tripolar pulse-width-modulation fringe projection," *Optics and Lasers in Engineering*, vol. 51, no. 8, pp. 953–960, 2013.

[25] L. Lu, J. Xi, Y. Yu, and Q. Guo, "New approach to improve the accuracy of 3-d shape measurement of moving object using phase shifting profilometry," *Opt. Express*, vol. 21, no. 25, pp. 30610–30622, 2013.

[26] L. Lu, Y. Ding, Y. Luan, Y. Yin, Q. Liu, and J. Xi, "Automated approach for the surface profile measurement of moving objects based on psp," *Opt. Express*, vol. 25, no. 25, pp. 32120–32131, 2017.

[27] H. Yuan, Y.-P. Cao, C. Chen, and Y.-P. Wang, "Online phase measuring profilometry for rectilinear moving object by image correction," *Optical Engineering*, vol. 54, no. 11, pp. 1–9, 2015.

[28] C. Chen, Y.-P. Cao, L.-J. Zhong, and K. Peng, "An on-line phase measuring profilometry for objects moving with straight-line motion," *Optics Communications*, vol. 336, pp. 301–305, 2015.

[29] H. Li, G. Feng, P. Yang, Z. Wang, S. Zhou, and A. Asundi, "Online fringe projection profilometry based on scale-invariant feature transform," *Optical Engineering*, vol. 55, no. 8, pp. 1–21, 2016.

[30] Q. Guo, Y. Ruan, J. Xi, L. Song, X. Zhu, Y. Yu, and J. Tong, "3d shape measurement of moving object with fft-based spatial matching," *Optics & Laser Technology*, vol. 100, pp. 325–331, 2018.

[31] J. L. Flores, M. Stronik, A. Muñoz, G. Garcia-Torales, S. Ordoñes, and A. Cruz, "Dynamic 3d shape measurement by iterative phase shifting algorithms and colored fringe patterns," *Opt. Express*, vol. 26, no. 10, pp. 12403–12414, 2018.

[32] L. Lu, Z. Jia, Y. Luan, and J. Xi, "Reconstruction of isolated moving objects with high 3d frame rate based on phase shifting profilometry," *Optics Communications*, vol. 438, pp. 61–66, 2019.

[33] A. Tikhonov and V. Arsenin, *Solution of ill-posed problems*. Wiston, 1977.

[34] M. Servin, J. Quiroga, and M. Padilla, *Fringe Pattern Analysis for Optical Metrology: Theory, Algorithms, and Applications*. Wiley-VCH, 2014.

[35] M. Takeda, H. Ina, and S. Kobayashi, "Fourier-transform method of fringe-pattern analysis for computer-based topography and interferometry," *J. Opt. Soc. Am.*, vol. 72, no. 1, pp. 156–160, 1982.

[36] W. W. Macy, "Two-dimensional fringe-pattern analysis," *Appl. Opt.*, vol. 22, no. 23, pp. 3898–3901, 1983.

[37] Q. Kemao, "Windowed fourier transform for fringe pattern analysis," *Appl. Opt.*, vol. 43, no. 13, pp. 2695–2702, 2004.

[38] Q. Kemao, "Two-dimensional windowed fourier transform for fringe pattern analysis: principles, applications and implementations," *Opt. Lasers Eng.*, vol. 45, no. 2, pp. 304–317, 2007.

[39] M. Servin and F. J. Cuevas, "A novel technique for spatial phase-shifting interferometry," *Journal of Modern Optics*, vol. 42, no. 9, pp. 1853–1862, 1995.

[40] J. L. Marroquin, J. E. Figueroa, and M. Servin, "Robust quadrature filters," *J. Opt. Soc. Am. A*, vol. 14, no. 4, pp. 779–, 1997.

[41] J. L. Marroquin, M. Rivera, S. Botello, R. Rodriguez-Vera, and M. Servin, "Regularization methods for processing fringe-pattern images," *Appl. Opt.*, vol. 38, no. 5, pp. 788–794, 1999.

[42] Q. Kemao and S. Soon, "Sequential demodulation of a single fringe pattern guided by local frequencies," *Opt. Lett.*, vol. 32, no. 2, pp. 127–129, 2007.

[43] E. Goodwin and J. Wyant, *Field Guide to Interferometric Optical Testing.* Spie Field Guides, SPIE Press, 1977.

[44] D. Malacara, *Optical shop testing.* Wiley, 2007.

[45] J. Garcia-Marquez, D. Malacara-Hernandez, and M. Servin, "Analysis of interferograms with a spatial radial carrier or closed fringes and its holographic analogy," *Appl. Opt.*, vol. 37, no. 34, pp. 7977–7982, 1998.

[46] M. Novak, J. Millerd, N. Brock, M. North-Morris, J. Hayes, and J. C. Wyant, "Analysis of a micropolarizer array-based simultaneous phase-shifting interferometer," *Appl. Opt.*, vol. 44, no. 32, pp. 6861–6868, 2005.

[47] M. Servin, J. C. Estrada, and O. Medina, "Fourier transform demodulation of pixelated phase-masked interferograms," *Opt. Express*, vol. 18, no. 15, pp. 16090–16095, 2010.

[48] J. L. Marroquin, M. Servin, and R. Rodriguez-Vera, "Adaptive quadrature filters and the recovery of phase from fringe pattern images," *J. Opt. Soc. Am. A*, vol. 14, no. 8, pp. 1742–1753, 1997.

[49] J. C. Estrada, M. Servin, and J. L. Marroquin, "Local adaptable quadrature filters to demodulate single fringe patterns with close fringes," *Opt. Express*, vol. 15, no. 5, pp. 2288–2298, 2007.

[50] J. Servin, M. Marroquin and F. Cuevas, "Demodulation of a single interferogram by use of a two-dimensional regularized phasetracking technique," *Appl. Opt.*, vol. 36, no. 19, pp. 4540–4548, 1997.

[51] M. Servin, J. L. Marroquin, and F. J. Cuevas, "Fringe-follower regularized phase tracker for demodulation of closed-fringe interferograms," *J. Opt. Soc. Am. A*, vol. 18, no. 3, pp. 689–, 2001.

[52] R. Legarda-Sáenz, W. Osten, and Jüptner, "Improvement of the regularized phase tracking technique for the processing of nonnormalized fringe patterns," *Appl. Opt.*, vol. 41, pp. 5519–5526, 2002.

[53] L. Kai and Q. Kemao, "A generalized regularized phase tracker for phase demodulation of a single fringe pattern," *Opt. Express*, vol. 20, no. 11, pp. 12579–12592, 2012.

[54] K. G. Larkin, D. J. Bone, and M. Oldfield, "Natural demodulation of two-dimensional fringe patterns. i. general background of the spiral phase quadrature transform," *J. Opt. Soc. Am. A*, vol. 18, no. 8, pp. 1862–1870, 2001.

[55] K. G. Larkin, "Natural demodulation of two-dimensional fringe patterns. ii. stationary phase analysis of the spiral phase quadrature transform," *J. Opt. Soc. Am. A*, vol. 18, no. 8, pp. 1871–1881, 2001.

[56] K. G. Larkin, "A self-calibrating phase-shifting algorithm based on the natural demodulation of twodimensional fringe patterns," *Opt. Express*, vol. 9, no. 5, pp. 236–253, 2001.

[57] E. Chu, *Discrete and Continuous Fourier Transforms: Analysis, Applications and Fast Algorithms*. CRC Press, 2008.

[58] C. S. Burrus, M. Frigo, and G. S. Johnson, *Fast Fourier Transforms*. Samurai Media Limited, 2018.

[59] K. R. Rao, D. N. Kim, and J. J. Hwang, *Fast Fourier Transform - Algorithms and Applications*. Signals and Communication Technology, Springer, 2010.

[60] Q. Kemao, *Windowed fringe pattern analysis*. SPIE Press, 2013.

[61] L. R. Watkins, "Continuous wavelet transforms," in *Phase estimation in optical interferometry* (P. Rastogi and E. Hack, eds.), ch. 2, pp. 69–120, CRC Press, 2015.

[62] J. Zhong and J. Weng, "Windowed fourier transforms," in *Phase estimation in optical interferometry* (P. Rastogi and E. Hack, eds.), ch. 2, pp. 31–68, CRC Press, 2015.

[63] M. Servin, J. C. Estrada, and J. A. Quiroga, "The general theory of phase shifting algorithms," *Opt. Express*, vol. 17, no. 24, pp. 21867–21881, 2009.

[64] J. Proakis and D. Manolakis, *Digital Signal Processing*. Pearson Prentice Hall, 4 ed., 2007.

[65] A. Oppenheim and R. Schafer, *Discrete-time Signal Processing*. Prentice-Hall signal processing series, Prentice Hall, 1989.

[66] Y. Surrel, "Design of algorithms for phase measurements by the use of phase stepping," *Appl. Opt.*, vol. 35, no. 1, pp. 51–60, 1996.

[67] A. Gonzalez, M. Servin, J. C. Estrada, and J. A. Quiroga, "Design of phase-shifting algorithms by finetuning spectral shaping," *Opt. Express*, vol. 19, no. 11, pp. 10692–10697, 2011.

[68] N. K. Mohan, "Speckle methods and applications," in *Handbook of optical metrology: principles and applications* (T. Yoshizawa, ed.), ch. 8, pp. 241–262, CRC Press, 2009.

[69] M. Servin, J. A. Quiroga, and J. C. Estrada, "Phase-shifting interferometry corrupted by white and non-white additive noise," *Opt. Express*, vol. 19, no. 10, pp. 9529–9534, 2011.

[70] A. Björck, *Numerical methods for least squares problems*. SIAM, 1996.

[71] G. A. Ayubi, I. Duarte, and J. A. Ferrari, "Optimal phase-shifting algorithm for interferograms with arbitrary steps and phase noise," *Opt. Lasers Eng.*, vol. 114, pp. 129–135, 2019.

[72] J. E. Greivenkamp, "Generalized data reduction for heterodyne interferometry," *Opt. Eng.*, vol. 23, no. 4, pp. 350–352–3, 1984.

[73] N. Ohyama, S. Kinoshita, A. Cornejo-Rodriguez, T. Honda, and J. Tsujiuchi, "Accuracy of phase determination with unequal reference phase shift," *J. Opt. Soc. Am. A*, vol. 5, no. 12, p. 2019, 1988.

[74] J. H. Bruning, D. R. Herriott, J. E. Gallagher, D. P. Rosenfeld, A. D. White, and D. J. Brangaccio, "Digital wavefront measuring interferometer for testing optical surfaces and lenses," *Appl. Opt.*, vol. 13, no. 11, pp. 2693–2703, 1974.

[75] A. Muñoz, S. Ordoñes, J. L. Flores, O. Aguilar, and A. Jimenez, "Esquemas de corrimiento de fase: estudio comparativo," *Acta Universitaria*, vol. 29, p. e2627, 2019.

[76] M. Servin, M. Padilla, G. Garnica, and G. Paez, "Fourier spectra for nonuniform phase-shifting algorithms based on principal component analysis," *Opt. Express*, vol. 27, no. 18, pp. 25861–25871, 2019.

[77] S. Ordones, M. Servin, M. Padilla, A. Muñoz, J. L. Flores, and I. Choque, "Spectral analysis for the generalized least squares phase-shifting algorithms with harmonic robustness," *Opt. Lett.*, vol. 44, no. 9, pp. 2358–2361, 2019.

[78] M. Servin, M. Padilla, G. Garnica, and G. Paez, "Design of nonlinearly spaced phase-shifting algorithms using their frequency transfer function," *Appl. Opt.*, vol. 58, no. 4, pp. 1134–1138, 2019.

[79] J. F. Mosiño, M. Servin, J. C. Estrada, and J. A. Quiroga, "Phasorial analysis of detuning error in temporal phase shifting algorithms," *Opt. Express*, vol. 17, no. 7, pp. 5618–5623, 2009.

[80] J. Schwider, R. Burow, K. E. Elssner, J. Grzanna, R. Spolaczyk, and K. Merkel, "Digital wave-front measuring interferometry: some systematic error sources," *Appl. Opt.*, vol. 22, no. 21, pp. 3421–3432, 1983.

[81] P. Hariharan, B. F. Oreb, and T. Eiju, "Digital phase-shifting interferometry: a simple error-compensating phase calculation algorithm," *Appl. Opt.*, vol. 26, no. 13, pp. 2504–2506, 1987.

[82] J. Schmit and K. Creath, "Extended averaging technique for derivation of error-compensating algorithms in phase-shifting interferometry," *Appl. Opt.*, vol. 34, no. 19, pp. 3610–3619, 1995.

[83] P. de Groot, "Derivation of algorithms for phase-shifting interferometry using the concept of a data-sampling windows," *Appl. Opt.*, vol. 34, no. 22, pp. 4723–4730, 1996.

[84] J. Schmit and K. Creath, "Window function influence on phase error in phase-shifting algorithms," *Appl. Opt.*, vol. 35, no. 28, pp. 5642–5649, 1996.

[85] K. Hibino, B. F. Oreb, D. I. Farrant, and K. G. Larkin, "Phase-shifting algorithms for nonlinear and spatially nonuniform phase shifts," *J. Opt. Soc. Am. A*, vol. 14, no. 4, pp. 918–930, 1996.

[86] H. Bi, Y. Zhang, K. V. Ling, and C. Wen, "Class of 4 + 1-phase algorithms with error compensation," *Appl. Opt.*, vol. 43, no. 21, pp. 4723–4730, 2004.

[87] J. C. Estrada, M. Servin, and J. A. Quiroga, "Easy and straightforward construction of wideband phase-shifting algorithms for interferometry," *Opt. Lett.*, vol. 34, no. 4, pp. 413–415, 2009.

[88] P. Carré, "Installation et utilisation du comparateur photoélectrique et interférentiel du bureau international des poids et mesures," *Metrologia*, vol. 2, no. 1, pp. 13–23, 1966.

[89] Y. Surrel, "Phase stepping: a new self-calibrating algorithm," *Appl. Opt.*, vol. 32, no. 19, p. 3598–3600, 1993.

[90] G. Stoilov and T. Dragostinov, "Phase-stepping interferometry: fiveframe algorithm with an arbitrary step," *Opt. Lasers Eng.*, vol. 28, no. 1, pp. 61–69, 1997.

[91] I. Choque, M. Padilla, M. Servin, M. Asmad, and S. Ordones, "Suppressing ripple distortions and spurious pistons in phase-shifting interferometry," *J. Opt. Soc. Am. A*, vol. 37, no. 4, pp. 614–620, 2020.

[92] I. Choque, M. Padilla, M. Servin, S. Ordones, and M. Asmad, "Suppressing ripple distortions and spurious pistons in phase-shifting interferometry," in *Interferometry XX* (M. B. N. Morris, K. Creath, and R. Porras-Aguilar, eds.), vol. 11490, pp. 1149006–10–19, International Society for Optics and Photonics, SPIE, 2020.

[93] S. Ordones, M. Servin, M. Padilla, I. Choque, J. L. Flores, and A. M. noz, "Windowed generalized phase-shifting algorithms," in *Interferometry XX* (M. B. N. Morris, K. Creath, and R. Porras-Aguilar, eds.), vol. 11490, pp. 1–9, International Society for Optics and Photonics, SPIE, 2020.

[94] F. J. Harris, "On the use of windows for harmonic analysis with the discrete fourier transforms," *Proc. IEEE*, vol. 66, no. 1, pp. 51–83, 1978.

[95] A. Patil, R. Langoju, and P. Rastogi, "Phase shifting interferometry using a robust parameter estimation method," *Opt. Lasers Eng.*, vol. 45, pp. 77–90, 2007.

[96] R. Kulkarni and P. Rastogi, "Direct unwrapped phase estimation in phase shifting interferometry using levenberg–marquardt algorithm," *Journal of Optics*, vol. 19, no. 1, pp. 1–9, 2017.

[97] K. Okada, A. Sato, and J. Tsuijiuchi, "Simultaneous calculation of phase distribution and scanning phase shift in phase shifting interferometry," *Optics Communications*, vol. 84, no. 3–4, pp. 118–124, 1991.

[98] C. T. Farrell and M. A. Player, "Phase step measurement and variable step algorithms in phase-shifting interferometry," *Meas. Sci. Technol.*, vol. 3, no. 10, p. 953–958, 1992.

[99] G. S. Han and S. W. Kim, "Numerical correction of reference phases in phase-shifting interferometry by iterative least-squares fitting," *Appl. Opt.*, vol. 33, pp. 7321–7325, 1994.

[100] I. B. Kong and S. W. Kim, "General algorithm of phase-shifting interferometry by iterative least-squares fitting," *Optical Engineering*, vol. 34, no. 1, pp. 183–188, 1995.

[101] K. E. Perry Jr. and J. McKelvie, "Reference phase shift determination in phase shifting interferometry," *Opt. Lasers Eng.*, vol. 22, pp. 77–90, 1995.

[102] Z. Wang and B. Han, "Advanced iterative algorithm for phase extraction of randomly phase-shifted interferograms," *Opt. Lett.*, vol. 29, no. 14, pp. 1671–1673, 2004.

[103] H. Guo, Z. Zhao, and M. Chen, "Efficient iterative algorithm for phase-shifting interferometry," *Optics and Lasers in Engineering*, vol. 45, no. 2, pp. 281–292, 2007.

[104] Q. Kemao, H. Wang, W. Gao, L. Feng, and S. H. Soon, "Phase extraction from arbitrary phase-shifted fringe patterns with noise suppression," *Optics and Lasers in Engineering*, vol. 48, no. 6, pp. 684–689, 2010.

[105] J. Xu, W. Jin, L. Chai, and Q. Xu, "Phase extraction from randomly phase-shifted interferograms by combining principal component analysis and least squares method," *Opt. Express*, vol. 19, no. 21, pp. 20483–20492, 2011.

[106] Q. Liu, Y. Wang, F. Ji, and J. He, "A three-step least-squares iterative method for tilt phase-shift interferometry," *Opt. Express*, vol. 21, no. 24, pp. 29505–29515, 2013.

[107] R. Juarez-Salazar, C. Robledo-Sánchez, C. Meneses-Fabian, F. Guerrero-Sánchez, and L. A. Aguilar, "Generalized phase-shifting interferometry by parameter estimation with the least squares method," *Optics and Lasers in Engineering*, vol. 51, no. 5, pp. 626–632, 2013.

[108] O. Medina, J. C. Estrada, and M. Servin, "Robust adaptive phase-shifting demodulation for testing moving wavefronts," *Opt. Express*, vol. 21, no. 24, pp. 29687–29694, 2013.

[109] A. Albertazzi Jr., A. V. Fantin, D. P. Willemann, and M. E. Benedet, "Phase maps retrieval from sequences of phase shifted images with unknown phase steps using generalized n-dimensional lissajous figures—principles and applications," *International Journal of Optomechatronics*, vol. 8, no. 4, pp. 340–356, 2014.

[110] K. Yatabe, K. Ishikawa, and Y. Oikawa, "Hyper ellipse fitting in subspace method for phase-shifting interferometry: practical implementation with automatic pixel selection," *Opt. Express*, vol. 25, no. 23, pp. 29401–29416, 2017.

[111] Y. Chen and Q. Kemao, "Advanced iterative algorithm for phase extraction: performance evaluation and enhancement," *Opt. Express*, vol. 27, no. 26, pp. 37634–37651, 2019.

[112] M. A. Esobar, J. C. Estrada, and J. Vargas, "Phase-shifting VU factorization for interferometry," *Opt. Lasers Eng.*, vol. 124, p. 105797, 2020.

[113] M. Servin, M. Padilla, I. Choque, and S. Ordones, "Phase-stepping algorithms for synchronous demodulation of nonlinear phase-shifted fringes," *Opt. Express*, vol. 27, no. 4, pp. 5824–5834, 2019.

[114] I. Choque, M. Servin, M. Padilla, M. Asmad, and S. Ordones, "Phase measurement of nonuniform phase-shifted interferograms using the frequency transfer function," *Appl. Opt.*, vol. 58, no. 15, pp. 4157–4162, 2019.

[115] P. J. Huber and E. M. Ronchetti, *Robust statistics*. Wiley, 2009.

[116] A. E. Beaton and J. W. Tukey, "The fitting of power series, meaning polynomials, illustrated on band-spectroscopic data," *Technometrics*, vol. 16, pp. 147–185, 1974.

[117] P. W. Holland and R. E. Welsch, "Robust regression using iteratively reweighted least-squares," *Commun. Stat. Theory Methods*, vol. 6, pp. 813–827, 1977.

[118] M. J. Black and A. Rangarajan, "On the unification of line processes, outlier rejection, and robust statistics with applications in early vision," *International Journal of Computer Vision*, vol. 19, no. 1, pp. 57–91, 1996.

[119] S. Ordones, M. Servin, M. Padilla, I. Choque, A. Muñoz, and J. L. Flores, "Tukey's robust m-estimator for phase demodulation of interferograms with nonuniform shifts," *Appl. Opt.*, vol. 59, no. 20, pp. 6224–6230, 2020.

[120] A. Savitzky and M. J. E. Golay, "Smoothing and differentiation of data by simplified least squares procedures," *Analytical Chemistry*, vol. 36, pp. 1627–1639, 1964.

[121] D. Lay, *Linear algebra and it's applications*. Addison-Wesley, 2000.

[122] J. Vargas, J. A. Quiroga, C. O. S. Sorzano, J. C. Estrada, and J. M. Carazo, "Two-step demodulation based on the gram–schmidt orthonormalization method," *Opt. Lett.*, vol. 37, no. 3, pp. 443–445, 2012.

[123] I. T. Jolliffe, *Principal component analysis*. Springer Science & Business Media, 2 ed., 2002.

[124] K. Yatabe, K. Ishikawa, and Y. Oikawa, "Simple, flexible, and accurate phase retrieval method for generalized phase-shifting interferometry," *J. Opt. Soc. Am. A*, vol. 34, no. 1, pp. 87–98, 2017.

[125] K. Itoh, "Analysis of the phase unwrapping algorithm," *Appl. Opt.*, vol. 21, no. 14, pp. 2470–2470, 1982.

[126] D. Ghiglia, D. Ghiglia, M. Pritt, and M. Pritt, *Two-Dimensional Phase Unwrapping: Theory, Algorithms, and Software*. Living Away from Home: Studies, Wiley, 1998.

[127] J. Estrada, M. Servin, and J. Quiroga, "Noise robust linear dynamic system for phase unwrapping and smoothing," *Opt. Express*, vol. 19, no. 6, pp. 5126–5133, 2011.

[128] D. C. Ghilia and L. A. Romero, "Robust two-dimensional weighted and unweighted phase unwrapping that uses fast transforms and iterative methods," *J. Opt. Soc. Am. A*, vol. 11, no. 1, pp. 107–117, 1994.

[129] R. Kulkarni and P. Rastogi, "Fringe denoising algorithms: A review," *Opt. Lasers Eng.*, p. 106190, 2020.

[130] C. R. Vogel, *Computational methods for inverse problems*. SIAM, 2002.

[131] Q. Kemao, "On window size selection in the windowed fourier ridges algorithm," *Opt. Lasers Eng.*, vol. 45, no. 12, pp. 1186–1192, 2007.

[132] J. Zhong and J. Weng, "Generalized fourier analysis for phase retrieval of fringe pattern," *Opt. Express*, vol. 18, no. 26, pp. 26806–26820, 2010.

[133] R. Kulkarni and P. Rastogi, "Optical measurement techniques: a push for digitization," *Opt. Lasers Eng.*, vol. 87, pp. 1–17, 2016.

[134] S. Zhang, "Absolute phase retrieval methods for digital fringe projection profilometry: a review," *Opt. Lasers Eng.*, vol. 107, pp. 28–37, 2018.

[135] M. Takeda, H. Ina, and S. Kobayashi, "Fourier-transform method of fringe-pattern analysis for computer-based topography and interferometry," *J. Opt. Soc. Am.*, vol. 72, no. 1, pp. 156–160, 1982.

[136] C. Zuo, S. Feng, L. Huang, T. Tao, W. Yin, and Q. Chen, "Phase shifting algorithms for fringe projection profilometry: A review," *Optics and Lasers in Engineering*, vol. 109, pp. 23–59, 2018.

[137] J. Geng, "Structured-light 3d surface imaging: a tutorial," *Adv. Opt. Photon.*, vol. 3, no. 2, pp. 128–160, 2011.

[138] W. Li, T. Bothe, W. Osten, and M. Kalms, "Object adapted pattern projection–part i: generation of inverse patterns," *Optics and Lasers in Engineering*, vol. 41, no. 1, pp. 31–50, 2004.

[139] M. K. Kalms, W. P. O. Jueptner, and W. Osten, "Automatic adaption of projected fringe patterns using a programmable LCD-projector," in *Sensors, Sensor Systems, and Sensor Data Processing* (O. Loffeld, ed.), vol. 3100, pp. 156–165, International Society for Optics and Photonics, SPIE, 1997.

[140] M. K. Kalms, W. Osten, and W. P. O. Jueptner, "Inverse projected-fringe technique with automatic pattern adaption using a programmable spatial light modulator," in *International Conference on Applied Optical Metrology* (P. K. Rastogi and F. Gyimesi, eds.), vol. 3407, pp. 483–489, International Society for Optics and Photonics, SPIE, 1998.

[141] S. Ordones, M. Servin, M. Padilla, I. Choque, J. L. F. Nuñez, and A. Muñoz, "Shape defect measurement by fringe projection profilometry and phase-shifting algorithms," *Optical Engineering*, vol. 59, no. 1, pp. 1–10, 2020.

[142] J. Salvi, J. Pagès, and J. Batlle, "Pattern codification strategies in structured light systems," *Pattern Recognition*, vol. 37, no. 4, pp. 827–849, 2004.

[143] J. Salvi, S. Fernandez, T. Pribanic, and X. Llado, "A state of the art in structured light patterns for surface profilometry," *Pattern Recognition*, vol. 43, no. 8, pp. 2666–2680, 2010.

[144] S. Van der Jeught and J. J. Dirckx, "Real-time structured light profilometry: a review," *Optics and Lasers in Engineering*, vol. 87, pp. 18–31, 2016.

[145] N. Tornero-Martínez, G. Trujillo-Schiaffino, M. Anguiano-Morales, P. G. Mendoza-Villegas, D. P. Salas-Peimbert1, and L. F. Corral-Martínez, "Color profilometry techniques: A review," *Opt. Pura Apl.*, vol. 51, no. 4, pp. 1–26, 2018.

[146] J. Posdamer and M. Altschuler, "Surface measurement by space-encoded projected beam systems," *Computer Graphics and Image Processing*, vol. 18, no. 1, pp. 1–17, 1982.

[147] M. Minou, T. Kanade, and T. Sakai, "A method of time-coded parallel planes of light for depth measurement," *IEICE Transactions on Information and Systems*, vol. 64, no. 8, pp. 521–528, 1981.

[148] F. J. MacWilliams and N. J. A. Sloane, "Pseudo-random sequences and arrays," *Proceedings of the IEEE*, vol. 64, no. 12, pp. 1715–1729, 1976.

[149] H. Fredricksen, "A survey of full length nonlinear shift register cycle algorithms," *SIAM Review*, vol. 24, no. 2, pp. 195–221, 1982.

[150] T. P. Monks and J. N. Carter, "Improved stripe matching for colour encoded structured light," in *Computer Analysis of Images and Patterns* (D. Chetverikov and W. G. Kropatsch, eds.), (Berlin, Heidelberg), pp. 476–485, Springer Berlin Heidelberg, 1993.

[151] P. M. Griffin, L. S. Narasimhan, and S. R. Yee, "Generation of uniquely encoded light patterns for range data acquisition," *Pattern Recognition*, vol. 25, no. 6, pp. 609–616, 1992.

[152] J. Tajima and M. Iwakawa, "3-d data acquisition by rainbow range finder," in *[1990] Proceedings. 10th International Conference on Pattern Recognition*, vol. 1, pp. 309–313, 1990.

[153] T. Sato, "Multispectral pattern projection range finder," in *Three-Dimensional Image Capture and Applications II* (J. H. Nurre and B. D. Corner, eds.), vol. 3640, pp. 28–37, International Society for Optics and Photonics, SPIE, 1999.

[154] Y. Hu, J. Xi, J. Chicharo, and Z. Yang, "Blind color isolation for color-channel-based fringe pattern profilometry using digital projection," *J. Opt. Soc. Am. A*, vol. 24, no. 8, pp. 2372–2382, 2007.

[155] M. Padilla, M. Servin, and G. Garnica, "Fourier analysis of rgb fringe-projection profilometry and robust phase-demodulation methods against crosstalk distortion," *Opt. Express*, vol. 24, no. 14, pp. 15417–15428, 2016.

[156] J. L. Flores, A. Muñoz, S. Ordoñes, G. Garcia-Torales, and J. A. Ferrari, "Color-fringe pattern profilometry using an efficient iterative algorithm," *Optics Communications*, vol. 391, pp. 88–93, 2017.

[157] S. Zhang, *High-speed 3D imaging with digital fringe projection techniques.* CRC Press, 2016.

[158] P. S. Huang, C. Zhang, and F. P. Chiang, "High-speed 3-d shape measurement based on digital fringe projection," *Opt. Eng.*, vol. 42, pp. l63–168, 2003.

[159] X. Zhang, L. Zhu, Y. Li, and D. Tu, "Generic nonsinusoidal fringe model and gamma calibration in phase measuring proflometry," *J. Opt. Soc. Am. A*, vol. 29, no. 6, pp. 1047–1058, 2012.

[160] P. Zhou, X. Liu, Y. He, and T. Zhu, "Phase error analysis and compensation considering ambient light for phase measuring profilometry," *Optics and Lasers in Engineering*, vol. 55, pp. 99–104, 2014.

[161] H. Guo, H. He, and M. Chen, "Gamma correction for digital fringe projection profilometry," *Appl. Opt.*, vol. 43, no. 14, pp. 2906–2914, 2004.

[162] S. Zhang and S. T. Yau, "Generic nonsinusoidal phase error correction for three-dimensional shape measurement using a digital video projector," *Appl. Opt.*, vol. 46, no. 1, pp. 36–43, 2007.

[163] B. Pan, Q. Kemao, L. Huang, and A. Asundi, "Phase error analysis and compensation for nonsinusoidal waveforms in phase-shifting digital fringe projection profilometry," *Opt. Lett.*, vol. 34, no. 4, pp. 2906–2914, 2009.

[164] K. Liu, Y. Wang, D. L. Lau, Q. Hao, and L. G. Hassebrook, "Gamma model and its analysis for phase measuring profilometry," *J. Opt. Soc. Am. A*, vol. 27, no. 3, pp. 553–562, 2010.

[165] Y. Xu, L. Ekstrand, J. Dai, and S. Zhang, "Phase error compensation for three-dimensional shape measurement with projector defocusing," *Appl. Opt.*, vol. 50, no. 17, pp. 2572–2581, 2011.

[166] G. Wu, Y. Wu, X. Hu, M. Wu, S. Zhang, and F. Liu, "Exponential taylor series method to eliminate the gamma distortion in phase shifting profilometry," *Opt. Commun.*, vol. 452, pp. 306–312, 2019.

[167] T. Hoang, B. Pan, D. Nguyen, and Z. Wang, "Generic gamma correction for accuracy enhancement in fringe-projection profilometry," *Opt. Lett.*, vol. 35, no. 12, pp. 1992–1994, 2010.

[168] A. Muñoz, J. L. Flores, G. Parra-Escamilla, L. A. Morales, S. Ordones, and M. Servin, "Least-squares gamma estimation in fringe projection profilometry," *Appl. Opt.*, vol. 60, no. 5, pp. 1137–1142, 2021.

[169] J. A. Nelder and R. Mead, "A simplex method for function minimization," *Computer Journal*, vol. 7, pp. 308–313, 1965.

[170] M. Halioua and H.-C. Liu, "Optical three-dimensional sensing by phase measuring profilometry," *Optics and Lasers in Engineering*, vol. 11, no. 3, pp. 185–215, 1989.

[171] Z. Zhang, D. Zhang, and X. Peng, "Performance analysis of a 3d full-field sensor-based on fringe projection," *Optics and Lasers in Engineering*, vol. 42, pp. 341–353, 2004.

[172] Z. Huang, J. Xi, Y. Yu, Q. Guo, and L. Song, "Improved geometrical model of fringe projection profilometry," *Opt. Express*, vol. 22, no. 26, pp. 32220–32232, 2014.

[173] P. Jia, J. Kofman, and C. English, "Comparison of linear and nonlinear calibration methods for phase-measuring profilometry," *Opt. Eng.*, vol. 46, no. 4, pp. 043601–10, 2007.

[174] M. Vo, Z. Wang, T. Hoang, and D. Nguyen, "Flexible calibration technique for fringe-projection-based three-dimensional imaging," *Opt. Lett.*, vol. 35, no. 19, pp. 3192–3194, 2010.

[175] L. Huang, P. S. K. Chua, and A. Asundi, "Least-squares calibration method for fringe projection profilometry considering camera lens distortion," *Appl. Opt.*, vol. 49, no. 9, pp. 1539–1548, 2010.

[176] W. Zhao, X. Su, and W. Chen, "Discussion on accurate phase–height mapping in fringe projection profilometry," *Optical Engineering*, vol. 56, no. 10, pp. 1–11, 2017.

[177] M. Servin, G. Garnica, J. C. Estrada, and A. Quiroga, "Coherent digtal demodulation of single-camera n-projection for 3d-object shape measurement co-phased profilometry," *Opt. Express*, vol. 21, no. 21, pp. 24878–24878,, 2013.

[178] M. Servin, G. Garnica, and J. M. Padilla, "Co-phased 360-degree profilometry of discontinuous solids with 2-projectors and 1-camera," in *Latin America Optics and Photonics Conference*, p. LTh2B.2, Optical Society of America, 2014.

[179] J. M. Padilla, M. Servin, and G. Garnica, "Profilometry of discontinuous solids by means of co-phased demodulation of projected fringes with RGB encoding," in *Videometrics, Range Imaging, and Applications XIII* (F. Remondino and M. R. Shortis, eds.), vol. 9528, pp. 84–92, International Society for Optics and Photonics, SPIE, 2015.

[180] M. Servin, M. Padilla, G. Garnica, and A. Gonzalez, "Profilometry of three-dimensional discontinuous solids by combining two-steps temporal phase unwrapping, co-phased profilometry and phase-shifting interferometry," *Opt. and Lasers Eng.*, vol. 87, pp. 75–82, 2016.

[181] M. Servin, M. Padilla, and G. Garnica, "Temporal-multiplexing interferometry applied to co-phased profilometry," *arXiv*, p. arXiv:1702.06098, 2017.

[182] M. Servin, G. Garnica, J. C. Estrada, and J. M. Padilla, "High-resolution low-noise 360-degree digital solid reconstruction using phase-stepping profilometry," *Opt. Express*, vol. 22, no. 9, pp. 10914–10922, 2014.